THE UNIVERSITY OF CHICAGO

EVALUATING THE APPLICATION OF ELEMENTAL AND ISOTOPIC RATIOS AS PALEOREDOX TRACERS IN EARTH'S OCEANS AND MARS' AQUEOUS ALTERATION

A DISSERTATION SUBMITTED TO

THE FACULTY OF THE DIVISION OF THE PHYSICAL SCIENCES

IN CANDIDACY FOR THE DEGREE OF

DOCTOR OF PHILOSOPHY

DEPARTMENT OF THE GEOPHYSICAL SCIENCES

BY

XINYI LIU

CHICAGO, ILLINOIS

JUNE 2024

DEDICATION

This dissertation is dedicated to 张起灵, whose solitary and magnificent spirit has accompanied and inspired me since I first knew him a decade ago and will continue to do so in the years to come.

TABLE OF CONTENTS

LIST OF FIGURES

LIST OF TABLES

ACKNOWLEDGEMENTS

I would like to express my profound gratitude to everyone who supported me throughout the journey of my PhD, without whom this dissertation would not have been possible.

First and foremost, my deepest thanks go to Dr. Nicolas Dauphas, my advisor, for his recognition of my potential upon admitting me to the PhD program, and his guidance on not only how to do research but also how to think like a scientist. I am also very grateful to my committee members – Dr. Stephanie L. Olson, Dr. Andrew J. Campbell, Dr. Clara Blättler and Dr. Malte F. Jansen, whose constructive and insightful suggestions were crucial in shaping this dissertation.

My appreciation extends to NASA and the DOE for providing the financial support necessary for my research, and to the University of Chicago and Department of the Geophysical Sciences for offering the resources and facilities instrumental in my work.

My heartfelt thanks go to my colleagues and peers here at DoGS, especially the former and current members of the Origins Lab – Dr. Andrew Heard, Dr. Justin (Jingya) Hu, Dr. Cindy (Xi) Chen, Dr. Timo Hopp, Dr. Aleisha Johnson, Dr. Eric Siciliano Rego, James (Zhe) Zhang, Andrew Regula, Debarun Mukherjee – and Ashika Capirala at Purdue University, for their camaraderie, editing help, late-night email exchanges, and moral support.

On a personal note, I would like to give a big shout-out to my grandparents, 袁金玉 and 刘盛永, and my best friends from old times as well as met in Chicago, for always believing in me and reminding me to stay true. Lastly, I would be remiss in not mentioning my cat, Nagi/奶盖, for being always by my side.

These five years have been a transformative journey shared with many brilliant individuals. As always, I am grateful to the universe for every moment.

ABSTRACT

This dissertation critically evaluates the application of elemental and isotopic ratios as paleoredox tracers in early Earth's oceans and on early Mars' surface. It begins by questioning a common assumption in the field regarding the constancy of ocean mixing timescale throughout Earth's history and demonstrates with an Earth system model that the ocean mixing timescale has indeed only fluctuated between a few hundred and a couple of thousand years since the Archean. This foundational understanding informs subsequent analyses of neodymium (Nd) and uranium (U) isotopes as proxies for early oceanic conditions. Nd isotope modelling suggests that the heterogeneous Nd isotopic compositions recorded in Archean sedimentary archives primarily reflect continental and sedimentary influences, with a global Nd residence time on the order of the ocean mixing timescale in the Archean; a U mass balance model indicates a significantly reduced global U residence time in the anoxic Precambrian oceans compared to today, highlighting the importance of understanding the biogeochemical cycles of (redox sensitive) proxies in early oceans prior to the interpretation of sedimentary records.

Extending beyond terrestrial environments, this dissertation explores the potential of iron-manganese and iron isotopic fractionations as tracers of redox conditions during aqueous alteration of mafic minerals on early Mars. Nuclear Resonant Inelastic X-ray Scattering (NRIXS) measurements of Martian clay analogs confirm a strong redox control on equilibrium iron isotopic fractionation during clay formation, and an iron oxidation kinetics-based alteration model exhibits good model-data correlation with paleosol records >1.85 Ga, promising a novel framework for inferring pedogenic redox conditions on Mars from future sample returns.

Together, these findings not only underscore the intricate understanding necessary for interpreting sedimentary archives with paleoredox tracers, but also bridge geochemical insights between early Earth and Mars. By questioning long-held assumptions and introducing novel methodologies, this dissertation significantly enhances our geochemical toolkit for investigating the redox evolution on the surface of planetary bodies.

1 INTRODUCTION

1.1 Objectives

Researchers have long explored Earth's redox evolution through the lens of sedimentary archives, primarily due to molecular oxygen's pivotal role in early life evolution. Oxygenic photosynthesis by cyanobacteria prompted the development of aerobic metabolism and multicellularity, allowing Earth to foster complex life, potentially unparalleled in the universe.

As we extend our curiosity to extraterrestrial worlds, Mars, with its Earth-like qualities, stands out as a focal point. Despite its present barrenness, early Mars likely hosted habitable conditions, as suggested by its geomorphological and geochemical features.

This dissertation answers the following key questions regarding redox evolution on early Earth and Mars through the application of geochemical tracers in sedimentary records:

1) How did Earth's geophysical evolution affect the mixing timescale of the Precambrian oceans? While modern and ancient oceans have been perceived as having similar mixing behaviors, variations in Earth's geophysical past suggest otherwise. Evolving ocean mixing patterns and timescales have important consequences for Earth's oxygenation, both directly by modifying marine biogeochemical cycles as well as indirectly by affecting the interpretation of marine sediments using paleoredox tracers. This work presents the first quantitative investigation of mixing timescales and patterns of Precambrian oceans using Earth system model simulations.
2) How did the evolution of tracers' biogeochemical cycles affect their expression in sedimentary archives? For paleoredox tracers, their residence times as determined by biogeochemical cycles should significantly exceed ocean mixing timescales to

faithfully record global oceanic redox states. Building upon our conclusion on Precambrian ocean mixing timescales, this work models the Nd and U budgets in early oceans as examples of isotopic tracers with endmember residence times to challenge the assumption of modern tracer residence times in early oceans.

3) Could the iron cation and isotopic chemistry of clay minerals trace the redox conditions during aqueous alteration on the surface of Mars and Earth? Interpreting redox conditions from the chemical composition of iron-bearing clay minerals is complex due to factors like post-depositional oxidation. The fractionation of iron from other common metals in clay minerals and iron isotopic fractionation could potentially record iron mobilization and thus redox conditions during clay formation. This work develops an interpretative framework that correlates the redox-driven fractionations of Fe/Mn and δ^{56}Fe, validated using terrestrial paleosol records.

1.2 Principles of paleoredox tracers

For the Precambrian when the macro-paleontological record was mostly missing, geochemical proxies in the sedimentary record provide the only window into the redox conditions on Earth's surface. Redox sensitive trace metals such as V, Mo, Re and rare earth elements (REEs), either dissolved in seawater or adsorbed onto particles, can be deposited into sediments through redox-driven biotic or abiotic processes. The resulting metal enrichment in marine sediments serves as an indicator of redox conditions during deposition or early diagenesis (Tribovillard et al., 2006). Yet, local factors at deposition sites, including varied sedimentation and mass accumulation rates, can influence these element abundances (Partin et al., 2013). Non-traditional stable isotopes,

such as Fe, Cr, and U, enhance our understanding of paleoredox conditions via equilibrium or kinetic fractionation between metal oxidation states. While theoretical models often predict heavier isotope enrichment in oxidized species, exceptions like U exist, and empirical studies on specific redox fractionation remain limited (*e.g.*, Welch et al., 2003; Andersen et al., 2014). With well-characterized isotope systematics, the combination of redox sensitive trace metals and their isotopes could yield powerful reconstruction of global redox conditions in deep time.

1.2.1 Redox sensitive trace metals and REEs

Trace metals such as vanadium (V), uranium (U), molybdenum (Mo), and rhenium (Re) have been widely used as paleoredox proxies due to their distinctive behaviors under varied redox conditions (Bennett and Canfield 2020; Fig. 1-1). Uranium, for example, exists in oxic seawater mainly as U(VI) in the conservative form of uranyl ions, binding to carbonate ions without undergoing reduction to U(IV) or being scavenged by particulates. Authigenic U enrichment is considered to take place primarily in sediments under conditions similar to those of Fe(III) to Fe(II) reduction, within the typical pH and alkalinity ranges of seawater (Tribovillard et al., 2006). Among the rare earth elements (REEs), cerium (Ce) has unique redox-sensitive properties that allow it to track redox cycling in various aqueous environments. Ce is oxidized from Ce(III) to insoluble Ce(IV) in oxygenated waters and accumulates either as discrete Ce oxide particles or on the surface of manganese and other oxides, and reverse reactions take place under intermediate manganous conditions. This behavior results in a strong negative Ce anomaly in modern oxygenated seawater, which potentially serves as a redox proxy in deep time since Ce anomalies can be preserved in chemical sediments (Tostevin 2021).

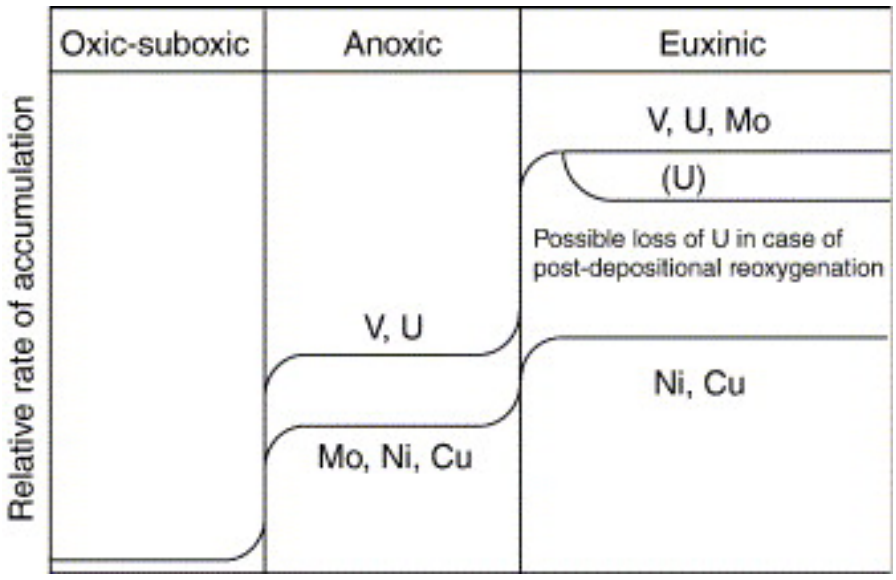

Figure 1-1 Schematic behavior of various trace metals as a function of the redox state of depositional environment, adapted from Tribovillard et al. (2006).

These paleoredox tracers have a wide range of applications regarding Earth's redox history. For example, Mo and Re abundances in 2.6- to 2.5-billion-year-old shales have been used to indicate that parts of Earth's surface were already oxygenated before the Great Oxidation Event (Anbar et al., 2007; Kendall et al., 2010). A multi-proxy approach combined with Ce anomalies was applied to other types of sediments (mudstones, carbonates) in the Proterozoic to deliver new insights into the regional redox conditions in the oceans (*e.g.*, Zhang et al., 2016; Mishra and Mohanty 2021; Liu et al., 2021).

Although the application of redox-sensitive trace metals and REEs yields important information about past redox conditions, several caveats exist. Post-depositional alteration could impact the preservation and distribution of these trace metals in the sediments (*e.g.*, Morford et al., 2001; Algeo and Maynard 2004). Accurate redox interpretations also require considering factors like sedimentation rate fluctuations and organic matter fluxes (*e.g.*, Crusius and Thomson, 2000; Tribovillard et al. 2006). Additionally, it is problematic to universally apply proxy thresholds

derived from one geological formation to different formations with distinct characteristics like age, depositional environment, and redox dynamics (Algeo and Liu 2020). Hence, a tailored, comprehensive examination of multiple redox indicators for each geological setting is essential.

1.2.2 Non-traditional stable isotopes

Over the past two decades, advancements in analytics have extended high-precision stable isotope analyses beyond traditional elements like H, C, O, N, and S. Now, Fe, Cr, Mo, and U isotopes are frequently employed as paleoredox proxies (*e.g.*, Johnson et al., 2008; Lau et al., 2019; Cole et al., 2016; Dickson 2017). These redox sensitive metals have multiple stable isotopes, and isotope fractionations typically occur during changes in redox states. It is worth noting that processes such as adsorption or ligand exchange can fractionate isotopes as a function of redox conditions without changing the redox state of the metals (Severmann and Anbar 2009).

Depending on the conservative or nonconservative behavior of metals in the ocean, isotope paleoredox tracers are regarded respectively as global or local proxies of redox conditions. Conservative elements have residence time in the ocean longer than the mixing time of the ocean, such as Mo (~780 kyr; Colodner et al., 1995), U (~400 kyr; Colodner et al., 1995) and Re (~130 kyr; Miller et al., 2011) in the modern ocean. The usefulness of conservative metals in recording global redox signals in ancient oceans comes from different isotopic compositions caused by uptake into oxic as compared to anoxic marine sediments, which reflect the seawater isotopic compositions either directly or with consistent offset. By analyzing the isotopic compositions of conservative metals in sedimentary records and thereby seawater, which depend on the relative sizes of their sinks (Fig. 1-2), we gain insights into the relative prevalence of oxygen-rich and

oxygen-poor environments at that time. Uranium isotopes ($^{238}U/^{235}U$), for example, provide unique information that cannot be inferred from metal abundance alone. The largest fractionation of $^{238}U/^{235}U$ occurs between U(VI) and U(IV) and therefore $\delta^{238}U$ is suggested to track biotic or abiotic U reduction (Brown et al., 2018). Since most or all U reduction takes place at the sediment-water interface (Lau et al., 2019), more extensive global seafloor anoxia is expected to result in more negative seawater $\delta^{238}U$, which is recorded in sedimentary archives.

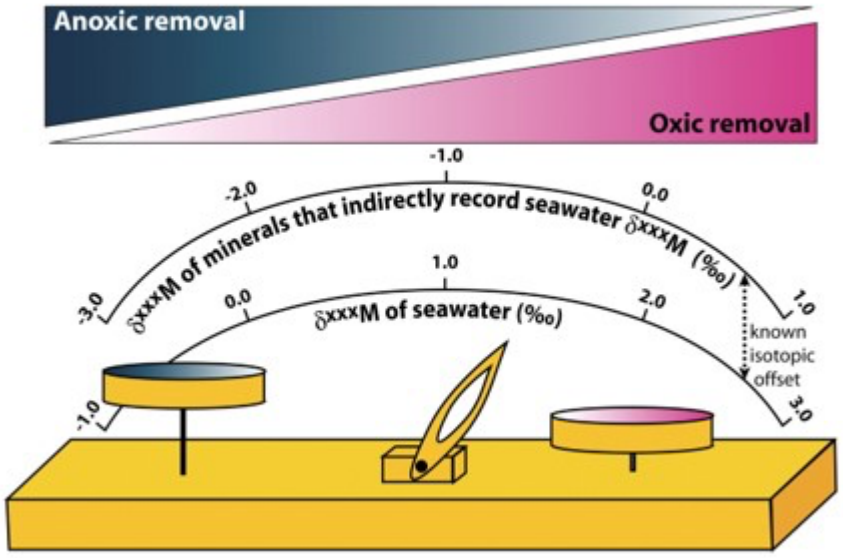

Figure 1-2 Schematic depiction of the relationship between seawater isotope composition and the relative sizes of the anoxic and oxic sinks, adapted from Severmann and Anbar (2009).

In contrast, redox sensitive trace metals with short residence times have concentrations that can vary significantly during local biological and chemical reactions in the ocean. Iron, with its residence time of 100 to 200 years in the modern ocean (Boyd and Ellwood 2010), is a good representative. Iron isotopes, specifically the $^{56}Fe/^{54}Fe$ ratio, vary primarily based on redox conditions. Iron in its reduced form, Fe(II), is more soluble (?) and has a lighter isotopic composition compared to its oxidized form, Fe(III). Many biotic and abiotic redox processes fractionate iron isotopes, such as dissimilatory Fe(III) reduction (Beard et al., 1999), anaerobic

photosynthetic Fe(II) oxidation (Croal et al., 2004), abiotic Fe(II) oxidation (Balci et al., 2006), and Fe(II) sorption onto ferric hydroxides (Icopini et al., 2004). Theoretical calculations have found equilibrium isotope fractionation as large as 3‰ between Fe(III) and Fe(II) aqueous species (Anbar et al., 2005). In the modern oxygenated ocean, iron isotopes can only be used to infer the redox conditions where iron is immediately oxidized or reduced, whereas in restricted reducing basins such as the Black Sea, isotopically light Fe(II) produced on basin margins can travel into the water column and to deeper, sulfide-rich waters and consequently be sequestered into pyrites (Wijsman et al., 2001). In this case, iron isotopes can provide insights into the redox conditions of both local sediments and the entire basin.

Since iron plays a role in maintaining the redox balance of Earth's surface, its concentration and isotopic composition in seawater were influenced by the emergence of atmospheric oxygen. Recent studies examining the iron isotope composition in ancient marine sediments have revealed three distinct stages in Earth's redox history, which resemble those identified by other paleoredox tracers (Fig. 1-3). In contrast to iron, trace metals with longer residence times such as Mo and its isotopes serve as an effective global redox proxy throughout Earth's history, assuming little variation in the ocean mixing timescale and oceanic concentration of metal. For example, Mo isotopes in modern and ancient black shales indicate expanded anoxia during the mid-Proterozoic compared to the modern ocean (Arnold et al., 2004).

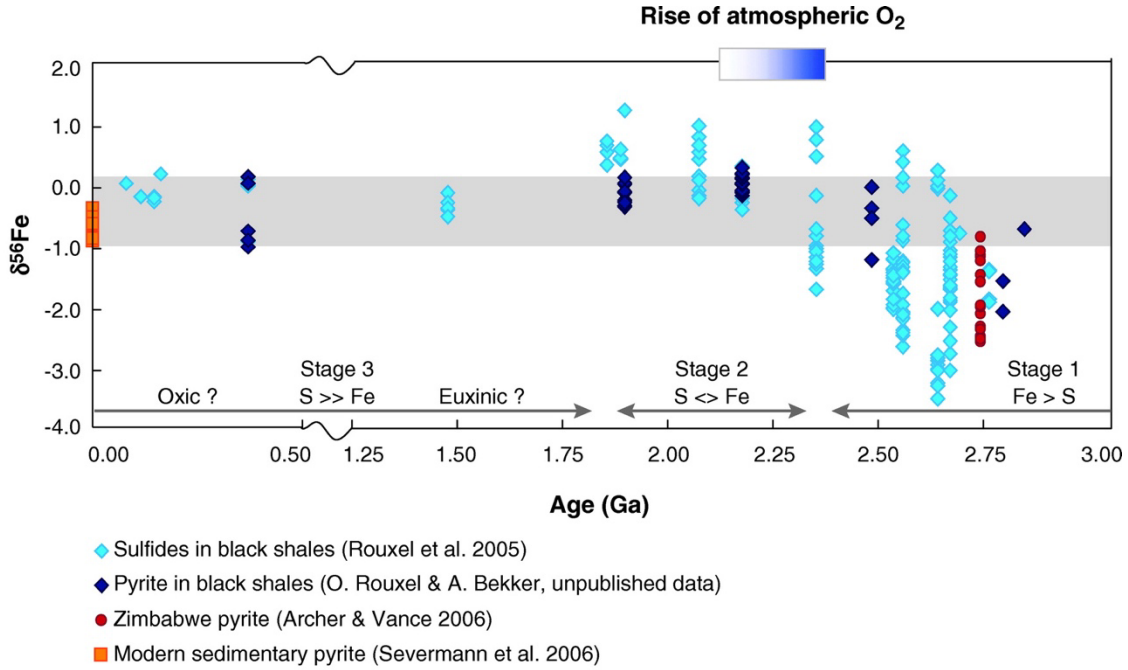

Figure 1-3 δ^{56}Fe values versus sample age for pyrite in organic-rich marine sediments, adapted from Anbar and Rouxel (2007).

Many new non-traditional stable isotope systems are under development for their paleoredox potential such as Re, V and Tl (*e.g.*, Miller et al., 2015; Heard et al., 2023). When exploring the isotope variations for less-well-studied trace metals, it is important to understand the metals' biogeochemical behavior, especially whether they are conservative or non-conservative in the geological time of interest.

1.3 Redox evolution on Earth and beyond

Redox reactions are integral to shaping the biogeochemical cycles on planets' surface. They drive the transformation of elements between different oxidation states, which directly affect the chemical compositions of rocky planets' surface, hydrosphere, and atmosphere. For example, the transformation of ferrous to ferric iron results in the deposition of specific mineral assemblages on Earth's surface, such as banded iron formations (BIFs). Similarly in the carbon cycle, the

reduction of CO_2 forms organic molecules, while the oxidation of organic carbon cycles CO_2 back into the atmosphere.

More importantly, redox evolution has been paramount to both the origin of life on Earth and the broader field of astrobiology. Planets with atmospheres ranging from weakly to highly reducing states are thought to create environments conducive for forming prebiotic molecules, setting the stage for biogenesis (Towe 1981). Later in Earth's history, the emergence of oxygenic photosynthesis dramatically altered the planet's redox state through the production of free oxygen, which in turn supported the development of an oxygen-rich atmosphere. An oxygenated atmosphere helps protect life from harmful ultraviolet radiation by facilitating the formation of an ozone layer. Given that the current highly oxidized condition of Earth's atmosphere and much of its surface is attributable to biological activity (Wordsworth et al., 2018), oxygen emerges as a potential biosignature (*e.g.*, Seager et al., 2012; Meadows et al., 2018). Thus, a comprehensive understanding of the factors that control the redox evolution of a planet's surface and atmosphere is fundamental to future endeavors aimed at detecting life on extraterrestrial worlds.

1.3.1 Earth's redox evolution

During the Hadean Eon, Earth's surface was dominated by volcanic activity, and its atmosphere was likely composed of volcanic gases such as methane, water vapor, and nitrogen, which provided a reducing environment (Zahnle et al., 2010). The absence of free oxygen implies that organic molecules could persist without the threat of oxidative stress (Taverne et al., 2018). Evidence for crust-forming processes and komatiitic volcanism further suggests that many suitable

sites could have supported the earliest living communities and the evolution of key enzymes in the Hadean (Harrison 2009; Arndt and Nisbet 2012).

By the Archean Eon, the formation of the first continents and the emergence of life began to influence Earth's redox state (Fig. 1-4). The oldest evidence of life dates back to ~3.5 billion years ago in the form of stromatolites (Schopf et al., 2007). This life possibly existed through anoxygenic photosynthesis, utilizing compounds like hydrogen, hydrogen sulfide, or ferrous iron (Olson 2006). The oxygen content of the Archean atmosphere was generally low ($<10^{-5}$ PAL) based on large degrees of mass-independent fractionation of the sulfur isotopes in pre-2.45 Gyr sedimentary rocks (Pavlov and Kasting 2002). While the deeper oceans and much of the shallow oceans remained similarly anoxic through the late Archean, locally oxygenated environments (oxygen oases) developed in habitats of aerobic ecosystems where the oxygen production rate exceeded its removal rate (Olson et al., 2013).

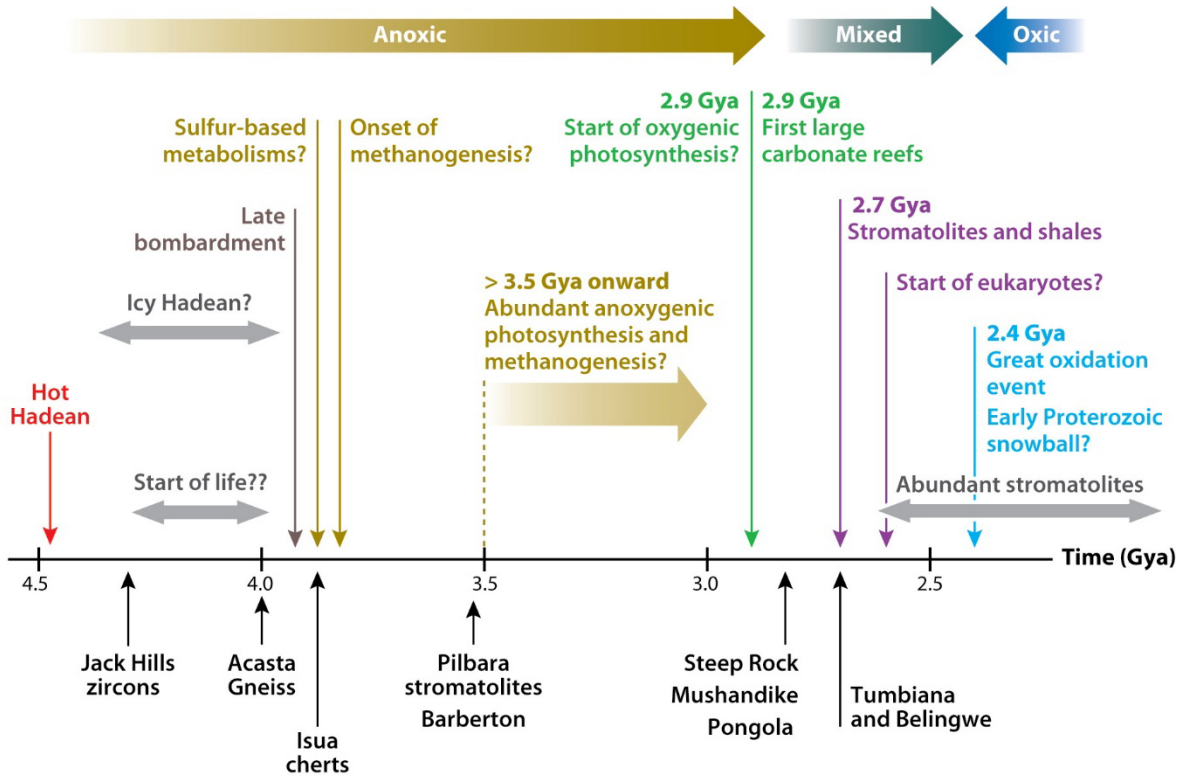

Figure 1-4 Earth's atmospheric evolution from Hadean to Archean Eons, adapted from Arndt and Nisbet (2012).

Between 2.4 and 2.2 billion years ago, a pivotal shift occurred: the Great Oxidation Event (Bekker et al., 2004). Atmospheric oxygen levels accumulated rapidly as a result of cyanobacterial activity (Schirrmeister et al., 2015), which eventually outstripped oxygen-consuming processes, as evidenced by the absence of BIFs from the geologic record between 2.4 and 2.0 Ga, for example (Canfield 2005). Along with other significant variations in Earth's redox system, such as decrease in the hydrothermal flux of H_2 and H_2S and changes in the nutrient flux to the oceans (Holland 2006), the surface ocean became mildly oxygenated and atmospheric pO_2 could have increased to between 0.1 and 5% PAL (Yang and Holland 2003).

During the Proterozoic, O_2 levels remained lower than modern concentrations but underwent multiple fluctuations. The absence of marine manganese deposits during 1.8 and 0.8

Ga suggests that the deep oceans were mildly oxygenated, probably due to a very small delivery rate of organic matter to the deep oceans (Holland 2006). The Neoproterozoic (~1,000 to 542 million years ago) was more interesting than the preceding "boring billion" due to several dramatic geological and biological events that shaped the Earth and life on it. Large fluctuations in the carbon cycle were associated with two glaciation events (possible Snowball Earth; Lenton et al., 2014), leading to massive changes in the redox state of the oceans, ultimately oxygenating the deep ocean during the Neoproterozoic Oxygenation Event (Shields-Zhou and Och, 2011) with occasional oceanic anoxia (Meyer and Kump, 2008). Molecular evidence from ancient rocks, particularly the presence of biomarkers like steranes and 2-methylhopanes, suggests that complex eukaryotic life began to evolve and diversify in these moderately oxygenated conditions (Gold 2018).

The onset of the Phanerozoic witnessed the Cambrian explosion (~541 million years ago; Marshall 2006), where the rapid diversification of multicellular life occurred. Higher oxygen levels might have been a catalyst, as more complex life forms require more O_2 for metabolic activities (Budd and Jensen 2000). Throughout the Phanerozoic, the redox state of the Earth's surface has oscillated, likely tied to various biological, tectonic, and climatic events (Fig. 1-5). However, it remained predominantly oxidizing, especially when compared to the early Earth. During this period, the evolution of land plants from the Silurian-Devonian further accelerated the oxygenation of the atmosphere due to increased organic carbon burial (Dahl and Arens 2020). Moreover, several mass extinctions, such as the Permian-Triassic and Ordovician-Silurian events, influenced Earth's redox state both directly by organic carbon burial and indirectly by perturbing Earth's ecosystems (*e.g.*, Xiang et al., 2016; Dahl et al., 2021).

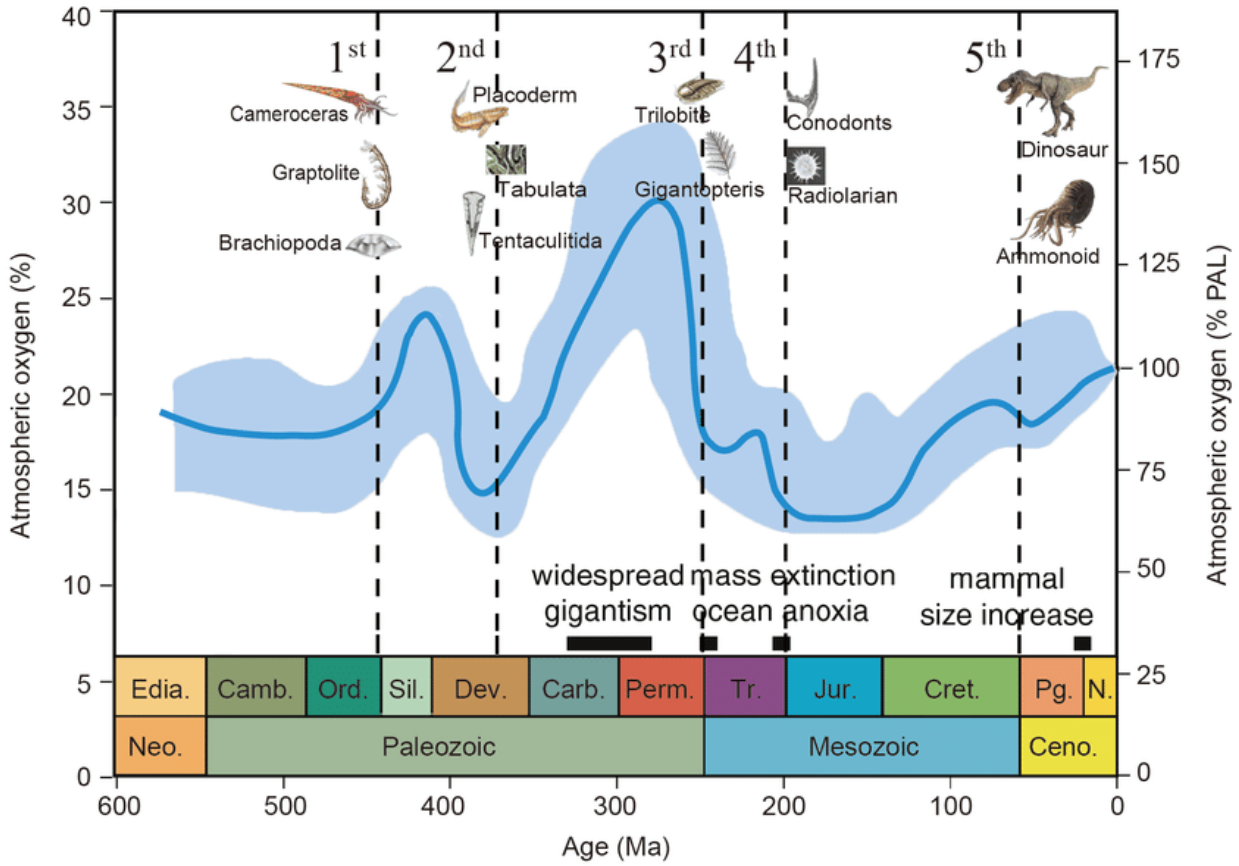

Figure 1-5 Reconstructed O_2 content during the Phanerozoic Eon, adapted from Huang et al. (2021).

1.3.2 Mars' redox evolution

The primordial Martian atmosphere is hypothesized to have been dominated by CO_2, N_2, and H_2O, with trace amounts of H_2 and other volatiles (Thomas et al., 2023). Early in its history, volcanic activity could have contributed significant amounts of reducing gases, such as H_2 and CO (Sholes et al., 2017). The presence of H_2, in combination with CO_2, could facilitate the formation of methane (CH_4), suggesting a reducing greenhouse environment on the early Martian surface as supported by widespread Fe loss in Martian paleosols (Liu et al., 2021).

Over the past two decades, orbital infrared spectroscopy and in situ exploration by rovers have discovered phyllosilicates, sulfates, and other hydrated minerals on Mars' surface (Ehlmann et al., 2014). Laboratory experiments under Mars-like conditions have been conducted to investigate the relationship between mineralogy and redox conditions on early Mars (*e.g.*, Dehouck et al., 2016; Gaudin et al., 2018). Phyllosilicates, such as clays, are typically associated with neutral to basic pH and reducing conditions (Chemtob et al., 2017). On the other hand, sulfates indicate an oxidizing, acidic environment (Dehouck et al., 2012). The spatial and temporal distribution of these minerals is pivotal to understanding the redox conditions on Mars (Fig. 1-6).

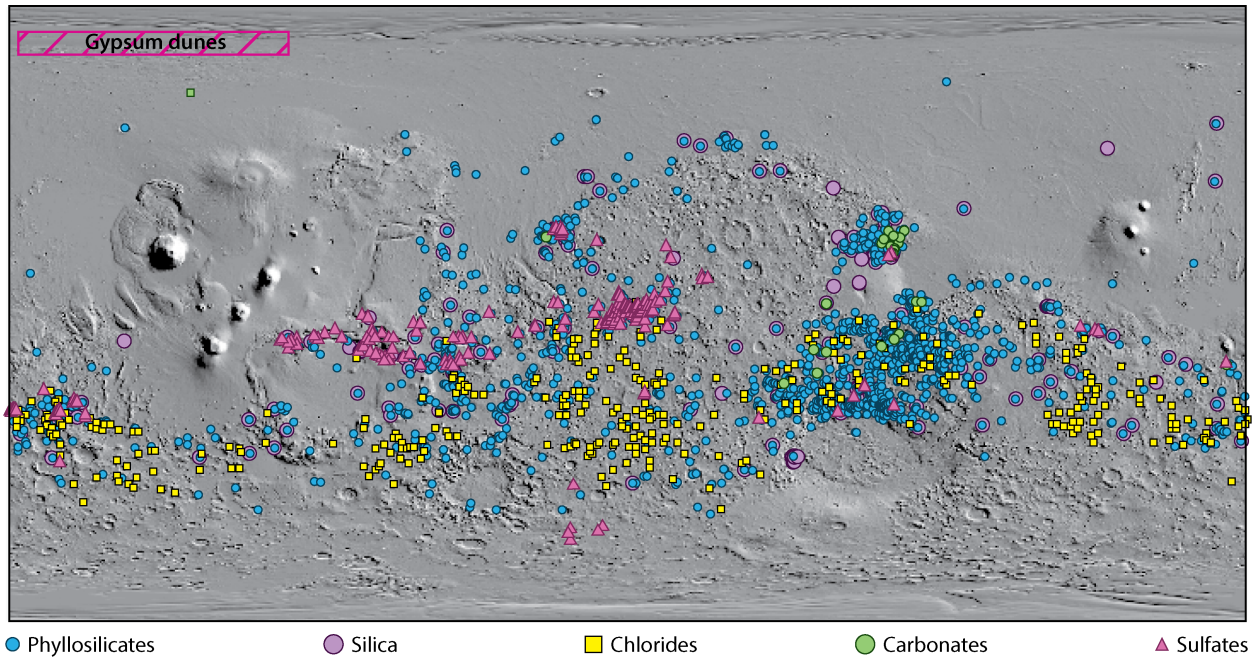

Figure 1-6 Global distribution of the major classes of aqueous minerals on Mars, adapted from Ehlmann and Edwards (2014). Dunes enriched in gypsum are located in and around the northern plains.

Around the Noachian-Hesperian boundary, roughly 3.5 billion years ago, there was a significant shift in the Martian surface environment (Fig. 1-7). The decline of Mars' magnetic field, combined with increased solar wind erosion, led to the significant loss of its atmosphere (Jakosky and Phillips, 2001). Consequently, Mars' surface began to oxidize. This transition is

evident from the widespread distribution of iron oxides like hematite that give Mars its distinctive red color. Moreover, the detection of perchlorates in the Martian soil by the Phoenix lander, later confirmed by the Curiosity rover, further attests to the oxidizing conditions of the surface (Hecht et al., 2009). Perchlorates are highly oxidized compounds, and their formation suggests an oxidation process potentially driven by photochemical reactions in the thin Martian atmosphere. The dichotomy between reducing and oxidizing environments offers tantalizing hints about potential habitats for life. Reducing conditions in the presence of liquid water could support methanogenesis, a form of microbial metabolism. However, the transition to more oxidizing conditions and a cooling climate might have made the surface less hospitable for such life forms (Sauterey et al., 2022). Yet, oxidizing conditions, particularly the presence of perchlorates, might still support certain extremophilic organisms known on Earth (Rummel et al., 2014).

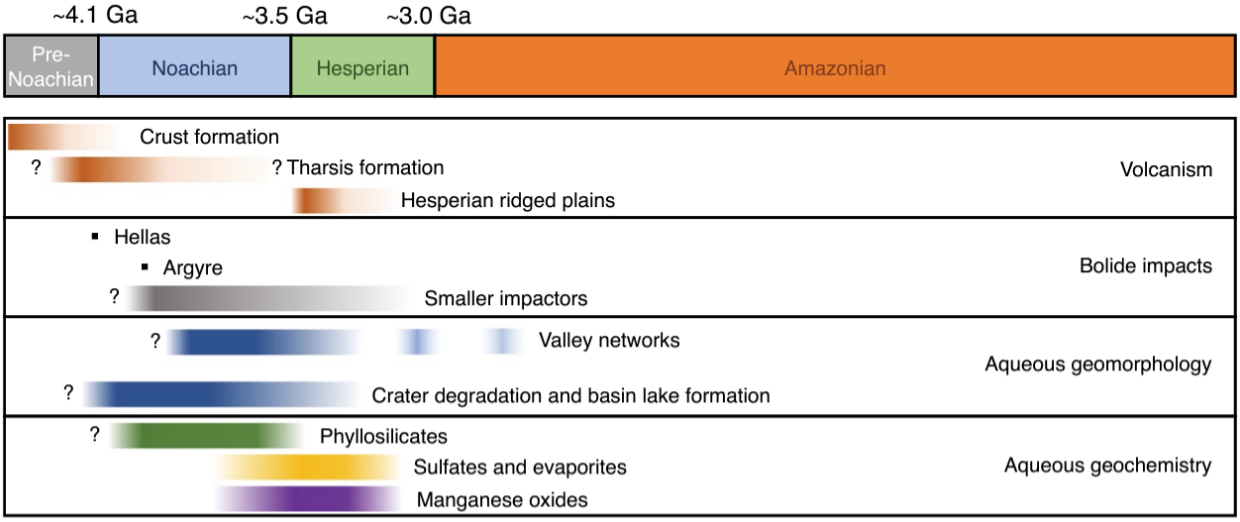

Figure 1-7 Timeline of major events on the Martian surface from geological observations, adapted from Wordsworth et al. (2021).

While contemporary Mars is largely oxidizing, there are potential niches where reducing conditions might prevail. For instance, deep subsurface environments, where liquid water aquifers might exist, could remain reducing, providing potential refuges for life (Michalski et al., 2013).

The potential seasonal flows of briny water, known as recurrent slope lineae, could also offer transient redox gradients suitable for microbial life (Jones 2018).

The redox histories of Earth and Mars share a number of similarities and differences (Fig. 1-8). In their early stages, both planets were characterized by reducing environments in the presence of liquid water. While Earth's oceans have been persistent, Mars displayed evidence of rivers, lakes, and possibly oceans as well during its Noachian epoch (Fassett and Head 2008). While the surface environments of both planets became oxidizing later in their histories, the distinct causes resulted in dramatic divergence in their fate. Earth has continuously benefited from its vast oceans, which influence its redox condition and facilitate life, whereas Mars saw a gradual decline in its surface water early on, which diminished crucial weathering processes that would otherwise impact redox conditions.

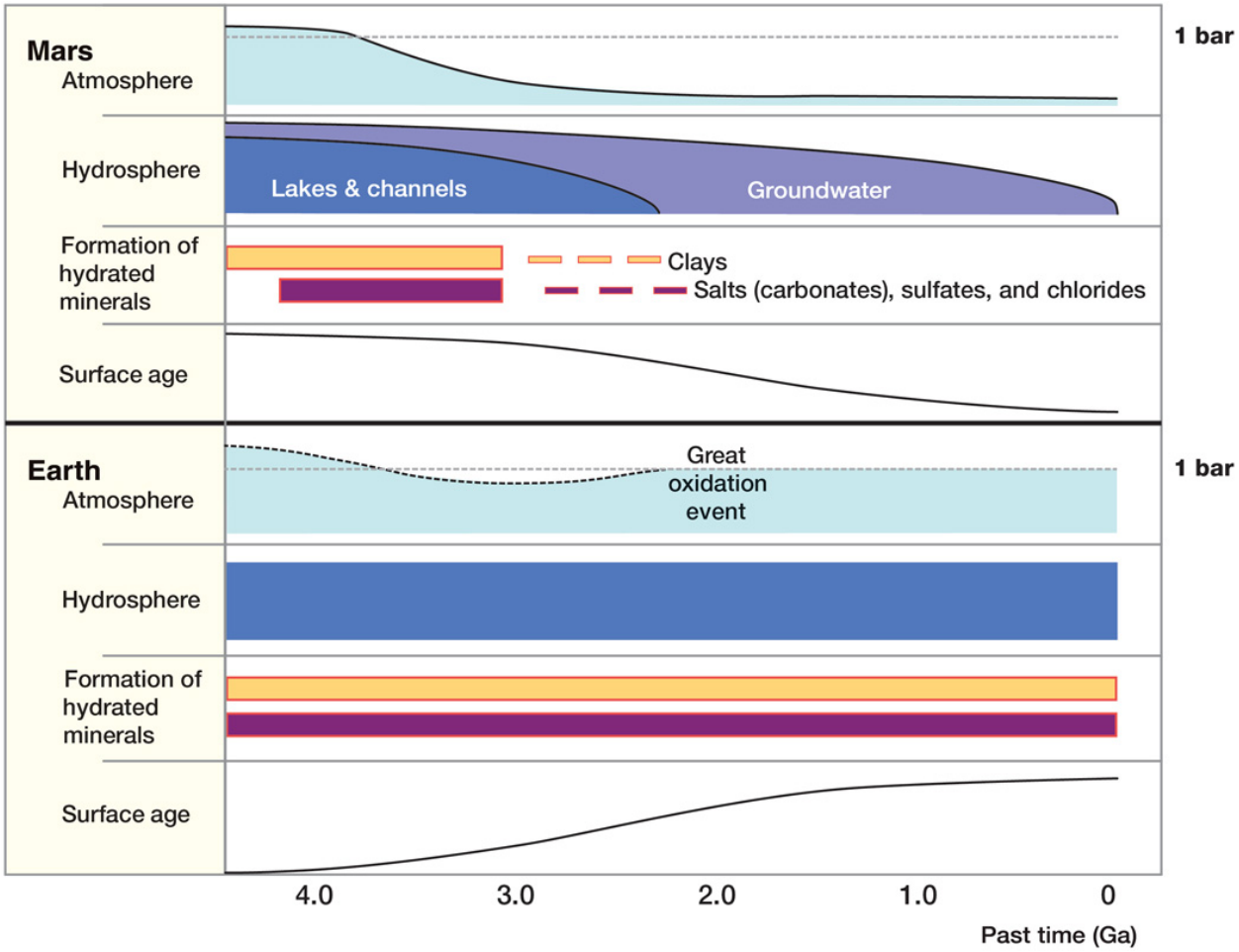

Figure 1-8 Schematic timeline for Mars and Earth, adapted from Sasselov et al. (2020). Surface age refers to crater retention age for Mars and preserved rock record for Earth.

In summary, the redox history of a planet provides a window into its past environmental conditions, potential biochemical pathways, and the possible evolution of life. Proper application of paleoredox tracers ensures that these reconstructions are accurate, guiding our investigations of the evolution of life on Earth and habitability on other planets.

1.4 Synopsis of chapters

Chapter 2 examines the common, but often implicit, assumption that the ocean mixing timescale did not differ substantially from present-day throughout Earth's history. An ocean

mixing timescale that was different than today could affect the spatial distributions of widely used geochemical tracers in ancient seawater, complicating interpretations of sedimentary archives. It is thus important to quantify the potential variability of ocean mixing timescales and patterns. We use an Earth system model called cGENIE to investigate the sensitivity of ocean mixing dynamics to several parameters and processes that are known to have changed through Earth's history, such as day length, surface pressure, continental configuration, and tidal dissipation. Model experiments indicate that Earth's ocean mixing timescale has only fluctuated between a few hundred and a couple of thousand years since the Archean. This result provides a robust framework for understanding the geochemical evolution of Earth's oceans using isotopic proxies with well-constrained residence times in Precambrian oceans.

Chapter 3 assesses the roles of neodymium (Nd) and uranium (U) isotopic ratios in reconstructing the geochemical conditions of early oceans from sedimentary records, building upon our model constraints on Precambrian ocean mixing timescales. Nd, with a short modern oceanic residence time of 0.3-0.8 kyr and minimal biochemical influence, potentially offers a window into the mixing processes and the provenance of rare earth elements (and iron) in early oceans. In contrast, U, with a long modern oceanic residence time of 400 kyr and redox sensitive behavior, presents its isotopic composition in seawater as a viable indicator of global oceanic redox evolution. However, accurately interpreting these isotopic signals requires a comprehensive understanding of Nd and U budgets in the early oceans. Our research includes Nd isotope modelling in cGENIE that maps the Nd isotopic variations in Archean oceans and a U mass balance model that integrates redox-sensitive trace metal burial rates with seafloor redox distribution, both further calibrated with sedimentary data. Results indicate that in the Precambrian oceans, Nd

residence time likely remained similar to the ocean mixing timescales, and the heterogeneous seawater Nd isotopic compositions recorded in Archean BIFs may reflect continental and sedimentary instead of hydrothermal influences. Meanwhile, the global U residence time potentially decreased to ~18 kyr, significantly lower than its present-day value but still longer than the Precambrian ocean mixing timescales. Nonetheless, these insights raise concerns about using paleoredox tracers with inherently shorter modern oceanic residence times (*e.g.*, Re, V and Cr) in sedimentary record interpretations.

Chapter 4 looks at the redox condition during aqueous alteration of mafic minerals and subsequently clay formation on early Mars. Noachian and early Hesperian-aged iron-bearing clay minerals formed by open-system low temperature aqueous alteration potentially recorded the redox conditions of the alteration fluids due to the immobility of oxidized Fe^{3+}. We select 16 Cenozoic terrestrial clays that have been used as Martian mineralogical analogues to study their major element and iron isotopic compositions (ranging from -0.38 to +1.41‰), and we also find strong redox control on their iron force constants from NRIXS measurements. To isolate the redox control on Fe mobilization from post-depositional processes, we develop an interpretative framework that correlates the redox-driven fractionations of Fe/Mn and δ^{56}Fe. Under more reducing conditions, little Fe/Mn fractionation and relatively large δ^{56}Fe due to Rayleigh distillation are expected in the residue. Under more oxidizing conditions, Fe/Mn fractionation will be significant, and instantaneous isotopic fractionation between fluid and mineral might result in large δ^{56}Fe, if not all Fe is oxidized *in situ*. We compile >1.85 Ga terrestrial paleosol profiles that developed from basaltic parents to evaluate the ability of our model to constrain redox conditions during the alteration of mafic minerals. Despite the lack of iron isotopic data, there exists a good

agreement between our model predictions and the redox condition during primary alteration inferred by other geochemical and mineralogical evidence. By combining our quantitative model with iron chemistry and isotope measurements of water-rock alteration products from future Martian sample return, we will be able to constrain the redox condition during their formation at the surface of Mars.

REFERENCES

Algeo, T. J., & Maynard, J. B. (2004). Trace-element behavior and redox facies in core shales of Upper Pennsylvanian Kansas-type cyclothems. *Chemical geology*, *206*(3-4), 289-318.

Algeo, T. J., & Liu, J. (2020). A re-assessment of elemental proxies for paleoredox analysis. *Chemical Geology*, *540*, 119549.

Anbar, A. D., Jarzecki, A. A., & Spiro, T. G. (2005). Theoretical investigation of iron isotope fractionation between Fe (H2O) 63+ and Fe (H2O) 62+: implications for iron stable isotope geochemistry. *Geochimica et Cosmochimica Acta*, *69*(4), 825-837.

Anbar, A. D., & Rouxel, O. (2007). Metal stable isotopes in paleoceanography. *Annu. Rev. Earth Planet. Sci.*, *35*, 717-746.

Anbar, A. D., Duan, Y., Lyons, T. W., Arnold, G. L., Kendall, B., Creaser, R. A., ... & Buick, R. (2007). A whiff of oxygen before the great oxidation event?. *Science*, *317*(5846), 1903-1906.

Andersen, M. B., Romaniello, S., Vance, D., Little, S. H., Herdman, R., & Lyons, T. W. (2014). A modern framework for the interpretation of 238U/235U in studies of ancient ocean redox. *Earth and Planetary Science Letters*, *400*, 184-194

Arndt, N. T., & Nisbet, E. G. (2012). Processes on the young Earth and the habitats of early life. *Annual Review of Earth and Planetary Sciences*, *40*, 521-549.

Arnold, G. L., Anbar, A. D., Barling, J., & Lyons, T. W. (2004). Molybdenum isotope evidence for widespread anoxia in mid-Proterozoic oceans. *science*, *304*(5667), 87-90.

Balci, N., Bullen, T. D., Witte-Lien, K., Shanks, W. C., Motelica, M., & Mandernack, K. W. (2006). Iron isotope fractionation during microbially stimulated Fe (II) oxidation and Fe (III) precipitation. *Geochimica et Cosmochimica Acta*, *70*(3), 622-639.

Beard, B. L., Johnson, C. M., Cox, L., Sun, H., Nealson, K. H., & Aguilar, C. (1999). Iron isotope biosignatures. *Science*, *285*(5435), 1889-1892.

Bekker, A., Holland, H. D., Wang, P. L., Rumble Iii, D., Stein, H. J., Hannah, J. L., ... & Beukes, N. J. (2004). Dating the rise of atmospheric oxygen. *Nature*, *427*(6970), 117-120.

Bennett, W. W., & Canfield, D. E. (2020). Redox-sensitive trace metals as paleoredox proxies: a review and analysis of data from modern sediments. *Earth-Science Reviews*, *204*, 103175.

Boyd, P. W., & Ellwood, M. J. (2010). The biogeochemical cycle of iron in the ocean. *Nature Geoscience*, *3*(10), 675-682.

Brown, S. T., Basu, A., Ding, X., Christensen, J. N., & DePaolo, D. J. (2018). Uranium isotope fractionation by abiotic reductive precipitation. *Proceedings of the National Academy of Sciences*, *115*(35), 8688-8693.

Budd, G. E., & Jensen, S. (2000). A critical reappraisal of the fossil record of the bilaterian phyla. *Biological Reviews*, *75*(2), 253-295.

Canfield, D. E. (2005). The early history of atmospheric oxygen: homage to Robert M. Garrels. *Annu. Rev. Earth Planet. Sci.*, *33*, 1-36.

Chemtob, S. M., Nickerson, R. D., Morris, R. V., Agresti, D. G., & Catalano, J. G. (2017). Oxidative alteration of ferrous smectites and implications for the redox evolution of early Mars. *Journal of Geophysical Research: Planets*, *122*(12), 2469-2488.

Cole, D. B., Reinhard, C. T., Wang, X., Gueguen, B., Halverson, G. P., Gibson, T., ... & Planavsky, N. J. (2016). A shale-hosted Cr isotope record of low atmospheric oxygen during the Proterozoic. *Geology*, *44*(7), 555-558.

Colodner, D., Edmond, J., & Boyle, E. (1995). Rhenium in the Black Sea: comparison with molybdenum and uranium. *Earth and Planetary Science Letters*, *131*(1-2), 1-15.

Croal, L. R., Johnson, C. M., Beard, B. L., & Newman, D. K. (2004). Iron isotope fractionation by Fe (II)-oxidizing photoautotrophic bacteria. *Geochimica et cosmochimica acta*, *68*(6), 1227-1242.

Crusius, J., & Thomson, J. (2000). Comparative behavior of authigenic Re, U, and Mo during reoxidation and subsequent long-term burial in marine sediments. *Geochimica et Cosmochimica Acta*, *64*(13), 2233-2242.

Dahl, T. W., & Arens, S. K. (2020). The impacts of land plant evolution on Earth's climate and oxygenation state–An interdisciplinary review. *Chemical Geology*, *547*, 119665.

Dahl, T. W., Hammarlund, E. U., Rasmussen, C. M. Ø., Bond, D. P., & Canfield, D. E. (2021). Sulfidic anoxia in the oceans during the Late Ordovician mass extinctions–insights from molybdenum and uranium isotopic global redox proxies. *Earth-Science Reviews*, *220*, 103748.

Dehouck, E., Chevrier, V., Gaudin, A., Mangold, N., Mathé, P. E., & Rochette, P. (2012). Evaluating the role of sulfide-weathering in the formation of sulfates or carbonates on Mars. *Geochimica et Cosmochimica Acta*, *90*, 47-63.

Dehouck, E., Gaudin, A., Chevrier, V., & Mangold, N. (2016). Mineralogical record of the redox conditions on early Mars. *Icarus*, *271*, 67-75.

Dickson, A. J. (2017). A molybdenum-isotope perspective on Phanerozoic deoxygenation events. *Nature Geoscience*, *10*(10), 721-726.

Ehlmann, B. L., & Edwards, C. S. (2014). Mineralogy of the Martian surface. *Annual Review of Earth and Planetary Sciences*, *42*, 291-315.

Fassett, C. I., & Head III, J. W. (2008). Valley network-fed, open-basin lakes on Mars: Distribution and implications for Noachian surface and subsurface hydrology. *Icarus*, *198*(1), 37-56.

Gaudin, A., Dehouck, E., Grauby, O., & Mangold, N. (2018). Formation of clay minerals on mars: insights from long-term experimental weathering of olivine. Icarus, 311, 210-223.

Gold, D. A. (2018). The slow rise of complex life as revealed through biomarker genetics. *Emerging Topics in Life Sciences*, *2*(2), 191-199.

Harrison, T. M. (2009). The Hadean crust: evidence from> 4 Ga zircons. *Annual Review of Earth and Planetary Sciences*, *37*, 479-505.

Heard, A. W., Wang, Y., Ostrander, C. M., Auro, M., Canfield, D. E., Zhang, S., ... & Nielsen, S. G. (2023). Coupled vanadium and thallium isotope constraints on Mesoproterozoic ocean oxygenation around 1.38-1.39 Ga. *Earth and Planetary Science Letters*, *610*, 118127.

Hecht, M. H., Kounaves, S. P., Quinn, R. C., West, S. J., Young, S. M., Ming, D. W., ... & Smith, P. H. (2009). Detection of perchlorate and the soluble chemistry of martian soil at the Phoenix lander site. *Science*, *325*(5936), 64-67.

Holland, H. D. (2006). The oxygenation of the atmosphere and oceans. *Philosophical Transactions of the Royal Society B: Biological Sciences*, *361*(1470), 903-915.

Huang, J., Liu, X., He, Y., Shen, S., Hou, Z., Li, S., ... & Huang, J. (2021). The oxygen cycle and a habitable Earth. *Science China Earth Sciences*, *64*, 511-528.

Icopini, G. A., Anbar, A. D., Ruebush, S. S., Tien, M., & Brantley, S. L. (2004). Iron isotope fractionation during microbial reduction of iron: the importance of adsorption. *Geology*, *32*(3), 205-208.

Jakosky, B. M., & Phillips, R. J. (2001). Mars' volatile and climate history. *nature*, *412*(6843), 237-244.

Johnson, C. M., Beard, B. L., & Roden, E. E. (2008). The iron isotope fingerprints of redox and biogeochemical cycling in modern and ancient Earth. *Annu. Rev. Earth Planet. Sci.*, *36*, 457-493.

Jones, E. G. (2018). Shallow transient liquid water environments on present-day mars, and their implications for life. *Acta Astronautica*, *146*, 144-150.

Kendall, B., Reinhard, C. T., Lyons, T. W., Kaufman, A. J., Poulton, S. W., & Anbar, A. D. (2010). Pervasive oxygenation along late Archaean ocean margins. *Nature Geoscience*, *3*(9), 647-652.

Lau, K. V., Romaniello, S. J., & Zhang, F. (2019). *The uranium isotope paleoredox proxy*. Cambridge University Press.

Lenton, T. M., Boyle, R. A., Poulton, S. W., Shields-Zhou, G. A., & Butterfield, N. J. (2014). Co-evolution of eukaryotes and ocean oxygenation in the Neoproterozoic era. *Nature Geoscience*, *7*(4), 257-265.

Liu, X. M., Kah, L. C., Knoll, A. H., Cui, H., Wang, C., Bekker, A., & Hazen, R. M. (2021). A persistently low level of atmospheric oxygen in Earth's middle age. *Nature communications*, *12*(1), 351.

Liu, J., Michalski, J. R., Tan, W., He, H., Ye, B., & Xiao, L. (2021). Anoxic chemical weathering under a reducing greenhouse on early Mars. *Nature Astronomy*, *5*(5), 503-509.

Marshall, C. R. (2006). Explaining the Cambrian "explosion" of animals. *Annu. Rev. Earth Planet. Sci.*, *34*, 355-384.

Meadows, V. S., Reinhard, C. T., Arney, G. N., Parenteau, M. N., Schwieterman, E. W., Domagal-Goldman, S. D., ... & Grenfell, J. L. (2018). Exoplanet biosignatures: understanding oxygen as a biosignature in the context of its environment. *Astrobiology*, *18*(6), 630-662.

Meyer, K. M., & Kump, L. R. (2008). Oceanic euxinia in Earth history: causes and consequences. *Annu. Rev. Earth Planet. Sci.*, *36*, 251-288.

Michalski, J. R., Cuadros, J., Niles, P. B., Parnell, J., Deanne Rogers, A., & Wright, S. P. (2013). Groundwater activity on Mars and implications for a deep biosphere. *Nature Geoscience*, *6*(2), 133-138.

Miller, C. A., Peucker-Ehrenbrink, B., Walker, B. D., & Marcantonio, F. (2011). Re-assessing the surface cycling of molybdenum and rhenium. *Geochimica et Cosmochimica Acta*, *75*(22), 7146-7179.

Miller, C. A., Peucker-Ehrenbrink, B., & Schauble, E. A. (2015). Theoretical modeling of rhenium isotope fractionation, natural variations across a black shale weathering profile, and potential as a paleoredox proxy. *Earth and Planetary Science Letters*, *430*, 339-348.

Mishra, P. K., & Mohanty, S. P. (2021). Geochemistry of carbonate rocks of the Chilpi Group, Bastar Craton, India: Implications on ocean paleoredox conditions at the late Paleoproterozoic Era. *Precambrian Research*, *353*, 106023.

Morford, J. L., Russell, A. D., & Emerson, S. (2001). Trace metal evidence for changes in the redox environment associated with the transition from terrigenous clay to diatomaceous sediment, Saanich Inlet, BC. *Marine Geology*, *174*(1-4), 355-369.

Olson, J. M. (2006). Photosynthesis in the Archean era. *Photosynthesis research*, *88*, 109-117.

Olson, S. L., Kump, L. R., & Kasting, J. F. (2013). Quantifying the areal extent and dissolved oxygen concentrations of Archean oxygen oases. *Chemical Geology*, *362*, 35-43.

Partin, C. A., Bekker, A., Planavsky, N. J., Scott, C. T., Gill, B. C., Li, C., ... & Lyons, T. W. (2013). Large-scale fluctuations in Precambrian atmospheric and oceanic oxygen levels from the record of U in shales. *Earth and Planetary Science Letters*, *369*, 284-293.

Pavlov, A. A., & Kasting, J. F. (2002). Mass-independent fractionation of sulfur isotopes in Archean sediments: strong evidence for an anoxic Archean atmosphere. *Astrobiology*, *2*(1), 27-41.

Rummel, J. D., Beaty, D. W., Jones, M. A., Bakermans, C., Barlow, N. G., Boston, P. J., ... & Wray, J. J. (2014). A new analysis of Mars "special regions": findings of the second MEPAG Special Regions Science Analysis Group (SR-SAG2).

Sasselov, D. D., Grotzinger, J. P., & Sutherland, J. D. (2020). The origin of life as a planetary phenomenon. *Science Advances*, *6*(6), eaax3419.

Sauterey, B., Charnay, B., Affholder, A., Mazevet, S., & Ferrière, R. (2022). Early Mars habitability and global cooling by H2-based methanogens. *Nature Astronomy*, *6*(11), 1263-1271.

Seager, S., Schrenk, M., & Bains, W. (2012). An astrophysical view of Earth-based metabolic biosignature gases. *Astrobiology*, *12*(1), 61-82.

Shields-Zhou, G., & Och, L. (2011). The case for a Neoproterozoic oxygenation event: geochemical evidence and biological consequences. *GSa Today*, *21*(3), 4-11.

Schirrmeister, B. E., Gugger, M., & Donoghue, P. C. (2015). Cyanobacteria and the Great Oxidation Event: evidence from genes and fossils. *Palaeontology*, *58*(5), 769-785.

Sholes, S. F., Smith, M. L., Claire, M. W., Zahnle, K. J., & Catling, D. C. (2017). Anoxic atmospheres on Mars driven by volcanism: Implications for past environments and life. *Icarus*, *290*, 46-62.

Schopf, J. W., Kudryavtsev, A. B., Czaja, A. D., & Tripathi, A. B. (2007). Evidence of Archean life: stromatolites and microfossils. *Precambrian Research*, *158*(3-4), 141-155.

Severmann, S., & Anbar, A. D. (2009). Reconstructing paleoredox conditions through a multitracer approach: the key to the past is the present. *Elements*, *5*(6), 359-364.

Taverne, Y. J., Merkus, D., Bogers, A. J., Halliwell, B., Duncker, D. J., & Lyons, T. W. (2018). Reactive Oxygen Species: Radical Factors in the Evolution of Animal Life: A molecular timescale from Earth's earliest history to the rise of complex life. *BioEssays*, *40*(3), 1700158.

Thomas, T. B., Hu, R., & Lo, D. Y. (2023). Constraints on the Size and Composition of the Ancient Martian Atmosphere from Coupled CO2–N2–Ar Isotopic Evolution Models. *The Planetary Science Journal*, *4*(3), 41.

Tostevin, R. (2021). *Cerium anomalies and paleoredox*. Cambridge University Press.

Towe, K. M. (1981). Environmental conditions surrounding the origin and early Archean evolution of life: a hypothesis. *Precambrian Research*, *16*(1-2), 1-10.

Tribovillard, N., Algeo, T. J., Lyons, T., & Riboulleau, A. (2006). Trace metals as paleoredox and paleoproductivity proxies: an update. *Chemical geology*, *232*(1-2), 12-32.

Welch, S. A., Beard, B. L., Johnson, C. M., & Braterman, P. S. (2003). Kinetic and equilibrium Fe isotope fractionation between aqueous Fe (II) and Fe (III). *Geochimica et Cosmochimica Acta*, *67*(22), 4231-4250.

Wijsman, J. W., Middelburg, J. J., & Heip, C. H. (2001). Reactive iron in Black Sea sediments: implications for iron cycling. *Marine Geology*, *172*(3-4), 167-180.

Wordsworth, R. D., Schaefer, L. K., & Fischer, R. A. (2018). Redox evolution via gravitational differentiation on low-mass planets: implications for abiotic oxygen, water loss, and habitability. *The Astronomical Journal*, *155*(5), 195.

Wordsworth, R., Knoll, A. H., Hurowitz, J., Baum, M., Ehlmann, B. L., Head, J. W., & Steakley, K. (2021). A coupled model of episodic warming, oxidation and geochemical transitions on early Mars. *Nature Geoscience*, *14*(3), 127-132.

Xiang, L., Schoepfer, S. D., Zhang, H., Yuan, D. X., Cao, C. Q., Zheng, Q. F., ... & Shen, S. Z. (2016). Oceanic redox evolution across the end-Permian mass extinction at Shangsi, South China. *Palaeogeography, Palaeoclimatology, Palaeoecology*, *448*, 59-71.

Yang, W., & Holland, H. D. (2003). The Hekpoort paleosol profile in Strata 1 at Gaborone, Botswana: soil formation during the Great Oxidation Event. *American Journal of Science*, *303*(3), 187-220.

Zahnle, K., Schaefer, L., & Fegley, B. (2010). Earth's earliest atmospheres. *Cold Spring Harbor perspectives in biology*, *2*(10), a004895.

Zhang, S., Wang, X., Wang, H., Bjerrum, C. J., Hammarlund, E. U., Costa, M. M., ... & Canfield, D. E. (2016). Sufficient oxygen for animal respiration 1,400 million years ago. *Proceedings of the National Academy of Sciences*, *113*(7), 1731-1736.

2 PRECAMBRIAN OCEAN MIXING TIMESCALE

2.1 Introduction

Ocean mixing is a key process in marine biogeochemistry, as it shapes the distribution of nutrients essential to life in the surface ocean (Meyer et al., 2016) and influences the distribution of geochemical tracers in seafloor sediments that are commonly used to reconstruct ancient surface conditions (Chen et al., 2021; Algeo and Lyons, 2006; Wang et al., 2016).

The overall ocean mixing timescale reflects the integrated effects of both vertical and horizontal mixing processes. The present-day ocean mixing timescale is about 1 kyr (Broecker and Peng, 1982; Matsumoto, 2007). Consequently, geochemical species with residence times that are much longer than 1 kyr are generally well-mixed in seawater and can thus be considered reliable tracers of global conditions. Changes in the abundance and/or isotopic composition of these species in marine sedimentary records are often interpreted as reflecting a different balance of sources and sinks resulting from environmental changes, assuming an ocean mixing timescale that was similar to present-day.

The problem with this assumption is that the drivers of ocean mixing, such as winds, tides, or density differences (Wunsch and Ferrari, 2004), are influenced by factors like day length, surface pressure, and continental configuration that have changed through Earth's history. Winds drive large-scale surface ocean currents, and upwelling from deep ocean replaces the surface water. Tides are generally important in a shallow coastal setting, but they might also be the dominant driver of diapycnal mixing. Differences in water density as a result of variable water temperature and salinity drive thermohaline circulation.

Winds could have been different in the Precambrian mainly due to changes in Earth's surface pressure and rotation rate. Earth's surface pressure has probably varied with its evolving atmospheric composition, but overall, it seems to have increased through time. For example, 2.7-Ga iron micrometeorites suggest a Neoarchean surface pressure of ~0.6 bar (Payne et al., 2020); analysis of nitrogen and argon isotopes in fluid inclusions trapped in 3.0- to 3.5-Ga hydrothermal quartz indicates that the partial pressure of nitrogen during Archean could be as low as 0.5 bar (Marty et al., 2013); the size distribution of gas bubbles in basaltic lava flows that solidified ~2.7 Ga gives 0.23 to 0.5 bar for late Archean atmospheric pressure (Som et al., 2016). Earth's rotation rate was faster in the past, likely resulting in a day length half as long as today in the early Archean (Webb, 1982), and the Boring Billion could have witnessed a resonance-stabilized 21-hour day length (Zahnle and Walker, 1987; Bartlett and Stevenson, 2016).

Tides in the Precambrian would be stronger with a shorter Earth-Moon distance (Webb, 1982; Green et al., 2017; Bills and Ray, 1999), but continental configurations and bathymetry could also affect tidal resonances (Yi et al., 2017; Davies et al., 2020). The influence of salinity on ocean circulation is less well understood and existing proxy constraints on Precambrian ocean salinity are limited. Knauth (2005) uses the absence of long-lived continental cratons to suggest 1.5 to 2 times present-day salinity throughout the Archean, and this high value probably started to decrease in the latest Precambrian due to the emergence of giant Neoproterozoic evaporite basins. In comparison, Marty et al. (2018) propose a near modern and constant salinity of Archean oceans by analyzing fluid inclusions in Archean hydrothermal quartz crystals.

Only two studies tackled the question of Precambrian ocean mixing timescale. Lowe (1994) made a qualitative argument that in the Archean, deep ocean mixing could have been

hampered due to high surface temperatures that prevented the formation of marine shelf ice, causing the ocean mixing timescale to slow to hundreds of thousands or even millions of years. If at any time in Earth's history ocean mixing became that sluggish, large heterogeneities in water masses would have been created for elements and chemical species that are well-mixed in the present-day ocean. Chen et al. (2021) however countered that deep ocean mixing is primarily constrained by the kinetic energy input from winds and tides, and the ocean mixing timescale likely remained within a factor of 10 of the present-day value.

Previous modeling studies that have explored ocean mixing under conditions unlike present-day Earth have focused either on Phanerozoic Earth (Pohl et al., 2022) or exoplanets (Olson et al., 2020), leaving a significant gap in our understanding of ocean mixing in the Precambrian era. We use here an Earth system model called cGENIE to simulate the sensitivity of ocean mixing to day length, surface pressure, continental configuration, and tidal dissipation, first individually and then in combination.

2.2 Model setup

cGENIE includes a 3-D frictional geostrophic ocean circulation model (GOLDSTEIN) with dynamic sea ice coupled to a 2-D energy-moisture balance model of the atmosphere (EMBM; Edwards and Marsh, 2005). The ocean and the atmosphere are divided into a 36×36 equal-area latitude-longitude grid, and the ocean includes 16 depth layers reaching an average depth of 3545.7m. EMBM exchanges heat and freshwater with the underlying ocean, but does not predict planetary albedo or wind fields, which need to be prescribed in cGENIE. To generate these fields, we perform atmosphere simulations using the ExoPlaSim atmospheric GCM with T21 resolution

(64×32 grid; Paradise et al. 2022). The decennially averaged surface wind and planetary albedo fields from ExoPlaSim are converted to cGENIE's 36×36 grid using modifications made to the 'muffingen' software (DOI: 10.5281/zenodo.10802839) and become input files for cGENIE boundary conditions.

We consider four factors that affect ocean mixing: day length, surface pressure, tidal dissipation, and continental configuration. We first carry out a series of sensitivity experiments in which we vary each of the four factors individually over a range of values or scenarios plausible for Precambrian Earth to isolate the effects of each on ocean mixing. Though ocean salinity may also affect ocean mixing timescales, we do not consider its effect because cGENIE's default equation of state designed for the present-day ocean is oversimplified in the way that it accounts for salinity (Marsh et al., 2009). As discussed above, Precambrian oceans were likely significantly more saline, potentially strengthening ocean circulation and decreasing ocean mixing timescales (Olson et al., 2022).

While continental configuration related fields can be easily changed in cGENIE following instructions in Ridgwell (2017), varying day length, surface pressure, and tidal dissipation requires additional code-modifications and/or parameterizations, for which we include detailed descriptions below.

Solar day length was explicitly hard-coded at its present-day value (86400 seconds/day) in the GOLDSTEIN ocean, GOLDSTEIN-SEAICE sea-ice, and EMBM atmosphere modules within the cGENIE model. In addition, present-day sidereal day length was implicitly used in deriving the Coriolis effect scaling factor $fsc = 2 \times 7.2921 \times 10^{-5}\ \mathrm{rad/s} = 2 \times 2\pi/86164\ \mathrm{s}$. To enable simulations with day lengths (rotation rates) different from Earth's present-day 24 hr day length,

we introduce solar day length and sidereal day length in cGENIE as namelist parameters, following the instructions in Ridgwell (2017). The code for the version of the "muffin" release of the cGENIE Earth system model used in this paper is tagged as v0.9.50 and is assigned a DOI: 10.5281/zenodo.10798347. cGENIE assumes a default year length of 365.25 days/year. In this paper, we modify the number of days per year such that all simulations have the same orbital period (total seconds/year).

We modify surface pressure in ExoPlaSim, and its effects are fed forward to cGENIE via wind stress. cGENIE's GOLDSTEIN, GOLDSTEIN-SEICE, and EMBM modules require wind stress fields in the form of x- and y- component (eastward and northward) wind stress at the u and v grid points of cGENIE's Arakawa C grid. Additionally, EMBM uses a wind speed field computed as the vector magnitude of the x- and y-wind velocity from ExoPlaSim. Our modifications to the 'muffingen' software enable the conversion of ExoPlaSim outputs on wind stress and velocities into formats compatible with cGENIE's grid system. We also develop a script to match cGENIE's land-sea masks with ExoPlaSim's land maps, ensuring accurate topographical alignment for the same simulations. Finally, we recalibrate the wind-stress scaling parameter within cGENIE to replicate present-day ocean ventilation ages when using ExoPlaSim wind fields, thereby considering the discrepancies in wind stress representation between ExoPlaSim and the default value in cGENIE (*e.g.*, Crichton et al. 2021).

We approximate the effects of tidal dissipation by parameterizing turbulent ocean mixing via a diapycnal diffusivity profile. GOLDSTEIN, the ocean circulation model within cGENIE, uses a stratification-dependent diapycnal mixing scheme (Oliver and Edwards, 2008):

$$\kappa(z) = \kappa_c f(z) \times (\rho_{z,lev}(z)/\rho_z(z)), \quad \text{(Eq. 2-1)}$$

where $f(z) = e^{-(2500m-z)/700m}$ is a reference vertical profile exponentially growing with depth and equal to 1 at a depth of 2500 m, $\rho_z(z)$ is the density stratification, $\rho_{z,lev}(z) = (-5.5 \times 10^{-3})e^{z/650m}\ kg\ m^{-4}$ is a reference stratification profile, and κ_c is the diffusivity at 2500 m when $\rho_z(z) = \rho_{z,lev}(z)$. κ_c is treated as an adjustable parameter and is set to $2.5 \times 10^{-5}\ m^2\ s^{-1}$ in our present-day ocean reference case. The resulting diffusivity profile is broadly consistent with observations (Fig. 2-1), with values below $10^{-5}\ m^2\ s^{-1}$ in the thermocline and around $10^{-4}\ m^2\ s^{-1}$ at depth (Kunze et al., 2006).

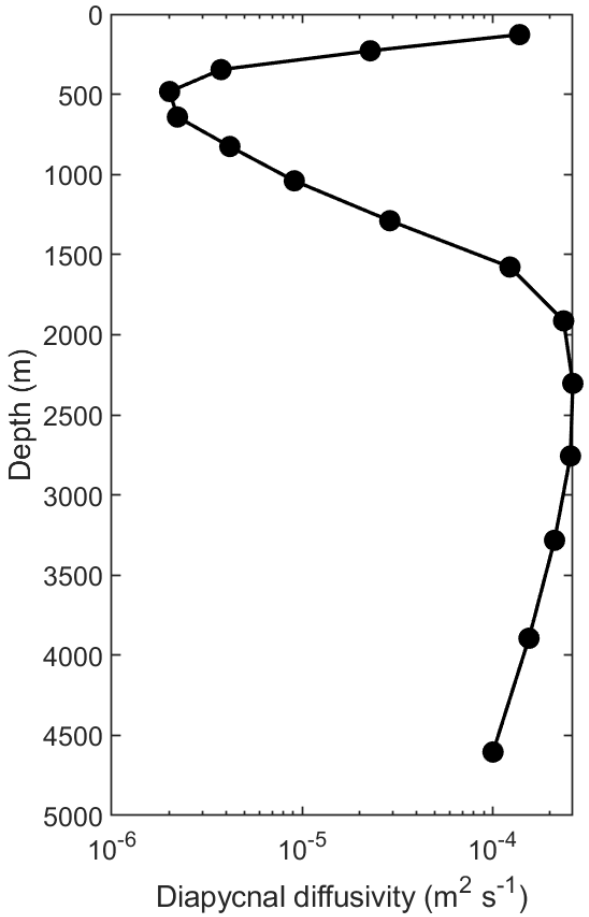

Figure 2-1 Depth profile of diapycnal diffusivity in the present-day baseline model simulation. The profile shows the stratification-weighted horizontal average of the model's 3-dimensional diffusivity field.

For a given stratification, with its effect explicitly accounted for in Eq. 2-1, diapycnal diffusivity κ is expected to be proportional to the turbulent kinetic energy dissipation rate ε in the ocean interior, which derives mainly from breaking of internal waves that are ultimately driven by lunisolar tides and surface wind stress (Yang et al., 2017). We therefore expect $\kappa_c/\kappa_{c,m} = \varepsilon/\varepsilon_m = (\varepsilon_t + \varepsilon_w)/\varepsilon_m = (\varepsilon_t/\varepsilon_{t,m})(\varepsilon_{t,m}/\varepsilon_m) + (\varepsilon_w/\varepsilon_{w,m})(\varepsilon_{w,m}/\varepsilon_m)$, where the subscript m indicates present-day conditions, ε_t is the tidal energy dissipation rate, and ε_w is wind-driven turbulent dissipation rate. Waterhouse et al. (2014) suggest that tides contribute about 3/4 of the dissipation rate today, thus indicating that $\varepsilon_{t,m}/\ \varepsilon_m \approx 3/4$, while $\varepsilon_{w,m}/\ \varepsilon_m \approx 1/4$. We therefore have,

$$\kappa_c/\kappa_{c,m} = \frac{3}{4}(\varepsilon_t/\varepsilon_{t,m}) + \frac{1}{4}(\varepsilon_w/\varepsilon_{w,m}), \quad \text{(Eq. 2-2)}$$

Lunisolar tides would have changed in the past due to the greater proximity of the Moon and different continentalities. Assuming a present-day continental configuration, Webb (1982) calculated the influence of Earth-Moon distance on tidal dissipation through time. Assuming that the fraction of tidal dissipation that contributes to deep ocean mixing stays roughly constant through time, the results suggest that $\varepsilon_t/\varepsilon_{t,m} = 0.7, 0.7, 1.6, 1.9, 2.7$ at 1, 1.6, 2.5, 2.8 and 3.6 Ga respectively.

Davies et al., (2020) found that the deep ocean tidal dissipation rate could vary by about a factor of 4 depending on the continental configuration. To take the continentality effect into account, we therefore apply a factor of 0.5 to the minimum $\varepsilon_t/\varepsilon_{t,m}$ and a factor of 2 to the maximum $\varepsilon_t/\varepsilon_{t,m}$ obtained from Webb (1982), resulting in a likely range for $\varepsilon_t/\varepsilon_{t,m}$ between 0.35 and 5.4.

We estimate $\varepsilon_w/\varepsilon_{w,m}$ in our simulations by estimating the spatially integrated wind energy over the ocean surface and normalizing it with the present-day value,

$$\frac{\varepsilon_w}{\varepsilon_{w,m}} = \frac{p}{p_m}\frac{\int v^2 dA}{\int {v_m}^2 dA}, \quad \text{(Eq. 2-3)}$$

where p is mean surface pressure in bar and v is surface wind speed in m/s. We calculate $\varepsilon_w/\varepsilon_{w,m}$ for three groups of sensitivity experiments: continentality, surface pressure, and day length, as well as all the historical simulations from ExoPlaSim (Table 2-1). The minimum and maximum $\varepsilon_w/\varepsilon_{w,m}$ values across all simulations are 0.61 and 1.7, which we use as the likely range for our diffusivity sensitivity experiments.

To estimate the minimum and maximum diffusivities, we combine the minimum and maximum of $\varepsilon_t/\varepsilon_{t,m}$ and $\varepsilon_w/\varepsilon_{w,m}$ respectively, which yields $\kappa_{c,min} = 1.0 \times 10^{-5}\ m^2\ s^{-1}$ and $\kappa_{c,max} = 1.1 \times 10^{-4}\ m^2\ s^{-1}$. Including the present-day baseline case with $\kappa_c = 2.5 \times 10^{-4}\ m^2\ s^{-1}$, and an additional intermediate value with $\kappa_c = 6.9 \times 10^{-5}\ m^2\ s^{-1}$ we therefore have four experiments in our diffusivity sensitivity series: $\kappa_c = 1.0 \times 10^{-5}, 2.5 \times 10^{-5}, 6.9 \times 10^{-5}, 1.1 \times 10^{-4}\ m^2 s^{-1}$.

Table 2-1 Model setup of historical experiments. AP: aquaplanet; LS: low-latitude supercontinent; HS: high-latitude supercontinents.

Period	Day length[a]	Surface pressure[b]	Continentality	Diapycnal diffusivity parameter
Paleoarchean (3.6-3.2 Ga)	15 hr	0.5 bar	AP	$5.6 \times 10^{-5}\ m^2\ s^{-1}$
			LS	$5.4 \times 10^{-5}\ m^2\ s^{-1}$
			HS	$5.6 \times 10^{-5}\ m^2\ s^{-1}$
		1.0 bar	AP	$5.9 \times 10^{-5}\ m^2\ s^{-1}$
			LS	$5.6 \times 10^{-5}\ m^2\ s^{-1}$
			HS	$5.8 \times 10^{-5}\ m^2\ s^{-1}$
		2.0 bar	AP	$6.1 \times 10^{-5}\ m^2\ s^{-1}$
			LS	$5.8 \times 10^{-5}\ m^2\ s^{-1}$
			HS	$6.1 \times 10^{-5}\ m^2\ s^{-1}$
Neoarchean (2.8-2.5 Ga)	18 hr	0.5 bar	AP	$4.2 \times 10^{-5}\ m^2\ s^{-1}$
			LS	$4.0 \times 10^{-5}\ m^2\ s^{-1}$
			HS	$4.1 \times 10^{-5}\ m^2\ s^{-1}$
		1.0 bar	AP	$4.4 \times 10^{-5}\ m^2\ s^{-1}$
			LS	$4.1 \times 10^{-5}\ m^2\ s^{-1}$

Table 2-1 Model setup of historical experiments. AP: aquaplanet; LS: low-latitude supercontinent; HS: high-latitude supercontinents (continued).

			HS	$4.4 \times 10^{-5}\ m^2\ s^{-1}$
Paleoproterozoic (2.5-1.6 Ga)	18 hr	1.0 bar	LS	$3.6 \times 10^{-5}\ m^2\ s^{-1}$
			HS	$3.8 \times 10^{-5}\ m^2\ s^{-1}$
			Pangaea	$3.7 \times 10^{-5}\ m^2\ s^{-1}$
Mesoproterozoic (1.6-1.0 Ga)	22.5 hr	1.0 bar	LS	$1.9 \times 10^{-5}\ m^2\ s^{-1}$
			HS	$2.2 \times 10^{-5}\ m^2\ s^{-1}$
			Pangaea	$2.1 \times 10^{-5}\ m^2\ s^{-1}$
Neoproterozoic (1.0-0.6 Ga)	22.5 hr	1.0 bar	LS	$1.9 \times 10^{-5}\ m^2\ s^{-1}$
			HS	$2.2 \times 10^{-5}\ m^2\ s^{-1}$
			Pangaea	$2.1 \times 10^{-5}\ m^2\ s^{-1}$

[a] Bartlett and Stevenson (2016); [b] Olson et al. (2018).

We then assess how day length, surface pressure, continental configuration and tidal dissipation may have jointly influenced the mixing of Earth's oceans through five Precambrian periods: Paleoarchean (3.6~3.2 Ga), Neoarchean (2.8~2.5 Ga), Paleoproterozoic (2.5~1.6 Ga), Mesoproterozoic (1.6~1.0 Ga), and Neoproterozoic (1.0~0.6 Ga). Table 2-1 shows the parameter values that we adopt for each period. Day length is relatively well constrained for the Precambrian Earth, so we assign the average value from Bartlett and Stevenson (2016) to each period. Surface pressures on Archean Earth depend on nitrogen degassing and recycling between the mantle and atmosphere. We test 0.5 to 2 bar for the Archean periods and keep the Proterozoic periods at 1 bar, as we expect the Proterozoic surface pressure to be similar to the present-day level (Olson et al., 2018). Continental configurations in deep time are highly uncertain, so we test four configuration endmembers: aquaplanet, low-latitude supercontinent, high-latitude supercontinents, and Pangaea supercontinent (Fig. 2-2). We estimate the wind-driven dissipation rate specific for each experiment from Eq. 2-3 and combine it with the tidal dissipation rate for the corresponding period from Webb (1982) to come up with a diapycnal diffusivity profile for each experiment.

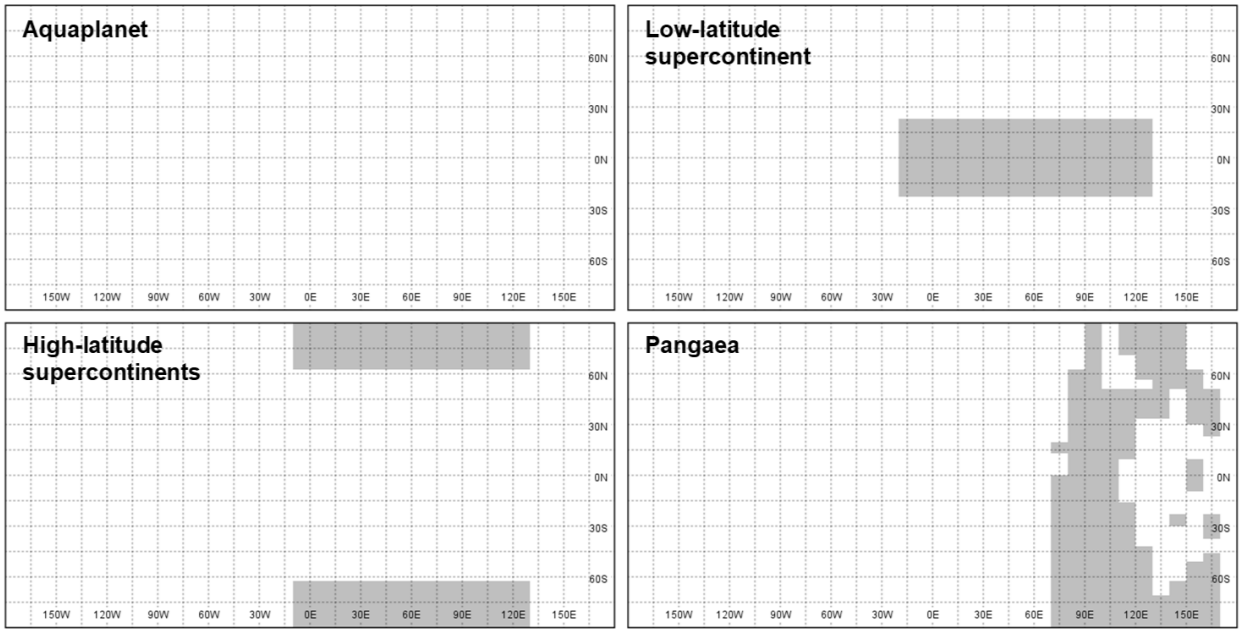

Figure 2-2 Continental configurations used in sensitivity and historical simulations.

We use a pre-industrial solar forcing, atmospheric chemistry, and geothermal heat flux across our experiments to isolate the effects of Earth's geophysical and planetary evolution on the ocean mixing timescale, except for those with non-present-day-level surface pressure in which we multiply pCO_2 in cGENIE and ExoPlaSim to keep its relative amount constant and we remove ozone from ExoPlaSim. Ozone is necessary to produce present-day Earth surface temperatures and sea-ice extents in our modelling, but we find its impact on climate to be exaggerated at higher surface pressures due to pressure broadening – a phenomenon where a higher surface pressure leads to an increase in molecular collisions in the atmosphere that widens the absorption and emission spectra of greenhouse gases and thus enhances the greenhouse effect (Pierrehumbert, 2010). This mechanism, represented in ExoPlaSim through a simplified adjustment factor that affects the absorption efficiencies of O_3, CO_2, and H_2O, counterbalances the cooling effect of Rayleigh scattering that also intensifies with pressure. At 2 atm surface pressure, we find that ozone and water vapor collectively contribute to strong warming when pressure broadening is

applied to both absorbers, resulting in significantly elevated global temperatures (averaging above 60 °C, with peaks between 75-80 °C), which are not representative of any historical periods studied in this research. Consequently, we incorporate ozone only into simulations with 1 atm surface pressure, and we provide a 1 atm simulation without ozone for comparison with pressure sensitivity experiments (Fig. 2-3).

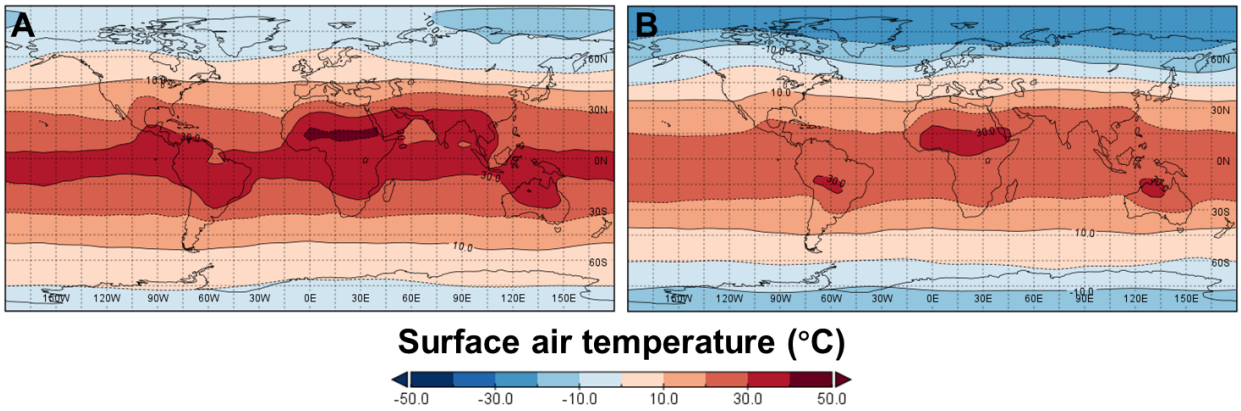

Figure 2-3 Annual mean surface air temperature in (A) present-day baseline with ozone and (B) ozone-less baseline.

We run each of our experiments for 10,000 model years to achieve steady state and capture long-term mean ocean circulation rather than transient variations. Six historical experiments reach a snowball state due to the cooling induced by their reduced surface pressures and increased rotation rates. For the remaining experiments, we take the mean benthic (> 2 km deep ocean floor) and maximum global ventilation ages as diagnostics for the ocean mixing timescale. Ventilation age (time since a water parcel last saw the surface ocean) is calculated in cGENIE by taking the concentration ratio of artificial color tracers. Red and blue color tracers are applied evenly to the entire ocean surface, with the concentration of red tracer C_R permanently set to 1 at the surface. The concentration of blue tracer C_B at the surface is set to a level equal to the remaining simulation run time ($t_{tot} - t$), and linearly declines to 0 per unit time as the simulation completes at $t = t_{tot}$.

The ventilation age of a water parcel in the simulation is given by $t_v = C_B/C_R - (t_{tot} - t)$. For example, a water parcel that last saw ocean surface in the 8500th year of a 10,000-year simulation and was isolated from air exchange thereafter will have an age of $t_v = (10000 - 8500)/1 - (10000 - 10000) = 1500$ yr at the end of the simulation. The implementation of the red tracer normalizes for the dispersion and dilution of the blue tracer during the first few thousand years of simulation when the simulation has not reached steady-state. Ventilation age is a measure of vertical mixing, as age is reset when a water parcel is at the top of the water column, not when different oceanic basins are homogenized (Ridgwell, 2017). In practice, however, this is also an approximate measure of lateral mixing in the deep ocean, as ages of the oldest water masses are limited by lateral transport from the regions of deep-water formation to the rest of global deep ocean.

2.3 Sensitivity experiments

Our baseline mean benthic ventilation age is 0.79 kyr, and the baseline maximum global ventilation age is 1.3 kyr. The present-day baseline ocean exhibits climatology fields that more closely resemble pre-industrial distributions (Fig. 2-5~6), yet the ozone-less baseline reflects slightly stronger North Atlantic Deep Water and Antarctic Bottom Water formation (Fig. 2-4).

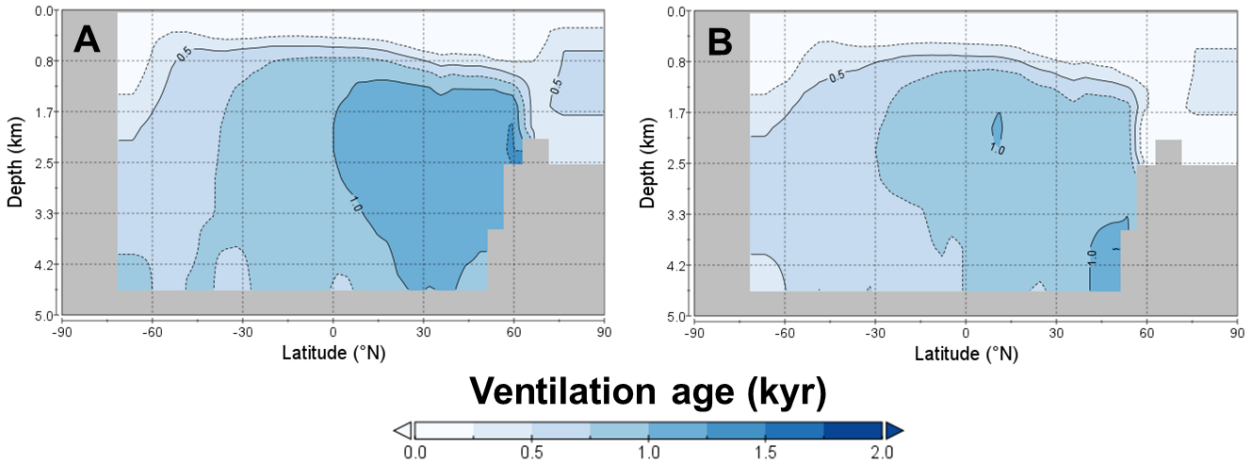

Figure 2-4 Zonal mean water mass ventilation age in (A) present-day baseline with ozone and (B) ozone-less baseline.

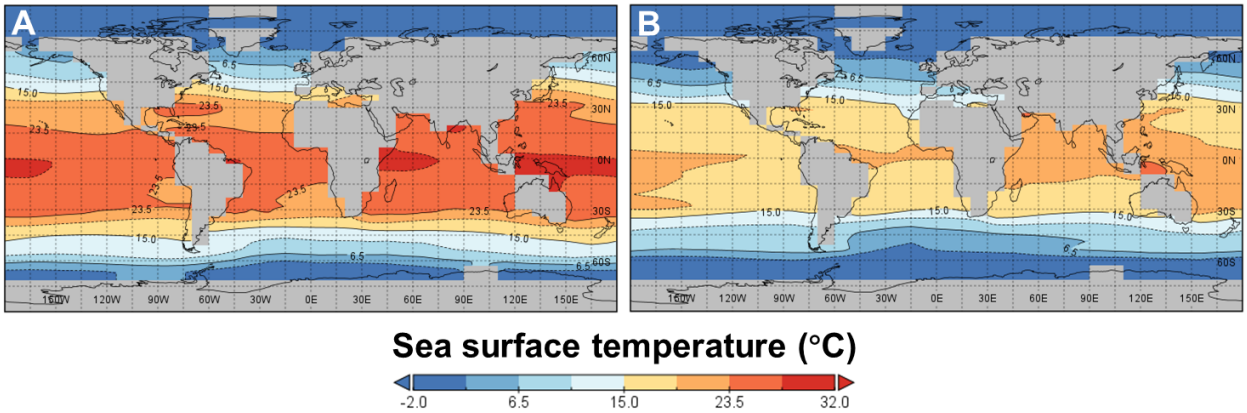

Figure 2-5 Annual mean sea surface temperature in (A) present-day baseline with ozone and (B) ozone-less baseline.

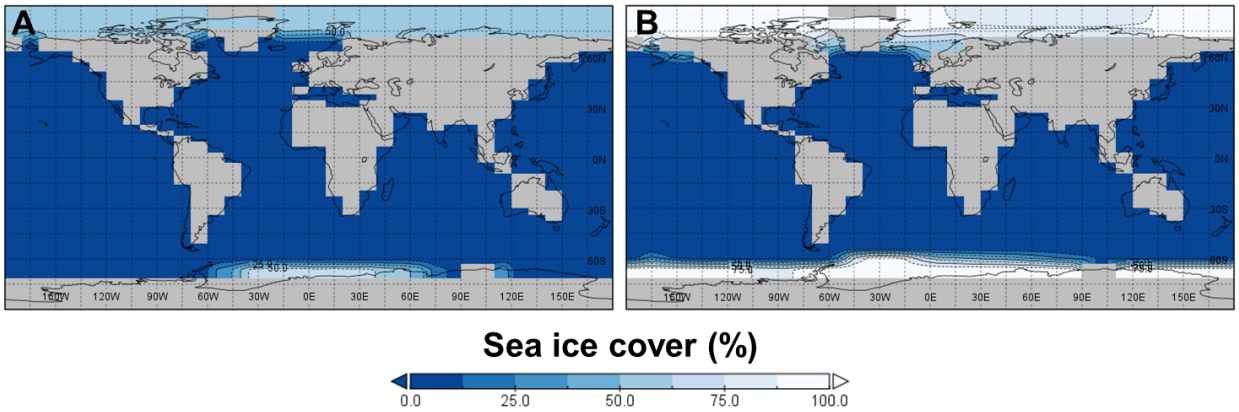

Figure 2-6 Annual mean sea ice cover in (A) present-day baseline with ozone and (B) ozone-less baseline.

Day length and ocean mixing timescale are negatively correlated. Increasing day length from 15 to 24 hr decreases mean benthic ventilation age by 0.32 kyr and maximum global ventilation age by 0.47 kyr (Fig. 2-8a). This inverse relationship between ocean mixing timescale and day length is qualitatively consistent with the expectation that wind-driven Ekman transport strengthens with longer day length (Olson et al., 2020). Ekman transport ($m^2\ s^{-1}$) is calculated as the horizontal velocity integrated in the vertical direction: $V = \tau/(2\rho\Omega \sin\varphi)$, where τ is wind stress (Pa), ρ is seawater density (kg m^{-3}), Ω is planet's rotation rate (rad s^{-1}) and φ is latitude (degrees). When day length increases (equivalently, rotation rate Ω decreases), Ekman transport induced by a given wind stress increases, causing the ocean's overturning circulation to strengthen (Nikurashin and Vallis, 2012).

Diapycnal diffusivity (κ) and ocean mixing timescale are also negatively correlated. A tenfold increase in κ reduces mean benthic ventilation age by 0.56 kyr and maximum global ventilation age by 0.85 kyr (Fig. 2-8b). Diapycnal diffusivity affects the ocean mixing timescale both directly via diffusive transport of tracers and indirectly via global overturning circulation (Nikurashin and Vallis, 2012).

Atmospheric surface pressure and ocean mixing timescale are negatively correlated beyond 1 bar. Increasing surface pressure from 1 to 2 bar decreases the mean benthic ventilation age by 0.25 kyr and the maximum global ventilation age by 0.46 kyr (Fig. 2-8c). Surface pressure affects ocean mixing via changes in the wind stress $\boldsymbol{\tau} = c_a \rho_a |\boldsymbol{u}| \boldsymbol{u}$, where $\boldsymbol{u}$ is wind speed and $|\boldsymbol{u}|$ is its magnitude (m s^{-1}), c_a is a dimensionless drag coefficient typically around 0.0015 at low to moderate wind speed (Wilson 1960), and ρ_a is air density (kg m^{-3}). Increasing surface pressure increases air density more significantly than it decreases wind speed due to friction, thereby

increasing wind stress (Fig. 2-7). Increasing wind stress enhances ocean mixing, with a deviation from this trend at surface pressure lower than 1 bar likely resulting from more extensive sea-ice cover due to diminished atmospheric heat transport (Olson et al., 2020).

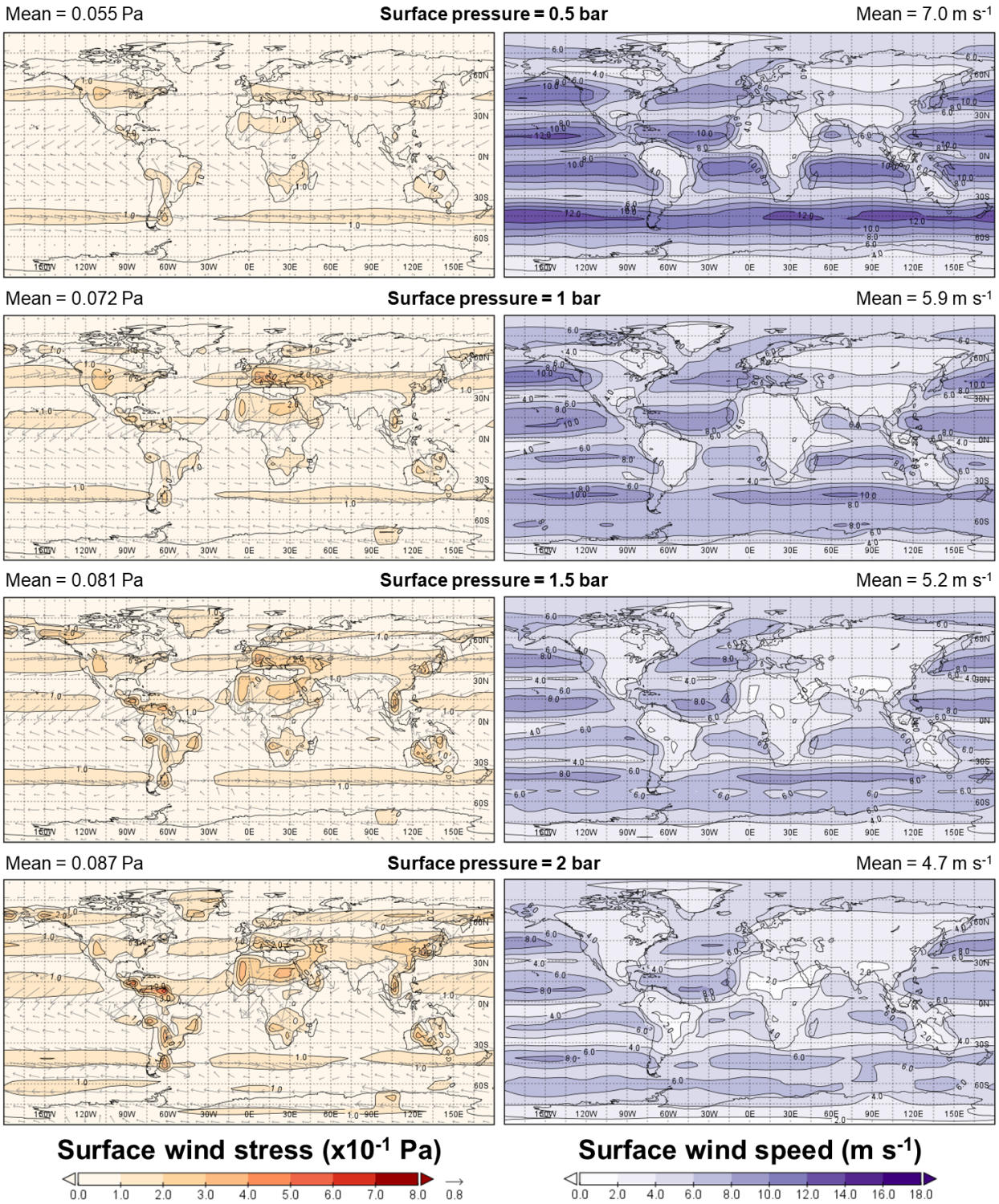

Figure 2-7 Annual mean surface wind stress and speed in ozone-less baseline vs. surface pressure sensitivity tests.

Continentality configurations with a larger high-latitude to low-latitude landmass ratio have longer ocean mixing timescales, with the mean benthic ventilation age varying between 0.23 and 0.80 kyr and the maximum global ventilation age between 0.59 and 1.6 kyr (Fig. 2-8d). The reasons for this behavior are not entirely clear, although multiple mechanisms may contribute. Low-latitude landmasses tend to reduce oceanic meridional heat transport out of the tropics (Enderton and Marshall 2009; Way et al., 2021), resulting in a larger equator-to-pole temperature difference that may strengthen deep ocean overturning circulation. Moreover, in our simulations, we find deep water formation at both poles (with upwelling in the low latitudes) in the case of the low-latitude supercontinent, while the aquaplanet and high-latitude supercontinents setups exhibit deep water formation in only one hemisphere (Fig. 2-9). The latter result, however, may depend on details of the model configuration (Enderton and Marshall, 2009).

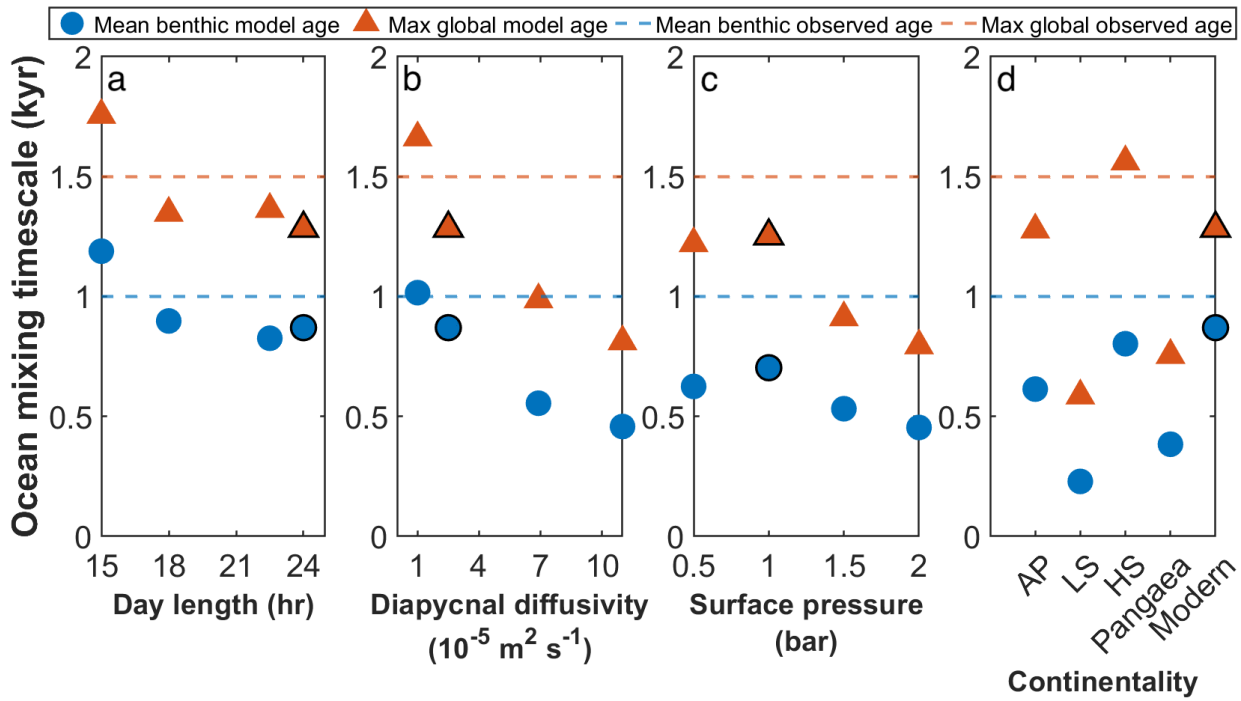

Figure 2-8 Sensitivity of the ocean mixing timescale to Earth's day length, tidal dissipation, surface pressure, and continental configuration. Dashed lines are data-constrained model estimates of present-day ventilation ages from DeVries and Primeau (2011). Symbols with black outline

(Figure 2-8 continued) indicate present-day baseline ages in (a), (b), (d) and ozone-less baseline ages in (c). AP: aquaplanet; LS: low-latitude supercontinent; HS: high-latitude supercontinents.

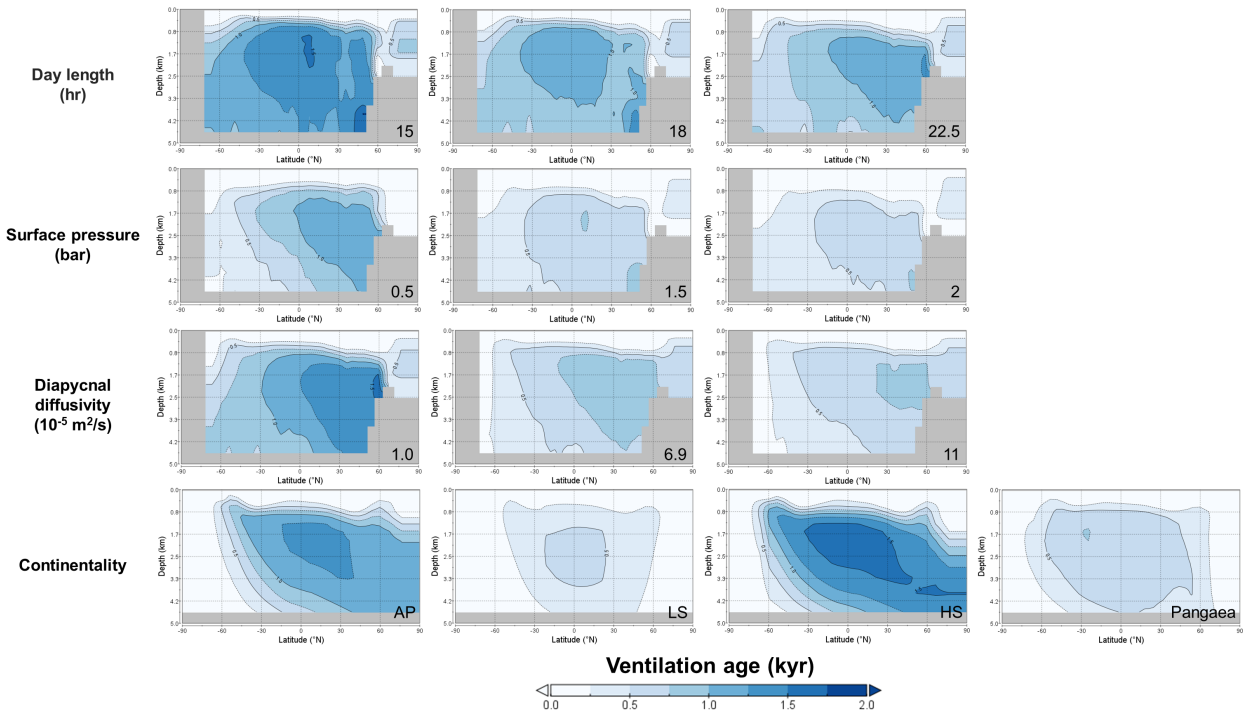

Figure 2-9 Zonal mean water mass ventilation age in sensitivity tests. AP: aquaplanet; LS: low-latitude supercontinent; HS: high-latitude supercontinents.

2.4 Historical simulations

Our sensitivity tests highlight that multiple factors could have influenced ocean mixing throughout Earth's history, several of which act in opposing directions. As a result of such cancellations, we find that the variations in ocean mixing timescale in our experiments aimed at simulating different intervals of Earth's history are relatively minor (Fig. 2-10). The mean benthic ventilation age varies from 0.26 to 0.96 kyr, and the maximum global ventilation age varies from 0.68 to 2.4 kyr. We therefore conclude that the ocean mixing timescale remained on the same order of magnitude of the present-day value, varying between a few hundred and a couple of thousand

years through Earth's history, whereas the ocean mixing and circulation patterns could have changed more dramatically (Fig. 2-11~14).

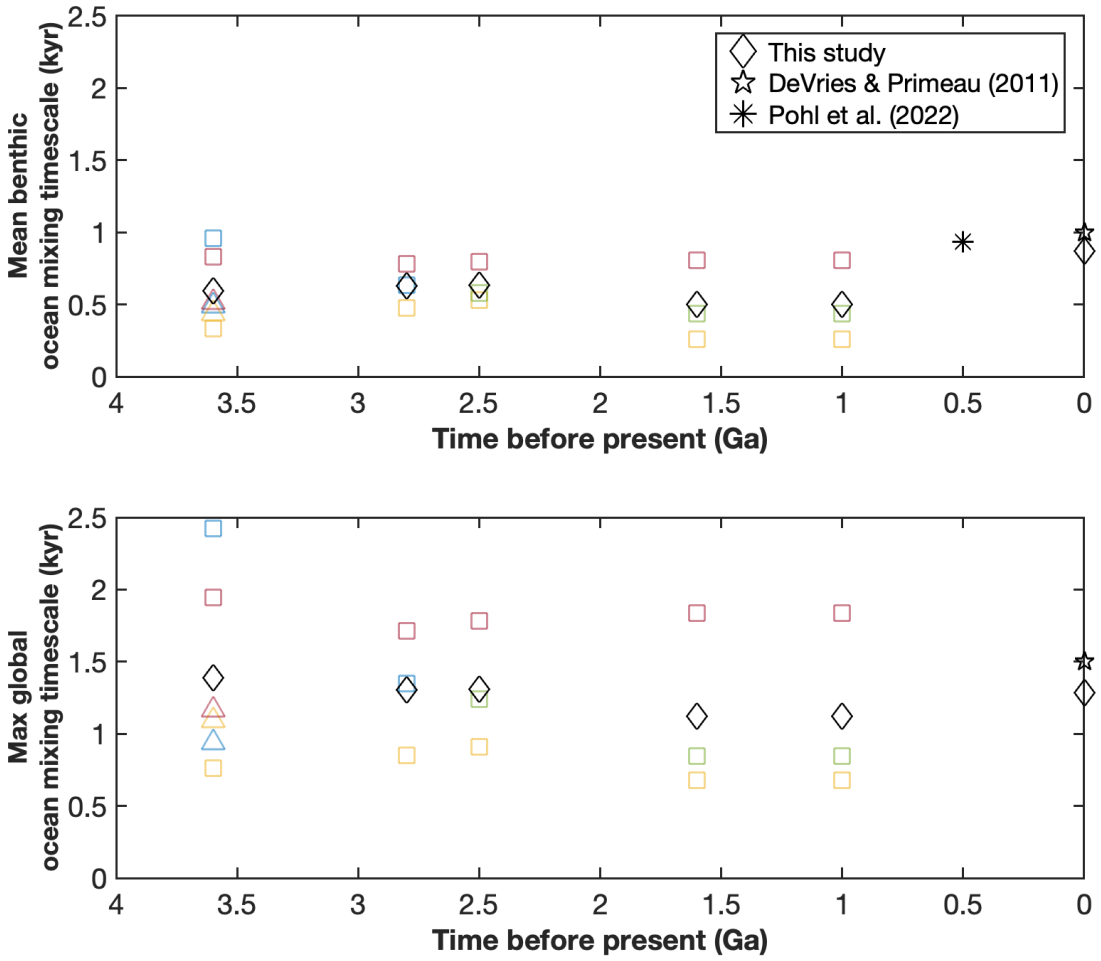

Figure 2-10 Variation in mean benthic (A) and maximum global (B) ocean mixing timescales through time. Squares and triangles correspond to historical experiments with surface pressure of 1 bar and 2 bar, respectively. Continental configuration is represented by blue (aquaplanet), yellow (low-latitude supercontinent), red (high-latitude supercontinents), and green (Pangaea) symbols. The black diamond at 0 Ga is our present-day baseline experiment, while black diamonds for the historical periods give the mean values of all experiments in the respective period. The asterisk at 0.5 Ga is the modeled Phanerozoic mean benthic ventilation age from Pohl et al. (2022), and the pentagrams at 0 Ga are data-constrained model estimates of present-day ventilation ages from DeVries and Primeau (2011).

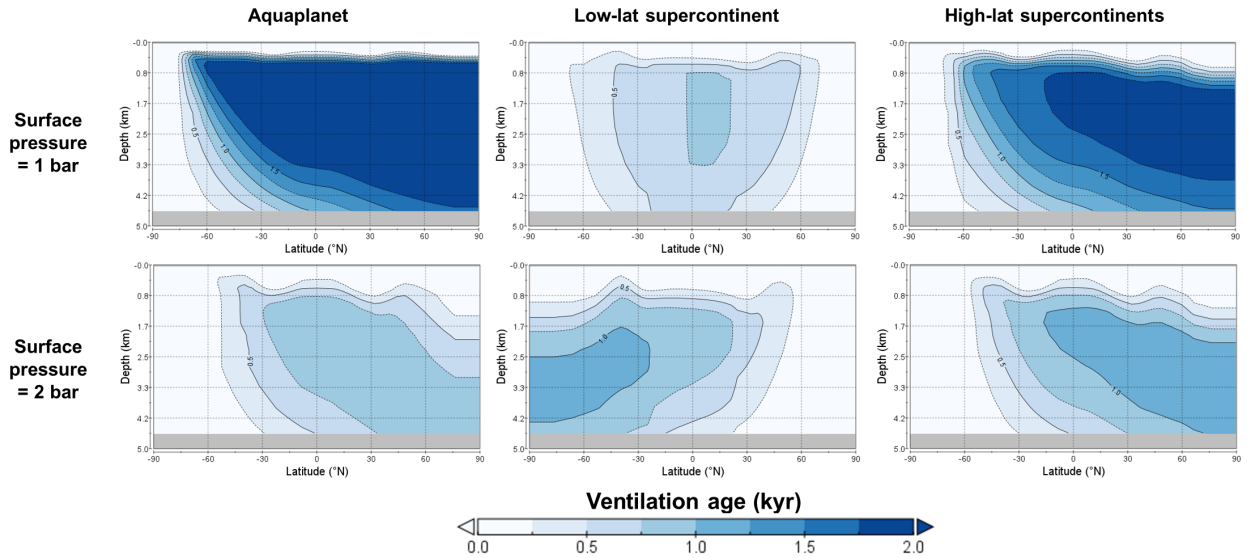

Figure 2-11 Zonal mean water mass ventilation age in 'Paleoarchean' simulations with day length = 15 hr and individual diapycnal diffusivities (see Table 2-1 for details). Note that the color bar is saturated in the top left panel, where the maximum age is 2.4 kyr.

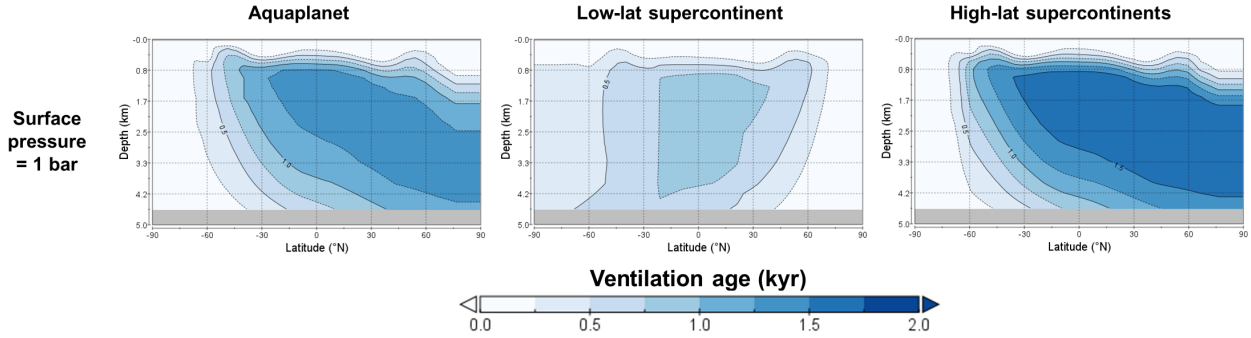

Figure 2-12 Zonal mean water mass ventilation age in 'Neoarchean' simulations with day length = 18 hr and individual diapycnal diffusivities (see Table 2-1 for details).

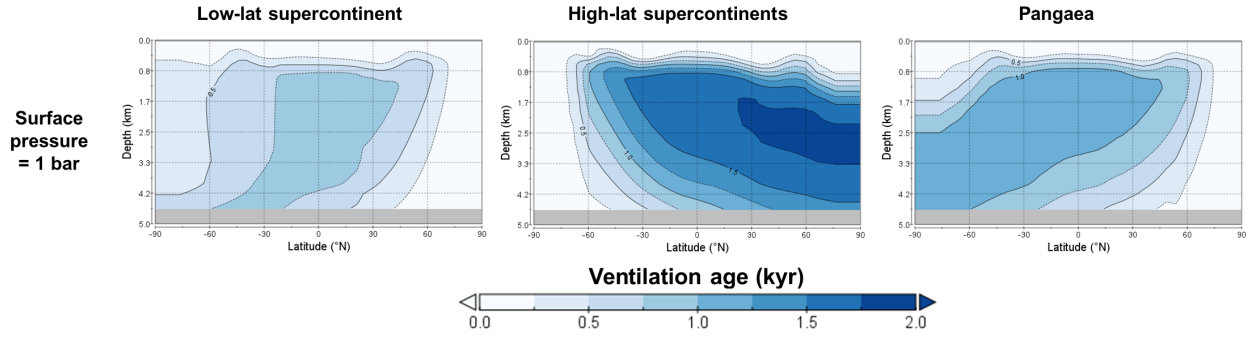

Figure 2-13 Zonal mean water mass ventilation age in 'Paleoproterozoic' simulations with day length = 18 hr and individual diapycnal diffusivities (see Table 2-1 for details).

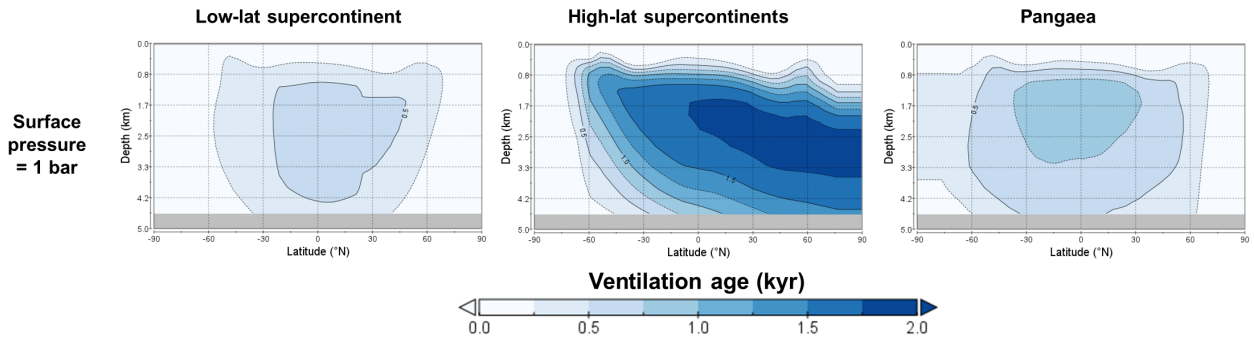

Figure 2-14 Zonal mean water mass ventilation age in 'Meso/Neoproterozoic' simulations with day length = 22.5 hr and individual diapycnal diffusivities (see Table 2-1 for details).

2.5 Conclusion

Our study provides the first quantitative evidence that despite the evolution of Earth's day length, surface pressure, continentality, and tidal dissipation, the ocean mixing timescales have remained relatively constant through geological eons, likely varying between a few hundred and a couple of thousand years since the Archean. Our work establishes a solid foundation upon which future research can build, particularly in the interpretation of sedimentary records using geochemical tracers with well-constrained residence times in the Precambrian oceans. Furthermore, our findings act as a critical reference point for reconstructing past climates with implications for evolution of life, and predicting future oceanic responses to environmental perturbations.

REFERENCES

Algeo, T. J., & Lyons, T. W. (2006). Mo–total organic carbon covariation in modern anoxic marine environments: Implications for analysis of paleoredox and paleohydrographic conditions. *Paleoceanography*, *21*(1).

Bartlett, B. C., & Stevenson, D. J. (2016). Analysis of a Precambrian resonance-stabilized day length. *Geophysical Research Letters*, *43*(11), 5716–5724.

Bills, B. G., & Ray, R. D. (1999). Lunar orbital evolution: A synthesis of recent results. *Geophysical Research Letters*, *26*(19), 3045-3048.

Broecker, W. S., & Peng, T. H. (1982). *Tracers in the Sea* (Vol. 690). Palisades, New York: Lamont-Doherty Geological Observatory, Columbia University.

Chen, X., Tissot, F. L. H., Jansen, M. F., Bekker, A., Liu, C. X., Nie, N. X., Halverson, G. P., Veizer, J., & Dauphas, N. (2021). The uranium isotopic record of shales and carbonates through geologic time. *Geochimica et Cosmochimica Acta*, *300*, 164–191.

Crichton, K. A., Ridgwell, A., Lunt, D. J., Farnsworth, A., & Pearson, P. N. (2021). Data-constrained assessment of ocean circulation changes since the middle Miocene in an Earth system model. *Climate of the Past*, *17*(5), 2223-2254.

Davies, H. S., Green, J. A. M., & Duarte, J. C. (2020). Back to the future II: tidal evolution of four supercontinent scenarios. *Earth System Dynamics*, *11*(1), 291–299.

DeVries, T., & Primeau, F. (2011). Dynamically and observationally constrained estimates of water-mass distributions and ages in the global ocean. *Journal of Physical Oceanography*, *41*(12), 2381-2401.

Enderton, D., & Marshall, J. (2009). Explorations of atmosphere–ocean–ice climates on an aquaplanet and their meridional energy transports. *Journal of the Atmospheric Sciences*, 66(6), 1593-1611.

Green, J. A. M., Huber, M., Waltham, D., Buzan, J., & Wells, M. (2017). Explicitly modelled deep-time tidal dissipation and its implication for Lunar history. *Earth and Planetary Science Letters*, *461*, 46-53.

Knauth, L. P. (2005). Temperature and salinity history of the Precambrian ocean: Implications for the course of microbial evolution. *Palaeogeography, Palaeoclimatology, Palaeoecology*, *219*(1–2), 53–69.

Kunze, E., Firing, E., Hummon, J. M., Chereskin, T. K., & Thurnherr, A. M. (2006). Global Abyssal Mixing Inferred from Lowered ADCP Shear and CTD Strain Profiles. *Journal of Physical Oceanography*, *36*(8), 1553–1576.

Lowe, D. R. (1994). Early environments: constraints and opportunities for early evolution. *Early life on Earth*, 25-35.

Marsh, R., Yool, A., Myerscough, R. J., Edwards, N. R., & Shepherd, J. G. (2009). *Incorporation of the C-GOLDSTEIN efficient climate model into the GENIE framework: the "genie eb go gs" configuration of GENIE* (Vol. 2).

Marty, B., Zimmermann, L., Pujol, M., Burgess, R., & Philippot, P. (2013). Nitrogen isotopic composition and density of the Archean atmosphere. *Science*, *342*(6154), 101-104.

Matsumoto, K. (2007). Radiocarbon-based circulation age of the world oceans. *Journal of Geophysical Research: Oceans*, *112*(C9).

Meyer, K. M., Ridgwell, A., & Payne, J. L. (2016). The influence of the biological pump on ocean chemistry: implications for long-term trends in marine redox chemistry, the global carbon cycle, and marine animal ecosystems. *Geobiology*, *14*(3), 207–219.

Nikurashin, M., & Vallis, G. (2012). A theory of the interhemispheric meridional overturning circulation and associated stratification. *Journal of Physical Oceanography*, *42*(10), 1652–1667.

Oliver, K. I. C., & Edwards, N. R. (2008). Location of potential energy sources and the export of dense water from the Atlantic Ocean. *Geophysical Research Letters*, *35*(22), L22604.

Olson, S., Jansen, M. F., Abbot, D. S., Halevy, I., & Goldblatt, C. (2022). The Effect of Ocean Salinity on Climate and Its Implications for Earth's Habitability. *Geophysical Research Letters*, *49*(10), e2021GL095748.

Olson, S. L., Jansen, M., & Abbot, D. S. (2020). Oceanographic Considerations for Exoplanet Life Detection. *The Astrophysical Journal*, *895*(1), 19.

Olson, S. L., Schwieterman, E. W., Reinhard, C. T., & Lyons, T. W. (2018). Earth: Atmospheric evolution of a habitable planet. In arXiv (pp. 1–37). arXiv.

Payne, R. C., Brownlee, D., & Kasting, J. F. (2020). Oxidized micrometeorites suggest either high p CO2 or low p N2 during the Neoarchean. *Proceedings of the National Academy of Sciences*, *117*(3), 1360-1366.

Pierrehumbert, R. T. (2010). *Principles of planetary climate*. Cambridge University Press.

Pohl, A., Ridgwell, A., Stockey, R. G., Thomazo, C., Keane, A., Vennin, E., & Scotese, C. R. (2022). Continental configuration controls ocean oxygenation during the Phanerozoic. *Nature 2022 608:7923*, *608*(7923), 523–527.

Ridgwell, A. (2017). The Bumper Book of .muffins (The cGENIE.muffin user-manual and introduction to Earth system modelling).

Som, S. M., Buick, R., Hagadorn, J. W., Blake, T. S., Perreault, J. M., Harnmeijer, J. P., & Catling, D. C. (2016). Earth's air pressure 2.7 billion years ago constrained to less than half of modern levels. *Nature Geoscience*, *9*(6), 448-451.

Wang, C., Konhauser, K. O., Zhang, L., Zhai, M., & Li, W. (2016). Decoupled sources of the 2.3–2.2 Ga Yuanjiacun banded iron formation: Implications for the Nd cycle in Earth's early oceans. *Precambrian Research*, *280*, 1-13.

Waterhouse, A. F., Mackinnon, J. A., Nash, J. D., Alford, M. H., Kunze, E., Simmons, H. L., Polzin, K. L., Laurent, L. C. S., Sun, O. M., Pinkel, R., Talley, L. D., Whalen, C. B., Huussen, T. N., Carter, G. S., Fer, I., Waterman, S., Naveira Garabato, A. C., Sanford, T. B., & Lee, C. M. (2014). Global Patterns of Diapycnal Mixing from Measurements of the Turbulent Dissipation Rate. *Journal of Physical Oceanography*, *44*(7), 1854–1872.

Way, M. J., Davies, H. S., Duarte, J. C., & Green, J. A. M. (2021). The climates of Earth's next supercontinent: effects of tectonics, rotation rate, and insolation. *Geochemistry, Geophysics, Geosystems*, *22*(8), e2021GC009983.

Webb, D. J. (1982). Tides and the evolution of the Earth-Moon system. In *Geophys. J. R. astr. Soc* (Vol. 70).

Wilson, B. W. (1960). Note on surface wind stress over water at low and high wind speeds. *Journal of Geophysical Research*, *65*(10), 3377–3382.

Wunsch, C., & Ferrari, R. (2004). Vertical mixing, energy, and the general circulation of the oceans. *Annu. Rev. Fluid Mech.*, *36*, 281-314.

Yang, J., Jansen, M. F., Macdonald, F. A., & Abbot, D. S. (2017). Persistence of a freshwater surface ocean after a snowball Earth. *Geology*, *45*(7), 615–618.

Yi, Y. R., Legg, S., & Nazarian, R. H. (2017). The impact of topographic steepness on tidal dissipation at bumpy topography. *Fluids*, *2*(4), 55.

Zahnle, K., & Walker, J. C. (1987). A constant daylength during the Precambrian era?. *Precambrian Research*, *37*(2), 95-105.

3 NEODYMIUM AND URANIUM ISOTOPES AS PALEOPROXIES

3.1 Introduction

Building upon our model constraints on the Precambrian ocean mixing timescale, we examine next the roles of two popular isotopic tracers with distinct oceanic residence times, neodymium (Nd) and uranium (U), in the interpretation of early oceanic conditions from sedimentary records.

Nd isotopic ratios in seawater can trace ocean mixing in present-day and potentially deep time, since Nd has a residence time of 0.3-0.8 kyr (Tachikawa et al., 2003; Arsouze et al., 2009; Gu et al., 2019) in the modern ocean and this rare earth element (REE) is minimally affected by biochemical processes (Goldstein and Hemming, 2003). Its isotopic composition in modern seawater displays distinct inter-ocean differences influenced by the weathering of regional sources of distinct age and lithologies (Osborne et al., 2014). Modern seawater ε_{Nd} endmembers consist of young weathered volcanic material in the northern Pacific Ocean and old weathered continental material in the deep North Atlantic (Piepgras and Wasserburg, 1980).

In contrast, Archean seawater ε_{Nd} was likely governed by the interplay between high-temperature hydrothermal fluids with ε_{Nd}-depleted signatures and terrestrial influx from rivers (and aeolian dust) with ε_{Nd}-enriched signatures (Derry and Jacobsen 1990; Jacobsen and Pimentel-Klose, 1988). If ocean mixing had been extremely efficient in the Archean, any change in the ε_{Nd} isotopic composition of homogeneous seawater would have reflected a secular change in the balance between deep hydrothermal fluids and continental weathering, which would have been slow and progressive. Conversely, if ocean mixing had been extremely inefficient, highly heterogeneous water parcels would coexist carrying either markedly enriched (low-ε_{Nd}) or

depleted (high-ε_{Nd}) signatures. Analyses of ancient BIFs and carbonates show that sedimentary archives record an oceanic state that is in-between these two endmembers (Alexander et al., 2009; Wang et al., 2016; Hu et al., 2020), whereby lateral heterogeneities and swift temporal changes can be detected but intermediate ε_{Nd} values are common. This most likely is because the ocean mixing timescale was similar to Nd residence time in the Archean oceans.

In this chapter, we examine the spatial pattern and scale of Nd isotopic variations predicted in our cGENIE simulations, which can be compared to ancient seawater ε_{Nd} recorded by Archean BIFs. To provide some constraints on the Nd-ε_{Nd} budget in the Archean oceans assuming steady state, we estimate Nd source fluxes using similar scaling arguments as those used for iron by Dauphas et al. (2024) and compile the corresponding ε_{Nd} values from Precambrian sedimentary archives (Hu et al. 2020; Vervoort and Blichert-Toft 2020; Jacobsen 1988).

The U isotopic ratio in seawater has been widely used to reconstruct global redox conditions in the past (see review in Lau et al., 2019) due to its sensitivity to the global extent of anoxia (Tissot and Dauphas, 2015). In the modern well-oxygenated ocean, U behaves conservatively due to formation of soluble U(VI) carbonate complexes (Langmuir 1978) and has a residence time of 400 kyr (Ku et al., 1977), far exceeding the modern ocean mixing timescale (~1 kyr), meaning the modern ocean is homogeneous with respect to the U concentration and isotopic composition. Therefore, the U isotopic compositions of anoxic marine sediments and carbonates are expected to reflect the global oceanic redox conditions.

However, such expectations cannot be easily applied to early oceans, in which the oceanic U budget was significantly different from the modern. Uranium is primarily supplied to the ocean by river runoff associated with oxidative weathering and is removed primarily into anoxic and

suboxic sediments by the reduction of U(VI) to U(IV), as well as biogenic carbonates (Dunk et al., 2002). Therefore, the oceanic residence time of U under a more anoxic Precambrian atmosphere would have undoubtedly decreased, possibly calling into question the use of the U isotopic proxy in deep time. To provide a quantitative estimate of U residence time in Precambrian oceans, we have constructed a mass balance model which correlates redox sensitive trace metal burial rates with seafloor redox distribution and further constrains the input flux using sedimentary data.

3.2 Neodymium isotope modelling

In the modern ocean, Nd is supplied by a dominant (~95%) sediment flux from boundary exchange, along with riverine and dust fluxes, while it is removed by scavenging on sinking particles (Tachikawa et al., 2020). The precise mechanism of boundary exchange is not fully understood, and it may include submarine groundwater discharge (Johannesson and Burdige, 2007) and benthic flux from porewater (Abbott et al., 2019). To test our model's ability to reconstruct the source heterogeneity of ε_{Nd} as observed in the modern ocean and how sensitive it is to the sediment flux, we model ε_{Nd} in the modern ocean with and without a sediment flux (Fig. 3-1). We introduce modern river, dust and sediment Nd input fluxes and corresponding ε_{Nd} values that vary among basins based on Table 1 in Du et al. (2020) in one simulation, and set the global Nd input flux to only include riverine and dust fluxes and the global seawater ε_{Nd} to only reflect riverine and dust ε_{Nd} in the other. Despite a depth dependence of seawater ε_{Nd} in the North Atlantic contrasting with observations due to reduced North Atlantic Deep Water formation in our modelled present-day ocean (Fig. 2-4), incorporating a sediment Nd source with variable ε_{Nd} significantly improves the model's ability in capturing the observed heterogeneity between Pacific and Atlantic

Oceans, especially at depths >200 m, which is the depth range relevant for Precambrian BIF formation (Trendall 2002).

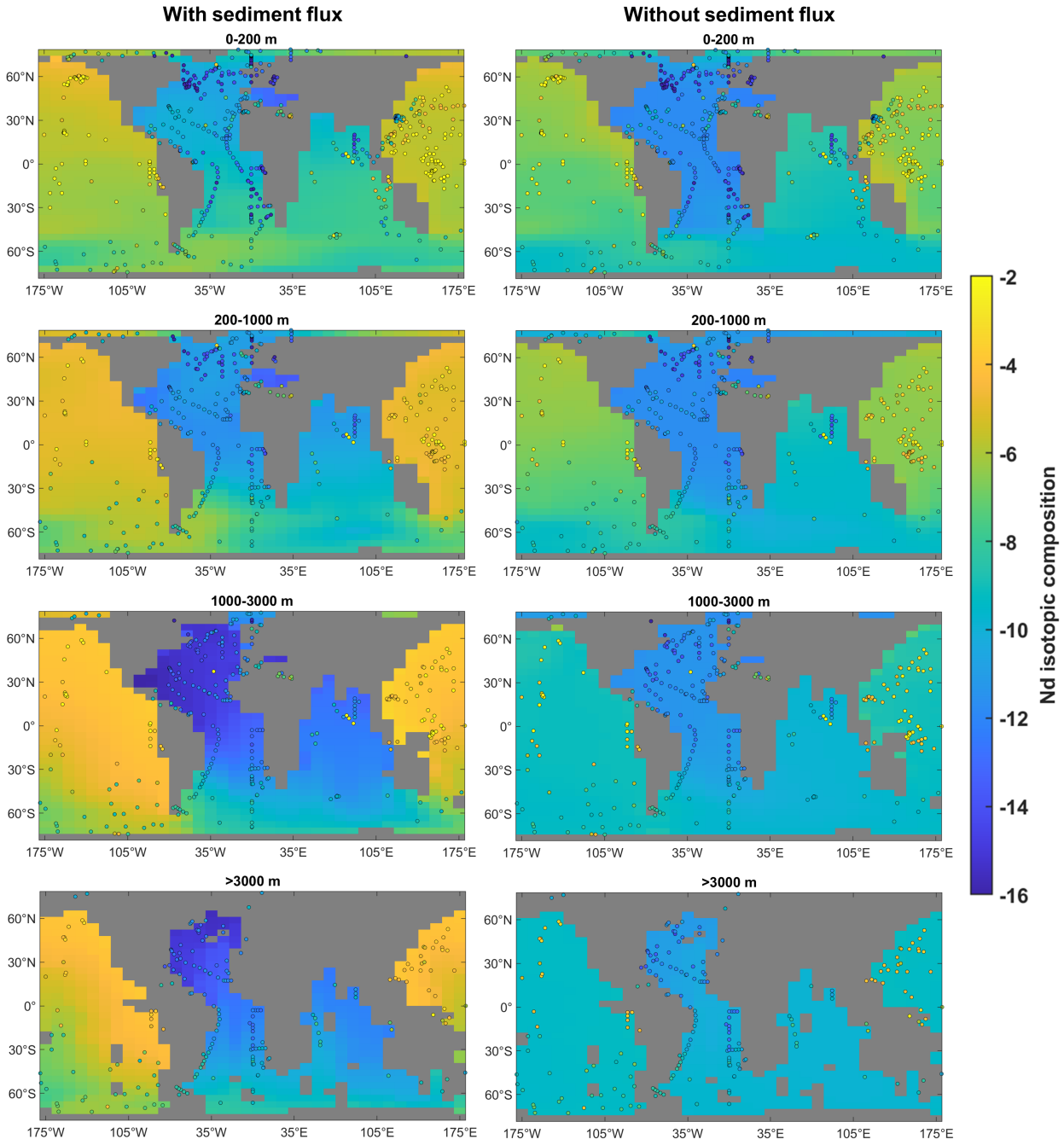

Figure 3-1 Modeled Nd isotopic composition in the modern ocean with (left) or without (right) a sediment source. Circles are observational data compiled by Robinson et al. (2023).

In ancient oceans, the same sources and sinks would have been present, but deep-sea hydrothermal vents could have contributed more significantly to the overall balance (Jacobsen and Pimentel-Klose 1988; Alexander et al., 2009). To estimate the Nd-$\boldsymbol{\varepsilon}_{\mathrm{Nd}}$ budget for Archean oceans (Table 3-1), we need to know the following:

1. Global mean seawater Nd concentration (g/kg) ($[\mathrm{Nd}]_{\mathrm{sw}}$).
2. Nd input fluxes (g/yr) of river ($\phi_{\mathrm{Nd,r}}$), dust ($\phi_{\mathrm{Nd,d}}$), hydrothermal ($\phi_{\mathrm{Nd,h}}$) and benthic sediment ($\phi_{\mathrm{Nd,s}}$).
3. Global mean Nd isotopic compositions of seawater ($\varepsilon_{\mathrm{Nd,sw}}$), river ($\varepsilon_{\mathrm{Nd,r}}$), dust ($\varepsilon_{\mathrm{Nd,d}}$), hydrothermal ($\varepsilon_{\mathrm{Nd,h}}$) and benthic sediment ($\varepsilon_{\mathrm{Nd,s}}$) sources.

We use $[Nd]_{\mathrm{sw}} = 1.43 \times 10^{-7}$ g/kg by taking the average of the Nd concentrations of 3.1-3.4 Ga seawater estimated from BIF magnetite of Badampahar greenstone belt (Ghosh and Baidya, 2017) and dolomite of Pilbara Block (Yamamoto et al., 2004). For an ocean with mass equal to 1.4×10^{21} kg, this gives a total Nd inventory equal to 2.0×10^{14} g.

We estimate $\phi_{\mathrm{Nd,r}}$, $\phi_{\mathrm{Nd,d}}$, and $\phi_{\mathrm{Nd,h}}$ following the approach used by Dauphas et al. (2024) for iron. We assume that at steady-state, the Nd flux from rivers scales with the rate of continental chemical weathering, which itself is going to scale with the rate of CO_2 degassing through

$$\phi_{\mathrm{Nd,r}}(t) = r_{CO_2} r_{\phi_{\mathrm{mantle}}} \phi_{\mathrm{Nd,r}}(0), \qquad \text{(Eq. 3-1)}$$

where $r_{CO_2} = 0.8$ is the Archean to present-day ratio of the fraction of CO_2 drawdown associated with continental weathering (Krissansen-Totton et al. 2018), $r_{\phi_{\mathrm{mantle}}} = 2.3$ is the Archean to present-day ratio of mantle heat flux (Patočka et al., 2020), and $\phi_{\mathrm{Nd,r}}(0) = 1.5 \times 10^9$ g/yr is the present-day global Nd river input flux (Xu et al., 2023), resulting in $\phi_{\mathrm{Nd,r}}(t) = 2.76 \times 10^9$ g/yr into the Archean oceans. The Nd river flux may have been affected by its speciation and pH-

dependent adsorption on solid particles (Goldstein and Jacobsen, 1987), which is not accounted for here due to lack of constraints. The Archean to present-day ratio of mantle heat flux is also uncertain, as it could have been significantly lower than what we adopted here. Indeed, Korenaga (2008) argued that the mantle heat flux did not change much since 4 Ga.

For the flux of dust, we use the following scaling:

$$\phi_{\mathrm{Nd,d}}(t) = r_A \cdot \phi_{\mathrm{dust}}(0) \cdot r_{[Nd]_{EC}} \cdot [Nd]_d(0) \cdot f(t), \quad \text{(Eq. 3-2)}$$

where $r_A = 0.5$ is the Archean to present-day ratio of areal extent of emerged continents (Korenaga et al., 2017), $\phi_{\mathrm{dust}}(0) = 440\ Tg/yr$ is the present-day dust input flux (Wu et al., 2020), $r_{[Nd]_{EC}} = 0.65$ is the Archean to present-day ratio of Nd concentration of emerged continents (Ptáček et al., 2020), $[Nd]_d(0) = 20\ \mu g/g$ is the present-day global mean Nd concentration in dust (Goldstein et al., 1984), and $f(t) = 0.1$ is the Archean fraction of Nd in dust that dissolves along with Fe in seawater (Dauphas et al., 2024; Greaves et al., 1994), resulting in $\phi_{\mathrm{Nd,d}}(t) = 2.86 \times 10^8$ g/yr during the Archean.

In the modern ocean, hydrothermal fluid is a negligible source and in fact represents a net sink due to scavenging of Nd by particulate iron (German et al., 1990). In the anoxic Archean ocean, high-temperature hydrothermal fluids could have released Fe and Nd into seawater without elemental fractionation (Jacobsen and Pimentel-Klose, 1988). We therefore use the following scaling:

$$\phi_{\mathrm{Nd,h}}(t) = r_{\phi_{\mathrm{hydro}}} \cdot \phi_{\mathrm{hw}}(0) \cdot [Fe]_h(0) \cdot \left(\frac{Nd}{Fe}\right)_{sw,t}, \quad \text{(Eq. 3-3)}$$

where $r_{\phi_{\mathrm{hydro}}} = 3$ is the Archean to present-day ratio of hydrothermal heat flux (Lowell and Keller, 2003), $\phi_{\mathrm{hw}}(0) = 5.9 \times 10^{16}$ g/yr is the present-day high-temperature hydrothermal water flux (Dauphas et al., 2024), $[Fe]_h(0) = 5.8\ mmol/kg$ is the present-day Fe concentration in high-

temperature hydrothermal fluid (Dauphas et al., 2024), and $\left(\frac{Nd}{Fe}\right)_{sw,t} = 9.53 \times 10^{-5}$, giving $\phi_{\mathrm{Nd,h}}(t) = 1.02 \times 10^{10}$ g/yr into the Archean oceans.

In the modern ocean, the flux from benthic sediments accounts for ~95% of total Nd sources (Rempfer et al., 2011; Abbott et al., 2015a, b; Haley et al., 2017; Du et al., 2020). The mechanisms of this sediment Nd input are not yet defined, but it is acknowledged that the sediment Nd flux is dominated by deep-sea sediments (water depth > 3 km) in the modern ocean, and may be controlled by the extent of benthic seafloor area and sediment provenance without dependency on sediment redox state (Du et al., 2018). We posit that the sediment source consistently represents 95% of the total Nd sources, scaling with other sources (Table 3-1). While the sediment source dominates the overall Nd flux, other sources play significant roles in the Nd cycle as they can influence the $\varepsilon_{\mathrm{Nd}}$ of nearby water masses.

Therefore for the Archean oceans, total Nd input flux $\phi_{\mathrm{Nd}} = (\phi_{\mathrm{Nd,r}} + \phi_{\mathrm{Nd,d}} + \phi_{\mathrm{Nd,h}})/5\% = 2.65 \times 10^{11}$ g/yr and $\phi_{\mathrm{Nd,s}} = 95\%\phi_{\mathrm{Nd}} = 2.52 \times 10^{11}$ g/yr. The calculated Nd residence time in the Archean oceans is therefore $\tau_{\mathrm{Nd}} = Nd/\phi_{\mathrm{Nd}} = (2.0 \times 10^{14}\ \mathrm{g})/(2.65 \times 10^{11}\ \mathrm{g/yr}) = 755\ yr$. In the modern ocean, Nd is removed from the water column by scavenging on particles following a first-order kinetic rate law $\phi_{\mathrm{Nd,sink}} = k \cdot dt \cdot [Nd]_{sw}$, where $k = 1/\tau_{\mathrm{Nd}}$ (Bacon and Anderson 1982; Du et al., 2020). For lack of better constraints, we assume that Nd removal in Precambrian oceans took place through the same mechanism and set $k = 1/755\ yr^{-1}$ in our model to balance the input fluxes.

The Nd riverine flux is applied in coastal grid cells around the supercontinents in the surface ocean, and the Nd dust flux is applied in all surface ocean grid cells. The Nd hydrothermal flux is applied along 'mid-ocean ridges' between 115°W and 125°W in the bottom ocean, and the

Nd sediment flux is applied in all bottom ocean grid cells except those occupied by the hydrothermal flux. The Nd removal flux is applied uniformly to all ocean cells.

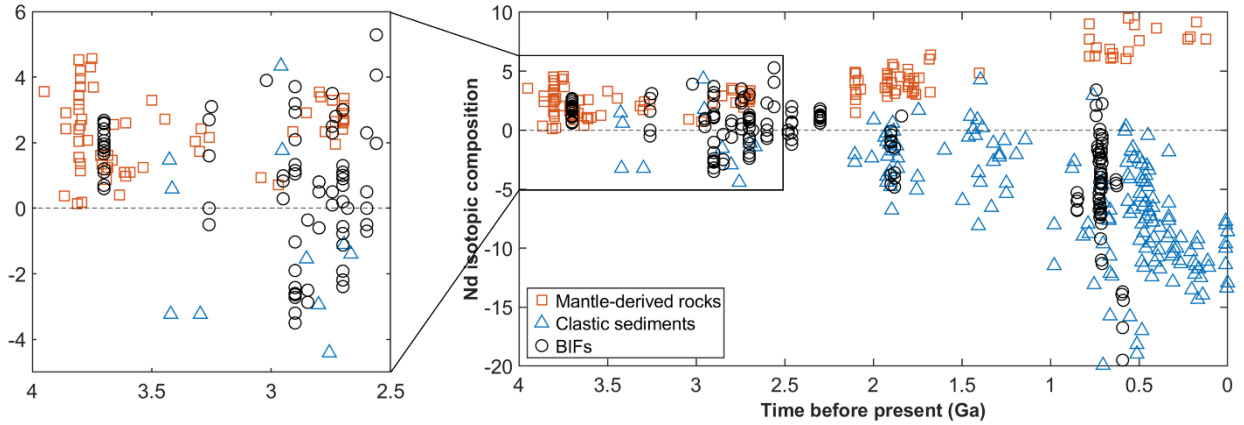

Figure 3-2 Temporal evolution of ε_{Nd} of Precambrian BIFs (black circles; Hu et al. 2020), depleted mantle-derived basalts (orange squares; Vervoort and Blichert-Toft 2020) and continent-eroded clastic sediments (blue triangles; Jacobsen 1988). Zoomed-in view focuses on the Archean.

We estimate the average Archean $\varepsilon_{Nd,sw}$, $\varepsilon_{Nd,h}$, $\varepsilon_{Nd,r}$ and $\varepsilon_{Nd,d}$ by taking the average ε_{Nd} of BIFs (Hu et al., 2020), depleted mantle-derived rocks (Vervoort and Blichert-Toft, 1999), and clastic sediments (Jacobsen 1988) respectively, assuming $\varepsilon_{Nd,r} = \varepsilon_{Nd,d}$ as river and dust Nd both reflect continental ε_{Nd}. Taking the average of ε_{Nd} of each rock type during the Archean (Fig. 3-2), we have $\varepsilon_{Nd,sw} = +0.8$, $\varepsilon_{Nd,h} = +2$, and $\varepsilon_{Nd,r} = \varepsilon_{Nd,d} = -1$. We then solve for Archean $\varepsilon_{Nd,s}$ through a simple mass balance calculation,

$$\varepsilon_{Nd,sw} = \left(\varepsilon_{Nd,r} \times \phi_{Nd,r} + \varepsilon_{Nd,d} \times \phi_{Nd,d} + \varepsilon_{Nd,h} \times \phi_{Nd,h} + \varepsilon_{Nd,s} \times \phi_{Nd,s}\right)/\left(\phi_{Nd,r} + \phi_{Nd,d} + \phi_{Nd,h} + \phi_{Nd,s}\right). \quad \text{(Eq. 3-4)}$$

By plugging in the values for Nd fluxes and isotopic compositions from above, we get $\varepsilon_{Nd,s} = +0.77$. Because the flux from benthic sediments always represents the major source of Nd in seawater, the isotopic composition of the sediment source is always close to that of seawater.

However, juvenile mafic and old felsic continental crusts could have coexisted in the late Archean. To account for the possible heterogeneity in continental ε_{Nd} values at that time, as is observed in detrital sediments of Archean age (Fig. 3-2), and subsequently the heterogeneity in sedimentary ε_{Nd}, we take the minimum and maximum ε_{Nd} values of Archean detrital sediments (-6 and +4) to represent the endmember Archean $\varepsilon_{Nd,r}$, $\varepsilon_{Nd,d}$ and $\varepsilon_{Nd,s}$. We then solve for the relative contributions of these two endmember ε_{Nd} values into the Archean ocean whose bulk $\varepsilon_{Nd,sw}$ remains constant,

$$\varepsilon_{Nd,sw} = \frac{[-6x+4(1-x)](\phi_{Nd,r}+\phi_{Nd,d}+\phi_{Nd,s})+\varepsilon_{Nd,h}\times\phi_{Nd,h}}{\phi_{Nd,r}+\phi_{Nd,d}+\phi_{Nd,h}+\phi_{Nd,s}}, \quad \text{(Eq. 3-5)}$$

where $x = 0.325$, meaning that 32.5% of the continental and sedimentary sources have enriched $\varepsilon_{Nd} = -6$ and the remaining 67.5% have depleted $\varepsilon_{Nd} = +4$. Table 3-1 compiles the parameter values used in the modelling the Nd cycle during the Archean.

Table 3-1 Nd-$\boldsymbol{\varepsilon}_{Nd}$ budget for Archean ocean modelling.

Seawater [Nd] (g/kg)	1.43×10^{-7}		
Seawater $\boldsymbol{\varepsilon}_{Nd}$	+0.8		
Hydrothermal Nd source (g/yr)	1.02×10^{10}		
Hydrothermal flux $\boldsymbol{\varepsilon}_{Nd}$	+2		
	Homogeneous source $\boldsymbol{\varepsilon}_{Nd}$	Heterogeneous source $\boldsymbol{\varepsilon}_{Nd}$	
Riverine Nd source (g/yr)	2.76×10^{9}	8.97×10^{8}	1.86×10^{9}
Riverine flux $\boldsymbol{\varepsilon}_{Nd}$	-1	-6	+4
Dust Nd source (g/yr)	2.86×10^{8}	9.30×10^{7}	1.93×10^{8}
Dust flux $\boldsymbol{\varepsilon}_{Nd}$	-1	-6	+4
Sediment Nd source (g/yr)	2.52×10^{11}	8.19×10^{10}	1.70×10^{11}
Sediment flux $\boldsymbol{\varepsilon}_{Nd}$	+0.77	-6	+4

When a single continental ε_{Nd} of -1 is applied to the whole surface ocean, along with a hydrothermal ε_{Nd} of +2 and a sediment ε_{Nd} of +0.77 applied to the benthic ocean, global seawater ε_{Nd} ranges from +0.3 to +1 in both Archean oceans regardless of whether the mean benthic ventilation age is shorter or longer than the Nd residence time (Fig. 3-3). BIFs are thought to have

been deposited at depths below the wave base and above the continental slope margin (equivalent to our 200-3000 m interval; Dauphas et al. 2024). At those depths, seawater ε_{Nd} ranges from +0.5 to +0.8. This predicted range is much smaller than that measured in Archean BIFs (Fig. 3-2), whose ε_{Nd} ranges from +0.5 to +3 in the early Archean (>3.5 Ga) and from -3.5 to +5.5 in the late Archean (3.5-2.5 Ga).

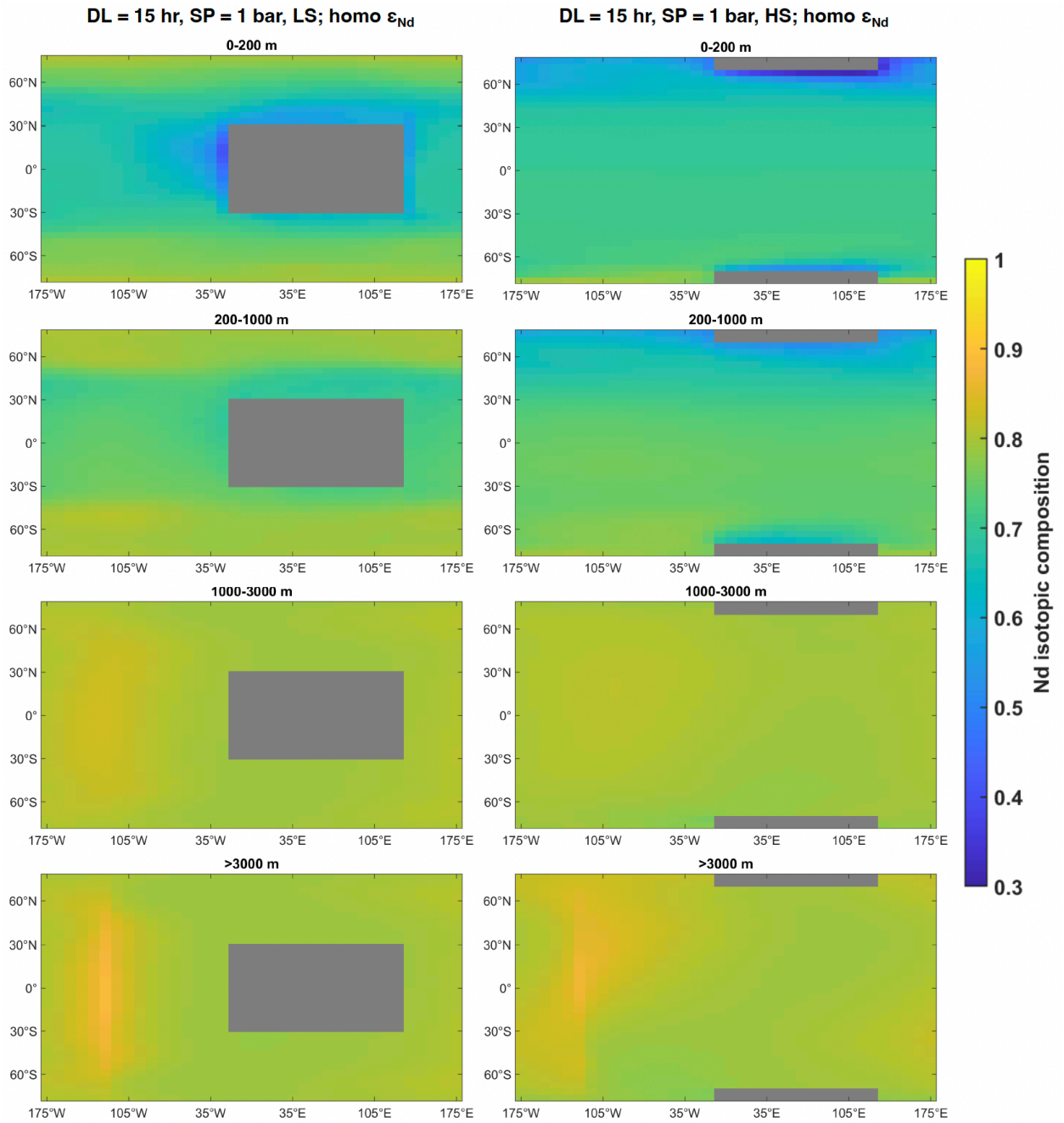

Figure 3-3 Modeled seawater ε_{Nd} averaged over various column depths in Archean experiments with the shortest (0.33 kyr, left) and longest (0.83 kyr, right) mean benthic ventilation ages and a single average ε_{Nd} value for the corresponding source. DL: day length, SP: surface pressure, LS: low-latitude supercontinent, HS: high-latitude supercontinents, homo ε_{Nd}: average continental and sedimentary source Nd isotopic compositions.

When endmember continental and sedimentary ε_{Nd} values of -6 and +4 are applied to account for the variations in ε_{Nd} of clastic sediments, global seawater ε_{Nd} ranges from -4 to +4 in both Archean oceans (Fig. 3-4), resulting in a similar degree of heterogeneity observed in the late Archean BIFs. Comparing Figures 3-3 and 3-4 leads to an updated understanding for the source of Nd in Archean oceans in contrary to previous suggestions by Jacobsen and Pimentel-Klose (1988) and Derry and Jacobsen (1990). Given a dominating sedimentary source, the positive ε_{Nd} values in Archean BIFs do not necessarily reflect hydrothermal input but may suggest instead the juvenile or mafic fraction within detrital sediments which offer a high ε_{Nd} sedimentary source. This is consistent with studies of modern porewater and authigenic ε_{Nd} in the North Pacific (Abbott et al., 2015a; Du et al., 2016). Consequently, the contribution of Nd (and Fe) by hydrothermal source in Archean oceans calculated based on a misunderstood ε_{Nd} budget may have been exaggerated and may be less significant than the continental source according to the estimates for Archean iron biogeochemical cycle in Dauphas et al. (2024).

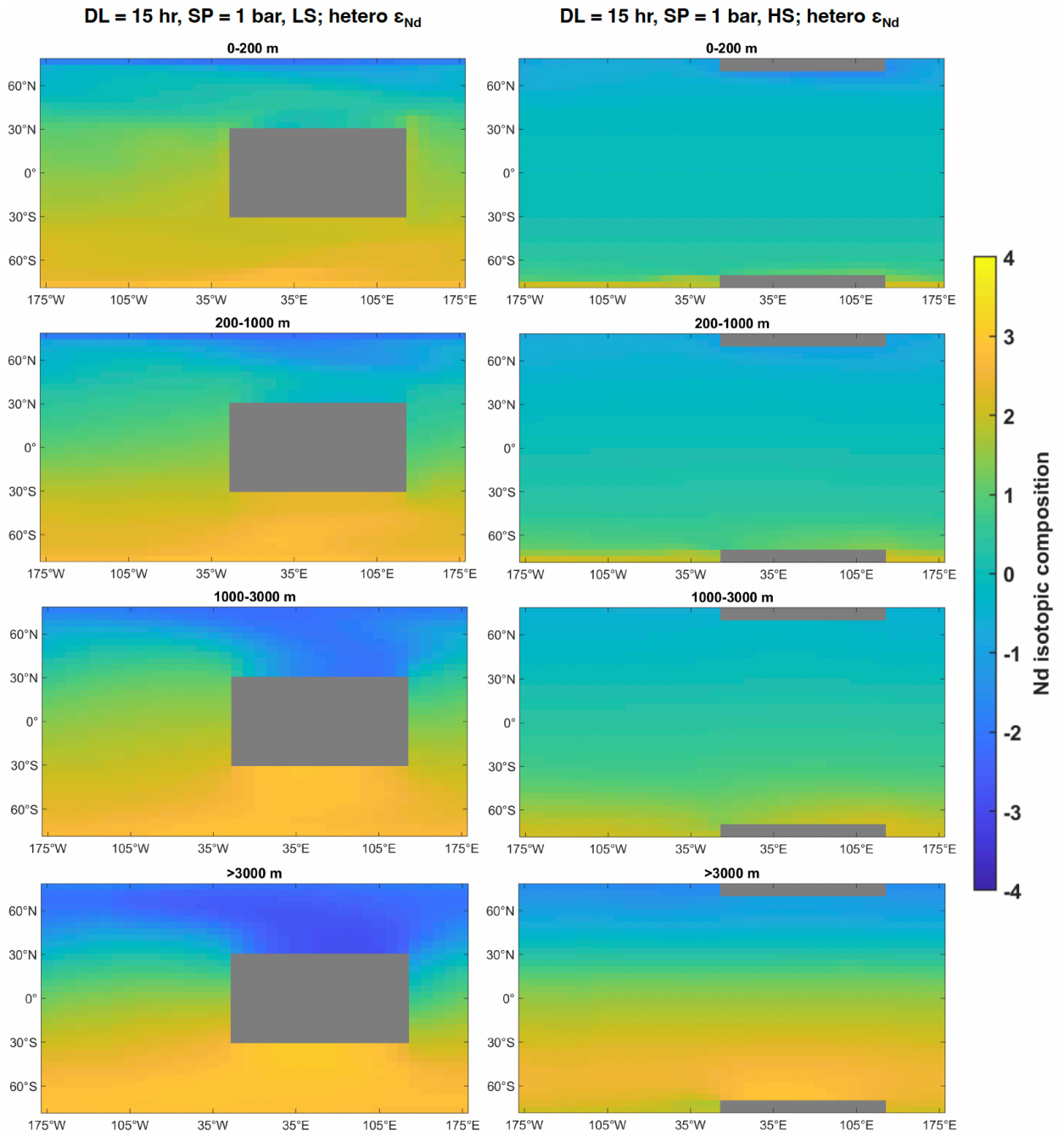

Figure 3-4 Modeled seawater ε_{Nd} averaged over various column depths in Archean experiments with the shortest (0.33 kyr, left) and longest (0.83 kyr, right) mean benthic ventilation ages and endmember ε_{Nd} values of -6 and +4 for the continental and sedimentary sources. DL: day length, SP: surface pressure, LS: low-latitude supercontinent, HS: high-latitude supercontinents, hetero ε_{Nd}: endmember continental and sedimentary source Nd isotopic compositions.

3.3 Uranium mass balance model

The residence time of uranium τ (kyr) is given by,

$$\tau = \frac{M_{sw}[U]_{sw,t}}{F_{in}}, \quad \text{(Eq. 3-6)}$$

where M_{sw} is the mass of the oceans, $[U]_{sw,t}$ is the seawater U concentration at time t, and F_{in} is the U input flux into the ocean. M_{sw} did not change much since the Archean (presumably by less than a factor of 2; Pope et al., 2012; Korenaga et al., 2017), whereas F_{in} and $[U]_{sw,t}$ could have changed more dramatically. These changes can be assessed by examining the composition of chemical sediments, which indirectly record the composition of seawater from which they precipitated.

We estimate F_{in} and $[U]_{sw,t}$ based on an oceanic mass-balance model modified from Reinhard et al. (2013) and Sheen et al. (2018). At steady-state, the flux of uranium into the oceans F_{in} (μg/yr) is equal to the flux out F_{out} (μg/yr) given by the U burial rate B_i (μg U cm^{-2} yr^{-1}) integrated over the seafloor surface area A_i (cm^2) covered by a particular sink *i*,

$$F_{in} = F_{out} = \sum_i F_i = \sum_i \int_{A_i} B_i \, dA. \quad \text{(Eq. 3-7)}$$

Separating the anoxic (*a*) from non-anoxic (*na*) sinks, Eq. 3-7 becomes,

$$F_{in} = \int_{A_{na}} B_{na} \, dA + \int_{A_a} B_a \, dA. \quad \text{(Eq. 3-8)}$$

U burial rates in past oceans are related to the modern (m subscript) burial rates by a dimensionless scaling factor ε_i,

$$B_{na} = \varepsilon_{na} B_{na,m}, \quad \text{(Eq. 3-9)}$$

$$B_a = \varepsilon_a B_{a,m}. \quad \text{(Eq. 3-10)}$$

U burial rates scale with U concentration in seawater at time t, $[\mathrm{U}]_{sw,t}$ (ppm), following a power relationship (Reinhard et al. 2013),

$$\varepsilon_{na} = k_{na}[\mathrm{U}]_{sw,t}{}^{\theta_{na}}, \quad \text{(Eq. 3-11)}$$

$$\varepsilon_{a} = k_{a}[\mathrm{U}]_{sw,t}{}^{\theta_{a}}. \quad \text{(Eq. 3-12)}$$

For the non-anoxic sink, we take k_{na} to be constant and we constrain it from the modern seawater U concentration $[\mathrm{U}]_{sw,m}$ ($\varepsilon_{na,m} = 1$),

$$k_{na} = \frac{1}{[U]_{sw,m}{}^{\theta_{na}}}. \quad \text{(Eq. 3-13)}$$

Modern burial rate for the non-anoxic sink $B_{na,m}$ is calculated by $F_{na,m}/A_{na,m}$, so that Eq. 3-9 becomes,

$$B_{na} = \left(\frac{[\mathrm{U}]_{sw,t}}{[\mathrm{U}]_{sw,m}}\right)^{\theta_{na}} \frac{F_{na,m}}{A_{na,m}}. \quad \text{(Eq. 3-14)}$$

We cannot assume the same scaling for anoxic sink, where the metal burial rate depends also on organic carbon burial rate (Algeo and Lyons, 2006). Modern anoxic burial rates are measured in shelf sediments, where organic burial rates are high due to high primary productivity. In the past, anoxia could have expanded into abyssal plains, which are characterized by lower carbon burial rates and presumably lower efficiency of redox metal removal (*e.g.*, U). In order to account for these two effects, we write k_a as a function of the organic carbon burial rate $B_{C_{org}}$ (mmol C cm^{-2} yr^{-1}),

$$k_a = \gamma B_{C_{org}}, \quad \text{(Eq. 3-15)}$$

where γ is a constant that did not change with time. The scaling factor relating anoxic metal burial rate to seawater concentration therefore takes the form (by combining Eqs. 3-12 and 3-15),

$$\varepsilon_a = \gamma B_{C_{org}} [U]_{sw,t}{}^{\theta_a}. \quad \text{(Eq. 3-16)}$$

The anoxic burial rate in Eq. 3-10 is therefore,

$$B_a = \gamma [U]_{sw,t}{}^{\theta_a} B_{C_{org}} B_{a,m}. \quad \text{(Eq. 3-17)}$$

Integrating the burial rates over the surface area of the sinks, we have from Eq. 3-8,

$$F_{in} = \left(\frac{[U]_{sw,t}}{[U]_{sw,m}}\right)^{\theta_{na}} \frac{A_{na}}{A_{na,m}} F_{na,m} + \int_{A_a} \gamma [U]_{sw,t}{}^{\theta_a} B_{C_{org}} B_{a,m}\, dA. \quad \text{(Eq. 3-18)}$$

Assuming that the oceans were homogeneous and given that $[U]_{sw,m}{}^{\theta_{na}}$, γ, $B_{na,m}$ and $B_{a,m}$ are constant, we can rewrite Eq. 3-18 as,

$$F_{in} = \left(\frac{[U]_{sw,t}}{[U]_{sw,m}}\right)^{\theta_{na}} \frac{A_{na}}{A_{na,m}} F_{na,m} + \gamma [U]_{sw,t}{}^{\theta_a} B_{a,m} \int_{A_a} B_{C_{org}}\, dA. \quad \text{(Eq. 3-19)}$$

We now focus on the anoxic flux (second term of Eq. 3-19). The carbon burial rate per unit time per unit surface depends on depth Z (m) following the equation (Middelburg et al., 1997; we assume that this relationship did not change through time),

$$B_{C_{org}} = \alpha 10^{-\beta Z}, \quad \text{(Eq. 3-20)}$$

with $\alpha = 0.63$, $\beta = 0.00062$. Following Reinhard et al. (2013) and Sheen et al. (2018), we posit that anoxia expands from the continental shelf to abyssal plains. This is obviously a simplification as in the modern, oxic and anoxic environments coexist laterally at the same bathymetry.

With this caveat in mind, we introduce $\zeta(A)$, a function that gives the seawater depth ζ above which seafloor covers a surface area A. The modern function $\zeta_m(A)$ is fitted linearly to bathymetric data from the Global Topography V19.1 database (Smith and Sandwell, 1997; Fig. 3-5),

$$\zeta_m(A) \approx aA + b, \quad \text{(Eq. 3-21)}$$

where $\zeta_m(A)$ in m and A in m^2, $a = 1.59 \times 10^{-15}$ and $b = 560$.

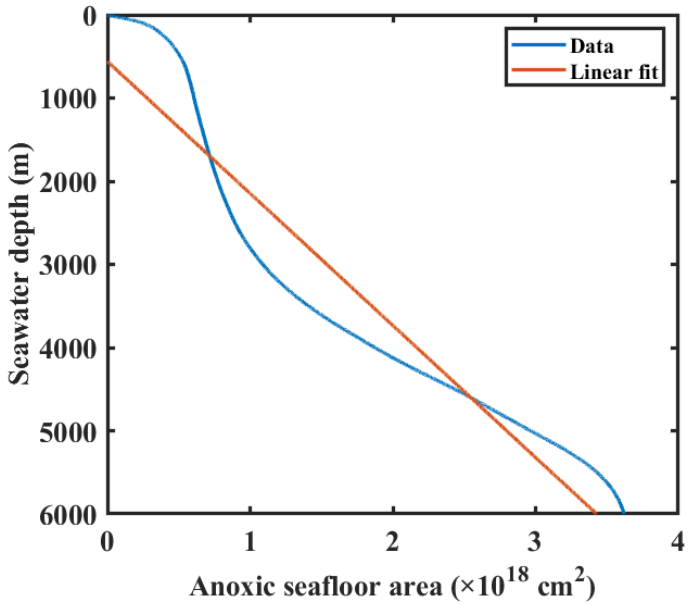

Figure 3-5 Seawater depth vs. seafloor area available for anoxia above that depth. Blue curve is the modern Global Topography V19.1 database (Smith and Sandwell, 1997). Orange line is an approximate best fit line (Eq. 3-21).

Eq. 3-19 therefore takes the form,

$$F_{in} = \left(\frac{[U]_{sw,t}}{[U]_{sw,m}}\right)^{\theta_{na}} \frac{A_{na}}{A_{na,m}} F_{na,m} + \gamma [U]_{sw,t}{}^{\theta_a} B_{a,m} \int_{A_a} \alpha 10^{-\beta \zeta_m(A)}\, dA. \quad \text{(Eq. 3-22)}$$

To constrain γ, we apply the expression for the anoxic sink to the modern ocean,

$$F_{a,m} = \gamma [U]_{sw,m}{}^{\theta_a} B_{a,m} \int_{A_{a,m}} \alpha 10^{-\beta \zeta_m(A)}\, dA, \quad \text{(Eq. 3-23)}$$

from which we can express γ as,

$$\gamma = \frac{F_{a,m}}{[U]_{sw,m}{}^{\theta_a} B_{a,m} \int_{A_{a,m}} \alpha 10^{-\beta \zeta_m(A)} dA}. \quad \text{(Eq. 3-24)}$$

We thus have for F_{in} (by combining Eqs. 3-22 and 3-24),

$$F_{in} = \left(\frac{[U]_{sw,t}}{[U]_{sw,m}}\right)^{\theta_{na}} \frac{A_{na}}{A_{na,m}} F_{na,m} + \left(\frac{[U]_{sw,t}}{[U]_{sw,m}}\right)^{\theta_a} \frac{\int_{A_a} 10^{-\beta \zeta_m(A} dA}{\int_{A_{a,m}} 10^{-\beta \zeta_m(A)} dA} F_{a,m}. \quad \text{(Eq. 3-25)}$$

We are interested in evaluating how the residence time of U could have changed in the past, which depends on the U input and output fluxes and the U inventory of seawater as expressed in Eq. 3-6. We first follow Reinhard et al. (2013) and Sheen et al. (2018) who applied the original mass balance model in the Proterozoic Eon to correlate the authigenic redox metal (Cr, Mo and Re) concentrations in shales as a function of the extent of oceanic anoxia under the assumption that the riverine flux remained the same as the modern values. We follow the same assumption to calculate the U residence time as a function of the extent of oceanic anoxia in Figure 3-6. Additionally, we can calculate the U seawater concentration using Eq. 3-25 in Figure 3-7, and the U concentrations in carbonates and black shales in Figure 3-8. We highlight in Figure 3-6 with thick solid lines the range of seafloor anoxia values that yield realistic U concentrations in carbonates and shales consistent with rock record. As expected, the oceanic U residence time decreases with greater extent of anoxia and could reach ~18 kyr for θ_a = 0.75 and around ≥30% anoxia.

This assumption of modern riverine U flux into early oceans works better for post-GOE; however, it is not valid for U in the Archean, as detrital uraninite was able to survive weathering due to the anoxic nature of the atmosphere at that time. Below, we further explore two approaches that use sediment data to constrain the residence time of U in the oceans within the framework of the model outlined above.

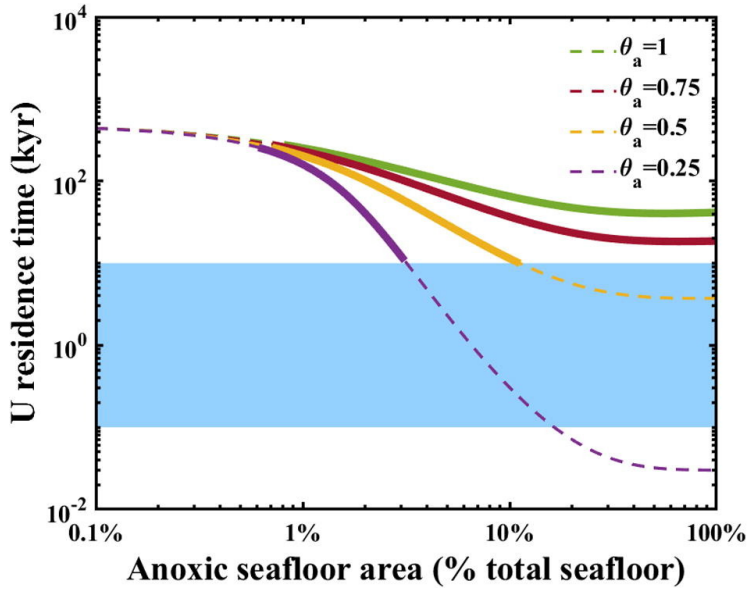

Figure 3-6 Modeled U residence time with increasing seafloor anoxia based on the assumption of constant modern-like U riverine flux after the GOE (Reinhard et al., 2013) with different exponents. The blue box shows the probable ocean mixing timescale range in the Precambrian (0.1–10 kyr). Thick solid lines are those that yield realistic U concentrations in carbonates and shales.

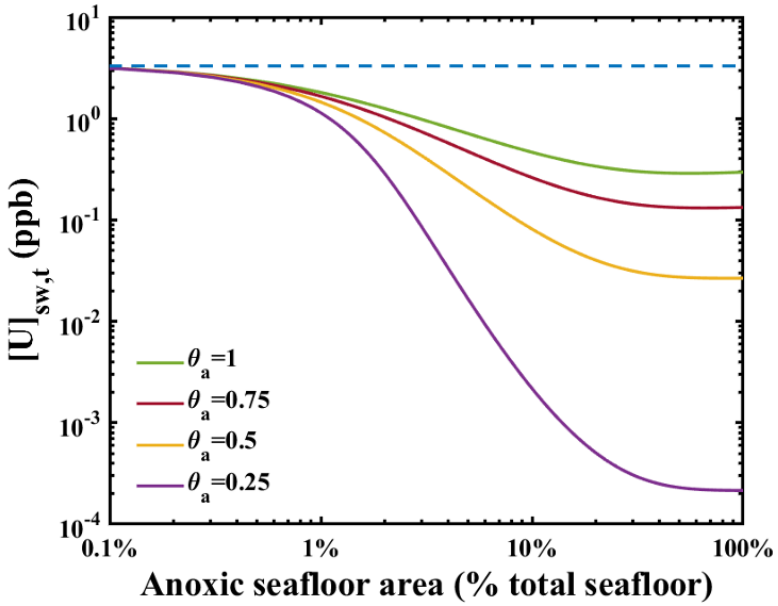

Figure 3-7 U concentration in seawater modeled using Eq. 3-25. The blue dashed line is the modern seawater concentration.

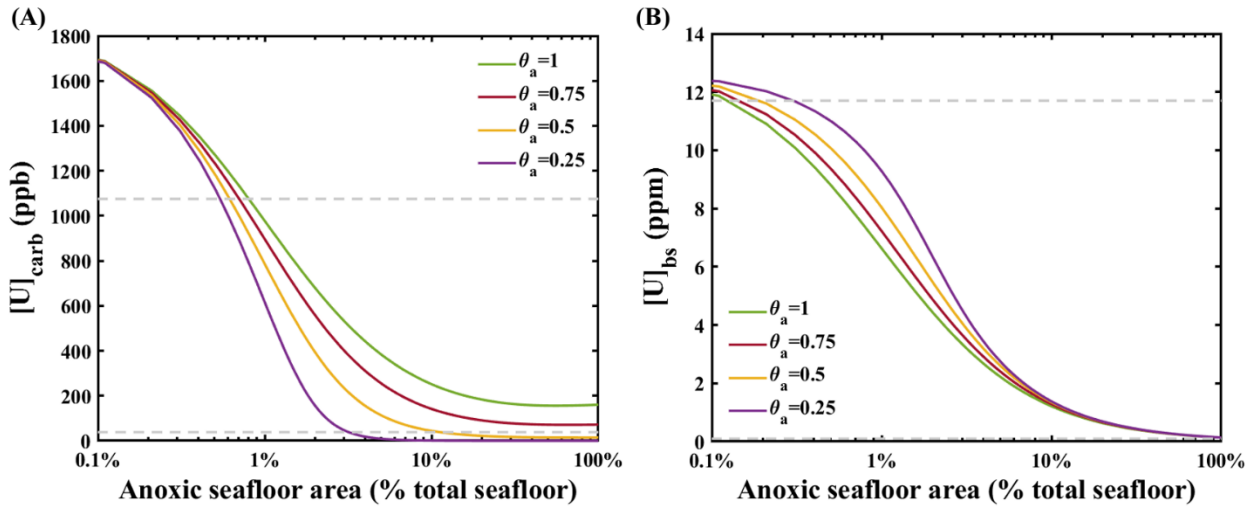

Figure 3-8 U concentrations predicted in carbonates (A) and black shales (B) using modelled U seawater concentration in Fig. 3-7 and Eqs. 3-27 and 3-31. The thick solid lines in Fig. 3-6 correspond to 38 ppb≤$[U]_{carb}$≤1075 ppb and 0.1 ppm≤$[U]_{bs}$≤11.7 ppm for the post-GOE to pre-NOE interval.

3.3.1 Using authigenic U concentration in shales

In our model, we can relate the concentration of authigenic U in black shales $[U]_{bs}$ (ppm) to the concentration of U in seawater. Since shale samples were usually collected from continental margins, we integrate the anoxic burial rate B_a over the anoxic area A_a until it reaches the boundary of continental margins ($A_a \leq A_{CM} = 1.014 \times 10^{18}\ cm^2$, 28% of global seafloor area; Cook and Carleton, 2000). The total amount of U deposited per unit time in anoxic sediments on the continental margin $F_{a,CM}$ is given by,

$$F_{a,CM} = \int_{min(A_a,A_{CM})} B_a\, dA = \left(\frac{[U]_{sw.t}}{[U]_{sw,m}}\right)^{\theta_a} \frac{\int_{min(A_a,A_{CM})} 10^{-\beta\zeta m(A)} dA}{\int_{A_{a,m}} 10^{-\beta\zeta m(A)} dA} F_{a,m}. \quad \text{(Eq. 3-26)}$$

The black shale bulk mass accumulation rate R is calculated using the dry bulk density measured in the Cariaco Basin (0.606 g cm^{-3} dry solid per volume of wet sediment; Sheen et al., 2018, Peterson et al., 2000) multiplied by a sedimentation rate S of 5-100 m/Myr (Einsele 1992).

We evaluate the two endmember values (5 and 100 m/Myr) and the average modern value of ~33 m/Myr (Partin et al., 2013) for S, which result in $R = 0.3 \times 10^{-3}$, 6.1×10^{-3} and 2.0×10^{-3}g cm^{-2} respectively. The predicted authigenic U concentration in anoxic shales $[\mathrm{U}]_{bs}$ (ppm) is obtained by dividing Eq. 3-26 by sediment flux $R \times min(A_a, A_{CM})$,

$$[\mathrm{U}]_{bs} = \frac{\int_{min(A_a,A_{CM})} B_a dA}{R \times min(A_a,A_{CM})} = \frac{1}{R \times min(A_a,A_{CM})} \left(\frac{[\mathrm{U}]_{sw,t}}{[\mathrm{U}]_{sw,m}}\right)^{\theta_a} \frac{\int_{min(A_a,A_{CM})} 10^{-\beta\zeta m(A)} dA}{\int_{A_{a,m}} 10^{-\beta\zeta m(A)} dA} F_{a,m}. \quad \text{(Eq. 3-27)}$$

For a given extent of anoxia A_a, this equation establishes a relationship between the authigenic U enrichment in black shale $[\mathrm{U}]_{bs}$ and the U concentration in seawater $[\mathrm{U}]_{sw,t}$. Authigenic U concentrations in black shales are measured data taken from Partin et al. (2013) (Table 3-2) to solve for Eq. 3-27 for the seawater U concentration as a function of anoxia extent,

$$[\mathrm{U}]_{sw.t} = [\mathrm{U}]_{sw,m} \left(\frac{[\mathrm{U}]_{bs} \times R \times min(A_a,A_{CM})}{F_{a,m}} \frac{\int_{A_{a,m}} 10^{-\beta\zeta m(A)} dA}{\int_{min(A_a,A_{CM})} 10^{-\beta\zeta m(A)} dA}\right)^{1/\theta_a}. \quad \text{(Eq. 3-28)}$$

Injecting Eq. 3-28 in Eq. 3-25, we can calculate the U input flux at any geological time for a given extent of anoxia based on the available black shale record,

$$F_{in} = \left(\frac{[\mathrm{U}]_{bs} \times R \times min(A_a,A_{CM})}{F_{a,m}} \frac{\int_{A_{a,m}} 10^{-\beta\zeta m(A)} dA}{\int_{min(A_a,A_{CM})} 10^{-\beta\zeta m(A)} dA}\right)^{\theta_{na}/\theta_a} \frac{A_{na}}{A_{na,m}} F_{na,m} + [\mathrm{U}]_{bs} \times R \times min(A_a, A_{CM}) \frac{\int_{A_a} 10^{-\beta\zeta m(A)} dA}{\int_{min(A_a,A_{CM})} 10^{-\beta\zeta m(A)} dA}. \quad \text{(Eq. 3-29)}$$

The residence time is the inventory in seawater divided by the input flux (Eq. 3-6), which we can calculate by combining Eqs. 3-28 and 3-29),

$$\tau = \frac{M_{sw}[\mathrm{U}]_{sw,m}\left(\frac{[\mathrm{U}]_{bs}\times R\times min(A_a,A_{CM})}{F_{a,m}}\frac{\int_{A_{a,m}}10^{-\beta\zeta m(A)}dA}{\int_{min(A_a,A_{CM})}10^{-\beta\zeta m(A)}dA}\right)^{1/\theta_a}}{\left(\frac{[\mathrm{U}]_{bs}\times R\times min(A_a,A_{CM})}{F_{a,m}}\frac{\int_{A_{a,m}}10^{-\beta\zeta m(A)}dA}{\int_{min(A_a,A_{CM})}10^{-\beta\zeta m(A)}dA}\right)^{\theta_{na}/\theta_a}\frac{A_{na}}{A_{na,m}}F_{na,m}+[\mathrm{U}]_{bs}\times R\times min(A_a,A_{CM})\frac{\int_{A_{a,m}}10^{-\beta\zeta m(A)}dA}{\int_{min(A_a,A_{CM})}10^{-\beta\zeta m(A)}dA}} \quad \text{(Eq. 3-30)}$$

.

Figure 3-9 shows the U residence time calculated using black shale data as a function of the areal extent of anoxic sinks with different sedimentation rates in the Archean and mid-Proterozoic. We highlight with thick solid lines in Figure 3-9 the range of values that yield realistic U concentrations in carbonates and U input flux compared to rock record. The former was calculated using the approach described in Section 3.3.2 with $[\mathrm{U}]_{sw.t}$ derived from black shale data and Eq. 3-28 and plotted in Fig. 3-10. The latter was calculated using Eq. 3-29 and plotted in Fig. 3-11, which we can conservatively assume to be smaller in the Archean oceans than its present value.

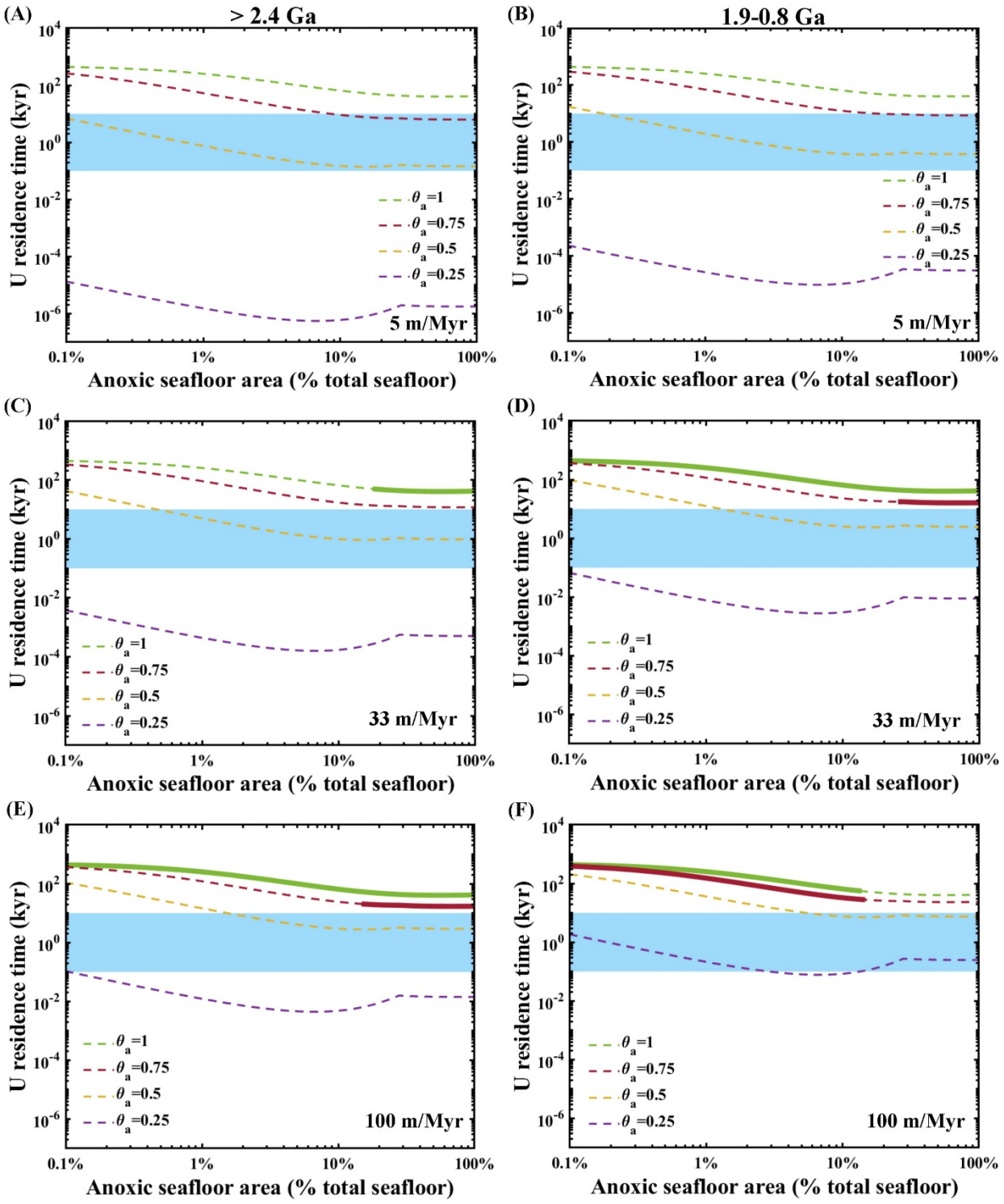

Figure 3-9 Modeled U residence time with increasing seafloor anoxia using authigenic U enrichment in shales with different assumptions for the sedimentation rates (top panels S = 5, middle panels S = 33, and bottom panels S = 100 m/Myr) in the Archean (left) and mid-Proterozoic (right).

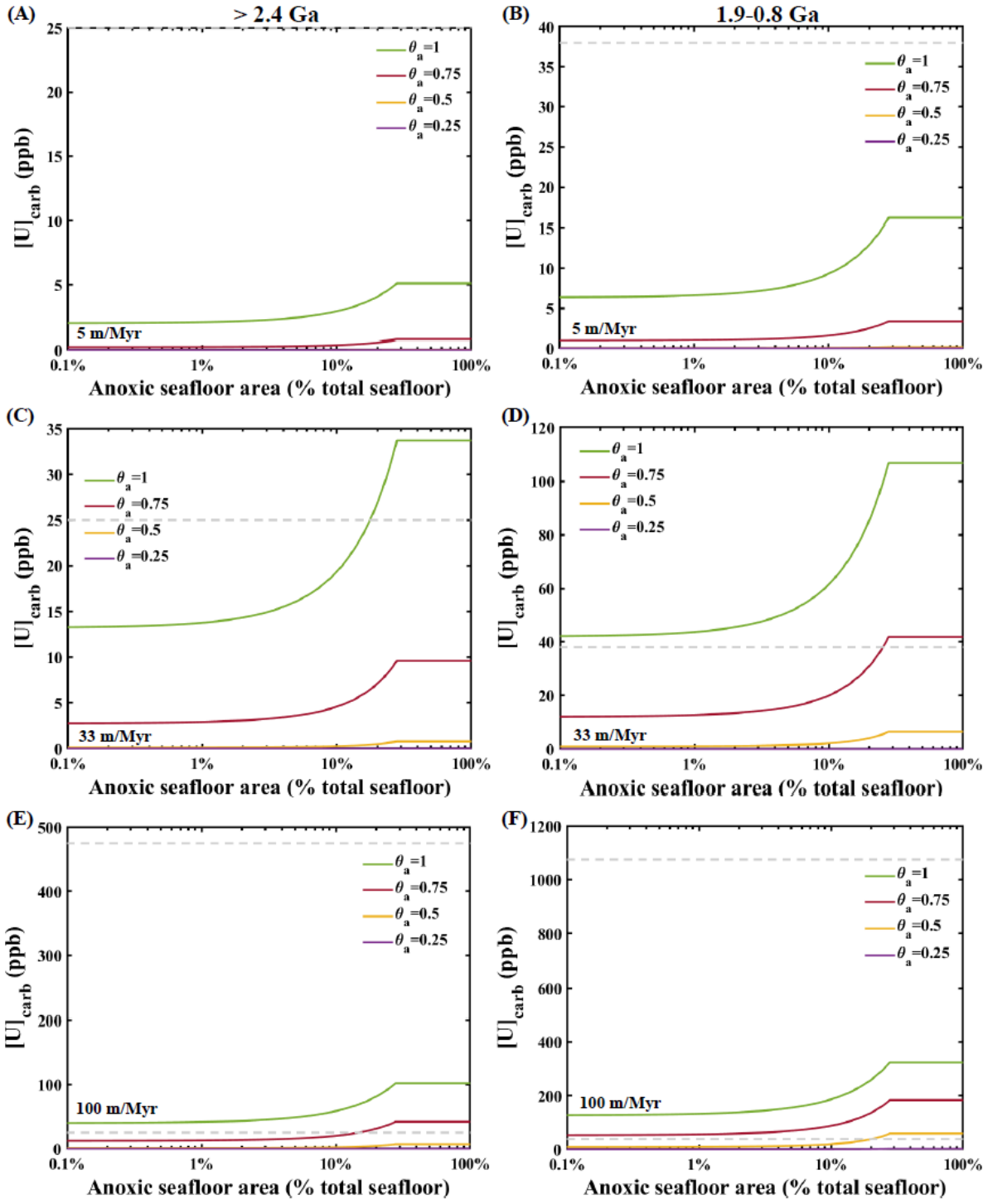

Figure 3-10 U concentrations predicted in carbonates using modeled [U]. Each panel corresponds to the panel in Figure 3-9. The thick solid lines in Figure 3-9 correspond to parameters that yield 25ppb≤[U]≤475ppb in the Archean and 38ppb≤[U]≤1075ppb in the mid-Proterozoic.

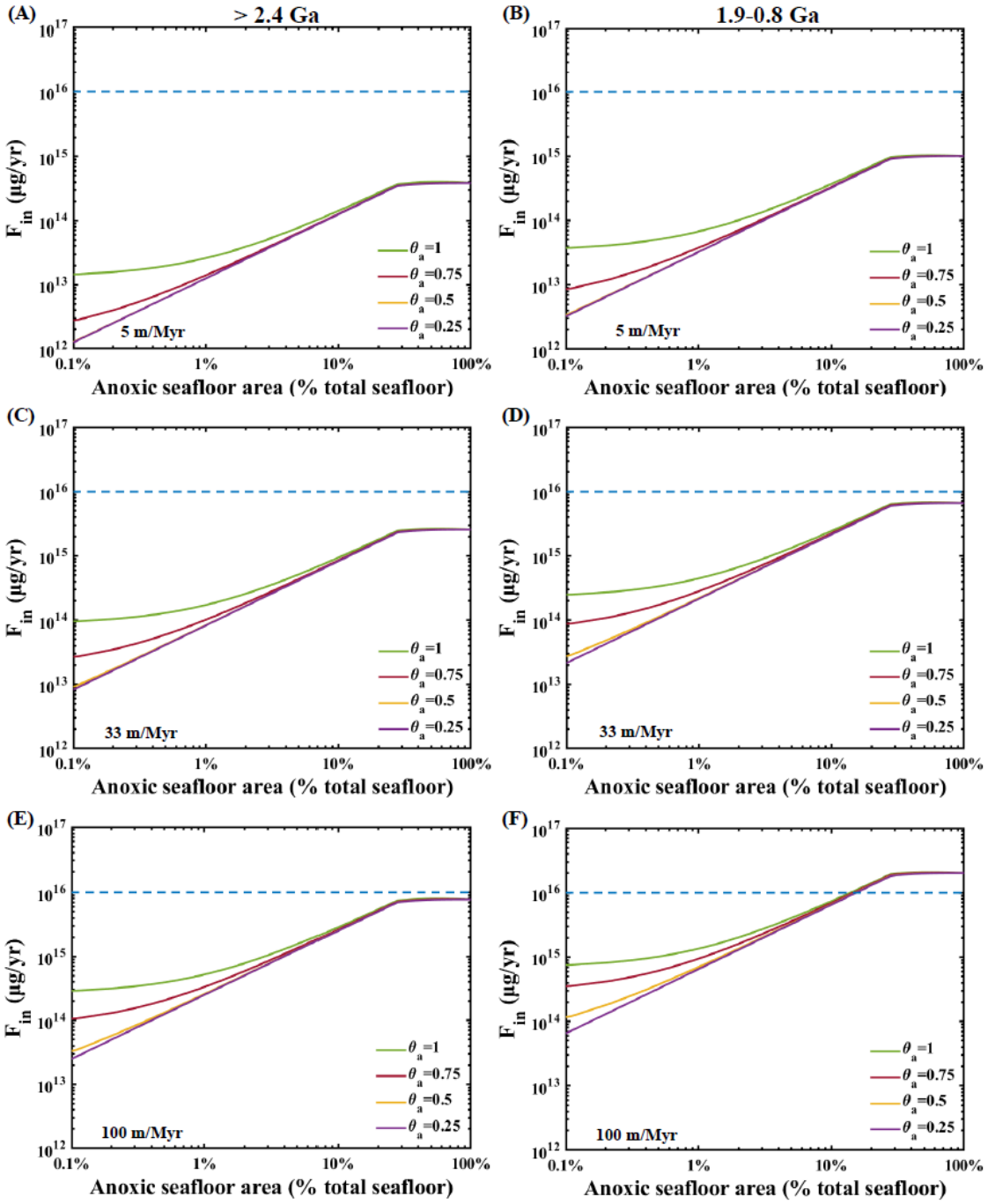

Figure 3-11 U input flux calculated using black shale data and Eq. 3-29. Each panel corresponds to the panel in Figure 3-9. The blue dashed line is the U modern input flux. The thick solid lines in Figure 3-9 correspond to parameters that yield U input flux in the Archean and mid-Proterozoic less than the modern value.

In the Archean and mid-Proterozoic, U residence time decreases with a greater extent of anoxia. It could have reached ~18 kyr for $\theta_a = 0.75$, $S = 100$ m/Myr and around ≥20% anoxia in the Archean and could have reached ~18 kyr for $\theta_a = 0.75$, $S = 33$ m/Myr and around ≥25% anoxia in the mid-Proterozoic, respectively.

3.3.2 Using U concentration in carbonates

Alternatively, we can infer seawater U concentration by using the U/Ca ratio in carbonates,

$$[U]_{sw,t} = [Ca]_{sw,t} \times \frac{(U/Ca)_{carb,t}}{D_U}, \quad \text{(Eq. 3-31)}$$

where $[Ca]_{sw,t}$ is the Ca concentration in seawater at time t (11 mmol/kg in modern seawater) and D_U is the U/Ca exchange coefficient between carbonate and seawater. For $(U/Ca)_{carb,t}$ (mass ratio), we use carbonates measured and literature data compiled by Chen et al. (2021). The values of $[Ca]_{sw,t}$ and D_U relevant to the Precambrian are discussed in Section 4.3.3 of Chen et al., (2021).

Incorporating Eq. 3-31 calculated from carbonate data in Eq. 3-25 and then Eq. 3-6, we have,

$$F_{in} = \left(\frac{[Ca]_{sw,t}\times\frac{(U/Ca)_{carb,t}}{D_U}}{[U]_{sw,m}}\right)^{\theta_{na}} \frac{A_{na}}{A_{na,m}} F_{na,m} + \left(\frac{[Ca]_{sw,t}\times\frac{(U/Ca)_{carb,t}}{D_U}}{[U]_{sw,m}}\right)^{\theta_a} \frac{\int_{A_a} 10^{-\beta\zeta m(A)} dA}{\int_{A_{a,m}} 10^{-\beta\zeta m(A)} dA} F_{a,m}; \quad \text{(Eq. 3-32)}$$

$$\tau = \frac{M_{sw}[Ca]_{sw,t}\times\frac{(U/Ca)_{carb,t}}{D_U}}{\left(\frac{[Ca]_{sw,t}\times\frac{(U/Ca)_{carb,t}}{D_U}}{[U]_{sw,m}}\right)^{\theta_{na}} \frac{A_{na}}{A_{na,m}} F_{na,m} + \left(\frac{[Ca]_{sw,t}\times\frac{(U/Ca)_{carb,t}}{D_U}}{[U]_{sw,m}}\right)^{\theta_a} \frac{\int_{A_a} 10^{-\beta\zeta m(A)} dA}{\int_{A_{a,m}} 10^{-\beta\zeta m(A)} dA} F_{a,m}}. \quad \text{(Eq. 3-33)}$$

In Figure 3-12, we plot the U residence time as a function of the areal extent of anoxia using estimated U concentration in seawater (Table 3-2) calculated from the measured U concentration in carbonates. We highlight with thick solid lines in Fig. 3-12 the range of values that yield realistic shale U concentrations and U input flux compared to rock records. The former was calculated using Eq. 3-27 and plotted in Figure 3-13. The latter was plotted in Figure 3-14, which we can conservatively assume to be smaller in the Archean oceans than its present value.

Again, the U residence time decreases with a greater extent of anoxia. It could have reached ~18 kyr for $\theta_a = 0.75$ and around ≥30% anoxia in both Archean and mid-Proterozoic.

Table 3-2 Parameters used in U residence time modelling.

Global seafloor area (cm^2)	3.62×10^{18}	
Mass of seawater (kg)	1.4×10^{21}	
Modern anoxic U burial rate (μg cm^{-2} yr^{-1}) [a]	0.251	
Sedimentation rates (m/Myr)	33[a,b], 5[c],100[c]	
Modern anoxic sink area fraction (%) [d]	0.11	
Modern U seawater concentration (ppb) [a]	3.3	
Modern U riverine input flux (μg/yr) [b]	1×10^{16}	
	>2.4 Ga	1.9-0.8 Ga
Historical U seawater concentration (ppb) [e]	0.10	0.14

[a] Partin et al. (2013); [b] Dunk et al. (2002); [c] Einsele (1992); [d] Sheen et al. (2018); [e] Chen et al. (2021).

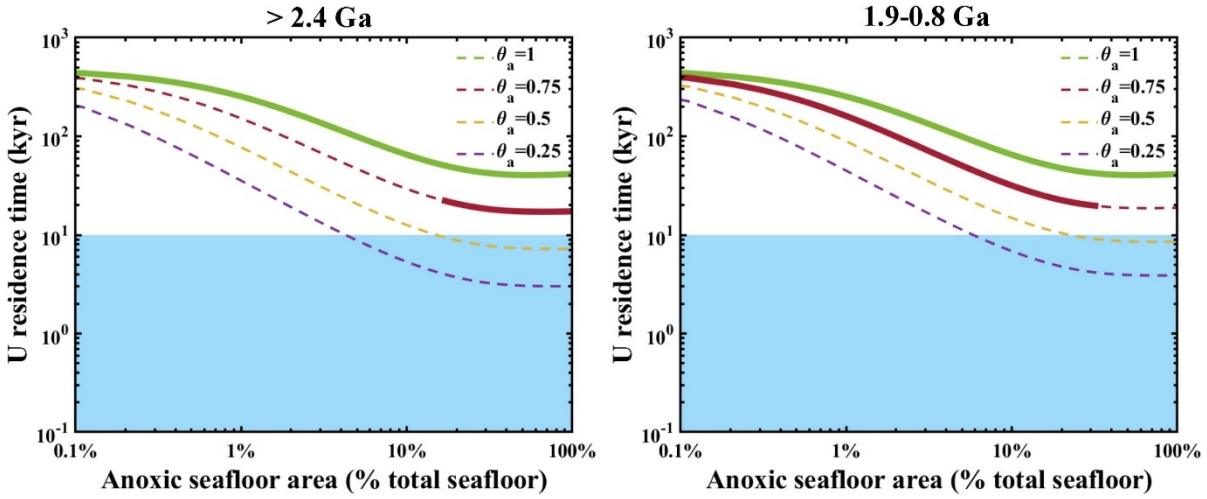

Figure 3-12 Modeled U residence time with increasing seafloor anoxia using U in carbonates in the Archean (left) and mid-Proterozoic (right). Different lines correspond to different exponents.

(Figure 3-12 continued) The blue box shows the probable ocean mixing timescale range in the Precambrian (0.1–10 kyr). The thick solid lines correspond to parameters that yield realistic U concentrations in black shales (Fig. 3-13) and U input flux (Fig. 3-14).

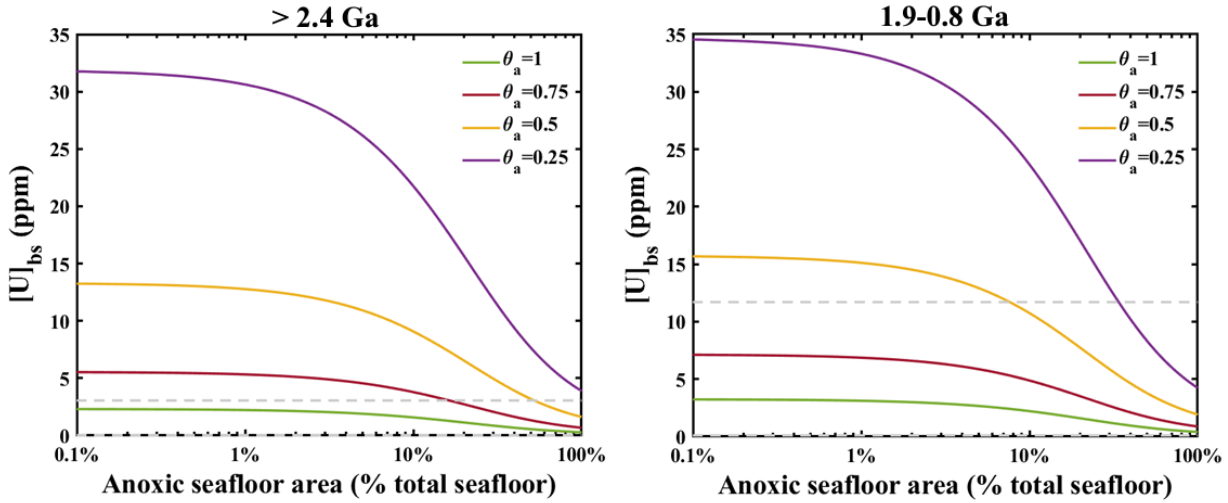

Figure 3-13 U concentrations predicted in shales using modeled [U]. Each panel corresponds to the panels in Figure 3-12. The thick solid lines in Figure 3-12 correspond to parameters that yield 0.04 ppm≤[U]≤3.06 ppm for the Archean, and 0.1 ppm≤[U]≤11.7 ppm for the mid-Proterozoic.

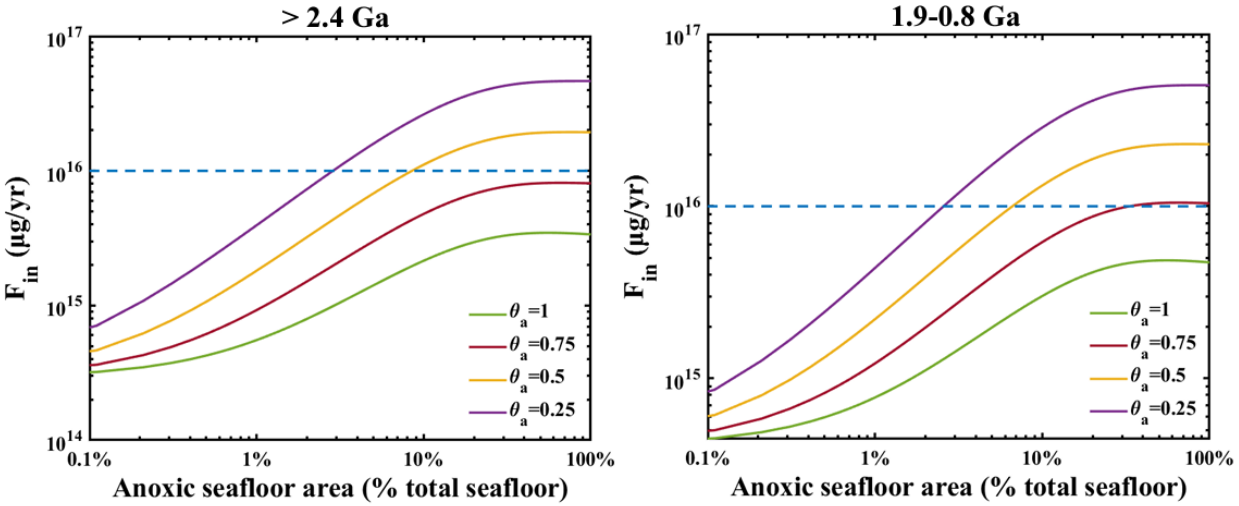

Figure 3-14 U input flux calculated using carbonate data and Eq. 3-32. Each panel corresponds to the panels in Figure 3-12. The blue dashed line is the U modern input flux. The thick solid lines in Figure 3-12 correspond to parameters that yield U input flux in the Archean and mid-Proterozoic less than the modern value.

3.4 Conclusion

Given an estimated Archean Nd oceanic residence time of 755 years, the spatial pattern and scale of Nd isotopic variations predicted in our modelled Archean oceans with mixing timescales on similar order of magnitude suggest that the degree of heterogeneity in seawater ε_{Nd} recorded in Archean BIFs may have been influenced by the contrasting ε_{Nd} values derived from juvenile or mafic materials versus ancient, felsic materials in the continental and sedimentary sources. Incorporating a dominant sedimentary source in the Archean oceans suggests that the positive ε_{Nd} values in Archean BIFs do not necessarily reflect hydrothermal input, and the contribution of Nd (and Fe) by hydrothermal source in Archean oceans calculated based on a misunderstood ε_{Nd} budget may have been exaggerated. For uranium, its global average residence time in the dominantly anoxic Precambrian oceans may be as low as ~18 kyr based on our evaluation, which is a two order of magnitude decrease from its modern value of ~400 kyr. While it is still significantly longer than our modelled Precambrian ocean mixing timescales, and thus the U isotopic composition of marine sediments could be a reliable tracer of the global oceanic redox conditions, it is still conceivable that for other paleoredox tracers with similar geochemical properties as U but a shorter residence time in the modern ocean (*e.g.*, Re, V and Cr), that a two order of magnitude reduction could bring their Precambrian residence time close to the ocean mixing timescale. Therefore, it is recommended that the assumption of a constant residence time of paleoredox tracers through time is carefully examined before applying them for interpretation of sedimentary records.

REFERENCES

Abbott, A. N., Haley, B. A., & McManus, J. (2015a). Bottoms up: Sedimentary control of the deep North Pacific Ocean's εNd signature. *Geology*, *43*(11), 1035-1035.

Abbott, A. N., Haley, B. A., McManus, J., & Reimers, C. E. (2015b). The sedimentary flux of dissolved rare earth elements to the ocean. *Geochimica et Cosmochimica Acta*, *154*, 186-200.

Abbott, A. N., Löhr, S., & Trethewy, M. (2019). Are clay minerals the primary control on the oceanic rare earth element budget?. *Frontiers in Marine Science*, *6*, 504.

Alexander, B. W., Bau, M., & Andersson, P. (2009). Neodymium isotopes in Archean seawater and implications for the marine Nd cycle in Earth's early oceans. *Earth and Planetary Science Letters*, *283*(1-4), 144-155.

Algeo, T. J., & Lyons, T. W. (2006). Mo–total organic carbon covariation in modern anoxic marine environments: Implications for analysis of paleoredox and paleohydrographic conditions. *Paleoceanography*, *21*(1).

Arsouze, T., Dutay, J. C., Lacan, F., & Jeandel, C. (2009). Reconstructing the Nd oceanic cycle using a coupled dynamical–biogeochemical model. *Biogeosciences*, *6*(12), 2829-2846.

Bacon, M. P., & Anderson, R. F. (1982). Distribution of thorium isotopes between dissolved and particulate forms in the deep sea. *Journal of Geophysical Research: Oceans*, *87*(C3), 2045-2056.

Cook, P. J., & Carleton, C. M. (Eds.). (2000). *Continental shelf limits: the scientific and legal interface*. Oxford University Press.

Chen, X., Tissot, F. L. H., Jansen, M. F., Bekker, A., Liu, C. X., Nie, N. X., ... & Dauphas, N. (2021). The uranium isotopic record of shales and carbonates through geologic time. *Geochimica et cosmochimica acta*, *300*, 164-191.

Dauphas, N., Heard, A. W., Rego, E. S., Rouxel, O., Marin-Carbonne, J., Pasquier, V., Bekker, A., & Rowley, D. (2024). Past and Present Dynamics of the Iron Biogeochemical Cycle. In *Treatise on Geochemistry*.

Derry, L. A., & Jacobsen, S. B. (1990). The chemical evolution of Precambrian seawater: evidence from REEs in banded iron formations. *Geochimica et Cosmochimica Acta*, *54*(11), 2965-2977.

Du, J., Haley, B. A., & Mix, A. C. (2016). Neodymium isotopes in authigenic phases, bottom waters and detrital sediments in the Gulf of Alaska and their implications for paleo-circulation reconstruction. Geochimica et Cosmochimica Acta, 193, 14-35.

Du, J., Haley, B. A., Mix, A. C., Walczak, M. H., & Praetorius, S. K. (2018). Flushing of the deep Pacific Ocean and the deglacial rise of atmospheric CO2 concentrations. *Nature Geoscience*, *11*(10), 749-755.

Du, J., Haley, B. A., & Mix, A. C. (2020). Evolution of the Global Overturning Circulation since the Last Glacial Maximum based on marine authigenic neodymium isotopes. *Quaternary Science Reviews*, *241*, 106396.

Dunk, R. M., Mills, R. A., & Jenkins, W. J. (2002). A reevaluation of the oceanic uranium budget for the Holocene. *Chemical Geology*, *190*(1–4), 45–67.

Einsele, G. (1992). Sedimentary basins: evolution, facies, and sediment budget.

German, C. R., Klinkhammer, G. P., Edmond, J. M., Mura, A., & Elderfield, H. (1990). Hydrothermal scavenging of rare-earth elements in the ocean. *Nature*, *345*(6275), 516-518.

Ghosh, R., & Baidya, T. K. (2017). Using BIF magnetite of the Badampahar greenstone belt, Iron Ore Group, East Indian Shield to reconstruct the water chemistry of a 3.3–3.1 Ga sea during iron oxyhydroxides precipitation. *Precambrian Research*, *301*, 102-112.

Goldstein, S. L., & Hemming, S. R. (2003). Long-lived isotopic tracers in oceanography, paleoceanography, and ice-sheet dynamics. *Treatise on geochemistry*, *6*, 625.

Goldstein, S. J., & Jacobsen, S. B. (1987). The Nd and Sr isotopic systematics of river-water dissolved material: Implications for the sources of Nd and Sr in seawater. *Chemical Geology: Isotope Geoscience section*, *66*(3-4), 245-272.

Goldstein, S. L., O'nions, R. K., & Hamilton, P. J. (1984). A Sm-Nd isotopic study of atmospheric dusts and particulates from major river systems. *Earth and planetary Science letters*, *70*(2), 221-236.

Greaves, M. J., Statham, P. J., & Elderfield, H. (1994). Rare earth element mobilization from marine atmospheric dust into seawater. *Marine Chemistry*, *46*(3), 255-260.

Gu, S., Liu, Z., Jahn, A., Rempfer, J., Zhang, J., & Joos, F. (2019). Modeling neodymium isotopes in the ocean component of the community earth system model (CESM1). *Journal of Advances in Modeling Earth Systems*, *11*(3), 624-640.

Haley, B. A., Du, J., Abbott, A. N., & McManus, J. (2017). The impact of benthic processes on rare earth element and neodymium isotope distributions in the oceans. *Frontiers in Marine Science*, *4*, 426.

Hu, J., Wang, H., & Zhang, L. (2020). A rare earth element and Nd isotopic investigation into the provenance and deposition of the Dahongliutan banded iron formation and associated carbonates, NW China: Implications on Neoproterozoic seawater compositions. *Precambrian Research*, *342*, 105685.

Jacobsen, S. B. (1988). Isotopic constraints on crustal growth and recycling. *Earth and Planetary Science Letters*, *90*(3), 315-329.

Jacobsen, S. B., & Pimentel-Klose, M. R. (1988). A Nd isotopic study of the Hamersley and Michipicoten banded iron formations: the source of REE and Fe in Archean oceans. *Earth and Planetary Science Letters*, *87*(1-2), 29-44.

Johannesson, K. H., & Burdige, D. J. (2007). Balancing the global oceanic neodymium budget: evaluating the role of groundwater. *Earth and Planetary Science Letters*, *253*(1-2), 129-142.

Korenaga, J. (2008). Urey ratio and the structure and evolution of Earth's mantle. *Reviews of Geophysics*, *46*(2).

Korenaga, J., Planavsky, N. J., & Evans, D. A. (2017). Global water cycle and the coevolution of the Earth's interior and surface environment. *Philosophical Transactions of the Royal Society A: Mathematical, Physical and Engineering Sciences*, *375*(2094), 20150393.

Krissansen-Totton, J., Arney, G. N., & Catling, D. C. (2018). Constraining the climate and ocean pH of the early Earth with a geological carbon cycle model. *Proceedings of the National Academy of Sciences*, *115*(16), 4105-4110.

Ku, T. L., Mathieu, G. G., & Knauss, K. G. (1977). Uranium in open ocean: concentration and isotopic composition. *Deep Sea Research*, *24*(11), 1005-1017.

Langmuir, D. (1978). Uranium solution-mineral equilibria at low temperatures with applications to sedimentary ore deposits. *Geochimica et Cosmochimica Acta*, *42*(6), 547-569.

Lau, K. V., Romaniello, S. J., & Zhang, F. (2019). The uranium isotope paleoredox proxy. *The Uranium Isotope Paleoredox Proxy*, 1–30.

Lowell, R. P., & Keller, S. M. (2003). High-temperature seafloor hydrothermal circulation over geologic time and Archean banded iron formations. *Geophysical research letters*, *30*(7).

Middelburg, J. J., Soetaert, K., & Herman, P. M. (1997). Empirical relationships for use in global diagenetic models. *Deep Sea Research Part I: Oceanographic Research Papers*, *44*(2), 327-344.

Osborne, A. H., Haley, B. A., Hathorne, E. C., Flögel, S., & Frank, M. (2014). Neodymium isotopes and concentrations in Caribbean seawater: tracing water mass mixing and continental input in a semi-enclosed ocean basin. Earth and Planetary Science Letters, 406, 174-186.

Partin, C. A., Bekker, A., Planavsky, N. J., Scott, C. T., Gill, B. C., Li, C., ... & Lyons, T. W. (2013). Large-scale fluctuations in Precambrian atmospheric and oceanic oxygen levels from the record of U in shales. *Earth and Planetary Science Letters*, *369*, 284-293.

Patočka, V., Šrámek, O., & Tosi, N. (2020). Minimum heat flow from the core and thermal evolution of the Earth. *Physics of the Earth and Planetary Interiors*, *305*, 106457.

Peterson, L. C., Haug, G. H., Murray, R. W., Yarincik, K. M., King, J. W., Bralower, T. J., ... & Pearce, R. B. (2000). Late Quaternary stratigraphy and sedimentation at site 1002, Cariaco Basin (Venezuela). In *Proc. Ocean Drill. Program Sci. Results* (Vol. 165, pp. 85-99). Ocean Drilling Program College Station, TX.

Piepgras, D. J., & Wasserburg, G. J. (1980). Neodymium isotopic variations in seawater. *Earth and Planetary Science Letters*, *50*(1), 128-138.

Pope, E. C., Bird, D. K., & Rosing, M. T. (2012). Isotope composition and volume of Earth's early oceans. *Proceedings of the National Academy of Sciences*, *109*(12), 4371-4376.

Ptáček, M. P., Dauphas, N., & Greber, N. D. (2020). Chemical evolution of the continental crust from a data-driven inversion of terrigenous sediment compositions. *Earth and Planetary Science Letters*, *539*, 116090.

Reinhard, C. T., Planavsky, N. J., Robbins, L. J., Partin, C. A., Gill, B. C., Lalonde, S. V., ... & Lyons, T. W. (2013). Proterozoic ocean redox and biogeochemical stasis. *Proceedings of the National Academy of Sciences*, *110*(14), 5357-5362.

Rempfer, J., Stocker, T. F., Joos, F., Dutay, J. C., & Siddall, M. (2011). Modelling Nd-isotopes with a coarse resolution ocean circulation model: Sensitivities to model parameters and source/sink distributions. *Geochimica et Cosmochimica Acta*, *75*(20), 5927-5950.

Robinson, S., Ivanovic, R. F., Gregoire, L. J., Tindall, J., van de Flierdt, T., Plancherel, Y., ... & Valdes, P. J. (2023). Simulating marine neodymium isotope distributions using Nd v1. 0 coupled to the ocean component of the FAMOUS–MOSES1 climate model: sensitivities to reversible scavenging efficiency and benthic source distributions. *Geoscientific Model Development*, *16*(4), 1231-1264.

Sheen, A. I., Kendall, B., Reinhard, C. T., Creaser, R. A., Lyons, T. W., Bekker, A., ... & Anbar, A. D. (2018). A model for the oceanic mass balance of rhenium and implications for the extent of Proterozoic ocean anoxia. *Geochimica et Cosmochimica Acta*, *227*, 75-95.

Sholkovitz, E. R., Landing, W. M., & Lewis, B. L. (1994). Ocean particle chemistry: the fractionation of rare earth elements between suspended particles and seawater. *Geochimica et Cosmochimica Acta*, *58*(6), 1567-1579.

Smith, W. H., & Sandwell, D. T. (1997). Global sea floor topography from satellite altimetry and ship depth soundings. *Science*, *277*(5334), 1956-1962.

Tachikawa, K., Athias, V., & Jeandel, C. (2003). Neodymium budget in the modern ocean and paleo-oceanographic implications. *Journal of Geophysical Research: Oceans*, *108*(C8).

Tachikawa, K., Rapuc, W., Dubois-Dauphin, Q., Guihou, A., & Skonieczny, C. (2020). Reconstruction of ocean circulation based on neodymium isotopic composition. *Oceanography*, *33*(2), 80-87.

Tissot, F. L. H., & Dauphas, N. (2015). Uranium isotopic compositions of the crust and ocean: Age corrections, U budget and global extent of modern anoxia. *Geochimica et Cosmochimica Acta*, *167*, 113–143.

Trendall, A. F. (2002). The significance of iron-formation in the Precambrian stratigraphic record. *Precambrian sedimentary environments: A modern approach to ancient depositional systems*, 33-66.

Vervoort, J. D., & Blichert-Toft, J. (1999). Evolution of the depleted mantle: Hf isotope evidence from juvenile rocks through time. *Geochimica et cosmochimica acta*, *63*(3-4), 533-556.

Wang, C., Konhauser, K. O., Zhang, L., Zhai, M., & Li, W. (2016). Decoupled sources of the 2.3–2.2 Ga Yuanjiacun banded iron formation: Implications for the Nd cycle in Earth's early oceans. *Precambrian Research*, *280*, 1-13.

Wu, C., Lin, Z., & Liu, X. (2020). The global dust cycle and uncertainty in CMIP5 (Coupled Model Intercomparison Project phase 5) models. *Atmospheric Chemistry and Physics*, *20*(17), 10401-10425.

Xu, A., Hathorne, E., Laukert, G., & Frank, M. (2023). Overlooked riverine contributions of dissolved neodymium and hafnium to the Amazon estuary and oceans. *Nature Communications*, *14*(1), 4156.

Yamamoto, K., Itoh, N., Matsumoto, T., Tanaka, T., & Adachi, M. (2004). Geochemistry of Precambrian carbonate intercalated in pillows and its host basalt: implications for the REE composition of circa 3.4 Ga seawater. *Precambrian Research*, *135*(4), 331-344.

4 REDOX CONDITIONS DURING MARTIAN CLAY FORMATION

4.1 Introduction

Water-laid sediments bear witness to water-rock interactions through time on Mars (Bibring et al. 2006). Clay minerals are abundant in sediments of Noachian-age (4.1-3.7 Ga), and occurrences extend into the early Hesperian (3.7-3.0 Ga) (Bibring et al., 2006; Ehlmann et al., 2008; Mustard et al., 2008; Poulet et al., 2005). Clay minerals have been detected at the surface of Mars by spacecraft orbiters (Poulet et al. 2005; Murchie et al. 2009; Ehlmann et al. 2011; Carter et al. 2013; Michalski et al., 2015) and the Curiosity Martian rover (Vaniman et al., 2014; Bristow et al., 2018; Rampe et al. 2020; Losa-Adams 2021). They are also found in Martian meteorites (Gooding et al., 1991; Gooding 1992; Changela and Bridges 2010; Gillet et al. 2002; Noguchi et al. 2009; Hicks et al., 2014; Suga et al., 2019). Orbital infrared characterization of clay minerals shows that the majority (~69 %) of these are dioctahedral or di-trioctahedral Fe-rich smectites (nontronite), containing significant Fe^{3+} in dioctahedral layers; while another ~22% are trioctahedral Mg-rich/Fe-poor smectites, with trioctahedral layers dominantly containing cations in 2+ valence states (saponite) (Michalski et al. 2015). The dichotomy between Mg- and Fe-rich smectites may be indicative of differences in redox conditions during clay formation, whereby more oxidized samples were able to retain preferentially Fe as insoluble Fe^{3+} relative to more soluble Mg^{2+}, while more reduced samples experienced more significant loss of both Mg^{2+} and Fe^{2+}.

How redox conditions evolved at the surface of Mars is a major scientific question posed by the trove of data recovered by Martian orbiters and rovers. On the one hand, escape to space of hydrogen produced by water photolysis could have allowed the development of oxidizing

conditions as early as 4.1-3.7 Ga (Chevrier et al. 2007). On the other hand, active volcanism and the accompanying release of reduced gases could have maintained anoxic conditions until volcanism subdued at around 3.7-3.1 Ga (Ramirez et al., 2014; Sholes et al., 2017). Redox conditions of subaerial environments can potentially be constrained by examining the chemistry of iron-bearing clays, but significant uncertainties remain in interpretations because iron in smectite can be oxidized after formation by (*i*) photochemically produced atmospheric oxidants (O_2, O_3, H_2O_2) and surficial chemical oxidants in Martian soil (nitrate, chlorate, and perchlorate) that would have become more available with Mars' atmospheric evolution (Dehouck et al., 2016; Wordsworth et al., 2021) or (*ii*) direct photochemical oxidation of smectite-bound iron by ultraviolet radiation (Rivera Banuchi et al., 2022; Nie et al., 2017). The present oxidation state of Fe in Martian clays could therefore be either due to formation under oxidizing conditions or post-depositional oxidation on the surface of Mars.

One must therefore use indirect proxies, such as cation chemistry and/or isotopic composition of alteration assemblages, to learn about the redox conditions of weathering and clay mineral formation without confusion from post-depositional Fe oxidation. We start by outlining the expectations for the chemical and isotopic fractionation of Fe during clay formation under different redox conditions:

Iron in fresh Martian basalts is dominantly Fe^{2+} (ferrous iron) in pyroxene, olivine, and glass (Herd et al., 2002, 2001; McSween, 1994). Because the behavior of Fe^{2+} is like that of Mn^{2+} and both are hosted in similar primary mineralogical sites to Mg^{2+}, we anticipate weathering of fresh basaltic Martian crust under reducing conditions to induce little decoupling of Fe and Mn, large fractionation between Fe^{2+} and Al^{3+}, and fractionation of Fe and Mg in clay minerals relative

to source rocks to be driven purely by differences in mobilization rates of Fe^{2+} and Mg from silicates (Brantley et al., 2008). The instantaneous isotopic fractionation of iron between fluid and residue would be smaller than when Fe is oxidized, but because Fe is more mobile under reducing conditions, it would be more efficiently lost, magnifying isotopic fractionation in the leached residue through a Rayleigh distillation.

Unlike Fe^{2+}, Fe^{3+} has very different geochemical behavior from both Mg^{2+} and Mn^{2+}. It is less mobile in solution under conditions that are not highly acidic and tends to precipitate into insoluble mineral phases such as hydrated Fe^{3+} silicates and oxides/oxyhydroxides. We would expect clay formation from mafic minerals under oxidizing conditions to produce clays that have Fe/Al similar to the source rocks and Fe/Mg and Fe/Mn fractionated towards Fe enrichment. Iron isotopic fractionation will be affected in two manners by iron oxidation. On the one hand, oxidation means that iron will become less mobile, providing less leverage to fractionate iron isotopes in the residue. On the other hand, iron isotopic fractionation ($\Delta^{56}Fe$ or $10^3\alpha$) between Fe^{2+} dissolved in water and Fe^{3+} in precipitates (-1.7 to 4.4 ‰) is higher than that between Fe^{2+}-bearing species (-3 to 0 ‰; Wu et al., 2019), so the presence of ferric iron in the system can increase instantaneous isotopic fractionation between fluid and mineral.

Here we assume that as long as all iron is not quantitatively oxidized, Mn remains mobile as Mn^{2+}. Oxidation of Mn^{2+} by O_2 is thermodynamically favorable but kinetically limited in the absence of catalysts, such that abiotic oxidation of Mn^{2+} by dissolved O_2 below pH 9.0 is extremely slow to negligible (timescale of years; Diem and Stumm, 1984; Morgan 2005; Hem 1963; Martin 2005). Catalyzed oxidation by Mn,Fe-oxide surfaces results in Mn^{2+} half-lives ranging from 5 to 2800 days (Diem and Stumm, 1984; Junta and Hochella 1994; Davies and Morgan 1989).

Bacterially mediated Mn oxidation occurs over hours (Tebo and Emerson, 1985; Nealson et al., 1988; Toyoda and Tebo, 2016) and is therefore considered as the primary pathway of Mn oxidation in the environment. We are primarily interested in probing iron mobility under relatively low pO_2, where a significant fraction of dissolved iron remains as mobile Fe^{2+}. Under such conditions, it is likely that any MnO_2 produced would rapidly react with Fe^{2+} ($MnO_{2s}+2Fe^{2+}_{aq}+4H^{+}_{aq}->Mn^{2+}_{aq}+2Fe^{3+}_{aq}+2H_2O$; Tekin and Bayramoğlu, 1993) or other reductants such as organics (Stone, 1987; Wang and Stone, 2006; Flynn and Catalano, 2019) to be recycled as dissolved Mn^{2+} (Siebecker et al., 2015, Liu et al., 2022). Supporting this view is the observation that before iron retention in paleosols approaches 100% at ~1.85 Ga, manganese retention remained below ~40% and was tightly coupled to Fe^{2+} (Murakami et al. 2011; Toma et al., 2019; Sindol et al., 2020; Babechuk et al., 2017). This is also consistent with the finding that Mn-bearing mineral occurrences comprise almost exclusively Mn^{2+}-bearing minerals until 2 to 1.5 Ga (Hummer et al., 2022).

Several studies have examined iron mobilization and isotopic fractionation in soils and during laboratory experiments of mineral leaching (Andriesse 1979; Huang et al., 2018; Wiederhold et al., 2007a; Schuth et al., 2015) but only a handful have examined soils developed on mafic bedrocks (Brantley et al. 2004; Thompson et al. 2007; Wiederhold et al., 2007b; Yamaguchi et al., 2007; Liu et al., 2014; Babechuk et al., 2019) or leaching of mafic materials (Brantley et al. 2004; Chapman et al., 2009). Brantley et al. (2004) studied Fe isotopic fractionation during dissolution of hornblende, an amphibole. They found that dissolved Fe always had light Fe isotopic composition relative to the mineral and the degree of isotopic fractionation correlated with the affinity of the ligands with Fe. Brantley et al. (2004) also analyzed the isotopic composition of

Fe in soils developed on granulite facies metagabbro and found that Fe-oxides had similar Fe isotopic composition to the bedrock while exchangeable Fe had light isotopic composition. The cause of Fe isotopic fractionation in those experiments and soils remains uncertain. A difficulty with laboratory experiments lasting only a few days is that they may capture transient phenomena of uncertain relevance for natural systems. Thompson et al. (2007) studied soils formed along a climate sequence from basalt in Hawaii. They found that iron was more extensively leached from soils developed under higher precipitation and more anoxic conditions. In all cases, leached iron has light isotopic composition, driving the residual soil towards heavy Fe isotopic composition (the instantaneous δ^{56}Fe isotopic fractionation factor between leached and solid-bound Fe is ~-0.3 to -0.4 ‰). Such negative fractionation could be related to redox conditions, as fluid-mobile Fe(II) is isotopically light relative to fluid-immobile Fe(III).

Overall, considerable uncertainties remain on the drivers of Fe mobilization and isotopic fractionation in weathering profiles but redox surely plays an important role (Fantle and DePaolo, 2004; Thompson et al., 2007; Johnson et al., 2008; Schuth et al., 2015). Since Fe cation chemistry and isotopic composition of Martian clays are not currently known, we report here the Fe/Mg-Fe/Mn-δ^{56}Fe values of modern terrestrial clays that can be taken as analogs of Martian clays (*e.g.,* Bristow et al., 2018; Craig et al., 2018; Morris et al., 2011; Singer, 1982; Treiman et al., 2014; Vaniman et al., 1992) to provide a preliminary understanding of how their compositions can help constrain the redox conditions that prevailed during formation of Fe/Mg-clays on the surface of Mars. Redox-related questions are also posed for terrestrial surface environments prior to the Great Oxidation Event (GOE), when anoxic conditions prevailed (Pavlov and Kasting 2002; Canfield 2005; Lyons et al., 2014) but oxidative weathering may have been active, at least locally (Anbar

et al., 2007; Crowe et al., 2013; Planavsky et al., 2014; Heard et al., 2020, 2022). Therefore, we also examine the top layers of terrestrial paleosols developed on basaltic bedrocks, since variations in Fe in paleo-weathering profiles could similarly record major changes in terrestrial surface environments associated with Earth's oxygenation (*e.g.,* Yamaguchi et al., 2007; Murakami et al., 2011; Yokota et al., 2013; Kanzaki and Murakami, 2016; Heard et al., 2021).

4.2 Iron isotope measurements

4.2.1 Sample description

The studied terrestrial clay samples comprise 7 nontronites, 4 saponites, 2 montmorillonite, 2 chlorites, and 1 antigorite (Table 4-1), many of which have been used in previous analog studies for Mars (*e.g.*, Morris et al., 2000; Singer 1982; Baird et al., 1977; Treiman et al., 2014; Bristow et al., 2018; Craig et al., 2018; Morris et al., 2011; Vaniman et al., 1992). Chemical and Fe isotopic compositions of the corresponding parent rocks are compiled from literature data for unaltered specimens of similar rock type and age (Table 4-2).

We offer a concise overview of the structural characteristics of the phyllosilicate minerals studied here (Deer et al., 2013). They predominantly belong to the smectite family, characterized by tetrahedral-octahedral-tetrahedral (TOT) layers separated by interlayer water and charge-balancing cations. These smectites differ in terms of the cations in the octahedral layer, where divalent ions such as Mg^{2+} typically form trioctahedral layers and trivalent ions like Al^{3+} and Fe^{3+} typically form dioctahedral layers, as well as in the nature of the main cations and the permissible substitutions. Nontronite is a dioctahedral smectite with Fe^{3+} and Al^{3+} occupying 2/3 of the octahedral sites and the rest remaining vacant. Some Fe^{3+} and Al^{3+} can also substitute for Si^{4+} in

the tetrahedral sheet with charge compensation achieved by cations in the interlayer. Saponite is a trioctahedral smectite, meaning that almost all octahedral sites are occupied by cations. Saponite typically contains Mg^{2+} as the dominant cation in the octahedral layer, but it can also include Fe^{2+}, Fe^{3+} and Al^{3+} in smaller quantities. In the tetrahedral sheet, Si^{4+} can be substituted with Al^{3+}. Montmorillonite is a dioctahedral smectite containing mostly Al^{3+} in the octahedral sheet, with some isomorphous substitution by divalent cations possible. In the tetrahedral sheet, Si^{4+} can be substituted with Al^{3+}. Chlorite has a TOT-O structure. The T sheets are made of tetrahedrally-coordinated silica. The O sheet sandwiched in TOT can be either trioctahedral (Mg^{2+}, Fe^{2+}) or dioctahedral (Al^{3+}). The O layer (-O) either has the structure of gibbsite (dioctahedral; Al^{3+}-bearing) or brucite (trioctahedral; Mg^{2+}-bearing). Clinochlore is part of the chlorite group of minerals. In this mineral, both octahedral sheets are trioctahedral. Antigorite is part of the serpentine group of minerals with a T-O-T structure. It is composed of silica tetrahedral and Mg octahedral layers. In phyllosilicates, ferrous iron (Fe^{2+}) will be primarily present in trioctahedral sheets by substituting for Mg^{2+} or in dioctahedral sheets through more complex substitution mechanisms. Ferric iron (Fe^{3+}) will be found in dioctahedral sheets in solution with Al^{3+}, and in trioctahedral sheets through complex substitution mechanisms. Like Al^{3+}, Fe^{3+} can also substitute for Si^{4+} in tetrahedra, with charge balance achieved with interlayer cations.

NAu-1 and *NAu-2* are nontronite standards from the Clay Mineral Society that were collected in the Uley Graphite Mine in South Australia (Keeling et al. 2000). Both NAu-1 and NAu-2 formed by low-temperature alteration of rocks that were previously metamorphosed to upper amphibolite-lower granulite facies. NAu-1 is a yellowish-green clay distributed as veinlets and masses within kaolinized schist and gneiss (originally carbonaceous sediments). Its bulk Fe

isotopic composition was previously measured by Shi et al. (2016) who obtained $\delta^{56}Fe$=+0.69 ‰. NAu-1 contains 90% nontronite, 4% kaolinite, 2% quartz, <1% biotite, and 3% goethite. Mössbauer spectroscopy indicates that ~12% of Fe is hosted in goethite with the rest in nontronite (Jaisi et al., 2005). The structural formula of NAu-1 is $M^{+}_{1.05}[Si_{6.98}Al_{1.02}][Al_{0.29}Fe_{3.68}Mg_{0.04}]O_{20}(OH)_4$. Iron in NAu-1 nontronite is present as 6% Fe^{2+} and 94% Fe^{3+}, with 98% of Fe^{3+} in octahedral coordination (Gates et al. 2002; Jaisi et al., 2005; Cashion et al. 2010). The equivalent unaltered rock to NAu-1 is the Cook Gap Schist (Lower Middleback Subgroup) of the Hutchison Group (~1900-1850 Ma). The major, minor and trace element composition of the Cook Gap Schist was reported in Simpson (1994) and Szpunar et al. (2011) and the average composition is provided in Table 4-2. The Fe isotopic composition of that formation is unknown but black shales of similar age have $\delta^{56}Fe$ values that span the range +0.3 to +1.2 ‰, defining an average of +0.9‰ (Rouxel et al., 2005). NAu-2 is a dark-brown clay found in fracture networks in amphibolite (originally basaltic volcanics or intrusive gabbro sills and dikes). NAu-2 contains 95% nontronite, 5% plagioclase, <1% quartz. Iron is almost 100% hosted in nontronite, which has a formula $M^{+}_{0.72}[Si_{7.55}A1_{0.16}Fe_{0.29}][Al_{0.34}Fe_{3.54}Mg_{0.05}]O_{20}(OH)_4$. Iron in NAu-2 nontronite is present as 2% Fe^{2+} and 98% Fe^{3+}, with ~92% of Fe^{3+} in octahedral sites and ~8% in tetrahedral sites (Gates et al. 2002; Jaisi et al., 2005). The major element compositions of equivalent non-altered Hutchison Group amphibolites are reported in Parker (1978) and Mortimer (1984). The Fe isotopic composition of that amphibolite was not measured but we can use global basalts as a baseline reference, which show limited $\delta^{56}Fe$ variations spanning the range ~+0-0.14 ‰, giving an average of +0.057 ± 0.029 ‰ (±2σ) (Dauphas et al., 2009a; Teng et al., 2013). Such

comparison could be violated if metamorphism has significantly altered the original basaltic isotopic signature that the amphibolite supposedly inherits (Poitrasson et al., 2013).

SWa-1 is another nontronite standard from the Clay Mineral Society that was collected in the Columbia River Basalts (CRB) in Washington (Baker 2017). SWa-1 is a yellowish green ferruginous smectite found at the contact between a paleosol and an overlying basalt flow. It was formed by hydrothermal alteration of aluminous paleosol clays, giving it an unusually aluminous and magnesian composition. Its Fe isotopic composition had not been previously measured. SWa-1 contains 90% montmorillonite, 4% goethite, 3% quartz, and 3% calcite (Derkowski et al., 2016). Mössbauer spectroscopy shows that 2.9% of Fe is hosted in goethite while a dominant fraction of Fe is incorporated into the clay lattice (Murad 1987; Bujdák and Rode 1996). The structural formula of SWa-1 is $(M^{+}_{0.95})[Al_{1.10}Fe_{2.61}Mg_{0.25}][Si_{7.40}Al_{0.60}]O_{20}(OH)_4$. SWa-1 has all its iron present as Fe^{3+} in octahedral sites (Gates et al., 2002; Gorski et al., 2012). The equivalent unaltered basalt to SWa-1 is the Frenchman Springs Member of the Wanapum Basalts of the Columbia River Basalt Group (CRBG; 15.0 Ma). The major and trace element composition of the Frenchman Springs Member was reported in Martin et al. (2013). The Fe isotopic composition of that specific member of the CRBG was not measured, but the USGS Columbia River Basalt standard BCR-2 has $\delta^{56}Fe$=+0.091 ‰ (Craddock and Dauphas, 2010).

API-H33a, or Garfield nontronite, is a nontronite standard from the American Petroleum Institute and was collected in exposed nontronite veins at Garfield, Washington (Kerr and Kulp, 1949). Garfield nontronite is a green, waxy clay that may be found *in situ* and fills vesicles and openings in the lava, or as material transported and redeposited as a filling in cracks, vesicles, and other voids in the partially decomposed basalts underneath. Its formation conditions could be

associated with drainage by alkaline solutions. Mössbauer spectrum shows 4.6 % of Fe to be bound in goethite (Murad 1987). The structural formula of Garfield nontronite is $(M^{+}_{1.07})[Al_{0.23}Fe_{3.71}Mg_{0.03}][Si_{7.03}Al_{0.97}]O_{20}(OH)_4$ (Manceau et al., 2000a,b). Iron in Garfield nontronite is present as Fe^{3+} completely in octahedral coordination (Gates et al., 2002; Manceau et al., 2000a; Murad 1987). The equivalent unaltered basalt to Garfield nontronite is the Priest Rapids Member of CRBG (15.0-15.6 Ma). The major and trace element composition of the Priest Rapids Member basalts was reported in Reidel et al. (2013). We take the $\delta^{56}Fe$=+0.091 ‰ of BCR-2 as representative of this sample (Craddock and Dauphas, 2010).

SapCa-1 is a saponite standard from the Clay Mineral Society that was collected in Panamint Valley near Ballarat, California (Post 1984). SapCa-1 is a white clay that occurs in joints and open fracture zones in limestone in the Late Cambrian (~635-632 Ma; Petterson et al., 2011) Noonday Dolomite Formation. It formed by hydrothermal alteration of metamorphosed dolomitic limestone possibly during Pliocene times, with additional Mg supplied by phreatic ground water. SapCa-1 contains <3% diopside and is free of major impurities (Kloprogge and Ponce, 2021). The structural formula for SapCa-1 is $(M^{+}_{0.37})[Al_{0.30}Fe_{0.12}Mg_{5.22}][Si_{7.54}Al_{0.46}]O_{20}(OH)_4$. Iron in SapCa-1 saponite is present as 21% Fe^{2+} and 79% Fe^{3+} that substitute for Mg^{2+} in the octahedral sites. The chemical and Fe isotopic compositions of the cap carbonate Noonday Dolomite Formation are unknown. Cap carbonate dolostones from Member 1 of Doushantuo Formation in the Three Gorges area of similar age give an average $\delta^{56}Fe$ of -0.452 ‰ (Sawaki et al., 2017).

RIVSM1 or Riverside nontronite is an iron-rich smectite clay that was collected at New City Quarry in Riverside, California by the Viking x-ray fluorescence team (Baird et al., 1977). It formed as an alteration product of a hedenbergite pyroxenite. Riverside nontronite is olive-yellow

in color and closely matches the composition of the martian fines (Weldon et al., 1982; Boslough et al., 1986). It contains 85% nontronite, 7-8% epidote, 3-4% hedenbergite, and 1-2% quartz. The structural formula of Riverside nontronite was not reported, but the ideal formula for nontronite is $(Ca_{0.5},Na)_{0.3}Fe^{3+}{}_2(Si,Al)_4O_{10}(OH)_2 \cdot nH_2O$. Iron in Riverside nontronite is present as Fe^{3+} dominantly in octahedral coordination with no detectable Fe^{2+} (Bancroft 1973; Weldon et al., 1982). The chemical and Fe isotopic composition of the parent material of Riverside nontronite had not been reported, and we take the average $\delta^{56}Fe$ of modern and ancient basalts equal to +0.057 ± 0.029 ‰ (±2σ) (Dauphas et al., 2009a).

STx-1 is a Ca-montmorillonite standard from the Clay Mineral Society that was collected in the Eocene-aged Manning Formation of the Jackson group in Gonzales, Texas (Moll 2001). It consists of extremely white Ca-bentonite that rests on a gray friable sandstone at the base of the Manning Formation. STx-1 formed by alteration of volcanic ash of rhyolitic composition. STx-1 contains ~67% smectite, 30% opal-CT and 3% quartz (Chipera and Bish, 2001). Its structural formula is $(M^+_{0.80})[Al_{3.08}Fe_{0.12}Ti_{0.02}Mg_{0.76}][Si_{7.98}Al_{0.02}]O_{20}(OH)_4$ and iron is present 100% in the octahedral coordination with 28% being Fe^{3+} (Finck et al., 2019; this work). The parent material of STx-1 is volcanic ash from silicic volcanics in west Texas that exploded during late Eocene (Chen 1968). The major element composition of the Manning Formation volcanic ash was reported in Chen (1968). Magmatic differentiation can fractionate iron isotopes, modulated by redox conditions in the magmas. In rhyolites with SiO_2 content similar to Manning Formation volcanic ash, $\delta^{56}Fe$ is ~+0.286±0.014 ‰ (Du et al., 2017).

SWy-1 is a Na-montmorillonite standard from the Clay Mineral Society that was collected in the Cretaceous-aged Newcastle Formation in Crook, Wyoming (Moll 2001). It has properties

associated with the Wyoming bentonite, which occur in rocks composed of shales, marls and argillaceous sandstones and is blue in color if unweathered. SWy-1 formed by alteration of latitic or rhyolitic volcanic ash that fell onto fresh-water lakes near the shore. The mineralogy of SWy-1 was not measured but its replacement SWy-2 reported a composition of ~75% smectite, 8% quartz, 16% feldspar and 1% gypsum (Chipera and Bish, 2001). The structural formula of SWy-1 is $(M^{+}_{0.70})[Al_{3.08}\ Fe_{0.42}Mg_{0.45}][Si_{7.74}Al_{0.26}]O_{20}(OH)_4$. Iron in SWy-1 is present as 96% Fe^{3+} and 4% Fe^{2+} (Gates et al., 1998; this work) almost completely in octahedral coordination (Finck et al., 2015). The volcanic ash from which SWy-1 was altered was erupted from volcanoes located west of the clay deposit and existed from Late Albian to early Cenomanian time (mid Cretaceous; Elzea and Murray, 1990). It was inferred to be rhyolitic (Slaughter and Earley, 1965) and glass shards constituted 95% of its mineralogy (Elzea 1990). The chemical and Fe isotopic compositions of the parent rhyolitic volcanic ash are unknown, and we take the average $\delta^{56}Fe$ of high-silica rhyolites equal to ~+0.275±0.008 ‰ (Du et al., 2017).

GP14M800, GP14Q10, MUGPLA1B or griffithite are iron-bearing saponites collected from the eastern Santa Monica Mountain near Griffith Park, California (Treiman et al., 2014). They are black lustrous clays found as fillings of vesicles in Miocene basalts of the Topanga Canyon Formation. They formed by aqueous solution associated with dissolution of olivine and glass from host basalts. XRD analysis (Komadel et al., 2000) indicates that the coarse fraction of the griffithite contains albite, calcite and quartz, while the fine clay fraction contains only smectite. Mössbauer spectroscopy results show that GP14M800 hosts 73% of Fe in saponite, 24% in a nanophase ferric oxide phase, and 3% in hematite; GP14Q10 hosts 74% of Fe in saponite and 26% in the ferric oxide phase; and MUGPLA1B hosts 100% of Fe in saponite. The structural formula

of griffithite is $[Ca_{0.62}Na_{0.20}K_{0.04}][Al_{0.28}Fe_{1.58}Mg_{2.92}Mn_{0.06}Ti_{0.04}][Si_{6.92}Al_{1.08}]O_{20}(OH)_4$ (Gandía et al., 2005). All Griffith saponites contain 0 tetrahedral Fe. GP14M800 contains 93% Fe^{3+}, GP14Q10 contains 92% Fe^{3+} and MUGPLA1B contains 90% Fe^{3+}. The major and trace element composition of the Topanga Group volcanic rocks was reported in Weigand et al. (2002). The Fe isotopic composition of the Miocene basalts of Topanga Canyon Formation is unknown, and we take the average $\delta^{56}Fe$ composition of global basalts worldwide (+0.057 ± 0.029 ‰) as representative.

CCa-1 is a chlorite standard from the Clay Mineral Society that was collected at Flagstaff Hill in El Dorado County, California (Post and Plummer, 1972). It is found as vein replacement material. CCa-1 formed by alteration of an ultramafic body (late Jurassic or early Cretaceous) found along a major fault zone in the Sierra Nevada foothills. CCa-1 contains 95-100% ripidolite and <2% quartz. The structural formula of CCa-1 is $(Ca_{0.042}Mg_{4.481}Fe^{2+}_{3.012}Fe^{3+}_{3.459}Al_{0.597}Ti_{0.063})(Si_{4.512}Al_{3.488})O_{20}(OH)_4(OH)_{16}$ (Kloprogge and Frost, 2000). Iron in CCa-1 is present in octahedral coordination with 22% Fe^{3+} (King and Clark, 1989; this work). The major element composition of metamorphic minerals in the ultramafic body in the western Sierra Nevada foothills was reported in Springer (1974). The Fe isotopic composition of the parent body of CCa-1 is unknown, but the Fe isotopic composition of ultramafic rocks found in the subduction-related Alpine orogen have $\delta^{56}Fe$=+0.12 ‰ on average (Inglis et al., 2017).

CHLCLV1 is a clinochlore collected in California. Mineralogy of CHLCLV1 is not documented, but XRD analysis of CLI101, another California clinochlore with similar composition to CHLCLV1, indicated no impurity (Cloutis et al., 2008). CHLCLV1 is trioctahedral and iron is present as 46% Fe^{3+}.

PHY07 or Pennsylvania nontronite is a pale greenish-yellow clay (Singer et al., 1982; Weldon et al., 1982). PHY07 has all its iron presented as Fe^{3+} in octahedral coordination (Morris et al., 2010).

ATGNC1 is an antigorite with unidentified origin. Antigorite has an ideal formula $Mg_3Si_2O_5(OH)_4$ (Baur, 2018), and iron in ATGNC1 is present as 86% Fe^{3+} probably all in octahedral coordination (Mellini et al., 2002; this work).

WASCDB1 is a nontronite with possible Washington state origin and has all iron present as Fe^{3+}.

The chemical and Fe isotopic composition of the parent materials of CHLCLV1, PHY07, ATGNC1 and WASCDB1 are unknown, and we take the average $\delta^{56}Fe$ of modern and ancient basalts equal to +0.057 ± 0.029 ‰ (±2σ) (Dauphas et al., 2009a).

Table 4-1 Chemical and iron isotopic compositions of Martian analog clays.

Sample	SiO_2	TiO_2	Al_2O_3	Cr_2O_3	Fe_2O_{3T}	MnO	MgO	CaO	Na_2O	K_2O	P_2O_5
NAu-1	52.18	0.55	14.39	0.03	29.15	0.10	1.29	2.15	0.23	0.34	0.07
NAu-2	55.09	0.85	5.63	0.01	34.39	0.02	0.94	2.36	0.93	0.17	0.11
WASCDB1	59.53	0.21	3.91	0.01	32.17	0.04	1.03	2.42	0.07	0.11	0.08
API-H33a	48.40	0.03	7.90		41.00	0.10	0.90	0.90	0.07	0.06	
RIVSM1	53.30	0.56	6.00		29.23	0.27	3.96	7.48	0.53	0.13	0.15
PHY07	52.00	0.01	15.90		30.90	0.03	0.09	0.05	0.00	0.00	0.03
SWa-1	58.00	0.71	10.23	0.01	26.91	0.01	2.29	2.21	0.07	0.08	0.03
SapCa-1	58.04	0.59	4.24	0.00	1.23	0.04	25.70	7.81	1.80	0.88	0.12
ATGNC1	48.00	0.02	0.17	0.00	2.82	0.02	48.40	0.09	0.05	0.00	0.01
CCa-1	27.78	0.99	22.52	0.04	27.89	0.11	19.50	0.04	0.11	0.08	0.02
STx-1	75.10	0.25	16.84	0.00	0.85	0.01	3.86	1.83	0.33	0.10	0.04
SWy-1	67.39	0.13	20.67	0.00	4.30	0.02	2.90	1.89	1.64	0.60	0.06
CHLCLV1	35.28	0.07	19.30	0.65	10.00	0.15	34.38	0.11	0.05	0.03	0.01
GP14M800	43.40	0.04	7.10	0.02	15.19	0.06	18.01	3.24	0.04	0.05	
GP14Q10	43.53	0.02	6.78	0.02	15.40	0.05	17.92	3.07	0.05	0.05	
MUGPLA1	43.68	0.02	7.93	0.01	18.17	0.56	18.87	3.02	0.13	0.03	

Table 4-1 Chemical and iron isotopic compositions of Martian analog clays (continued).

Sample	SO_3R	Total	%LOI	FeO	Fe_2O_3	SO_3 Actual	$Fe^{3+}/\Sigma Fe$ (%)	$\delta^{56}Fe$	95% C.I.	Ref[a]
NAu-1	0.07	100.55	19.77	1.62	27.35		94	0.59	0.03	[1]
NAu-2	0.08	100.58	12.11	0.49	33.85		98	1.41	0.03	[1]
WASCDB1	0.09	99.67	19.11	0.09	32.07	0.16	100	-0.25	0.03	[1]
API-H33a		99.36	13.02					0.42	0.03	[2]
RIVSM1		101.61	14.48					-0.13	0.03	[3]
PHY07		99.01	19.23					-0.38	0.03	[2]
SWa-1	0.08	100.63	23.57	0.07	26.83	0.28	100	0.77	0.03	[1]
SapCa-1	0.08	100.53	12.88	0.23	0.97	0.20	79	0.22	0.03	[1]
ATGNC1		99.58	13.50	0.35	2.43		86	0.61	0.03	[1]
CCa-1	0.04	99.12	11.64	19.65	6.05	0.12	22	0.05	0.03	[1]
STx-1	0.08	99.29	18.55	0.55	0.24	0.11	28	0.52	0.03	[1]
SWy-1	0.20	99.80	15.31	0.16	4.12	0.22	96	0.40	0.03	[1]
CHLCLV1		100.03	12.77	4.83	4.63		46	-0.08	0.03	[1]
GP14M800		85.70					93	0.33	0.03	[4]
GP14Q10		85.42					92	0.02	0.03	[4]
MUGPLA1		88.98					90	-0.10	0.03	[4]

[a] Chemical compositions are reported in previous work: [1] unpubslihed data from Morris and Mertzman. [2] Singer et al., 1982. [3] Baird et al., 1977. [4] Treiman et al., 2014.

Table 4-2 Major and trace element compositions of equivalent unaltered rocks to studied clays.

	Middleback Range Cook Gap Schist[a]	Hutchison Group amphibolites[b]	Frenchman Springs Member basalt[c]	Priest Rapids basalts[d]	Manning Formation volcanic ash[e]	Topanga Group volcanics[f]	Sierra Nevada ultramafic body[g]	Average global basalts[h]
Major (wt%)								
SiO_2	70.68	50.08	50.85	50.22	72.58	60.19	51.32	51.41
TiO_2	0.38	1.15	3.10	3.22	0.16	1.11	0.08	0.86
Al_2O_3	12.41	13.91	13.09	13.38	13.11	15.92	1.90	11.83
Fe_2O_3	6.04	12.31	15.61	15.67	0.93	6.78	5.88	9.91
MnO	0.12	0.24	0.24	0.23	0.06	0.10	0.13	0.18
MgO	2.13	6.78	3.92	5.01	0.42	5.20	36.66	14.64
CaO	1.06	10.79	8.23	9.53	0.14	6.69	7.69	7.30
Na_2O	2.03	2.44	2.91	2.79	2.46	4.23		1.89
K_2O	2.58	0.90	1.28	1.07	3.71	0.67		0.41
P_2O_5	0.07	0.13	0.70	0.76		0.17		0.10
LOI	2.46	1.26				1.98		
Total	99.95	99.12		100.30		100.37	98.76	
Fe/Mg	3.30	2.12	4.65	3.65	2.58	1.52	0.19	0.79
Fe/Mn	47.75	46.63	59.63	61.40	14.09	59.27	40.50	51.46
Fe/Al	0.64	1.17	1.58	1.55	0.09	0.56	4.09	1.11
Trace and REE								
Cr	100.00		15	73.5		167.59		
V	67.50		341	371.3		122.19		
Sc	10.00			41.5		19.23		
Ba	677.50		596	529.5		202.74		
Be	2.13							
Hf	2.25					3.14		
Rb	67.25		33.6	25		12.74		
Sn	<10							
Sr	140.75		331	291.2		381.48		
Ta	<2					0.44		
Zr	107.50		194	192.3		122.00		
Ag	1.18							
As	5.50							
Bi	0.63							

Table 4-2 Major and trace element compositions of equivalent unaltered rocks to studied clays (continued).

	Middleback Range Cook Gap Schist[a]	Hutchison Group amphibolites[b]	Frenchman Springs Member basalt[c]	Priest Rapids basalts[d]	Manning Formation volcanic ash[e]	Topanga Group volcanics[f]	Sierra Nevada ultramafic body[g]	Average global basalts[h]
Cd	<0.1							
Co	11.25							
Cs	1.20					0.82		
Cu	84.75			24.67		36.08		
Ga	18.25		22	51		19.08		
In	<0.05							
Mo	2.08							
Nb	7.38		14.4	17.78		7.16		
Pb	15.50		6			2.78		
Sb	<0.5							
Se	3.00							
Te	0.40							
Th	12.13		4			1.44		
Tl	0.45							
U	3.08		0			0.57		
W	3.73							
Zn	62.63		148	179.67		65.77		
Y	13.63		40.1	48.5		19.73		
Ni	39.25		9	23		100.50		
Ce	47.75		56			19.38		
La	23.75		24			9.35		
Dy	2.23					3.64		
Er	1.43					1.83		
Eu	0.89					1.23		
Gd	2.55					3.76		
Ho	0.46					0.71		
Lu	0.24					0.23		
Nd	17.13					11.90		
Pr	5.20					2.61		
Sm	2.93					3.52		
Tb	0.41					0.61		
Tm	0.20					0.25		
Yb	1.49					1.55		

[a]Szpunar et al., 2011; [b]Mortimer 1984; [c]Martin et al., 2013; [d]Reidel et al., 2013; [e]Chen 1968; [f]Weigand et al., 2002; [g]Springer 1974; [h]Dauphas et al., 2009.

4.2.2 Iron isotopic analyses

Powder samples containing ≥220 mg Fe were weighed and transferred to fluoropolymer (PFA) beakers for digestion in acids on a hot plate at 130 °C in a sequence of 1 ml of 28 M HF + 0.5 ml of 15 M HNO_3 + a few drops of 11 M $HClO_4$ and aqua regia (0.75 ml of 11 M HCl + 0.25 ml of 15 M HNO_3), with the solution dried down between each step. The aqua regia step was repeated two more times to release all iron into solution. After digestion, no residue was found, and the sample was re-dissolved in 0.5 mL of 6 M HCl. Approximately 50% (0.25 mL) of that was loaded on an AG1-X8 anion exchange column for Fe purification, while the rest was saved for replication or chemical characterization. Iron was separated from matrix elements and interfering Cr and Ni by running more 6 M HCl through the column before Fe elution in 0.4 M HCl, following the protocol of Dauphas et al. (2009b).

Iron isotopic compositions were measured by sample-standard bracketing on concentration-matched solutions using a ThermoScientific Neptune MultiCollector Inductively Coupled Plasma Mass Spectrometer (MC-ICPMS) in medium resolution following the protocol of Dauphas et al. (2009b). The samples were measured at a concentration of 0.1-0.7 ppm iron using a nebulizer aspiration rate of 100 μL/min. Purified sample solution of WASCDB1, SWa-1, STx-1, CHLCLV1 and PHY07 were measured 5 times, API-H33a was measured 6 times, MUGPLA1B was measured 7 times, ATGNC1, GP14M800, NAu-1 and SWy-1 were measured 8 times, and the other samples were measured 9 times. The reported Fe isotopic composition is the average of the corresponding sample-standard brackets, where each sample's isotopic measurement is compared with nearest measurements of the reference material. Iron isotopic compositions are expressed using the δ notation (Dauphas et al., 2017),

$$\delta^{i}Fe_{sample}(‰) = \left[\left(^{i}Fe/^{54}Fe\right)_{sample}/\left(^{i}Fe/^{54}Fe\right)_{IRMM014} - 1\right] \times 1000, \quad \text{(Eq. 4-1)}$$

where *i* is isotope ^{56}Fe, ^{57}Fe, or ^{58}Fe, and IRMM014 is a reference material. We used IRMM-524 for bracketing the measurements but as shown by Craddock and Dauphas (2010), the two reference materials have identical compositions within error. The accuracy and precision of measured δ^{56}Fe was assessed through repeated analysis of the USGS basalt standard BHVO-2 and the SARM iron formation standard IF-G. All standards were processed in the same manner as the samples. Measured δ^{56}Fe values were +0.099±0.044‰ (2σ, n=18) for BHVO-2 and 0.61±0.031‰ (2σ, n=23) for IF-G, which are within the uncertainty of previously reported values (0.114±0.011‰ for BHVO-2 and 0.639±0.013‰ for IF-G) (Craddock and Dauphas, 2011). We also measured the Fe isotopic composition of NAu-1 (+0.594±0.029 ‰) that had been analyzed by Shi et al. (2016) (0.59 ‰) and the results agree.

To discuss Fe isotopic fractionation during clay formation, we normalize the compositions measured in clay minerals to those of the source rocks, and we use the following notations: $\delta^{56}Fe^{*} = \delta^{56}Fe_{measured} - \delta^{56}Fe_{source\ rock}$ and $(A/B)^{*} = (A/B)_{measured}/(A/B)_{source\ rock}$. The measured δ^{56}Fe values of terrestrial analog clay samples exhibit a wide range from -0.38±0.03‰ in nontronite PHYO7 to +1.41±0.03‰ in nontronite NAu-2. Half of clay samples have heavy Fe isotopic compositions relative to their source rocks (positive δ^{56}Fe* values), and much of those δ^{56}Fe variations reflect Fe mobilization during clay formation rather than inheritance from the source rocks (Fig. 4-1). We do not see any correlation between δ^{56}Fe* and the degree of iron oxidation in the clays (Fig. 4-2), although this is difficult to assess because the ratio Fe^{3+}/Fe_{tot} in our sample set follows a bimodal distribution with 3 samples clustering between 0.2-0.5 and another 10 samples clustering between ~0.8-1. We do not find any correlation between $\delta^{56}Fe^{*}$ and $(Fe/Mn)^{*}$, $(Fe/Mg)^{*}$, and $(Fe/Al)^{*}$ ratios,

either (Fig. 4-3). The only noteworthy observation is that the two samples with the highest (Fe/Mn)* ratios (33.5 and 41.0) are also the ones with the highest δ^{56}Fe* values (+1.35 and +0.68 ‰ for nontronites NAu-2 and SWa-1).

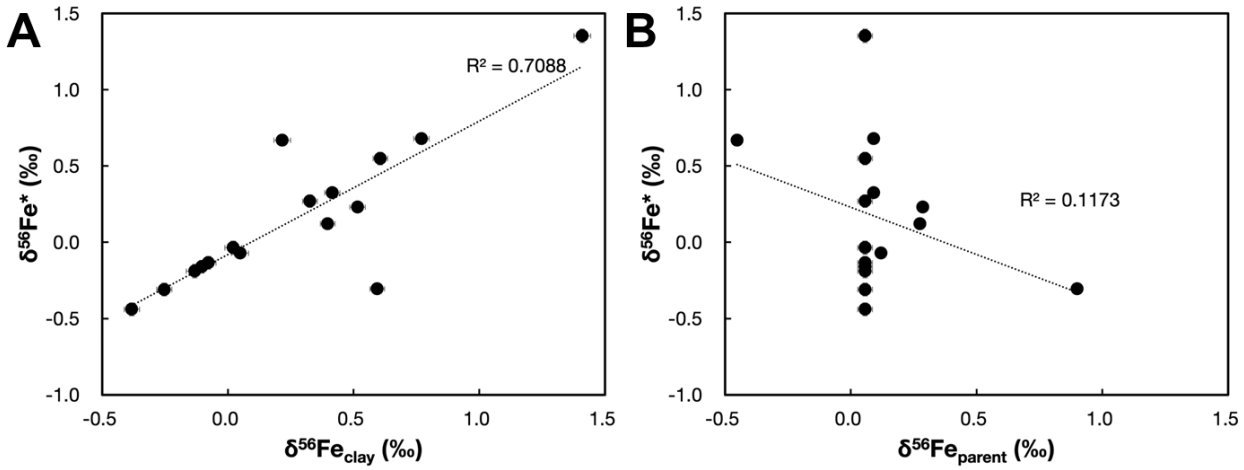

Figure 4-1 Relationship between δ^{56}Fe of Martian clay analogs normalized to source rocks (δ^{56}Fe*) and δ^{56}Fe of (A) Martian clay analogs and (B) source-rock-equivalent unaltered rocks.

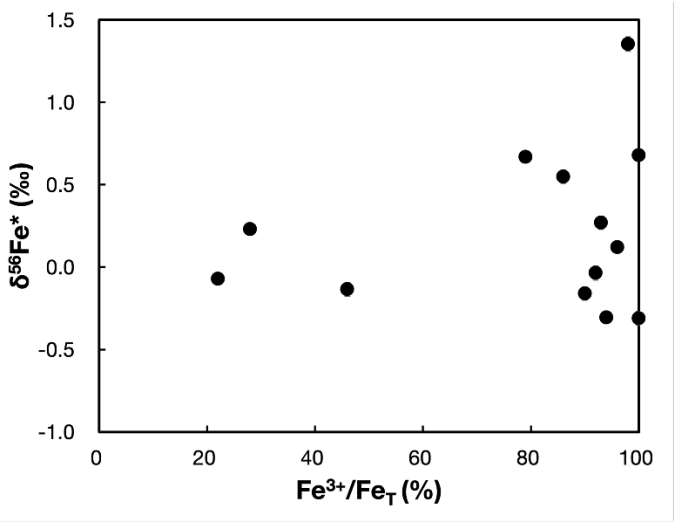

Figure 4-2 Correlation between δ^{56}Fe* and degree of iron oxidation in Martian clay analogs.

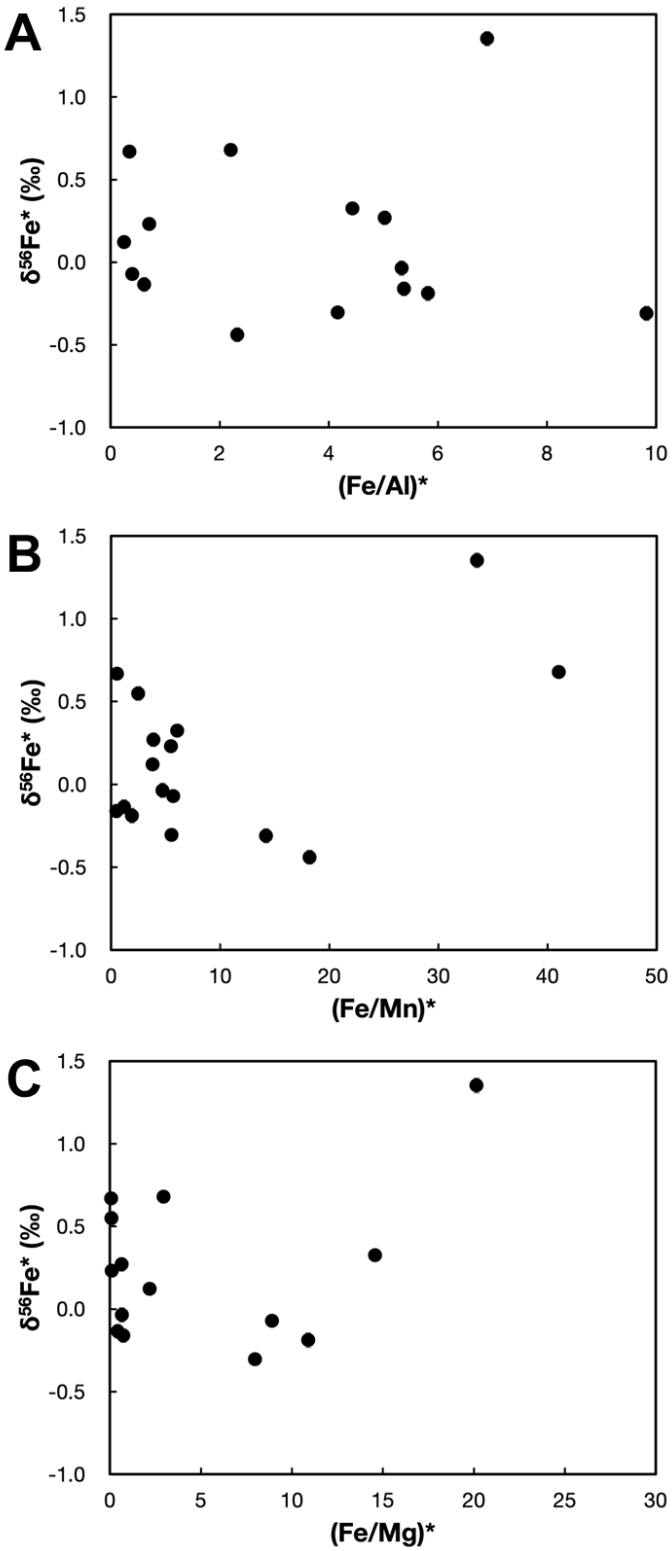

Figure 4-3 Correlation between δ^{56}Fe* and (A) (Fe/Al), (B) (Fe/Mn), and (C) (Fe/Mg) of Martian clay analogs normalized to source rocks.

4.2.3 Determination of β-factors by NRIXS

Nuclear Resonant Inelastic X-ray Scattering (NRIXS) is a synchrotron technique that uses the Mössbauer effect to probe the lattice vibration properties of solids (Seto et al 1995; Sturhahn et al. 1995), from which equilibrium isotopic fractionation factors can be derived (Polyakov et al., 2007; Dauphas et al. 2012, 2018). Iron-57 has a low-lying nuclear excited state at 14.4125 keV. The samples are irradiated by X-rays whose energy is varied over a ~±100-200 meV span around the nominal resonance energy of ^{57}Fe. When incident X-rays with lower energy than the resonance energy interact with the sample, they can still induce a nuclear transition if the solid lattice provides the missing energy in the form of lattice vibrations (a process known as phonon annihilation). Conversely, if the incoming photons have too much energy, they can still induce a nuclear transition by exciting lattice vibrations (a process known as phonon creation). The quantity measured is the flux of X-rays generated by the deexcitation of ^{57}Fe as a function of the energy of the incident X-rays, which yields the phonon excitation probability density *S(E)*. Through a Fourier-Log transformation of *S(E)*, one can derive the partial phonon density of states of iron *g(E)*. Our motivation for acquiring NRIXS data is that one can use either *S(E)* or *g(E)* to derive reduced partition function ratios (*β*-factors) that can be used to calculate iron equilibrium isotopic fractionation between phases (Polyakov et al., 2007; Dauphas et al. 2012, 2018). The temperature-dependence of the *β*-factors can be calculated from either *S(E)* or *g(E)* with the following polynomials (Dauphas et al., 2012; Hu et al., 2013),

$$1000\ln\beta = 1000\left(\frac{M}{M^*}-1\right)\frac{1}{E_R}\left[\frac{R_3^S}{8k_B^2T^2}-\frac{R_5^S-10R_2^SR_3^S}{480k_B^4T^4}+\frac{R_7^S+210\left(R_2^S\right)^2R_3^S-35R_3^SR_4^S-21R_2^SR_5^S}{20160k_B^6T^6}\right], \quad \text{(Eq. 4-2)}$$

$$1000\ln\beta = 1000\left(\frac{M}{M^*} - 1\right)\left(\frac{m_2^g}{8k_B^2T^2} - \frac{m_4^g}{480k_B^4T^4} + \frac{m_6^g}{20160k_B^6T^6}\right), \quad \text{(Eq. 4-3)}$$

where M and M^* are the masses of the two isotopes considered (^{56}Fe and ^{54}Fe here), E_R is the recoil energy, k_B is the Boltzmann constant, T is the temperature, $R_i^S = \int_{-\infty}^{+\infty} S(E)(E - E_R)^i \mathrm{d}E$ is the i^{th} centered moment of $S(E)$ and $m_i^g = \int_0^{+\infty} E^i g(E)\mathrm{d}E$ is the i^{th} moment of $g(E)$. The first term in those polynomials dominates and the main control on equilibrium isotopic fractionation is always the strength of the chemical bonds that Fe forms with its neighbors (the mean force constant $\langle F \rangle$ in N/m) as we have $R_3^S = \hbar^2 E_R \langle F \rangle / M$ and $m_2^g = \hbar^2 \langle F \rangle / M$.

NRIXS uses the nuclear excitation of ^{57}Fe, which is only 2.12% of total iron, so NRIXS measurements often involve laboratory synthesis of ^{57}Fe-enriched materials. This, however, restricts the application of this technique to minerals that can be readily synthesized. An additional complication for complex minerals such as clays that host iron in various redox states and offer multiple site occupancies is that the laboratory-synthesized minerals are never fully representative of those encountered in nature. For those reasons, we have decided to analyze the natural samples that we also analyzed for their Fe isotopic compositions.

The measurements were performed at sector 3ID of the Advanced Photon Source (APS) using an incident X-ray beam monochromated to a full width at half maximum of approximately 1.2 meV. The scans were performed between minimum values as low as -106 meV and maximum values as high as +140 meV, with steps of 0.25 meV. These scans were repeated between 20 and 54 times for each sample, and samples with a higher Fe content and thus a more intense signal, such as the nontronites were subjected to fewer scans. Data treatment was performed using the SciPhon software (Dauphas et al., 2018), which involved removing the elastic peak, normalizing the intensity of *S(E),* removing a baseline by interpolating linearly the counts in the low and high

energy tails of the measured spectrum, calculating *g(E)* by doing a Log-Fourier transformation, and iterating between *g(E)* and *S(E)* by extrapolating *S(E)* outside of its acquisition interval in a physically sound manner. SciPhon provides as output quantities the phonon density of states *g(E)*, a normalized-extrapolated version of *S(E)*, and all the quantities that can be derived from those functions.

NRIXS spectra were acquired for six Martian clay analogs (NAu-2, WASCDB1, API-H33a, CCa-1, CHLCLV1, and MUGPLA1B). The derived iron PDOS are plotted in Figure 4-4 and the data are provided in the Appendix. The coefficients used in the polynomial expression $1000\ln\beta = A_1/T^2 + A_2/T^4 + A_3/T^6$ derived from the PDOS *g(E)* and phonon excitation probability density *S(E)* are compiled in Table 4-3. The force constant has dominant control on $1000\ln\beta$ and this quantity is also reported in Table 4-3. As discussed by Schauble (2004), redox state and coordination number are expected to exert strong controls on equilibrium isotopic fractionation, with more oxidized and lower coordinated species expected to concentrate heavy isotopes.

The Fe force constants measured in clay minerals largely overlap with those measured in silicate glasses and spinels synthetized under a range of redox conditions (Dauphas et al. 2014; Roskosz et al. 2015; 2022). The clay mineral with the lowest Fe force constant of ~190 N/m contains ~22% Fe^{3+}, and clays with pure Fe^{3+} are characterized by force constants of ~290 N/m, defining a linear correlation that extrapolates to $\langle F \rangle$ =182±17 N/m for Fe^{2+} and 284±17 N/m for Fe^{3+} (Fig. 4-5) and demonstrating a strong control of redox on the clay Fe force constant. Coordination is also expected to exert a secondary control on Fe isotopic fractionation. In smectite, both Fe^{2+} and Fe^{3+} are predominantly occupying octahedral sites (6-fold coordination) (Manceau

et al., 2000a, b). In basaltic glasses, Fe^{2+} and Fe^{3+} are in 5-fold average coordination (Wilke et al. 2004; Jackson et al. 2005), while in rhyolitic glasses, Fe^{2+} and Fe^{3+} are both in 4 to 5-fold coordination (Métrich et al. 2006, Giuli et al. 2012). Iron in lower coordination is expected to form stiffer bonds. The finding that the force constant of Fe in smectite is lower than silicate glasses (Fig. 4-5) at the same redox state is therefore consistent with the lower coordination of Fe in the glasses relative to smectite.

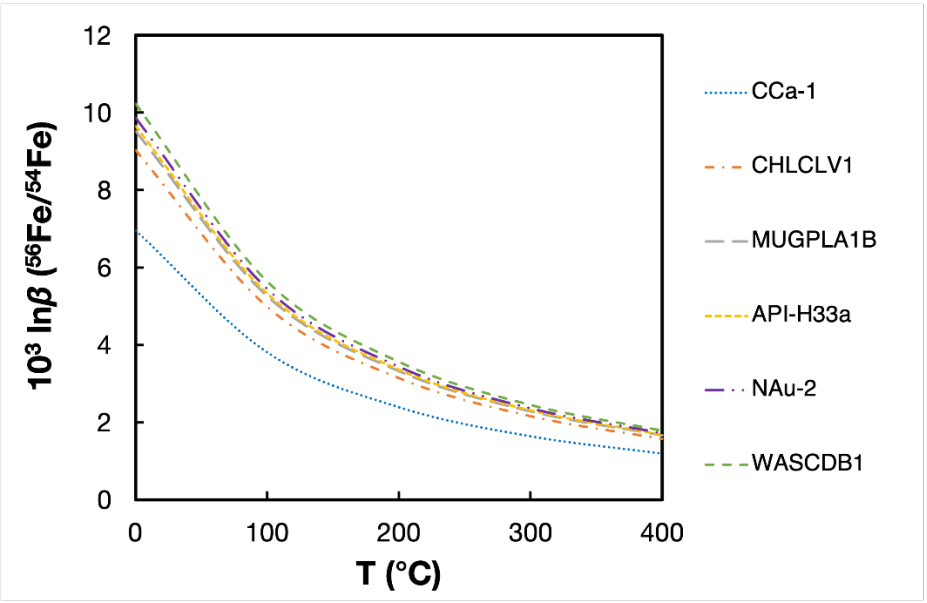

Figure 4-4 Temperature dependence of the iron β-factor of Martian clay analogs (CCa-1: chlorite, CHLCLV1: clinochlore, MUGPLA1B: griffithite, API-H3a/NAu-2/WASCDB1: nontronite).

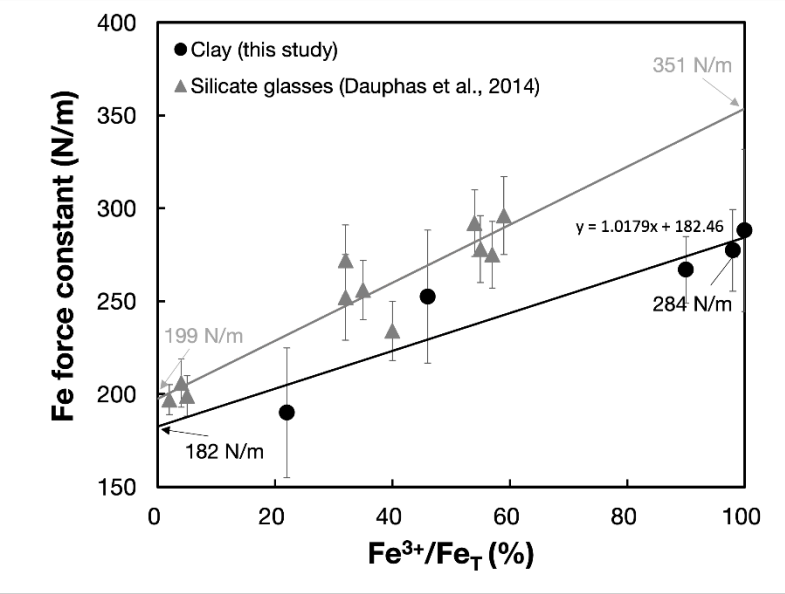

Figure 4-5 Correlation between Fe mean force constant measured by NRIXS and Fe^{3+}/Fe_T ratio of Martian clay analogs and silicate glasses from Dauphas et al. (2014). The glass data were acquired on ^{57}Fe-enriched samples while the clay data were acquired on natural specimens. The Fe^{3+}/Fe_T ratios in the clay samples were measured by Mössbauer spectroscopy. Extrapolating linearly the relationship between the force constant and Fe^{3+}/Fe_T ratio to $Fe^{3+}/Fe_T = 0$ and 1 yields force constant estimates for Fe^{2+} and Fe^{3+} in clays of 182±17 N/m and 284±17 N/m.

To obtain $\Delta_{Fe(III)clay\text{-}Fe(II)aq}$ for the alteration model we developed in Section 4.4, we have $\Delta_{Fe(III)clay\text{-}Fe(II)aq} = 1000 \ln \beta_{Fe(III)clay} - 1000 \ln \beta_{Fe(II)aq}$, where at 25°C $1000 \ln \beta_{Fe(II)aq} = 7.35$ (Polyakov and Soultanov, 2011), $1000 \ln \beta_{Fe(III)clay} = 8.66$ as calculated from g(E) of the Fe(III) clay WASCDB1 (Table 4-3), and consequently $\Delta_{Fe(III)clay\text{-}Fe(II)aq} = +1.31‰$, comparable with the extent of fractionation during oxidation of $Fe(II)_{aq}$ and $Fe(III)_{oxides}$ precipitation (Wu et al., 2019; Dauphas and Rouxel, 2006; Johnson et al., 2002; Johnson and Beard, 2004).

Table 4-3 Martian analog clay $^{56}Fe/^{54}Fe$ β coefficients derived from NRIXS, based on the phonon excitation probability density, *S(E)* , or the phonon density of states, *g(E)* .

	CCa-1	CHLCLV1	MUGPLA1B
From S			
$1000 \ln \beta = A_1/T^2 + A_2/T^4 + A_3/T^6$ (T in K)			
A_1	5.420E+05±1.000E+05	7.203E+05±1.021E+5	7.615E+05±5.105E+04
A_2	-1.831E+09±1.619E+09	-3.978E+09±1.735E+09	-4.759E+09±6.844E+08
A_3	7.826E+12±4.321E+13	3.974E+13±4.869E+13	5.997E+13±1.551E+13
From g			
$1000 \ln \beta = A_1/T^2 + A_2/T^4 + A_3/T^6$ (T in K)			
A_1	5.420E+05	7.203E+05	7.632E+05
A_2	-1.828E+09	-3.965E+09	-4.860E+09
A_3	7.597E+12	3.815E+13	6.794E+13
Fe force constant (N/m)	189.9±35.0	252.4±35.8	266.9±17.9

Table 4-3 Martian analog clay $^{56}Fe/^{54}Fe$ β coefficients derived from NRIXS, based on the phonon excitation probability density, *S(E)* , or the phonon density of states, *g(E)* (continued).

	API-H33a	NAu-2	WASCDB1
From S			
$1000 \ln \beta = A_1/T^2 + A_2/T^4 + A_3/T^6$ (T in K)			
A_1	7.714E+05±6.853e+04	7.915E+05±6.269E+04	8.221E+05±1.247E+05
A_2	-4.688E+09±1.115E+09	-5.174E+09±1.315E+09	-6.022E+09±3.552E+09
A_3	6.063E+13±3.083E+13	7.700E+13±4.637E+13	1.194E+14±1.637E+14
From g			
$1000 \ln \beta = A_1/T^2 + A_2/T^4 + A_3/T^6$ (T in K)			
A_1	7.718E+05	7.916E+05	8.221E+05
A_2	-4.715E+09	-5.187E+09	-6.030E+09
A_3	6.326E+13	7.858E+13	1.206E+14
Fe force constant (N/m)	270.3±24.0	277.4±22.0	288.1±43.7

4.3 Terrestrial paleosol compilation

To better serve our goal of quantitatively constraining the redox condition during pedogenic processes on early Mars, we have constrained our paleosol compilation to paleosols formed:

1) before 1.85 Ga since they have witnessed major changes in surface conditions, notably the first rise in atmospheric oxygen during the Great Oxidation Event at 2.45-2.22 Ga (Bekker et al., 2004), and the complication introduced by Mn retention poses a smaller problem;

2) in the upper leached layer since Fe can reprecipitate in the lower part of soil profile, which can complicate interpretations, and because the upper layer is in direct contact with the atmosphere and O_2 transport in the soil column is less of a concern;

3) from basaltic parents whose Fe/Mn and Fe/Mg ratios are within 40% of the bulk silicate Earth values (Allègre et al., 1995; McDonough and Sun, 1995).

We retained 38 paleosols from 3 formations that fulfilled the above criteria and whose ages and chemical compositions are available in the literature (Table 4-4; Prasad and Roscoe, 1991; Yang and Holland, 2003; Babechuk and Kamber, 2013).

The secular evolutions of $(Fe/Mg)^*$, $(Fe/Mn)^*$, and $(Fe/Al)^*$ in paleosols are plotted in Figure 4-6, and the correlations between these ratios are plotted in Figure 4-7. A zeroth order expectation would be for iron to become more immobile as the atmosphere became oxygenated and iron was oxidized. The $(Fe/Al)^*$ ratio generally increases with younger paleosols, with 1.85 Ga paleosols centered around 1, indicating more Fe retention in younger (and more oxic) paleosols. The $(Fe/Mg)^*$ and $(Fe/Mn)^*$ ratios show larger variations compared to $(Fe/Al)^*$ and the 2.45 Ga paleosols generally have ratios closer to 1 and smaller than 2.2 and 1.85 Ga paleosols, indicating

less fractionation between Fe and Mg or Mn in the more anoxic pre-GOE paleosols. The 2.2 Ga paleosols have the highest (Fe/Mg)* and (Fe/Mn)* ratios, consistent with high level of Fe retention and Mn as well as Mg loss during the GOE.

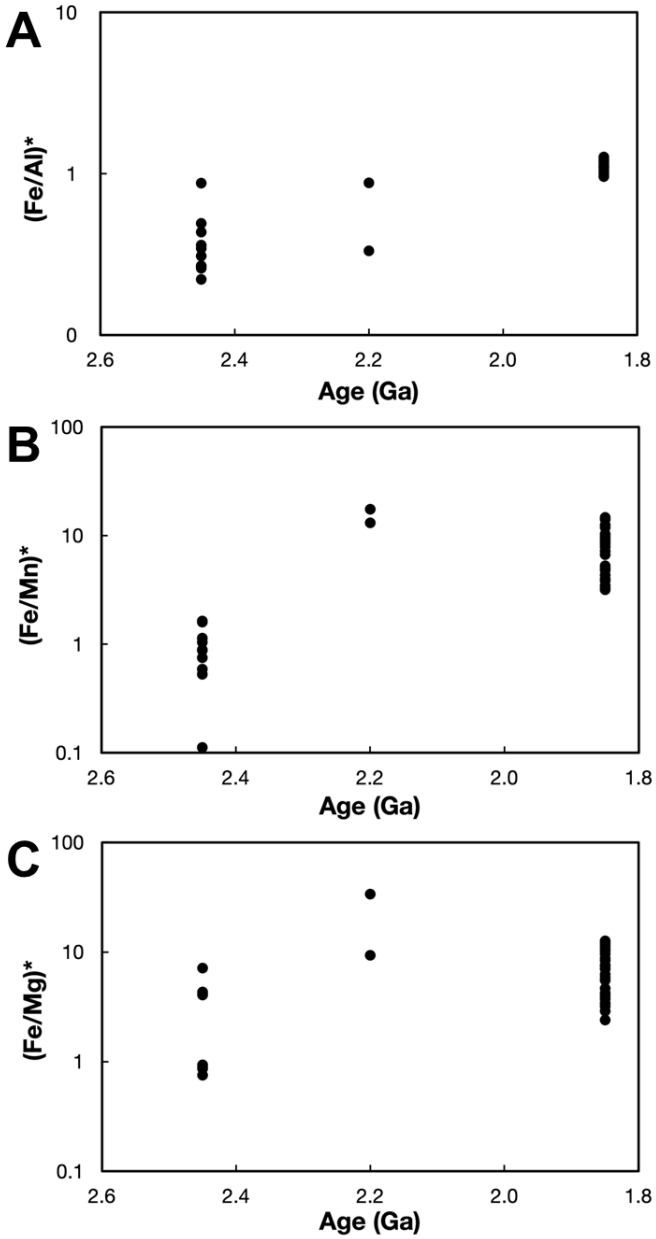

Figure 4-6 Secular evolution of (A) (Fe/Al)*, (B) (Fe/Mn)*, and (C) (Fe/Mg)* of compiled paleosols.

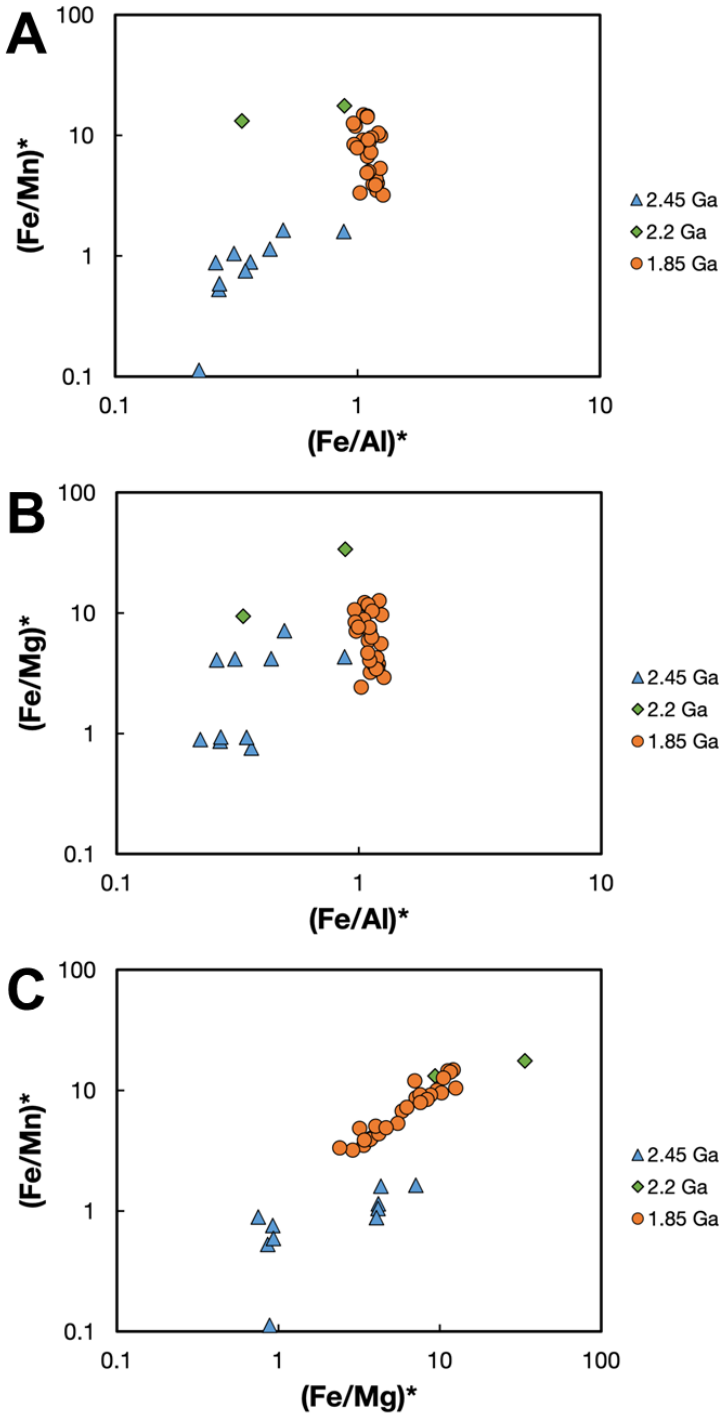

Figure 4-7 Correlation between Fe mobilization (Fe/Al)* and (Fe/Mn)* (A), (Fe/Mg)* (B) of compiled paleosols grouped by formation age. (C) shows the correlation between (Fe/Mn)* and (Fe/Mg)* of compiled paleosols.

Table 4-4 Major element compositions of >1.8 Ga paleosols and their parent basaltic rocks.

	Age	SiO_2 (wt%)	TiO_2 (wt%)	Al_2O_3 (wt%)	Fe_2O_{3T} (wt%)	MnO (wt%)	MgO (wt%)	CaO (wt%)
Quirke II DH-269 diabase[a]		**44.20**	**2.43**	**16.95**	**19.72**	**0.25**	**2.34**	**4.58**
6	2.45	43.20	4.05	27.30	8.50	0.20	1.17	1.24
7		42.70	3.31	25.60	10.74	0.15	1.69	2.15
8		43.5	4.63	28.1	7.25	0.8	0.97	1.22
Quirke II DH-268 diabase[a]		**48.88**	**1.93**	**13.08**	**13.52**	**0.27**	**4.78**	**5.99**
44	2.45	51.60	2.72	17.70	16.01	0.20	1.31	0.79
45		40.00	4.07	26.70	12.00	0.21	1.02	1.00
46		42.20	4.34	27.90	8.90	0.17	0.76	1.26
47		38.30	4.05	25.70	13.10	0.16	0.65	0.83
48		42.90	4.52	29.60	7.93	0.18	0.69	0.21
Quirke II DH-270 diabase[a]		**47.60**	**2.16**	**15.70**	**18.15**	**0.21**	**2.20**	**3.26**
67	2.45	46.40	2.94	24.40	9.71	0.15	1.27	0.87
68		43.70	3.45	27.70	8.62	0.17	1.12	0.65
Hekpoort basalt[b]		**59.35**	**0.63**	**14.26**	**10.76**	**0.18**	**6.40**	**4.89**
99WY17a	2.20	38.90	1.34	31.61	20.98	0.02	0.37	0.18
99WY26		55.02	1.35	31.26	7.86	0.01	0.50	0.14

Table 4-4 Major element compositions of >1.8 Ga paleosols and their parent basaltic rocks (continued).

	Na_2O (wt%)	K_2O (wt%)	P_2O_5 (wt%)	Total	LOI	(Fe/Mn)*	(Fe/Mg)*	(Fe/Al)*
Quirke II DH-269 diabase[a]	**2.20**	**3.52**	**0.50**	**98.70**		**73.17**	**9.83**	**1.54**
6	0.10	9.63	0.49	100.00		0.53	0.86	0.27
7	0.10	8.10	0.63	99.60		0.89	0.75	0.36
8	0.2	10.07	0.17	100.3		0.11	0.89	0.22
Quirke II DH-268 diabase[a]	**3.30**	**1.33**	**0.35**	**99.33**		**45.52**	**3.30**	**1.37**
44	0.20	4.51	0.48	99.60		1.60	4.32	0.88
45	0.20	9.06	0.68	99.30		1.14	4.16	0.43
46	0.20	9.95	0.79	100.50		1.05	4.14	0.31
47	0.20	9.02	0.50	98.30		1.64	7.13	0.49
48	0.20	10.18	0.12	100.70		0.88	4.06	0.26
Quirke II DH-270 diabase[a]	**1.36**	**4.12**	**0.68**	**99.93**		**78.12**	**9.63**	**1.53**
67	0.00	8.75	0.63	99.70		0.75	0.93	0.34
68	0.12	9.96	0.44	100.30		0.59	0.93	0.27
Hekpoort basalt[b]	**2.51**	**0.64**	**0.10**	**99.77**	**5.33**	**54.34**	**1.96**	**1.00**
99WY17a	1.07	4.41	0.17	99.07	5.62	17.55	33.73	0.88
99WY26	0.55	3.09	0.06	99.84	6.11	13.15	9.35	0.33

Table 4-4 Major element compositions of >1.8 Ga paleosols and their parent basaltic rocks (continued).

	Age	SiO_2 (wt%)	TiO_2 (wt%)	Al_2O_3 (wt%)	Fe_2O_{3T} (wt%)	MnO (wt%)	MgO (wt%)	CaO (wt%)
Flin Flon hydrothermally altered basalt[c]		**44.20**	**0.58**	**14.10**	**12.05**	**0.24**	**4.85**	**9.81**
FF021A-001	1.85	52.30	1.55	18.10	17.30	0.07	2.18	0.43
FF021A-002		65.30	0.78	14.60	12.20	0.02	0.70	0.28
FF021A-003		63.70	0.81	14.60	13.70	0.04	0.94	0.61
FF021A-005		57.70	0.90	15.90	16.40	0.08	1.75	0.52
FF021A-007		58.40	0.90	15.70	16.10	0.09	1.91	0.50
FF021A-009		58.60	0.89	15.00	16.30	0.10	2.26	0.54
FF021A-010		57.60	0.88	16.20	16.00	0.08	1.73	0.51
FF021A-011		60.00	0.95	16.70	15.10	0.02	0.50	0.23
FF021A-014		60.60	0.87	15.80	14.80	0.02	0.53	0.63
FF021A-016/017		53.90	0.96	17.50	17.80	0.08	1.70	0.57
FF021A-018		53.30	0.99	17.60	17.80	0.09	2.09	0.58
FF021A-020		59.90	0.85	15.40	16.30	0.06	1.19	0.48
FF021A-023		62.00	0.81	14.40	15.30	0.03	0.64	0.54
FF021A-027		60.50	0.84	15.40	16.00	0.03	0.51	0.54
FF021A-030		61.20	0.86	15.50	14.50	0.02	0.50	0.53
FF021A-035		62.30	0.83	15.00	14.60	0.03	0.57	0.54
FF021A-037		64.30	0.21	14.00	13.30	0.03	0.75	0.58
FF021B-039		61.50	0.90	15.60	14.00	0.03	0.64	0.47
FF021B-043		61.60	0.85	15.30	14.80	0.04	0.95	0.47
FF021B-046		61.80	0.83	14.90	14.10	0.03	0.75	0.56
FF021B-049		57.00	0.89	16.20	15.40	0.06	1.54	1.02
FF021B-052		62.70	0.87	15.70	12.90	0.02	0.49	0.50
FF021B-054/055		63.20	0.86	15.60	12.90	0.03	0.62	0.59
FF021B-057		61.90	0.75	13.60	11.90	0.07	1.99	2.06
FF021B-058		65.50	0.82	14.20	12.10	0.03	0.64	0.60
FF021B-059		66.00	0.75	13.40	12.50	0.05	1.08	0.58

Table 4-4 Major element compositions of >1.8 Ga paleosols and their parent basaltic rocks (continued).

	Na_2O (wt%)	K_2O (wt%)	P_2O_5 (wt%)	Total	LOI	(Fe/Mn)*	(Fe/Mg)*	(Fe/Al)*
Flin Flon hydrothermally altered basalt[c]	**2.86**	**0.37**	**0.06**	**99.65**	**10.54**	**46.62**	**2.90**	**1.13**
FF021A-001	1.34	1.74	0.28	98.40	3.19	4.82	3.19	1.12
FF021A-002	1.20	2.29	0.19	99.90	2.35	11.90	7.01	0.98
FF021A-003	1.14	2.29	0.44	100.90	2.55	6.68	5.86	1.10
FF021A-005	1.11	2.26	0.36	100.40	3.30	4.00	3.77	1.21
FF021A-007	1.07	2.10	0.36	100.40	3.30	3.49	3.39	1.20
FF021A-009	0.95	1.87	0.37	100.20	3.38	3.18	2.90	1.27
FF021A-010	1.16	2.17	0.36	100.00	3.31	3.90	3.72	1.16
FF021A-011	1.52	2.73	0.15	100.70	2.72	14.72	12.14	1.06
FF021A-014	1.42	2.56	0.45	100.30	2.61	14.43	11.23	1.10
FF021A-016/017	1.25	2.50	0.40	100.20	3.52	4.34	4.21	1.19
FF021A-018	1.21	2.37	0.42	100.10	3.68	3.86	3.42	1.18
FF021A-020	1.11	2.32	0.34	100.70	2.87	5.30	5.51	1.24
FF021A-023	1.22	2.34	0.38	100.20	2.50	9.95	9.61	1.24
FF021A-027	1.32	2.58	0.38	100.60	2.51	10.40	12.61	1.22
FF021A-030	1.31	2.69	0.38	100.10	2.61	14.14	11.66	1.09
FF021A-035	1.26	2.61	0.36	100.70	2.54	9.49	10.30	1.14
FF021A-037	1.10	2.44	0.34	100.20	2.59	8.65	7.13	1.11
FF021B-039	1.35	2.59	0.34	100.10	2.63	9.10	8.80	1.05
FF021B-043	1.25	2.35	0.33	100.70	2.80	7.22	6.26	1.13
FF021B-046	1.27	2.41	0.31	99.70	2.75	9.17	7.56	1.11
FF021B-049	1.27	2.49	0.34	100.00	3.90	5.01	4.02	1.11
FF021B-052	1.35	2.71	0.35	100.10	2.51	12.58	10.59	0.96
FF021B-054/055	1.30	2.63	0.36	100.70	2.70	8.39	8.37	0.97
FF021B-057	0.97	2.17	0.35	100.90	5.15	3.32	2.40	1.02
FF021B-058	1.22	2.31	0.35	100.30	2.55	7.87	7.60	1.00
FF021B-059	0.99	2.14	0.27	100.60	2.80	4.88	4.65	1.09

[a] Prasad and Roscoe, 1991; [b] Yang and Holland, 2003; [c] Babechuk and Kamber, 2013.

4.4 Alteration model

To help guide interpretations and outline expectations in a quantitative manner, we have developed a simple alteration model to describe the mobilization, oxidation, and isotopic fractionation of iron relative to other minerals. We recognize that weathering in natural settings is a complex process, but the goal of the model is to assess how one can parameterize Fe/Mn and δ^{56}Fe fractionations depending on alteration conditions.

Murakami et al. (2011), Yokota et al. (2013), and Kanzaki and Murakami (2016) used iron oxidation kinetics in paleosols to constrain past atmospheric pO_2. We use a similar approach and expand it to include Fe isotopic fractionation and Mn oxidation kinetics to try to use Fe isotopic fractionation and Fe/Mn ratios as tracers of past redox conditions. The rationale for doing so is that the combined use of those two proxies together may provide constraints on redox conditions for samples for which the geological context is not as well constrained as paleosols. Recognizing that key parameters such as Mn oxidation kinetics are uncertain and the fact that it is a first pass on this question, we use a model of intermediate complexity more similar to that used by Kanzaki and Murakami (2016), Another virtue of using such a simplified model is that it is amenable to resolution through analytical equations.

We consider a system of total volume V composed initially of parent material and water. In the following, we use crystalline basalt consisting mostly of olivine, pyroxene, and plagioclase as the parent material to represent Mars' basaltic upper crust (Ehlmann and Edwards, 2014). However, the final equations are independent of the type of mineral being dissolved and can be applied to terrestrial systems using independently constrained paleosol data as anchors to fit some of the model parameters. As alteration proceeds, the basalt dissolves and Fe^{2+} is either oxidized to

precipitate as Fe^{3+} in the residue or advected away as dissolved Fe^{2+}. The model outlined below neglects Fe/Mn and $^{56}Fe/^{54}Fe$ fractionation during basalt dissolution to focus on larger fractionations associated with iron-oxidation. This means that the Fe/Mn and $^{56}Fe/^{54}Fe$ ratios of the basalt remain unchanged. The rate of Fe release from crystalline basalt is dominated by the dissolution of its three major minerals (olivine – ol, pyroxene – py, and plagioclase – pg) and can be approximated by (Gudbrandsson et al., 2011),

$$R_{\text{Fe-diss}}(\text{mol.cm}^{-2}.s^{-1}) = f_{\text{S,ol}} v_{\text{Fe,ol}} R_{\text{ol}} + f_{\text{S,py}} v_{\text{Fe,py}} R_{\text{py}} + f_{\text{S,pg}} v_{\text{Fe,pg}} R_{\text{pg}}, \quad \text{(Eq. 4-4)}$$

where $f_{\text{S,x}}$ is the relative reactive surface area of x mineral in contact with water, $v_{\text{Fe,x}}$ is the stoichiometric number of Fe in x mineral, and R_{x} is the dissolution rate of x mineral normalized to its specific surface area.

During an increment of time dt, the amount of Fe dissolved is,

$$d\text{Fe}_{\text{dissolution}} = R_{\text{Fe-diss}} S dt, \quad \text{(Eq. 4-5)}$$

where S is the total surface area of crystalline basalt. As alteration proceeds, the total surface area of basalt can change but as a first approximation, we assume that it remains constant and we write,

$$d\text{Fe}_{\text{dissolution}} = R_{\text{Fe-diss}} \sigma V dt, \quad \text{(Eq. 4-6)}$$

where σ is the basalt surface area per unit volume of solid and liquid (in m^{-1}), which is assumed to remain constant.

For natural freshwaters in the pH range 6.5-7.5 and temperature range 5-35 °C, the rate of iron oxidation per unit volume of liquid is (Davison and Seed, 1983),

$$R_{\text{Fe-ox}}\left(\text{mol.L}^{-1}.s^{-1}\right) = 3.33 \times 10^{2\text{pH}-17} P_{O_2} \left[Fe^{2+}\right]_{\text{aq}} = k_{\text{Fe-ox}} \left[Fe^{2+}\right]_{\text{aq}}. \quad \text{(Eq. 4-7)}$$

The amount of Fe oxidized and precipitated as Fe-oxyhydroxide during dt is,

$$d\mathrm{Fe}_{\mathrm{oxidation}} = R_{\mathrm{Fe\text{-}ox}} V\Phi dt = k_{\mathrm{Fe\text{-}ox}}\left[\mathrm{Fe}^{2+}\right]_{\mathrm{aq}} V\Phi dt, \quad \text{(Eq. 4-8)}$$

where Φ is porosity and $V\Phi$ is the liquid volume. Some Fe avoids oxidation and is advected away. We assume that water flowing in the system is pure and the rate of liquid removal per unit time is F (the residence time of water in the system is $\tau = V/F$). The amount of Fe advected away per unit time is,

$$d\mathrm{Fe}_{\mathrm{advection}} = \left[\mathrm{Fe}^{2+}\right]_{\mathrm{aq}} Fdt = \left[\mathrm{Fe}^{2+}\right]_{\mathrm{aq}} Vdt/\tau, \quad \text{(Eq. 4-9)}$$

At steady-state, Fe dissolution is balanced by oxidation and advection,

$$d\mathrm{Fe}_{\mathrm{dissolution}} = d\mathrm{Fe}_{\mathrm{oxidation}} + d\mathrm{Fe}_{\mathrm{advection}}, \quad \text{(Eq. 4-10)}$$

$$R_{\mathrm{Fe\text{-}diss}}\sigma Vdt = k_{\mathrm{Fe\text{-}ox}}\left[\mathrm{Fe}^{2+}\right]_{\mathrm{aq}} V\Phi dt + \left[\mathrm{Fe}^{2+}\right]_{\mathrm{aq}} V/\tau dt. \quad \text{(Eq. 4-11)}$$

We therefore have,

$$\left[\mathrm{Fe}^{2+}\right]_{\mathrm{aq}} = \frac{R_{\mathrm{Fe\text{-}diss}}\sigma}{k_{\mathrm{Fe\text{-}ox}}\Phi + 1/\tau}. \quad \text{(Eq. 4-12)}$$

The amount of Fe being preserved in the residue (basalt + solution) is therefore,

$$d\mathrm{Fe}_{\mathrm{residue}} = -d\mathrm{Fe}_{\mathrm{advection}} = -\frac{R_{\mathrm{Fe\text{-}diss}}\sigma}{1 + k_{\mathrm{Fe\text{-}ox}}\Phi\tau} Vdt, \quad \text{(Eq. 4-13)}$$

$$d[\mathrm{Fe}]_{\mathrm{residue}} = -\frac{R_{\mathrm{Fe\text{-}diss}}\sigma}{1 + k_{\mathrm{Fe\text{-}ox}}\Phi\tau} dt. \quad \text{(Eq. 4-14)}$$

We assume that Mn^{2+} behaves identically to Fe^{2+} during mineral dissolution (Krauskopf 1957),

$$d\mathrm{Mn}_{\mathrm{dissolution}} = (\mathrm{Mn/Fe})_{\mathrm{basalt}} R_{\mathrm{Fe\text{-}diss}}\sigma Vdt. \quad \text{(Eq. 4-15)}$$

Dissolved Mn can be removed via advection, which does not fractionate the Mn/Fe ratio, and we have,

$$d\mathrm{Mn}_{\mathrm{advection}} = \left[\mathrm{Mn}^{2+}\right]_{\mathrm{aq}} Vdt/\tau. \quad \text{(Eq. 4-16)}$$

Here we assume that as long as all iron is not quantitatively oxidized, Mn remains mobile as Mn^{2+}, and most Mn dissolved would be advected away. Then at steady state, Mn dissolution is balanced by advection,

$$d\mathrm{Mn}_{\mathrm{dissolution}} = d\mathrm{Mn}_{\mathrm{advection}}. \quad \text{(Eq. 4-17)}$$

$$(\mathrm{Mn/Fe})_{\mathrm{basalt}} R_{\mathrm{Fe\text{-}diss}} \sigma V dt = \left[\mathrm{Mn}^{2+}\right]_{\mathrm{aq}} V dt/\tau.$$

We therefore have,

$$\left[\mathrm{Mn}^{2+}\right]_{\mathrm{aq}} = (\mathrm{Mn/Fe})_{\mathrm{basalt}} R_{\mathrm{Fe\text{-}diss}} \sigma\tau. \quad \text{(Eq. 4-18)}$$

Introducing Eq. 4-12, we have,

$$\frac{(\mathrm{Fe/Mn})_{\mathrm{aq}}}{(\mathrm{Fe/Mn})_{\mathrm{basalt}}} = \frac{1}{1+k_{\mathrm{Fe\text{-}ox}}\Phi\tau}. \quad \text{(Eq. 4-19)}$$

The amount of Mn being preserved in the residue (basalt + solution) is therefore,

$$d\mathrm{Mn}_{\mathrm{residue}} = -d\mathrm{Mn}_{\mathrm{advection}} = -(\mathrm{Mn/Fe})_{\mathrm{basalt}} R_{\mathrm{Fe\text{-}diss}} \sigma V dt, \quad \text{(Eq. 4-20)}$$

$$d[\mathrm{Mn}]_{\mathrm{residue}} = -(\mathrm{Mn/Fe})_{\mathrm{basalt}} R_{\mathrm{Fe\text{-}diss}} \sigma dt. \quad \text{(Eq. 4-21)}$$

We are interested in tracking the evolution of Fe/Mn ratio in the residue, so by combing Eqs. 4-14 and 4-21,

$$d[\mathrm{Mn}]_{\mathrm{residue}} = (\mathrm{Mn/Fe})_{\mathrm{basalt}}(1 + k_{\mathrm{Fe\text{-}ox}}\Phi\tau) d[\mathrm{Fe}]_{\mathrm{residue}}, \quad \text{(Eq. 4-22)}$$

$$d\ln[\mathrm{Mn}]_{\mathrm{residue}} = \frac{(\mathrm{Fe/Mn})_{\mathrm{residue}}}{(\mathrm{Fe/Mn})_{\mathrm{basalt}}}(1 + k_{\mathrm{Fe\text{-}ox}}\Phi\tau) d\ln[\mathrm{Fe}]_{\mathrm{residue}}. \quad \text{(Eq. 4-23)}$$

Additionally, we can write,

$$d\ln\frac{(\mathrm{Fe/Mn})_{\mathrm{residue}}}{(\mathrm{Fe/Mn})_{\mathrm{basalt}}} = d\ln(\mathrm{Fe/Mn})_{\mathrm{residue}} = d\ln[\mathrm{Fe}]_{\mathrm{residue}} - d\ln[\mathrm{Mn}]_{\mathrm{residue}}. \quad \text{(Eq. 4-24)}$$

We note $f_{\mathrm{Mn}} = [\mathrm{Mn}]_{\mathrm{residue}}/[\mathrm{Mn}]_{\mathrm{basalt}}$. Because $d\ln[\mathrm{Mn}]_{\mathrm{basalt}} = 0$, we can write $d\ln[\mathrm{Mn}]_{\mathrm{residue}} = d\ln([\mathrm{Mn}]_{\mathrm{residue}}/[\mathrm{Mn}]_{\mathrm{basalt}}) = d\ln f_{\mathrm{Mn}}$.

Combining Eqs. 4-23 and 4-24, we have,

$$d\ln\frac{(\mathrm{Fe/Mn})_{\mathrm{residue}}}{(\mathrm{Fe/Mn})_{\mathrm{basalt}}} = \left(\frac{(\mathrm{Fe/Mn})_{\mathrm{basalt}}}{(\mathrm{Fe/Mn})_{\mathrm{residue}}}\frac{1}{1+k_{\text{Fe-ox}}\Phi\tau} - 1\right) d\ln f_{\mathrm{Mn}}, \quad \text{(Eq. 4-25)}$$

$$d\,\frac{(\mathrm{Fe/Mn})_{\mathrm{residue}}}{(\mathrm{Fe/Mn})_{\mathrm{basalt}}} = -\left(\frac{(\mathrm{Fe/Mn})_{\mathrm{residue}}}{(\mathrm{Fe/Mn})_{\mathrm{basalt}}} - \frac{1}{1+k_{\text{Fe-ox}}\Phi\tau}\right) d\ln f_{\mathrm{Mn}}, \quad \text{(Eq. 4-26)}$$

$$d\left(\frac{(\mathrm{Fe/Mn})_{\mathrm{residue}}}{(\mathrm{Fe/Mn})_{\mathrm{basalt}}} - \frac{1}{1+k_{\text{Fe-ox}}\Phi\tau}\right) = -\left(\frac{(\mathrm{Fe/Mn})_{\mathrm{residue}}}{(\mathrm{Fe/Mn})_{\mathrm{basalt}}} - \frac{1}{1+k_{\text{Fe-ox}}\Phi\tau}\right) d\ln f_{\mathrm{Mn}}, \quad \text{(Eq. 4-27)}$$

$$d\ln\left(\frac{(\mathrm{Fe/Mn})_{\mathrm{residue}}}{(\mathrm{Fe/Mn})_{\mathrm{basalt}}} - \frac{1}{1+k_{\text{Fe-ox}}\Phi\tau}\right) = d\ln\frac{1}{f_{\mathrm{Mn}}}, \quad \text{(Eq. 4-28)}$$

$$\ln\left(\frac{(\mathrm{Fe/Mn})_{\mathrm{residue}}}{(\mathrm{Fe/Mn})_{\mathrm{basalt}}} - \frac{1}{1+k_{\text{Fe-ox}}\Phi\tau}\right) = \ln\frac{1}{f_{\mathrm{Mn}}} + C, \quad \text{(Eq. 4-29)}$$

$$\frac{(\mathrm{Fe/Mn})_{\mathrm{residue}}}{(\mathrm{Fe/Mn})_{\mathrm{basalt}}} - \frac{1}{1+k_{\text{Fe-ox}}\Phi\tau} = \frac{e^C}{f_{\mathrm{Mn}}}. \quad \text{(Eq. 4-30)}$$

Since $\frac{(\mathrm{Fe/Mn})_{\mathrm{residue}}}{(\mathrm{Fe/Mn})_{\mathrm{basalt}}} = f_{\mathrm{Mn}} = 1$ when alteration begins, $e^C = \frac{k_{\text{Fe-ox}}\Phi\tau}{1+k_{\text{Fe-ox}}\Phi\tau}$, and Eq. 4-30 becomes,

$$(\mathrm{Fe/Mn})^* = \frac{(\mathrm{Fe/Mn})_{\mathrm{residue}}}{(\mathrm{Fe/Mn})_{\mathrm{basalt}}} = \frac{(k_{\text{Fe-ox}}\Phi\tau)/f_{\mathrm{Mn}}+1}{1+k_{\text{Fe-ox}}\Phi\tau}. \quad \text{(Eq. 4-31)}$$

We now examine Fe isotopic fractionation during dissolution-oxidation-advection. We assume that basalt dissolution induces no Fe isotopic fractionation, but Fe oxidation and precipitation does, with an isotopic fractionation factor (Dauphas and Rouxel, 2006),

$$\alpha_{\text{ox-aq}} = \frac{\left({}^{56}\mathrm{Fe}/{}^{54}\mathrm{Fe}\right)_{\mathrm{aq}\rightarrow\mathrm{ox}}}{\left({}^{56}\mathrm{Fe}/{}^{54}\mathrm{Fe}\right)_{\mathrm{aq}}}. \quad \text{(Eq. 4-32)}$$

Changes in the isotopic composition of the residue is mass-balanced by advection of isotopically fractionated iron,

$$d\left[\left(\frac{{}^{56}\mathrm{Fe}}{{}^{54}\mathrm{Fe}}\right)_{\mathrm{residue}}\left(\frac{\mathrm{Fe}}{\mathrm{Mn}}\right)_{\mathrm{residue}}\mathrm{Mn}_{\mathrm{residue}}\right] = -\left(\frac{{}^{56}\mathrm{Fe}}{{}^{54}\mathrm{Fe}}\right)_{\mathrm{aq}} d\mathrm{Fe}_{\mathrm{advection}} \quad \text{(Eq. 4-33)}$$

$$= -\left(\frac{{}^{56}\mathrm{Fe}}{{}^{54}\mathrm{Fe}}\right)_{\mathrm{aq}}\left(\frac{\mathrm{Fe}}{\mathrm{Mn}}\right)_{\mathrm{aq}} d\mathrm{Mn}_{\mathrm{advection}}$$

$= \left(\frac{^{56}\mathrm{Fe}}{^{54}\mathrm{Fe}}\right)_{\mathrm{aq}} \left(\frac{\mathrm{Fe}}{\mathrm{Mn}}\right)_{\mathrm{aq}} d\mathrm{Mn}_{\mathrm{residue}}$.

Dividing both sides by $\left(^{56}\mathrm{Fe}/^{54}\mathrm{Fe}\right)_{\mathrm{residue}}(\mathrm{Fe/Mn})_{\mathrm{residue}}\mathrm{Mn}_{\mathrm{residue}}$ and rearranging, we have,

$$d\ln\left(\frac{^{56}\mathrm{Fe}}{^{54}\mathrm{Fe}}\right)_{\mathrm{residue}} = \frac{\left(^{56}\mathrm{Fe}/^{54}\mathrm{Fe}\right)_{\mathrm{aq}}}{\left(^{56}\mathrm{Fe}/^{54}\mathrm{Fe}\right)_{\mathrm{residue}}} \frac{(\mathrm{Fe/Mn})_{\mathrm{aq}}}{(\mathrm{Fe/Mn})_{\mathrm{residue}}} d\ln\mathrm{Mn}_{\mathrm{residue}} - d\ln\left(\frac{\mathrm{Fe}}{\mathrm{Mn}}\right)_{\mathrm{residue}} - \quad \text{(Eq. 4-34)}$$

$d\ln\mathrm{Mn}_{\mathrm{residue}}$.

Given Eq. 4-25 and $d\ln[\mathrm{Mn}]_{\mathrm{residue}} = d\ln f_{\mathrm{Mn}}$, it follows,

$$d\ln\left(\frac{^{56}\mathrm{Fe}}{^{54}\mathrm{Fe}}\right)_{\mathrm{residue}} = \left[\frac{\left(^{56}\mathrm{Fe}/^{54}\mathrm{Fe}\right)_{\mathrm{aq}}}{\left(^{56}\mathrm{Fe}/^{54}\mathrm{Fe}\right)_{\mathrm{residue}}} \frac{(\mathrm{Fe/Mn})_{\mathrm{aq}}}{(\mathrm{Fe/Mn})_{\mathrm{residue}}} - \frac{(\mathrm{Fe/Mn})_{\mathrm{basalt}}}{(\mathrm{Fe/Mn})_{\mathrm{residue}}} \frac{1}{1+k_{\text{Fe-ox}}\Phi\tau}\right] d\ln f_{\mathrm{Mn}}. \quad \text{(Eq. 4-35)}$$

Given Eq. 4-19, it follows,

$$d\ln\left(\frac{^{56}\mathrm{Fe}}{^{54}\mathrm{Fe}}\right)_{\mathrm{residue}} = \left[\frac{\left(^{56}\mathrm{Fe}/^{54}\mathrm{Fe}\right)_{\mathrm{aq}}}{\left(^{56}\mathrm{Fe}/^{54}\mathrm{Fe}\right)_{\mathrm{residue}}} - 1\right] \frac{(\mathrm{Fe/Mn})_{\mathrm{basalt}}}{(\mathrm{Fe/Mn})_{\mathrm{residue}}} \frac{1}{1+k_{\text{Fe-ox}}\Phi\tau} d\ln f_{\mathrm{Mn}}. \quad \text{(Eq. 4-36)}$$

The isotopic mass balance for dissolved iron is,

$$d\left[\left(\frac{^{56}\mathrm{Fe}}{^{54}\mathrm{Fe}}\right)_{\mathrm{aq}} \mathrm{Fe}_{\mathrm{aq}}\right] = \left(\frac{^{56}\mathrm{Fe}}{^{54}\mathrm{Fe}}\right)_{\mathrm{basalt}} d\mathrm{Fe}_{\mathrm{dissolution}} - \left(\frac{^{56}\mathrm{Fe}}{^{54}\mathrm{Fe}}\right)_{\mathrm{aq}} d\mathrm{Fe}_{\mathrm{advection}} - \quad \text{(Eq. 4-37)}$$

$\left(\frac{^{56}\mathrm{Fe}}{^{54}\mathrm{Fe}}\right)_{\mathrm{aq}\rightarrow\mathrm{ox}} d\mathrm{Fe}_{\mathrm{oxidation}}$.

At steady-state $d\left[\left(^{56}\mathrm{Fe}/^{54}\mathrm{Fe}\right)_{\mathrm{aq}}\mathrm{Fe}_{\mathrm{aq}}\right] = 0$. Injecting instantaneous isotopic fractionation factors in the steady-state relationship we have,

$$0 = \left(\frac{^{56}\mathrm{Fe}}{^{54}\mathrm{Fe}}\right)_{\mathrm{basalt}} d\mathrm{Fe}_{\mathrm{dissolution}} - \left(\frac{^{56}\mathrm{Fe}}{^{54}\mathrm{Fe}}\right)_{\mathrm{aq}} d\mathrm{Fe}_{\mathrm{advection}} - \alpha_{\text{ox-aq}} \left(\frac{^{56}\mathrm{Fe}}{^{54}\mathrm{Fe}}\right)_{\mathrm{aq}} d\mathrm{Fe}_{\mathrm{oxidation}}. \quad \text{(Eq. 4-38)}$$

Given Eqs. 4-6, 4-8 and 4-9, it follows,

$$\left(\frac{^{56}\mathrm{Fe}}{^{54}\mathrm{Fe}}\right)_{\mathrm{aq}} = \frac{\left(^{56}\mathrm{Fe}/^{54}\mathrm{Fe}\right)_{ol} d\mathrm{Fe}_{\mathrm{dissolution}}}{d\mathrm{Fe}_{\mathrm{advection}} + \alpha_{\text{ox-aq}} d\mathrm{Fe}_{\mathrm{oxidation}}} \quad \text{(Eq. 4-39)}$$

$$= \frac{\left(^{56}\mathrm{Fe}/^{54}\mathrm{Fe}\right)_{ol} R_{\text{Fe-diss}}\sigma}{\left[\mathrm{Fe}^{2+}\right]_{\mathrm{aq}}/\tau + \alpha_{\text{ox-aq}} k_{\text{Fe-ox}} \left[\mathrm{Fe}^{2+}\right]_{\mathrm{aq}} \Phi}.$$

Given Eq. 4-12, it follows,

$$\left(\frac{^{56}\mathrm{Fe}}{^{54}\mathrm{Fe}}\right)_{\mathrm{aq}} \Big/ \left(\frac{^{56}\mathrm{Fe}}{^{54}\mathrm{Fe}}\right)_{\mathrm{basalt}} = \frac{1 + k_{\text{Fe-ox}}\Phi\tau}{1 + \alpha_{\text{ox-aq}} k_{\text{Fe-ox}}\Phi\tau}. \quad \text{(Eq. 4-40)}$$

Eq. 4-36 can then be rewritten as,

$$d\ln\left(\frac{^{56}\mathrm{Fe}}{^{54}\mathrm{Fe}}\right)_{\mathrm{residue}} = \left[\frac{\left(^{56}\mathrm{Fe}/^{54}\mathrm{Fe}\right)_{\mathrm{aq}}}{\left(^{56}\mathrm{Fe}/^{54}\mathrm{Fe}\right)_{\mathrm{basalt}}} \frac{\left(^{56}\mathrm{Fe}/^{54}\mathrm{Fe}\right)_{\mathrm{basalt}}}{\left(^{56}\mathrm{Fe}/^{54}\mathrm{Fe}\right)_{\mathrm{residue}}} - \right. \quad \text{(Eq. 4-41)}$$

$$\left. 1\right] \frac{(\mathrm{Fe/Mn})_{\mathrm{basalt}}}{(\mathrm{Fe/Mn})_{\mathrm{residue}}} \frac{1}{1 + k_{\text{Fe-ox}}\Phi\tau} d\ln f_{\mathrm{Mn}}$$

$$= \left[\frac{1 + k_{\text{Fe-ox}}\Phi\tau}{1 + \alpha_{\text{ox-aq}} k_{\text{Fe-ox}}\Phi\tau} \frac{\left(^{56}\mathrm{Fe}/^{54}\mathrm{Fe}\right)_{\mathrm{basalt}}}{\left(^{56}\mathrm{Fe}/^{54}\mathrm{Fe}\right)_{\mathrm{residue}}} - 1\right] \frac{(\mathrm{Fe/Mn})_{\mathrm{basalt}}}{(\mathrm{Fe/Mn})_{\mathrm{residue}}} \frac{1}{1 + k_{\text{Fe-ox}}\Phi\tau} d\ln f_{\mathrm{Mn}}.$$

Injecting Eq. 4-31 in this formula, we have,

$$d\ln\left(\frac{^{56}\mathrm{Fe}}{^{54}\mathrm{Fe}}\right)_{\mathrm{residue}} = \left[\frac{1 + k_{\text{Fe-ox}}\Phi\tau}{1 + \alpha_{\text{ox-aq}} k_{\text{Fe-ox}}\Phi\tau} \frac{\left(^{56}\mathrm{Fe}/^{54}\mathrm{Fe}\right)_{\mathrm{basalt}}}{\left(^{56}\mathrm{Fe}/^{54}\mathrm{Fe}\right)_{\mathrm{residue}}} - 1\right] \frac{1}{f_{\mathrm{Mn}} + k_{\text{Fe-ox}}\Phi\tau} df_{\mathrm{Mn}}. \quad \text{(Eq. 4-42)}$$

Given $\delta_{\mathrm{residue}} = \left[\left(^{56}\mathrm{Fe}/^{54}\mathrm{Fe}\right)_{\mathrm{residue}} / \left(^{56}\mathrm{Fe}/^{54}\mathrm{Fe}\right)_{\mathrm{basalt}} - 1\right] \times 1000$, it follows,

$$d\ln\left(\frac{^{56}\mathrm{Fe}}{^{54}\mathrm{Fe}}\right)_{\mathrm{residue}} = d\ln\left[\frac{\left(^{56}\mathrm{Fe}/^{54}\mathrm{Fe}\right)_{\mathrm{residue}}}{\left(^{56}\mathrm{Fe}/^{54}\mathrm{Fe}\right)_{\mathrm{basalt}}}\right] = \frac{d\delta_{\mathrm{residue}}}{\left[\frac{\left(^{56}Fe/^{54}Fe\right)_{\mathrm{residue}}}{\left(^{56}Fe/^{54}Fe\right)_{\mathrm{basalt}}}\right] \times 1000}. \quad \text{(Eq. 4-43)}$$

Given $\alpha_{\text{ox-aq}} = 1 + \Delta_{\text{ox-aq}}/1000$, Eq. 4-43 becomes,

$$d\delta_{\mathrm{residue}} = 1000\left[\frac{1 + k_{\text{Fe-ox}}\Phi\tau}{1 + (1 + \Delta_{\text{ox-aq}}/1000) k_{\text{Fe-ox}}\Phi\tau} - (1 + \delta_{\mathrm{residue}}/ \right. \quad \text{(Eq. 4-44)}$$

$$\left. 1000)\right] \frac{1}{f_{\mathrm{Mn}} + k_{\text{Fe-ox}}\Phi\tau} df_{\mathrm{Mn}}.$$

Because $\delta_{\text{residue}}/1000 \ll 1$ and $\Delta_{\text{ox-aq}}/1000 \ll 1$, we can approximate this expression using a Taylor series expansion truncated to the first order,

$$d\delta_{\text{residue}} = -\left(\frac{k_{\text{Fe-ox}}\Phi\tau}{1+k_{\text{Fe-ox}}\Phi\tau}\Delta_{\text{ox-aq}} + \delta_{\text{residue}}\right)\frac{1}{f_{\text{Mn}}+k_{\text{Fe-ox}}\Phi\tau}df_{\text{Mn}}, \quad \text{(Eq. 4-45)}$$

$$d(\delta_{\text{residue}} - \delta_{\text{basalt}}) = -\left(\frac{k_{\text{Fe-ox}}\Phi\tau}{1+k_{\text{Fe-ox}}\Phi\tau}\Delta_{\text{ox-aq}} + \delta_{\text{residue}}\right)\frac{1}{f_{\text{Mn}}+k_{\text{Fe-ox}}\Phi\tau}df_{\text{Mn}}, \quad \text{(Eq. 4-46)}$$

$$\frac{d(\delta_{\text{residue}}-\delta_{\text{basalt}})}{\frac{k_{\text{Fe-ox}}\Phi\tau}{1+k_{\text{Fe-ox}}\Phi\tau}\Delta_{\text{ox-aq}}+\delta_{\text{residue}}} = -\frac{df_{\text{Mn}}}{f_{\text{Mn}}+k_{\text{Fe-ox}}\Phi\tau}, \quad \text{(Eq. 4-47)}$$

$$\ln\left(\frac{k_{\text{Fe-ox}}\Phi\tau}{1+k_{\text{Fe-ox}}\Phi\tau}\Delta_{\text{ox-aq}} + \delta_{\text{residue}}\right) = -\ln[f_{\text{Mn}} + k_{\text{Fe-ox}}\Phi\tau] + C, \quad \text{(Eq. 4-48)}$$

$$\frac{k_{\text{Fe-ox}}\Phi\tau}{1+k_{\text{Fe-ox}}\Phi\tau}\Delta_{\text{ox-aq}} + \delta_{\text{residue}} = \frac{e^C}{f_{\text{Mn}}+k_{\text{Fe-ox}}\Phi\tau}, \quad \text{(Eq. 4-49)}$$

Since $\delta_{\text{residue}} = 0$ when $f_{\text{Mn}} = 1$, $e^C = k_{\text{Fe-ox}}\Phi\tau\Delta_{\text{ox-aq}}$, and Eq. 4-49 becomes,

$$\delta_{\text{residue}} = \frac{k_{\text{Fe-ox}}\Phi\tau\Delta_{\text{ox-aq}}}{f_{\text{Mn}}+k_{\text{Fe-ox}}\Phi\tau} - \frac{k_{\text{Fe-ox}}\Phi\tau\Delta_{\text{ox-aq}}}{1+k_{\text{Fe-ox}}\Phi\tau}, \quad \text{(Eq. 4-50)}$$

$$= \left(\frac{1-f_{\text{Mn}}}{f_{\text{Mn}}+k_{\text{Fe-ox}}\Phi\tau}\right)\frac{k_{\text{Fe-ox}}\Phi\tau}{1+k_{\text{Fe-ox}}\Phi\tau}\Delta_{\text{ox-aq}}.$$

Therefore, assuming that Mn is not oxidized, we find that both $(\text{Fe/Mn})^*$ and $\delta^{56}\text{Fe}$ depend on the fraction of Mn remaining $f_{\text{Mn}} = \left([\text{Mn}]_{\text{residue}}/[\text{Mn}]_{\text{parent}}\right)/\left([\text{Al}]_{\text{residue}}/[\text{Al}]_{\text{parent}}\right)$, and the dimensionless parameter $k_{\text{Fe-ox}}\Phi\tau$ where τ is the residence time of water in the system (in s), Φ is porosity, $k_{\text{Fe-ox}}$ is the rate constant for iron oxidation (in s^{-1}) = $3.33 \times 10^{2\text{pH}-17}P_{\text{O}_2}$ (Davison and Seed, 1983), where P_{O_2} is partial pressure of oxygen in atm (Eqs. 4-31 and 4-50).

We can also establish a relationship between $f_{\text{Fe}} = \left([\text{Fe}]_{\text{residue}}/[\text{Fe}]_{\text{parent}}\right)/\left([\text{Al}]_{\text{residue}}/[\text{Al}]_{\text{parent}}\right)$ and f_{Mn},

$$f_{\text{Fe}} = \frac{f_{\text{Mn}}+k_{\text{Fe-ox}}\Phi\tau}{1+k_{\text{Fe-ox}}\Phi\tau}, \quad \text{(Eq. 4-51)}$$

and eliminate f_{Mn} from Eqs. 4-31 and 4-50 to establish a relationship between Fe/Mn and δ^{56}Fe fractionations,

$$\delta_{\mathrm{residue}} = \frac{(\mathrm{Fe/Mn})^{*}-1}{(\mathrm{Fe/Mn})^{*}(1+k_{\mathrm{Fe\text{-}ox}}\Phi\tau)}\Delta_{\mathrm{ox\text{-}aq}}. \quad \text{(Eq. 4-52)}$$

Knowing $\frac{(\mathrm{Fe/Mn})_{\mathrm{residue}}}{(\mathrm{Fe/Mn})_{\mathrm{parent}}}$ and therefore f_{Mn}, we can use Eq. 4-31 to solve for $k_{\mathrm{Fe\text{-}ox}}\Phi\tau$ for each sample, and we can further constrain $k_{\mathrm{Fe\text{-}ox}}\Phi\tau$ for samples with δ^{56}Fe data using Eq. 4-52. Note that by definition, our model is designed to accurately constrain pO_2 during surface weathering characterized by mobilization of both Fe and Mn with partial Fe oxidation, and iron isotope fractionation is expected to enrich the residue with heavy isotopes (as observed on early Mars and Earth). Therefore, it performs optimally for samples with $f_{\mathrm{Mn}} < 1$, $f_{\mathrm{Fe}} < 1$, $f_{\mathrm{Fe}} > f_{\mathrm{Mn}}$, and $\delta^{56}\mathrm{Fe} > 1$.

4.4.1 Application of terrestrial paleosols

The correlation between (Fe/Mn)* and f_{Mn} in our paleosol compilation is plotted together with the model expectation in Figure 4-8 and the calculated atmospheric oxygen levels during paleosol formation are shown in Figure 4-9. Despite the lack of Fe isotopic composition and thus constraint from the δ^{56}Fe-(Fe/Mn)* correlation, the paleosol record gives a preliminary corroboration of the ability of our model to capture the redox condition during alteration.

Pre-GOE paleosols from Quirke II (2.45 Ga) exhibit relatively significant Mn loss (30% to 60%) but small Fe/Mn fractionations compared to bedrocks, consistent with subaerial weathering under reducing conditions as suggested by other geochemical signatures for this formation (Prasad and Roscoe, 1991). From the modelling perspective, three of the four Quirke II paleosols fall between curves with $\tau k_{ox}\Phi = 0.0001$ and 0.5, which are the smallest among compiled paleosols,

and one paleosol falls on curve with $\tau k_{ox}\Phi = 2$ (Fig. 4-8). Assuming a water residence time between 2 weeks and 1 year (characteristic of rivers and lakes; Maher 2010), a near-neutral pH between 6.5 and 7.5, and an average porosity for basaltic mineral grains of 0.46 (Brantley and Mellott, 2000), the lower and upper limits on pO_2 during formation of Quirke II paleosols given by our model are 1×10^{-8} and 1×10^{-2} atm, respectively (Fig. 4-9).

By contrast, GOE paleosols from Hekpoort (2.2 Ga) exhibit the most significant Mn loss and Fe/Mn fractionations compared to bedrock, indicating oxidizing alteration environment in which strong weathering of Mn occurred along with Fe oxidation. The two samples fall between curves with $\tau k_{ox}\Phi = 0.5$ and 4 (Fig. 4-8), which agree with an intermediate level of oxygen fugacity. The atmospheric pO_2 during the formation of Hekpoort paleosol is calculated to be between 2.5×10^{-4} and 9×10^{-3} atm (Yang and Holland, 2003), within our model prediction between 1×10^{-7} and 1×10^{-1} atm (Fig. 4-9).

Post-GOE paleosols from Flin Flon (1.85 Ga) exhibit significant loss of Mn and large (Fe/Mn) fractionation from bedrock, therefore falling close to the GOE paleosols and falling exclusively on the curve with the largest $\tau k_{ox}\Phi$ in Figure 4-8. This is consistent with the suggestion that the Flin Flon is the oldest known profile that underwent oxidative weathering that completely oxidized Fe but not Mn^{2+} (Babechuk and Kamber, 2013). Our model prediction indicates that the pO_2 during formation of Flin Flon paleosols was at least 1×10^{-5} atm (Fig. 4-9).

To sum up, there exists a good agreement between the development history of >1.85 Ga terrestrial paleosols from basaltic bedrocks and our model predictions. Furthermore, our model is able to identify the redox condition during primary alteration despite the influence of post-

depositional redox changes. If Fe isotopic compositions of the alteration product are also known, our model can provide better constraints especially for weathering taking place at more oxidizing conditions.

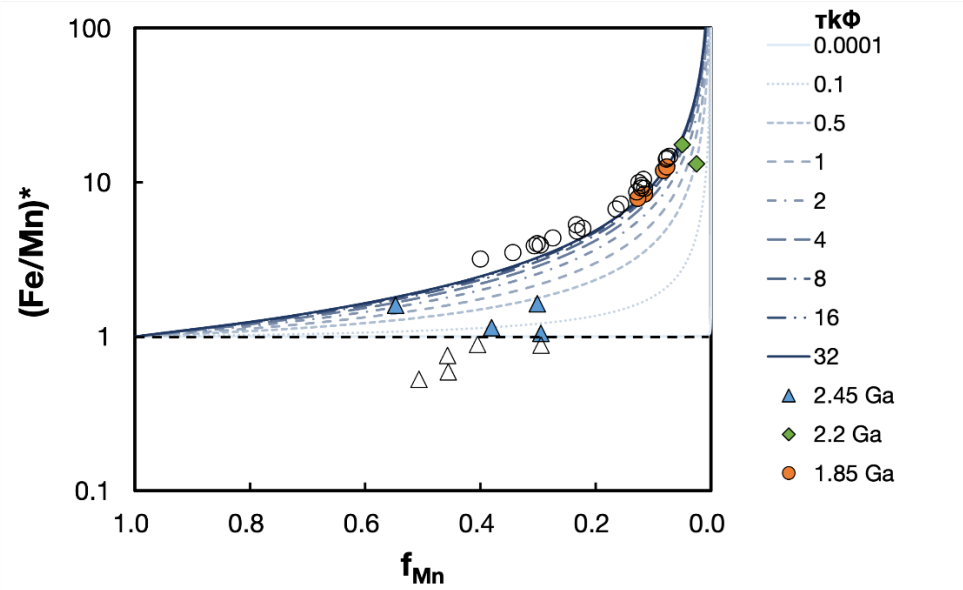

Figure 4-8 Correlation between (Fe/Mn)* and f_{Mn} at various alteration environments ($\tau k_{ox} \Phi$, colored lines) for compiled paleosols grouped by formation age (colored symbols).

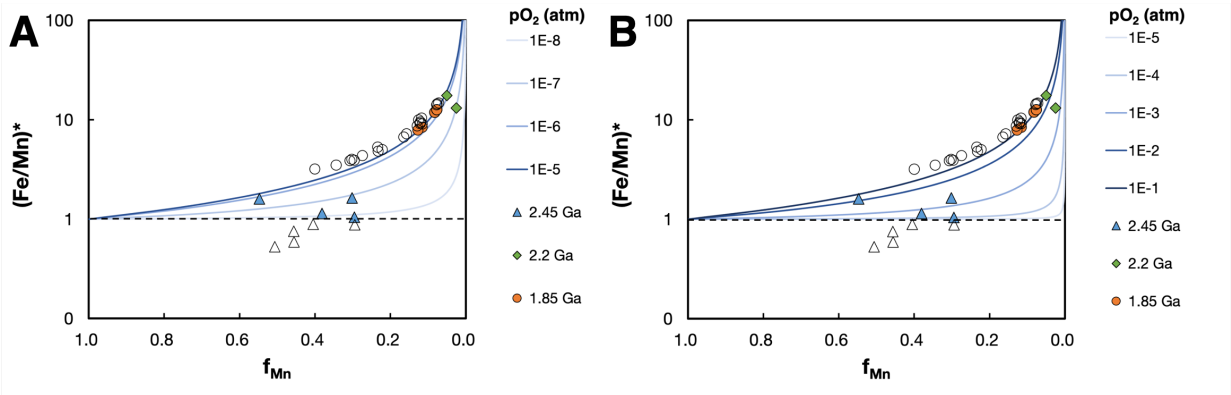

Figure 4-9 Calculated atmospheric oxygen levels (colored lines) during formation of compiled paleosols (colored symbols) assuming (A) τ = 10 years, pH = 7.5, Φ = 0.46 (A), and (B) τ = 2 weeks, pH = 6.5, Φ = 0.46, giving the lower and upper limits, respectively.

4.4.2 Application of analog clays

Due to the diversity of samples analyzed and the uncertainty associated with their source rock compositions, the Martian mineralogical analog clays may not serve as the most effective proxies for analyzing pedogenic pO_2 using our alteration model, in comparison to the paleosols. In fact, 11 out of 16 clay samples have $f_{Fe} > 1$, indicating post-depositional iron enrichment and therefore not compatible with the assumptions of our model (Fig. 4-11). Nevertheless, a comparative analysis of Figures 4-10 and 4-12 shows the potential of iron isotopic composition as an additional constraint on distinguishing between redox conditions during petrogenesis or diagenesis, as negative $\delta^{56}Fe$ in Fe^{3+} oxides within a weathering profile typically reflects the post-alteration oxidation of low- $\delta^{56}Fe$ Fe^{2+}_{aq} produced by Fe^{3+}-reducing bacteria (Johnson and Beard, 2006). Furthermore, our findings in Figure 4-12 question the reliability of the Fe^{3+}/Fe_T ratio as an indicator of pedogenic redox conditions, as samples with similar Fe^{3+}/Fe_T fall on curves with markedly different $\tau k_{ox}\Phi$ values, whereas samples with contrasting Fe^{3+}/Fe_T fall on curves with similar $\tau k_{ox}\Phi$ values. These insights highlight the necessity for calibrating our model against an extensive dataset of chemical analogs of Martian clays with multiple samples at each locality prior to its application.

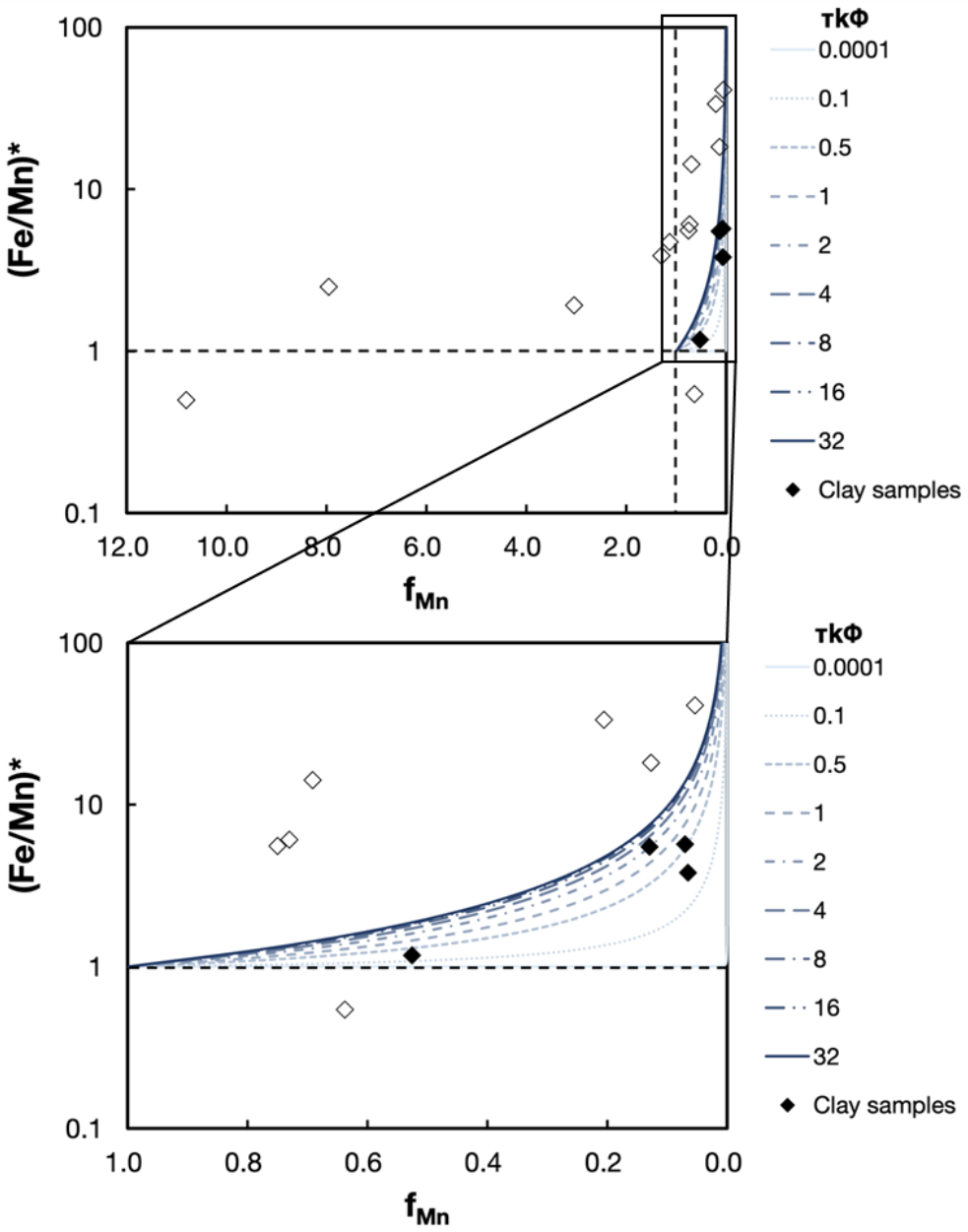

Figure 4-10 Correlation between (Fe/Mn)* and f_{Mn} at various alteration environments ($\tau k_{ox} \Phi$, colored lines) for Martian clay analogs (black diamonds).

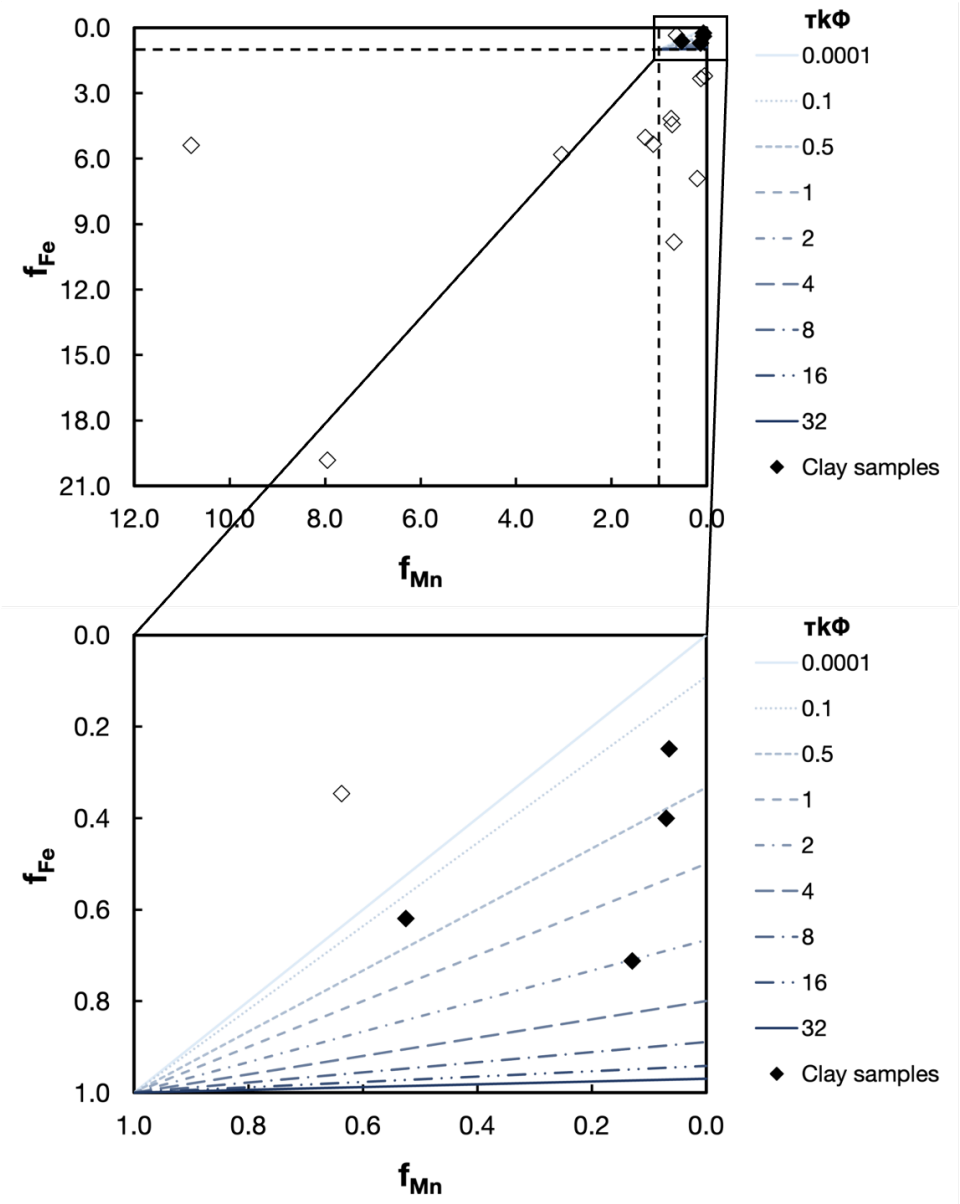

Figure 4-11 Correlation between f_{Fe} and f_{Mn} at various alteration environments ($\tau k_{ox} \Phi$, colored lines) for Martian clay analogs (black diamonds).

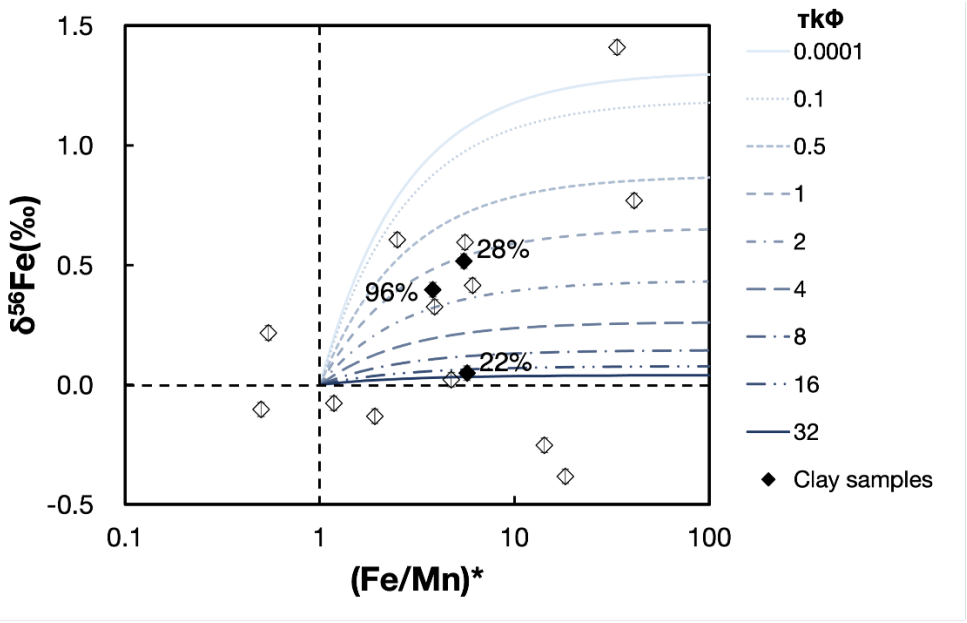

Figure 4-12 Correlation between δ^{56}Fe and (Fe/Mn)* at various alteration environments ($\tau k_{ox}\Phi$, colored lines) for Martian clay analogs (black diamonds).

4.5 Conclusion

Our study presents an interpretative framework that exploits the potential of iron-bearing clay minerals from Noachian and early Hesperian periods as indicators of the redox conditions during their formation on Mars. We analyzed 16 terrestrial clay samples regarded as Martian clay analogs for major element and iron isotopic compositions, and performed NRIXS measurements on 6 samples, which yield a correlation $\langle F \rangle$ =182 N/m for Fe^{2+} and 284 N/m for Fe^{3+}, showing a strong control of redox on iron force constants and therefore equilibrium isotopic fractionation. Through a simple alteration model, we can constrain the redox condition during alteration of mafic minerals using the correlation between Fe/Mn and iron isotopic fractionations, distinguishing primary alteration signals from post-depositional changes. Our evaluation using terrestrial paleosol compilation supports the reliability and applicability of our model, since there is a notable consistency between model predictions and inferences of redox condition during weathering drawn

from geochemical and mineralogical evidence. With Martian sample return missions underway, integrating our framework with iron chemistry and isotope measurements from Martian clays will be instrumental in constraining the redox conditions prevalent during their formation.

REFERENCES

Allègre, C. J., Poirier, J. P., Humler, E., & Hofmann, A. W. (1995). The chemical composition of the Earth. *Earth and Planetary Science Letters*, *134*(3–4), 515–526.

Anbar, A. D., Duan, Y., Lyons, T. W., Arnold, G. L., Kendall, B., Creaser, R. A., ... & Buick, R. (2007). A whiff of oxygen before the great oxidation event?. *Science*, *317*(5846), 1903-1906.

Andriesse, J. P. (1979). A study into the mobility of iron in podzolized Sarawak upland soils by means of selective iron extractions. *Netherlands Journal of Agricultural Science*, *27*(1), 1-12.

Babechuk, M. G., & Kamber, B. S. (2013). The Flin Flon paleosol revisited. *Canadian Journal of Earth Sciences*, *50*(12), 1223–1243.

Babechuk, M. G., Kleinhanns, I. C., & Schoenberg, R. (2017). Chromium geochemistry of the ca. 1.85 Ga Flin Flon paleosol. *Geobiology*, *15*(1), 30-50.

Babechuk, M. G., Weimar, N. E., Kleinhanns, I. C., Eroglu, S., Swanner, E. D., Kenny, G. G., ... & Schoenberg, R. (2019). Pervasively anoxic surface conditions at the onset of the Great Oxidation Event: New multi-proxy constraints from the Cooper Lake paleosol. *Precambrian Research*, *323*, 126-163.

Baird, A. K., Castro, A. J., Clark, B. C., Toulmin, P., Rose, H., Keil, K., & Gooding, J. L. (1977). The Viking X Ray Fluorescence Experiment: Sampling strategies and laboratory simulations. *Journal of Geophysical Research*, *82*(28), 4595–4624.

Baker, L. L. (2017). Formation of the ferruginous smectite SWa-1 by alteration of soil clays. *American Mineralogist*, *102*(1), 33–41.

Bancroft, G. M. (1973). *Mössbauer spectroscopy: an introduction for inorganic chemists and geochemists*. John Wiley & Sons.

Baur, X. (2018). Review on the adverse health effects of asbestiform antigorite, a non-regulated asbestiform serpentine mineral. *American Journal of Industrial Medicine*, *61*(7), 625–630.

Bekker, A., Holland, H. D., Wang, P. L., Rumble Iii, D., Stein, H. J., Hannah, J. L., ... & Beukes, N. J. (2004). Dating the rise of atmospheric oxygen. *Nature*, *427*(6970), 117-120.

Bibring, J. P., Langevin, Y., Mustard, J. F., Poulet, F., Arvidson, R., Gendrin, A., Gondet, B., Mangold, N., Pinet, P., Forget, F., Berthe, M., Gomez, C., Jouglet, D., Soufflot, A., Vincendon, M., Combes, M., Drossart, P., Encrenaz, T., Fouchet, T., … Neukum, G. (2006). Global mineralogical and aqueous Mars history derived from OMEGA/Mars express data. *Science*, *312*(5772), 400–404.

Boslough, M. B., Venturini, E. L., Morosin, B., Graham, R. A., & Williamson, D. L. (1986). Physical properties of shocked and thermally altered nontronite: Implications for the Martian surface. *Journal of Geophysical Research*, *91*(B13), E207.

Brantley, S. L., Liermann, L. J., Guynn, R. L., Anbar, A., Icopini, G. A., & Barling, J. (2004). Fe isotopic fractionation during mineral dissolution with and without bacteria. *Geochimica et Cosmochimica Acta*, *68*(15), 3189-3204.

Brantley, S. L., & Mellott, N. P. (2000). Surface area and porosity of primary silicate minerals. *American Mineralogist*, *85*(11-12), 1767-1783.

Brantley, S. L., White, A. F., & Kubicki, J. D. (2008). Kinetics of water-rock interaction. In *Kinetics of Water-Rock Interaction*. Springer New York.

Bristow, T. F., Rampe, E. B., Achilles, C. N., Blake, D. F., Chipera, S. J., Craig, P., Crisp, J. A., des Marais, D. J., Downs, R. T., Gellert, R., Grotzinger, J. P., Gupta, S., Hazen, R. M., Horgan, B., Hogancamp, J. v., Mangold, N., Mahaffy, P. R., McAdam, A. C., Ming, D. W., … Yen, A. S. (2018). Clay mineral diversity and abundance in sedimentary rocks of Gale crater, Mars. *Science Advances*, *4*(6), eaar3330.

Bujdák, J., & Rode, B. M. (1996). The effect of smectite composition on the catalysis of peptide bond formation. *Journal of Molecular Evolution*, *43*(4), 326–333.

Canfield, D. E. (2005). The early history of atmospheric oxygen: homage to Robert M. Garrels. *Annu. Rev. Earth Planet. Sci.*, *33*, 1-36.

Cashion, J. D., Gates, W. P., & Riley, G. M. (2010). Origin of the two quadrupole doublets in NAu-1 nontronite. *Journal of Physics: Conference Series*, *217*, 012065.

Carter, J., Poulet, F., Bibring, J. P., Mangold, N., & Murchie, S. (2013). Hydrous minerals on Mars as seen by the CRISM and OMEGA imaging spectrometers: Updated global view. *Journal of Geophysical Research: Planets*, *118*(4), 831-858.

Changela, H. G., & Bridges, J. C. (2010). Alteration assemblages in the nakhlites: Variation with depth on Mars. *Meteoritics & Planetary Science*, *45*(12), 1847-1867.

Chapman, J. B., Weiss, D. J., Shan, Y., & Lemburger, M. (2009). Iron isotope fractionation during leaching of granite and basalt by hydrochloric and oxalic acids. *Geochimica et Cosmochimica Acta*, *73*(5), 1312-1324.

Chen, P. Y. (1968). *Geology and mineralogy of the white bentonite beds of Gonzales County, Texas*. The University of Texas at Austin.

Chevrier, V., Poulet, F., & Bibring, J. P. (2007). Early geochemical environment of Mars as

determined from thermodynamics of phyllosilicates. *Nature*, *448*(7149), 60-63.

Chipera, S. J., & Bish, D. L. (2001). Baseline Studies of the Clay Minerals Society Source Clays: Powder X-ray Diffraction Analyses. *Clays and Clay Minerals*, *49*(5), 398–409.

Cloutis, E., Craig, M., Kruzelecky, R., Jamroz, W., Scott, A., Hawthorne, F., & Mertzman, S. (2008). Spectral reflectance properties of minerals exposed to simulated Mars surface conditions. *Icarus*, *195*(1), 140–168.

Craddock, P. R., & Dauphas, N. (2010). Iron Isotopic Compositions of Geological Reference Materials and Chondrites. *Geostandards and Geoanalytical Research*, *35*(1), 101–123.

Craddock, P. R., & Dauphas, N. (2011). Iron and carbon isotope evidence for microbial iron respiration throughout the Archean. *Earth and Planetary Science Letters*, *303*(1–2), 121–132.

Craig, P.I., Rudolph, A., Morris, R.V., Achilles, C.N., Rampe, E.B., Treiman, A.H., Bristow, T.F., Ming, D.W., Blake, D.F., Vaniman, D.T., Downs, R.T., Morrison, S.M., Yen, A.S., Farmer, J., Des Marais, D.J., Castle, N., Chipera, S.J., Hazen, R.M., Peretyazhko, T.S., Tu, V., 2018. COLLAPSED SMECTITE IN GALE CRATER: MARTIAN CLAY MINERALS MAY HAVE BEEN ON ACID. LPSC XLIX.

Crowe, S. A., Døssing, L. N., Beukes, N. J., Bau, M., Kruger, S. J., Frei, R., & Canfield, D. E. (2013). Atmospheric oxygenation three billion years ago. *Nature*, *501*(7468), 535-538.

Dauphas, N., Craddock, P. R., Asimow, P. D., Bennett, V. C., Nutman, A. P., & Ohnenstetter, D. (2009a). Iron isotopes may reveal the redox conditions of mantle melting from Archean to Present. *Earth and Planetary Science Letters*, *288*(1–2), 255–267.

Dauphas, N., Hu, M. Y., Baker, E. M., Hu, J., Tissot, F. L. H., Alp, E. E., Roskosz, M., Zhao, J., Bi, W., Liu, J., Lin, J. F., Nie, N. X., & Heard, A. (2018). SciPhon: a data analysis software for nuclear resonant inelastic X-ray scattering with applications to Fe, Kr, Sn, Eu and Dy. *Journal of Synchrotron Radiation*, *25*(5), 1581–1599.

Dauphas, N., John, S. G., & Rouxel, O. (2017). Iron Isotope Systematics. *Reviews in Mineralogy & Geochemistry*, *82*, 415–510.

Dauphas, N., Pourmand, A., & Teng, F. Z. (2009b). Routine isotopic analysis of iron by HR-MC-ICPMS: How precise and how accurate? *Chemical Geology*, *267*(3–4), 175–184.

Dauphas, N., & Rouxel, O. (2006). Mass spectrometry and natural variations of iron isotopes. *Mass spectrometry reviews*, *25*(4), 515-550.

Dauphas, N., Roskosz, M., Alp, E. E., Golden, D. C., Sio, C. K., Tissot, F. L. H., Hu, M. Y., Zhao, J., Gao, L., & Morris, R. v. (2012). A general moment NRIXS approach to the determination

of equilibrium Fe isotopic fractionation factors: Application to goethite and jarosite. *Geochimica et Cosmochimica Acta*, *94*, 254–275.

Dauphas, N., Roskosz, M., Alp, E. E., Neuville, D. R., Hu, M. Y., Sio, C. K., Tissot, F. L. H., Zhao, J., Tissandier, L., Médard, E., & Cordier, C. (2014). Magma redox and structural controls on iron isotope variations in Earth's mantle and crust. *Earth and Planetary Science Letters*, *398*, 127–140.

Davies, S. H., & Morgan, J. J. (1989). Manganese (II) oxidation kinetics on metal oxide surfaces. *Journal of Colloid and Interface Science*, *129*(1), 63-77.

Davison, W., & Seed, G. (1983). The kinetics of the oxidation of ferrous iron in synthetic and natural waters. *Geochimica et Cosmochimica Acta*, *47*(1), 67-79.

Deer, W. A., Howie, R. A., & Zussman, J. (2013). *An introduction to the rock-forming minerals*. Mineralogical Society of Great Britain and Ireland.

Dehouck, E., Gaudin, A., Chevrier, V., & Mangold, N. (2016). Mineralogical record of the redox conditions on early Mars. *Icarus*, *271*, 67-75.

Derkowski, Arkadiusz; Kuligiewicz, Artur; Lempart, Małgorzata; Gionis, Vassilis; Chryssikos, Georgios (2016). SSHADE/LSD: Layered Silicates Database. SSHADE (OSUG Data Center). Service/Database.

Diem, D., & Stumm, W. (1984). Is dissolved Mn2+ being oxidized by O2 in absence of Mn-bacteria or surface catalysts?. *Geochimica et Cosmochimica Acta*, *48*(7), 1571-1573.

Du, D. H., Wang, X. L., Yang, T., Chen, X., Li, J. Y., & Li, W. (2017). Origin of heavy Fe isotope compositions in high-silica igneous rocks: a rhyolite perspective. *Geochimica et Cosmochimica Acta*, *218*, 58-72.

Ehlmann, B. L., & Edwards, C. S. (2014). Mineralogy of the Martian surface. *Annual Review of Earth and Planetary Sciences*, *42*, 291-315.

Ehlmann, B. L., Mustard, J. F., Fassett, C. I., Schon, S. C., Head, J. W., des Marais, D. J., Grant, J. A., & Murchie, S. L. (2008). Clay minerals in delta deposits and organic preservation potential on Mars. *Nature Geoscience*, *1*(6), 355–358.

Ehlmann, B. L., Mustard, J. F., Murchie, S. L., Bibring, J. P., Meunier, A., Fraeman, A. A., & Langevin, Y. (2011). Subsurface water and clay mineral formation during the early history of Mars. In *Nature* (Vol. 479, Issue 7371, pp. 53–60).

Elzea, J. M. (1990). *Geology, geochemistry, selected physical properties, and genesis of the Cretaceous Clay Spur Bentonite in Wyoming and Montana*. Indiana University.

Elzea, J., & Murray, H. (1990). Variation in the mineralogical, chemical and physical properties of the Cretaceous Clay Spur bentonite in Wyoming and Montana (U.S.A.). *Applied Clay Science*, *5*(3), 229–248.

Fantle, M. S., & DePaolo, D. J. (2004). Iron isotopic fractionation during continental weathering. *Earth and Planetary Science Letters*, *228*(3-4), 547-562.

Finck, N., Schlegel, M. L., & Bauer, A. (2015). Structural iron in dioctahedral and trioctahedral smectites: a polarized XAS study. *Physics and Chemistry of Minerals*, *42*(10), 847–859.

Finck, N., Schlegel, M. L., Dardenne, K., Adam, C., Kraft, S., Bauer, A., & Robert, J. L. (2019). Structural iron in smectites with different charge locations. *Physics and Chemistry of Minerals*, *46*(7), 639–661.

Flynn, E. D., & Catalano, J. G. (2019). Reductive transformations of layered manganese oxides by small organic acids and the fate of trace metals. *Geochimica et Cosmochimica Acta*, *250*, 149-172.

Gandía, L., Gil, A., Vicente, M., & Belver, C. (2005). Dehydrogenation of ethylbenzene on alumina-pillared Fe-rich saponites. *Catalysis Letters*, *101*(3–4), 229–234.

Gates, W. P., Jaunet, A. M., Tessier, D., Cole, M. A., Wilkinson, H. T., & Stucki, J. W. (1998). Swelling and Texture of Iron-Bearing Smectites Reduced by Bacteria. *Clays and Clay Minerals*, *46*(5), 487–497.

Gates, W. P., Slade, P. G., Manceau, A., & Lanson, B. (2002). Site Occupancies by Iron in Nontronites. *Clays and Clay Minerals*, *50*(2), 223–239.

Gillet, P., Barrat, J. A., Deloule, E., Wadhwa, M., Jambon, A., Sautter, V., ... & Lesourd, M. (2002). Aqueous alteration in the Northwest Africa 817 (NWA 817) Martian meteorite. *Earth and Planetary Science Letters*, *203*(1), 431-444.

Giuli, G., Alonso-Mori, R., Cicconi, M. R., Paris, E., Glatzel, P., Eeckhout, S. G., & Scaillet, B. (2012). Effect of alkalis on the Fe oxidation state and local environment in peralkaline rhyolitic glasses. *American Mineralogist*, *97*(2-3), 468-475.

Gooding, J. L. (1992). Soil mineralogy and chemistry on Mars: Possible clues from salts and clays in SNC meteorites. *Icarus*, *99*(1), 28–41.

Gooding, J. L., Wentworth, S. J., & Zolensky, M. E. (1991). Aqueous alteration of the Nakhla meteorite. *Meteoritics*, *26*(2), 135-143.

Gorski, C. A., Klüpfel, L., Voegelin, A., Sander, M., & Hofstetter, T. B. (2012). Redox Properties

of Structural Fe in Clay Minerals. 2. Electrochemical and Spectroscopic Characterization of Electron Transfer Irreversibility in Ferruginous Smectite, SWa-1. *Environmental Science & Technology*, *46*(17), 9369–9377.

Gudbrandsson, S., Wolff-Boenisch, D., Gislason, S. R., & Oelkers, E. H. (2011). An experimental study of crystalline basalt dissolution from 2⩽ pH⩽ 11 and temperatures from 5 to 75 C. *Geochimica et Cosmochimica Acta*, *75*(19), 5496-5509.

Heard, A. W., Dauphas, N., Guilbaud, R., Rouxel, O. J., Butler, I. B., Nie, N. X., & Bekker, A. (2020). Triple iron isotope constraints on the role of ocean iron sinks in early atmospheric oxygenation. *Science*, *370*(6515), 446-449.

Heard, A. W., Aarons, S. M., Hofmann, A., He, X., Ireland, T., Bekker, A., Qin, L., & Dauphas, N. (2021). Anoxic continental surface weathering recorded by the 2.95 Ga Denny Dalton Paleosol (Pongola Supergroup, South Africa). *Geochimica et Cosmochimica Acta*, *295*, 1–23.

Heard, A. W., Bekker, A., Kovalick, A., Tsikos, H., Ireland, T., & Dauphas, N. (2022). Oxygen production and rapid iron oxidation in stromatolites immediately predating the Great Oxidation Event. *Earth and Planetary Science Letters*, *582*, 117416.

Hem, J. D. (1963). *Chemical equilibria and rates of manganese oxidation* (No. 1667). US Government Printing Office.

Herd, C. D. K., Borg, L. E., Jones, J. H., & Papike, J. J. (2002). Oxygen fugacity and geochemical variations in the martian basalts: implications for martian basalt petrogenesis and the oxidation state of the upper mantle of Mars. *Geochimica et Cosmochimica Acta*, *66*(11), 2025–2036.

Herd, C. D. K., Papike, J. J., & Brearley, A. J. (2001). Oxygen fugacity of martian basalts from electron microprobe oxygen and TEM-EELS analyses of Fe-Ti oxides. *American Mineralogist*, *86*(9), 1015–1024.

Hicks, L. J., Bridges, J. C., & Gurman, S. J. (2014). Ferric saponite and serpentine in the nakhlite martian meteorites. *Geochimica et Cosmochimica Acta*, *136*, 194–210.

Hu, M. Y., Toellner, T. S., Dauphas, N., Alp, E. E., & Zhao, J. (2013). Moments in nuclear resonant inelastic x-ray scattering and their applications. *Physical Review B*, *87*(6), 064301.

Huang, L. M., Jia, X. X., Zhang, G. L., Thompson, A., Huang, F., Shao, M. A., & Chen, L. M. (2018). Variations and controls of iron oxides and isotope compositions during paddy soil evolution over a millennial time scale. *Chemical Geology*, *476*, 340-351.

Hummer, D. R., Golden, J. J., Hystad, G., Downs, R. T., Eleish, A., Liu, C., ... & Hazen, R. M. (2022). Evidence for the oxidation of Earth's crust from the evolution of manganese minerals. *Nature Communications*, *13*(1), 960.

Inglis, E. C., Debret, B., Burton, K. W., Millet, M. A., Pons, M. L., Dale, C. W., ... & Williams, H. M. (2017). The behavior of iron and zinc stable isotopes accompanying the subduction of mafic oceanic crust: A case study from W estern A lpine ophiolites. *Geochemistry, Geophysics, Geosystems*, *18*(7), 2562-2579.

Jackson, W. E., Farges, F., Yeager, M., Mabrouk, P. A., Rossano, S., Waychunas, G. A., ... & Brown Jr, G. E. (2005). Multi-spectroscopic study of Fe (II) in silicate glasses: Implications for the coordination environment of Fe (II) in silicate melts. *Geochimica et Cosmochimica Acta*, *69*(17), 4315-4332.

Jaisi, D. P., Kukkadapu, R. K., Eberl, D. D., & Dong, H. (2005). Control of Fe(III) site occupancy on the rate and extent of microbial reduction of Fe(III) in nontronite. *Geochimica et Cosmochimica Acta*, *69*(23), 5429–5440.

Johnson, C. M., & Beard, B. L. (2006). Fe isotopes: An emerging technique for understanding modern and ancient biogeochemical cycles. *GSA today*, *16*(11), 4.

Johnson, C. M., Beard, B. L., & Roden, E. E. (2008). The iron isotope fingerprints of redox and biogeochemical cycling in modern and ancient Earth. *Annu. Rev. Earth Planet. Sci.*, *36*, 457-493.

Johnson, C. M., Beard, B. L., Roden, E. E., Newman, D. K., & Nealson, K. H. (2004). Isotopic constraints on biogeochemical cycling of Fe. *Reviews in mineralogy and geochemistry*, *55*(1), 359-408.

Johnson, C. M., Skulan, J. L., Beard, B. L., Sun, H., Nealson, K. H., & Braterman, P. S. (2002). Isotopic fractionation between Fe (III) and Fe (II) in aqueous solutions. *Earth and Planetary Science Letters*, *195*(1-2), 141-153.

Junta, J. L., & Hochella Jr, M. F. (1994). Manganese (II) oxidation at mineral surfaces: A microscopic and spectroscopic study. *Geochimica et Cosmochimica Acta*, *58*(22), 4985-4999.

Kanzaki, Y., & Murakami, T. (2016). Estimates of atmospheric O2 in the Paleoproterozoic from paleosols. *Geochimica et Cosmochimica Acta*, *174*, 263-290.

Keeling, J. L., Raven, M. D., & Gates, W. P. (2000). Geology and Characterization of Two Hydrothermal Nontronites from Weathered Metamorphic Rocks at the Uley Graphite Mine, South Australia. *Clays and Clay Minerals 2000 48:5*, *48*(5), 537–548.

Kerr P. F., Kulp J. L. (1949). Reference clay localities, United States. Pp 69-73 in: *Reference Clay Minerals; American Petroleum Institute Research Project 49, Preliminary Reports no. 1-8* (Kerr P. F., Kulp J. L., editors). Columbia University, New York.

King, T. V. V., & Clark, R. N. (1989). Spectral characteristics of chlorites and Mg-serpentines using high-resolution reflectance spectroscopy. *Journal of Geophysical Research: Solid Earth*, *94*(B10), 13997–14008.

Kloprogge, J. T., & Frost, R. L. (2000). Thermal decomposition of Ferrian chamosite: an infrared emission spectroscopic study. *Contributions to Mineralogy and Petrology*, *138*(1), 59–67.

Kloprogge, J. T., & Ponce, C. P. (2021). Spectroscopic Studies of Synthetic and Natural Saponites: A Review. *Minerals*, *11*(2), 112.

Komadel, P. E. T. E. R., Madejová, J. A. N. A., Laird, D. A., Xia, Y., & Stucki, J. W. (2000). Reduction of Fe (III) in griffithite. *Clay Minerals*, *35*(4), 625-634.

Krauskopf, K. B. (1957). Separation of manganese from iron in sedimentary processes. *Geochimica et Cosmochimica Acta*, *12*(1-2), 61-84.

Liu, J., Chen, Q., Yang, Y., Wei, H., Laipan, M., Zhu, R., ... & Hochella Jr, M. F. (2022). Coupled redox cycling of Fe and Mn in the environment: The complex interplay of solution species with Fe-and Mn-(oxyhydr) oxide crystallization and transformation. *Earth-Science Reviews*, *232*, 104105.

Liu, S. A., Teng, F. Z., Li, S., Wei, G. J., Ma, J. L., & Li, D. (2014). Copper and iron isotope fractionation during weathering and pedogenesis: Insights from saprolite profiles. *Geochimica et Cosmochimica Acta*, *146*, 59-75.

Losa-Adams, E., Gil-Lozano, C., Fairén, A. G., Bishop, J. L., Rampe, E. B., & Gago-Duport, L. (2021). Long-lasting habitable periods in Gale crater constrained by glauconitic clays. *Nature astronomy*, *5*(9), 936-942.

Lyons, T. W., Reinhard, C. T., & Planavsky, N. J. (2014). The rise of oxygen in Earth's early ocean and atmosphere. *Nature*, *506*(7488), 307-315.

Maher, K. (2010). The dependence of chemical weathering rates on fluid residence time. *Earth and Planetary Science Letters*, *294*(1-2), 101-110.

Manceau, A., Drits, V., Lanson, B., Chateigner, D., Wu, J., Huo, D., Gates, W., & Stucki, J. (2000). Oxidation-reduction mechanism of iron in dioctahedral smectites: II. Crystal chemistry of reduced Garfield nontronite. *American Mineralogist*, *85*(1), 153–172.

Manceau, A., Lanson, B., Drits, V., Chateigner, D., Gates, W., Wu, J., Huo, D., & Stucki, J. (2000). Oxidation-reduction mechanism of iron in dioctahedral smectites: I. Crystal chemistry of oxidized reference nontronites. *American Mineralogist*, *85*(1), 133–152.

Martin, S. T. (2005). Precipitation and dissolution of iron and manganese oxides. *Environmental*

catalysis, *1*, 61-82.

Martin, B. S., Tolan, T. L., Reidel, S. P., Camp, V. E., Ross, M. E., Wolff, J. A., & Wells, R. E. (2013). Revisions to the stratigraphy and distribution of the Frenchman Springs Member, Wanapum Basalt. *Geological Society of America Special Papers*, *497*, 155-179.

McDonough, W. F., & Sun, S. S. (1995). The composition of the Earth. *Chemical geology*, *120*(3-4), 223-253.

McSween, H. Y. (1994). What we have learned about Mars from SNC meteorites. *Meteoritics*, *29*(6), 757–779.

Mellini, M., Fuchs, Y., Viti, C., Lemaire, C., & Linarè S, J. (2002). Insights into the antigorite structure from Mossbauer and FTIR spectroscopies. *European Journal of Mineralogy*, *14*(1), 97–104.

Métrich, N., Susini, J., Foy, E., Farges, F., Massare, D., Sylla, L., ... & Bonnin-Mosbah, M. (2006). Redox state of iron in peralkaline rhyolitic glass/melt: X-ray absorption micro-spectroscopy experiments at high temperature. *Chemical geology*, *231*(4), 350-363.

Michalski, J. R., Cuadros, J., Bishop, J. L., Darby Dyar, M., Dekov, V., & Fiore, S. (2015). Constraints on the crystal-chemistry of Fe/Mg-rich smectitic clays on Mars and links to global alteration trends. *Earth and Planetary Science Letters*, *427*, 215–225.

Moll, W. F. (2001). Baseline Studies of the Clay Minerals Society Source Clays: Geological Origin. *Clays and Clay Minerals*, *49*(5), 374–380.

Morgan, J. J. (2005). Kinetics of reaction between O2 and Mn (II) species in aqueous solutions. *Geochimica et Cosmochimica Acta*, *69*(1), 35-48.

Morris, R. v., Golden, D. C., Bell, J. F., Shelfer, T. D., Scheinost, A. C., Hinman, N. W., Furniss, G., Mertzman, S. A., Bishop, J. L., Ming, D. W., Allen, C. C., & Britt, D. T. (2000). Mineralogy, composition, and alteration of Mars Pathfinder rocks and soils: Evidence from multispectral, elemental, and magnetic data on terrestrial analogue, SNC meteorite, and Pathfinder samples. *Journal of Geophysical Research: Planets*, *105*(E1), 1757–1817.

Morris, R. v, Graff, T. G., Achilles, C. N., Agresti, D. G., Ming, D. W., & Golden, D. C. (2011). VISIBLE AND NEAR-IR REFLECTANCE SPECTRA OF MARS ANALOGUE MATERIALS UNDER ARID CONDITIONS FOR INTERPRETATION OF MARTIAN SURFACE MINERALOGY. *LPI*, *1608*, 2757.

Morris, R. V., Ming, D. W., Golden, D. C., Graff, T. G., & Achilles, C. N. (2010, March). Evidence for interlayer collapse of nontronite on Mars from laboratory visible and near-IR reflectance spectra. In *Lunar and Planetary Science Conference* (No. 1533, p. 2156).

Mortimer, G. E. (1984). *Early to middle Proterozoic granitoids, basaltic dykes and associated layered rocks of SE Eyre Peninsula, South Australia/by Graham E. Mortimer* (Doctoral dissertation).

Murad, E. (1987). Mössbauer spectra of nontronites: Structural implications and characterization of associated iron oxides. *Zeitschrift Für Pflanzenernährung Und Bodenkunde*, *150*(5), 279–285.

Murakami, T., Sreenivas, B., Sharma, S. D., & Sugimori, H. (2011). Quantification of atmospheric oxygen levels during the Paleoproterozoic using paleosol compositions and iron oxidation kinetics. *Geochimica et cosmochimica acta*, *75*(14), 3982-4004.

Murchie, S. L., Mustard, J. F., Ehlmann, B. L., Milliken, R. E., Bishop, J. L., McKeown, N. K., ... & Bibring, J. P. (2009). A synthesis of Martian aqueous mineralogy after 1 Mars year of observations from the Mars Reconnaissance Orbiter. *Journal of Geophysical Research: Planets*, *114*(E2).

Mustard, J. F., Murchie, S. L., Pelkey, S. M., Ehlmann, B. L., Milliken, R. E., Grant, J. A., Bibring, J. P., Poulet, F., Bishop, J., Dobrea, E. N., Roach, L., Seelos, F., Arvidson, R. E., Wiseman, S., Green, R., Hash, C., Humm, D., Malaret, E., McGovern, J. A., … Wolff, M. (2008). Hydrated silicate minerals on Mars observed by the Mars Reconnaissance Orbiter CRISM instrument. *Nature*, *454*(7202), 305–309.

Nealson, K. H., Tebo, B. M., & Rosson, R. A. (1988). Occurrence and mechanisms of microbial oxidation of manganese. In *Advances in applied microbiology* (Vol. 33, pp. 279-318). Academic Press.

Nie, N. X., Dauphas, N., & Greenwood, R. C. (2017). Iron and oxygen isotope fractionation during iron UV photo-oxidation: Implications for early Earth and Mars. *Earth and Planetary Science Letters*, *458*, 179-191.

Noguchi, T., Nakamura, T., Misawa, K., Imae, N., Aoki, T., & Toh, S. (2009). Laihunite and jarosite in the Yamato 00 nakhlites: Alteration products on Mars?. *Journal of Geophysical Research: Planets*, *114*(E10).

Parker, A. J. (1978). *Structural, stratigraphic and metamorphic geology of Lower Proterozoic rocks in the Cowell/Cleve district, eastern Eyre Peninsula* (Doctoral dissertation, Adelaide,).

Pavlov, A. A., & Kasting, J. F. (2002). Mass-independent fractionation of sulfur isotopes in Archean sediments: strong evidence for an anoxic Archean atmosphere. *Astrobiology*, *2*(1), 27-41.

Petterson, R., Prave, A. R., Wernicke, B. P., & Fallick, A. E. (2011). The Neoproterozoic Noonday

Formation, Death Valley region, California. *Bulletin*, *123*(7-8), 1317-1336.

Planavsky, N. J., Asael, D., Hofmann, A., Reinhard, C. T., Lalonde, S. V., Knudsen, A., ... & Rouxel, O. J. (2014). Evidence for oxygenic photosynthesis half a billion years before the Great Oxidation Event. *Nature Geoscience*, *7*(4), 283-286.

Poitrasson, F., Delpech, G., & Grégoire, M. (2013). On the iron isotope heterogeneity of lithospheric mantle xenoliths: implications for mantle metasomatism, the origin of basalts and the iron isotope composition of the Earth. *Contributions to Mineralogy and Petrology*, *165*, 1243-1258.

Polyakov, V. B., Clayton, R. N., Horita, J., & Mineev, S. D. (2007). Equilibrium iron isotope fractionation factors of minerals: reevaluation from the data of nuclear inelastic resonant X-ray scattering and Mössbauer spectroscopy. *Geochimica et Cosmochimica Acta*, *71*(15), 3833-3846.

Polyakov, V. B., & Soultanov, D. M. (2011). New data on equilibrium iron isotope fractionation among sulfides: Constraints on mechanisms of sulfide formation in hydrothermal and igneous systems. *Geochimica et Cosmochimica Acta*, *75*(7), 1957-1974.

Post, J. L. (1984). Saponite from Near Ballarat, California. *Clays and Clay Minerals*, *32*(2), 147–153.

Post, J. L., & Plummer, C. C. (1972). The chlorite series of Flagstaff Hill area, California: A preliminary investigation. *Clays and Clay Minerals*, *20*(5), 271–283.

Poulet, F., Bibring, J. P., Mustard, J. F., Gendrin, A., Mangold, N., Langevin, Y., Arvidson, R. E., Gondet, B., Gomez, C., Berthe, M., Erard, S., Forni, O., Manaud, N., Poulleau, G., Soufflot, A., Combes, M., Drossart, P., Encrenaz, T., Fouchet, T., … Forget, F. (2005). Phyllosilicates on Mars and implications for early martian climate. *Nature*, *438*(7068), 623–627.

Prasad, N., & Roscoe, S. M. (1991). *Profiles of Altered Zones At Ca 2.45 Ga Unconformities Beneath Huronian Strata, Elliot Lake, Ontario: Evidence For Early Aphebian Weathering Under Anoxic Conditions*.

Ramirez, R. M., Kopparapu, R., Zugger, M. E., Robinson, T. D., Freedman, R., & Kasting, J. F. (2014). Warming early Mars with CO2 and H2. *Nature Geoscience*, *7*(1), 59-63.

Rampe, E. B., Bristow, T. F., Morris, R. V., Morrison, S. M., Achilles, C. N., Ming, D. W., ... & Salvatore, M. R. (2020). Mineralogy of Vera Rubin ridge from the Mars science laboratory CheMin instrument. *Journal of Geophysical Research: Planets*, *125*(9), e2019JE006306.

Reidel, S. P., Camp, V. E., Tolan, T. L., Martin, B. S., Ross, M. E., Wolff, J. A., & Wells, R. E. (2013). The Columbia River flood basalt province: Stratigraphy, areal extent, volume, and

physical volcanology. *The Columbia River flood basalt province: geological society of America special paper*, *497*, 1-43.

Rivera Banuchi, V. B., Liu, W., Yee, N., Legett, C., Glotch, T. D., & Chemtob, S. M. (2022). Ultraviolet Photooxidation of Smectite-Bound Fe (II) and Implications for the Origin of Martian Nontronites. *Journal of Geophysical Research: Planets*, *127*(5), e2021JE007150.

Roskosz, M., Sio, C. K. I., Dauphas, N., Bi, W., Tissot, F. L. H., Hu, M. Y., Zhao, J., & Alp, E. E. (2015). Spinel-olivine-pyroxene equilibrium iron isotopic fractionation and applications to natural peridotites. *Geochimica et Cosmochimica Acta*, *169*, 184–199.

Roskosz, M., Dauphas, N., Hu, J., Hu, M. Y., Neuville, D. R., Brown, D., ... & Alp, E. E. (2022). Structural, redox and isotopic behaviors of iron in geological silicate glasses: A NRIXS study of Lamb-Mössbauer factors and force constants. *Geochimica et Cosmochimica Acta*, *321*, 184-205.

Rouxel, O. J., Bekker, A., & Edwards, K. J. (2005). Iron Isotope Constraints on the Archean and Paleoproterozoic Ocean Redox State. *Science*, *307*(5712), 1088–1091.

Sawaki, Y., Tahata, M., Komiya, T., Hirata, T., Han, J., & Shu, D. (2018). Redox history of the Three Gorges region during the Ediacaran and Early Cambrian as indicated by the Fe isotope. *Geoscience Frontiers*, *9*(1), 155-172.

Schauble, E. A. (2004). Applying stable isotope fractionation theory to new systems. *Reviews in mineralogy and geochemistry*, *55*(1), 65-111.

Schuth, S., Hurraß, J., Muenker, C., & Mansfeldt, T. (2015). Redox-dependent fractionation of iron isotopes in suspensions of a groundwater-influenced soil. *Chemical Geology*, *392*, 74-86.

Seto, M., Yoda, Y., Kikuta, S., Zhang, X. W., & Ando, M. (1995). Observation of nuclear resonant scattering accompanied by phonon excitation using synchrotron radiation. *Physical review letters*, *74*(19), 3828.

Sholes, S. F., Smith, M. L., Claire, M. W., Zahnle, K. J., & Catling, D. C. (2017). Anoxic atmospheres on Mars driven by volcanism: Implications for past environments and life. *Icarus*, *290*, 46-62.

Siebecker, M., Madison, A. S., & Luther, G. W. (2015). Reduction kinetics of polymeric (soluble) manganese (IV) oxide (MnO 2) by ferrous iron (Fe 2+). *Aquatic Geochemistry*, *21*, 143-158.

Simpson, C. A. (1994). *Constraints on Proterozoic crustal evolution from an isotopic and geochemical study of clastic sediments of the Gawler Craton, South Australia* (Doctoral dissertation).

Sindol, G. P., Babechuk, M. G., Petrus, J. A., & Kamber, B. S. (2020). New insights into Paleoproterozoic surficial conditions revealed by 1.85 Ga corestone-rich saprolith. *Chemical Geology*, *545*, 119621.

Singer, R. B. (1982). Spectral evidence for the mineralogy of high-albedo soils and dust on Mars. *Journal of Geophysical Research*, *87*(B12), 10159.

Shi, B., Liu, K., Wu, L., Li, W., Smeaton, C. M., Beard, B. L., Johnson, C. M., Roden, E. E., & van Cappellen, P. (2016). Iron Isotope Fractionations Reveal a Finite Bioavailable Fe Pool for Structural Fe(III) Reduction in Nontronite. *Environmental Science & Technology*, *50*(16), 8661–8669.

Slaughter, M., & Earley, J. W. (1965). *Mineralogy and geological significance of the Mowry bentonites, Wyoming* (Vol. 83). Geological Society of America.

Springer, R. K. (1974). Contact Metamorphosed Ultramafic Rocks in the Western Sierra Nevada Foothills, California. *Journal of Petrology*, *15*(1), 160–195.

Stone, A. T. (1987). Microbial metabolites and the reductive dissolution of manganese oxides: oxalate and pyruvate. *Geochimica et Cosmochimica Acta*, *51*(4), 919-925.

Sturhahn, W., Toellner, T. S., Alp, E. E., Zhang, X., Ando, M., Yoda, Y., ... & Dabrowski, B. (1995). Phonon density of states measured by inelastic nuclear resonant scattering. *Physical review letters*, *74*(19), 3832.

Suga, H., Miyahara, M., Ito, M., Takeichi, Y., Yabuta, H., Yamaguchi, A., ... & Ohtani, E. (2019, March). Search for the Martian carbonaceous materials in the Northwest Africa 7034. In *Lunar and Planetary Science Conference* (p. 2000).

Szpunar, M., Hand, M., Barovich, K., Jagodzinski, E., & Belousova, E. (2011). Isotopic and geochemical constraints on the Paleoproterozoic Hutchison Group, southern Australia: Implications for Paleoproterozoic continental reconstructions. *Precambrian Research*, *187*(1–2), 99–126.

Tebo, B. M., & Emerson, S. (1985). Effect of oxygen tension, Mn (II) concentration, and temperature on the microbially catalyzed Mn (II) oxidation rate in a marine fjord. *Applied and Environmental Microbiology*, *50*(5), 1268-1273.

Tekin, T., & Bayramoğlu, M. (1993). Kinetics of the reduction of MnO2 with Fe2+ ions in acidic solutions. *Hydrometallurgy*, *32*(1), 9-20.

Teng, F. Z., Dauphas, N., Huang, S., & Marty, B. (2013). Iron isotopic systematics of oceanic basalts. *Geochimica et Cosmochimica Acta*, *107*, 12-26.

Thompson, A., Ruiz, J., Chadwick, O. A., Titus, M., & Chorover, J. (2007). Rayleigh fractionation of iron isotopes during pedogenesis along a climate sequence of Hawaiian basalt. *Chemical Geology*, *238*(1-2), 72-83.

Toma, J., Holmden, C., Shakotko, P., Pan, Y., & Ootes, L. (2019). Cr isotopic insights into ca. 1.9 Ga oxidative weathering of the continents using the Beaverlodge Lake paleosol, Northwest Territories, Canada. *Geobiology*, *17*(5), 467-489.

Toyoda, K., & Tebo, B. M. (2016). Kinetics of Mn (II) oxidation by spores of the marine Bacillus sp. SG-1. *Geochimica et Cosmochimica Acta*, *189*, 58-69.

Treiman, A. H., Morris, R. v., Agresti, D. G., Graff, T. G., Achilles, C. N., Rampe, E. B., Bristow, T. F., Blake, D. F., Vaniman, D. T., Bish, D. L., Chipera, S. J., Morrison, S. M., & Downs, R. T. (2014). Ferrian saponite from the Santa Monica Mountains (California, U.S.A., Earth): Characterization as an analog for clay minerals on Mars with application to Yellowknife Bay in Gale Crater. *American Mineralogist*, *99*(11–12), 2234–2250.

Vaniman, D. T., Heiken, G., Wohletz, K., Blacic, J., Vaniman, D. T., Heiken, G., Wohletz, K., & Blacic, J. (1992). Palagonites and Martian Soil Simulants. In *LPI* (Vol. 23).

Vaniman, D. T., Bish, D. L., Ming, D. W., Bristow, T. F., Morris, R. V., Blake, D. F., ... & Freissinet, C. (2014). Mineralogy of a mudstone at Yellowknife Bay, Gale crater, Mars. *science*, *343*(6169), 1243480.

Wang, Y., & Stone, A. T. (2006). Reaction of MnIII, IV (hydr) oxides with oxalic acid, glyoxylic acid, phosphonoformic acid, and structurally-related organic compounds. *Geochimica et Cosmochimica Acta*, *70*(17), 4477-4490.

Weigand, P. W., Savage, K. L., Nicholson, C., & Barth, A. (2002). The Conejo Volcanics and other Miocene volcanic suites in southwestern California. *SPECIAL PAPERS-GEOLOGICAL SOCIETY OF AMERICA*, 187-204.

Weldon, R. J., Thomas, W. M., Boslough, M. B., & Ahrens, T. J. (1982). Shock-induced color changes in nontronite: Implications for the Martian fines. *Journal of Geophysical Research*, *87*(B12), 10102.

Wiederhold, J. G., Teutsch, N., Kraemer, S. M., Halliday, A. N., & Kretzschmar, R. (2007a). Iron isotope fractionation during pedogenesis in redoximorphic soils. *Soil Science Society of America Journal*, *71*(6), 1840-1850.

Wiederhold, J. G., Teutsch, N., Kraemer, S. M., Halliday, A. N., & Kretzschmar, R. (2007b). Iron isotope fractionation in oxic soils by mineral weathering and podzolization. *Geochimica et Cosmochimica Acta*, *71*(23), 5821-5833.

Wilke, M., Partzsch, G. M., Bernhardt, R., & Lattard, D. (2004). Determination of the iron oxidation state in basaltic glasses using XANES at the K-edge. *Chemical Geology*, *213*(1-3), 71-87.

Wordsworth, R., Knoll, A. H., Hurowitz, J., Baum, M., Ehlmann, B. L., Head, J. W., & Steakley, K. (2021). A coupled model of episodic warming, oxidation and geochemical transitions on early Mars. *Nature Geoscience*, *14*(3), 127-132.

Wu, B., Amelung, W., Xing, Y., Bol, R., & Berns, A. E. (2019). Iron cycling and isotope fractionation in terrestrial ecosystems. *Earth-Science Reviews*, *190*, 323-352.

Yamaguchi, K. E., Johnson, C. M., Beard, B. L., Beukes, N. J., Gutzmer, J., & Ohmoto, H. (2007). Isotopic evidence for iron mobilization during Paleoproterozoic lateritization of the Hekpoort paleosol profile from Gaborone, Botswana. *Earth and Planetary Science Letters*, *256*(3-4), 577-587.

Yang, W., & Holland, H. D. (2003). The Hekpoort paleosol profile in strata 1 at Gaborone, Botswana: Soil formation during the great oxidation event. *American Journal of Science*, *303*(3), 187–220.

Yokota, K., Kanzaki, Y., & Murakami, T. (2013). Weathering model for the quantification of atmospheric oxygen evolution during the Paleoproterozoic. *Geochimica et cosmochimica acta*, *117*, 332-347.

APPENDIX

Following is iron PDOS derived from NRIXS measurements for clay samples NAu-2, WASCDB1, API-H33a, CCa-1, CHLCLV1, and MUGPLA1B.

NAu-2

Element: Fe

Total energy range: -106.351 to 136.387

Energy cutoff (left and right in meV): 24.8 and 17.400000000000002

Baseline subtracted: linear

a= 0.00012199196251111843 ± 0.003495963382954267

b= 9.355023028765043 ± 0.38271994252792574

Input temperature (K): 300

Temperature from detailed balance (K): 294.0517580382228

----------From S----------

lamb-mossbauer factor from S: 0. ± 0.002300517127238267

Mean square displacement <z^2> from S (A^2): Indeterminate ± Indeterminate

Internal energy/atom from S (meV): 29.692038459440003 ± 0.8339245936967722

Kinetic energy/atom from S (meV): 14.846019229720001 ± 0.4169622968483861

Force constant from S (N/m): 277.3705268737093 ± 21.968340041848514

----------beta-value coefficients from S----------

1000ln(beta56Fe/54Fe)=A1/T^2+A2/T^4+A3/T6 (T in K)

A1: 791461.6955474715 ± 62685.46212843092

A2: -5.174010047627436e9 ± 1.3148185944747858e9

A3: 7.699965682802144e13 ± 4.6366159297131484e13

1000ln(beta56Fe/54Fe)=B1<F>/T2-B2<F>^2/T^4 (T in K)

B1: 2904.4824915408

B2: 56441.93474404957

----------From g----------

lamb-mossbauer factor from g: 0.6956853292744357

Mean square displacement <z^2> (A^2): 0.006810013890197816

d<z^2>/dT (A^2/K): 0.00002116858540829335

Critical temperature (K): 886.5835249046385

Resilience (N/m): 65.22166093626144

Internal energy/atom from g (meV): 29.717020182350698

Kinetic energy/atom from g (meV): 14.858510091175349

Vibrational entropy (kb/atom): 1.034053864171201

Helmholtz free energy (meV): 2.984631832615584

Vibrational specific heat (kb/atom): 0.8687671407181593

lamb-mossbauer factor at T=0 from g: 0.9153781178062228

Kinetic energy/atom at T=0 from g (meV): 7.817315929114969

Force constant from g (N/m): 277.4190007956014

----------beta-value coefficients from g----------

1000ln(beta56Fe/54Fe)=A1/T^2+A2/T^4+A3/T6 (T in K)

A1: 791600.0132441748

A2: -5.186528378661208e9

A3: 7.857569336417512e13

----------Velocities from g----------

Input density (g/cc): 3.5 ± 0.

Input bulk modulus (GPa): 100. ± 0.

Debye velocity (m/s): 2967.8417227774135 ± 35.304089559849764

p-wave velocity (m/s): 6145.360744053009 ± 20.011873206519425

s-wave velocity (m/s): 2625.932706171157 ± 33.609493260976976

Poisson ratio: 0.38831330010490445

Comparison 1000ln(beta56Fe/54Fe) at 300 K----------

from A1-A3 S coefficients (‰): 8.260875838787479

from A1-A3 g coefficients (‰): 8.263029144804504

from kinetic energy from S (‰): 8.252121855499535

from kinetic energy from g (‰): 8.305807146215953

WASCDB1

Element: Fe

Total energy range: -106.019 to 140.172

Energy cutoff (left and right in meV): 15.200000000000001 and 3.4000000000000004

Baseline subtracted: linear

a= 0.00007736221465774553 ± 0.005341363966955912

b= 8.638253571644166 ± 0.576155431496014

Input temperature (K): 300

Temperature from detailed balance (K): 299.34962549480804

----------From S----------

lamb-mossbauer factor from S: 2.6201263381153694e-14 ± 0.0022546804802178635

Mean square displacement <z^2> from S (A^2): 0.5869222922138811 ± 1.4381829980219066e9

Internal energy/atom from S (meV): 29.818347347364526 ± 1.2081108008940513

Kinetic energy/atom from S (meV): 14.909173673682263 ± 0.6040554004470257

Force constant from S (N/m): 288.09946128394245 ± 43.710028706500154

----------beta-value coefficients from S----------

1000ln(beta56Fe/54Fe)=A1/T^2+A2/T^4+A3/T6 (T in K)

A1: 822076.1256942155 ± 124724.18689324828

A2: -6.022311663642034e9 ± 3.5522808493073072e9

A3: 1.19366170092366e14 ± 1.637187905271709e14

1000ln(beta56Fe/54Fe)=B1<F>/T2-B2<F>^2/T^4 (T in K)

B1: 2904.4824915408

B2: 57023.47326218192

----------From g----------

lamb-mossbauer factor from g: 0.6956211460636321

Mean square displacement <z^2> (A^2): 0.006811745460475802

d<z^2>/dT (A^2/K): 0.00002147394760844943

Critical temperature (K): 873.9761971452799

Resilience (N/m): 64.29420082298938

Internal energy/atom from g (meV): 29.855446868382074

Kinetic energy/atom from g (meV): 14.927723434191037

Vibrational entropy (kb/atom): 1.0260428746650112

Helmholtz free energy (meV): 3.330158835144264

Vibrational specific heat (kb/atom): 0.8655749143846032

lamb-mossbauer factor at T=0 from g: 0.9156441129187016

Kinetic energy/atom at T=0 from g (meV): 7.927594326377463

Force constant from g (N/m): 288.1212188785172

----------beta-value coefficients from g----------

1000ln(beta56Fe/54Fe)=A1/T^2+A2/T^4+A3/T6 (T in K)

A1: 822138.2098056286

A2: -6.029744414622246e9

A3: 1.2061569400555814e14

----------Velocities from g----------

Input density (g/cc): 3.5 ± 0.

Input bulk modulus (GPa): 100. ± 0.

Debye velocity (m/s): 2904.1735490591095 ± 30.03753444481815

p-wave velocity (m/s): 6112.6325512123385 ± 16.852680791402808

s-wave velocity (m/s): 2568.002356119263 ± 28.595732791466876

Poisson ratio: 0.39283859071237204

Comparison 1000ln(beta56Fe/54Fe) at 300 K----------

from A1-A3 S coefficients (‰): 8.554423509585362

from A1-A3 g coefficients (‰): 8.555909734039984

from kinetic energy from S (‰): 8.523557472351731

from kinetic energy from g (‰): 8.603283701738981

API-H33a

Element: Fe

Total energy range: -98.6219 to 117.402

Energy cutoff (left and right in meV): 13. and 11.4

Baseline subtracted: linear

a= 0.001126890718598957 ± 0.002405088327418908

b= 2.603134649279287 ± 0.24502642316191237

Input temperature (K): 300

Temperature from detailed balance (K): 285.11243817767263

----------From S----------

lamb-mossbauer factor from S: -1.3322676295501878e-14 ± 0.0038663363396507036

Mean square displacement <z^2> from S (A^2): 0.5996156524968601 ± -4.17757410221092e9

Internal energy/atom from S (meV): 29.608982351284645 ± 0.9833525989109303

Kinetic energy/atom from S (meV): 14.804491175642323 ± 0.49167629945546515

Force constant from S (N/m): 270.34928768896475 ± 24.015009519819184

----------beta-value coefficients from S----------

1000ln(beta56Fe/54Fe)=A1/T^2+A2/T^4+A3/T6 (T in K)

A1: 771426.9718418325 ± 68525.52204221358

A2: -4.688236025466929e9 ± 1.1151705354669592e9

A3: 6.062869972231293e13 ± 3.08319799303765e13

1000ln(beta56Fe/54Fe)=B1<F>/T2-B2<F>^2/T^4 (T in K)

B1: 2904.4824915408

B2: 55184.667687140034

----------From g----------

lamb-mossbauer factor from g: 0.6998765665165483

Mean square displacement <z^2> (A^2): 0.006697284816924455

d<z^2>/dT (A^2/K): 0.00002067006117473747

Critical temperature (K): 907.9663049796455

Resilience (N/m): 66.79468862372808

Internal energy/atom from g (meV): 29.627578793133242

Kinetic energy/atom from g (meV): 14.813789396566621

Vibrational entropy (kb/atom): 1.0309126627777658

Helmholtz free energy (meV): 2.976396866432328

Vibrational specific heat (kb/atom): 0.8707687213401725

lamb-mossbauer factor at T=0 from g: 0.9161882901975616

Kinetic energy/atom at T=0 from g (meV): 7.7711039082139015

Force constant from g (N/m): 270.47791380671237

----------beta-value coefficients from g----------

1000ln(beta56Fe/54Fe)=A1/T^2+A2/T^4+A3/T6 (T in K)

A1: 771793.9994651048

A2: -4.71472627737801e9

A3: 6.326371966384285e13

----------Velocities from g----------

Input density (g/cc): 3.5 ± 0.

Input bulk modulus (GPa): 100. ± 0.

Debye velocity (m/s): 2946.32658552825 ± 83.40988833514332

p-wave velocity (m/s): 6134.232646967266 ± 47.117137784451685

s-wave velocity (m/s): 2606.345371735639 ± 79.40621369505644

Poisson ratio: 0.38985137517061635

Comparison 1000ln(beta56Fe/54Fe) at 300 K----------

from A1-A3 S coefficients (‰): 8.075783167831457

from A1-A3 g coefficients (‰): 8.080205418885008

from kinetic energy from S (‰): 8.073635714730385

from kinetic energy from g (‰): 8.113599146816394

CCa-1

Element: Fe

Total energy range: -89.5643 to 117.524

Energy cutoff (left and right in meV): 5.800000000000001 and 14.

Baseline subtracted: linear

a= 0.0013301930040137168 ± 0.004238441695057089

b= 6.362205285163517 ± 0.4411140580079538

Input temperature (K): 300

Temperature from detailed balance (K): 291.90087976751636

----------From S----------

lamb-mossbauer factor from S: 2.0539125955565396e-14 ± 0.004162139720834302

Mean square displacement <z^2> from S (A^2): 0.5914917810054666 ± 3.374455841017449e9

Internal energy/atom from S (meV): 28.55803220661775 ± 1.4035866006078683

Kinetic energy/atom from S (meV): 14.279016103308875 ± 0.7017933003039342

Force constant from S (N/m): 189.94651059999978 ± 35.04620441079462

----------beta-value coefficients from S----------

1000ln(beta56Fe/54Fe)=A1/T^2+A2/T^4+A3/T6 (T in K)

A1: 542002.025367502 ± 100002.4360126055

A2: -1.8305537952960405e9 ± 1.6190558087482777e9

A3: 7.826015269225653e12 ± 4.321234272844009e13

1000ln(beta56Fe/54Fe)=B1<F>/T2-B2<F>^2/T^4 (T in K)

B1: 2904.4824915408

B2: 48393.55985447521

----------From g----------

lamb-mossbauer factor from g: 0.7260740110971322

Mean square displacement <z^2> (A^2): 0.006007609289513538

d<z^2>/dT (A^2/K): 0.000018238212011637583

Critical temperature (K): 1029.0328381178024

Resilience (N/m): 75.70096778779762

Internal energy/atom from g (meV): 28.567091766857093

Kinetic energy/atom from g (meV): 14.283545883428546

Vibrational entropy (kb/atom): 1.1088048410807365

Helmholtz free energy (meV): -0.09776085142888036

Vibrational specific heat (kb/atom): 0.9026070668406745

lamb-mossbauer factor at T=0 from g: 0.9134955005718636

Kinetic energy/atom at T=0 from g (meV): 6.744447263159264

Force constant from g (N/m): 189.93394395747112

----------beta-value coefficients from g----------

1000ln(beta56Fe/54Fe)=A1/T^2+A2/T^4+A3/T6 (T in K)

A1: 541966.1671373029

A2: -1.8281108563429842e9

A3: 7.59729461234004e12

----------Velocities from g----------

Input density (g/cc): 3.5 ± 0.

Input bulk modulus (GPa): 100. ± 0.

Debye velocity (m/s): 3657.682423934092 ± 168.13015147151444

p-wave velocity (m/s): 6537.695918268378 ± 105.84882608928132

s-wave velocity (m/s): 3259.9891888219354 ± 160.05990420088173

Poisson ratio: 0.3345340055142438

Comparison 1000ln(beta56Fe/54Fe) at 300 K----------

from A1-A3 S coefficients (‰): 5.806985705307748

from A1-A3 g coefficients (‰): 5.806575132172326

from kinetic energy from S (‰): 5.815162019917855

from kinetic energy from g (‰): 5.834630858274239

CHLCLV1

Element: Fe

Total energy range: -97.1197 to 117.719

Energy cutoff (left and right in meV): 16.7 and 12.8

Baseline subtracted: linear

a= 0.0007230115700695909 ± 0.00470425922448749

b= 9.551270463078405 ± 0.4672820939063236

Input temperature (K): 300

Temperature from detailed balance (K): 286.6342695081863

----------From S----------

lamb-mossbauer factor from S: 0.7464292712290956 ± 0.0037820923280602672

Mean square displacement <z^2> from S (A^2): 0.005488702276167826 ± 0.00008417512034961971

Internal energy/atom from S (meV): 29.37700714751416 ± 1.3199726351832985

Kinetic energy/atom from S (meV): 14.68850357375708 ± 0.6599863175916493

Force constant from S (N/m): 252.42692589889896 ± 35.78950222490231

----------beta-value coefficients from S----------

1000ln(beta56Fe/54Fe)=A1/T^2+A2/T^4+A3/T6 (T in K)

A1: 720286.4883504511 ± 102123.39585243106

A2: -3.9775715678028803e9 ± 1.7354799305614367e9

A3: 3.974123305342843e13 ± 4.869001320656955e13

1000ln(beta56Fe/54Fe)=B1<F>/T2-B2<F>^2/T^4 (T in K)

B1: 2904.4824915408

B2: 55686.714668511944

----------From g----------

lamb-mossbauer factor from g: 0.7442561165887389

Mean square displacement <z^2> (A^2): 0.005543422319724784

d<z^2>/dT (A^2/K): 0.00001685909802434314

Critical temperature (K): 1113.2101516599869

Resilience (N/m): 81.8934855237484

Internal energy/atom from g (meV): 29.385494698253652

Kinetic energy/atom from g (meV): 14.692747349126826

Vibrational entropy (kb/atom): 1.0352238893246501

Helmholtz free energy (meV): 2.6228588267358752

Vibrational specific heat (kb/atom): 0.8778173090274932

lamb-mossbauer factor at T=0 from g: 0.9187124066864186

Kinetic energy/atom at T=0 from g (meV): 7.564084918631247

Force constant from g (N/m): 252.43703134738232

----------beta-value coefficients from g----------

1000ln(beta56Fe/54Fe)=A1/T^2+A2/T^4+A3/T6 (T in K)

A1: 720315.3236974545

A2: -3.9654194126438327e9

A3: 3.8154897051421734e13

----------Velocities from g----------

Input density (g/cc): 3.5 ± 0.

Input bulk modulus (GPa): 100. ± 0.

Debye velocity (m/s): 3652.0574878271486 ± 69.68839626685636

p-wave velocity (m/s): 6534.229499795453 ± 43.837720758008025

s-wave velocity (m/s): 3254.772640051285 ± 66.34335324604724

Poisson ratio: 0.33500492846796226

Comparison 1000ln(beta56Fe/54Fe) at 300 K----------

from A1-A3 S coefficients (‰): 7.566639708628015

from A1-A3 g coefficients (‰): 7.566284323543016

from kinetic energy from S (‰): 7.575125011608039

from kinetic energy from g (‰): 7.593364611436642

MUGPLA1B

Element: Fe

Total energy range: -97.9896 to 114.47

Energy cutoff (left and right in meV): 33.300000000000004 and 20.400000000000002

Baseline subtracted: linear

a= 0.002609221609043184 ± 0.0031893004538596764

b= 6.763966008266661 ± 0.2908987683633857

Input temperature (K): 300

Temperature from detailed balance (K): 287.4150477946311

----------From S----------

lamb-mossbauer factor from S: 7.105427357601002e-15 ± 0.0034400287799307224

Mean square displacement <z^2> from S (A^2): 0.6114132032209443 ± 6.9780638044411e9

Internal energy/atom from S (meV): 29.553856188002275 ± 0.8197114897167396

Kinetic energy/atom from S (meV): 14.776928094001137 ± 0.4098557448583698

Force constant from S (N/m): 266.8580023496675 ± 17.89166048342398

----------beta-value coefficients from S----------

1000ln(beta56Fe/54Fe)=A1/T^2+A2/T^4+A3/T6 (T in K)

A1: 761464.7792274085 ± 51052.87898457192

A2: -4.758877984323149e9 ± 6.844254490437657e8

A3: 5.997409069280984e13 ± 1.5512690788461045e13

1000ln(beta56Fe/54Fe)=B1<F>/T2-B2<F>^2/T^4 (T in K)

B1: 2904.4824915408

B2: 57729.33300651119

----------From g----------

lamb-mossbauer factor from g: 0.7290718904500648

Mean square displacement <z^2> (A^2): 0.005930278986017833

d<z^2>/dT (A^2/K): 0.00001832885540914401

Critical temperature (K): 1023.943866083785

Resilience (N/m): 75.32659673397899

Internal energy/atom from g (meV): 29.56780310298176

Kinetic energy/atom from g (meV): 14.78390155149088

Vibrational entropy (kb/atom): 1.0345501038164278

Helmholtz free energy (meV): 2.8225859525715755

Vibrational specific heat (kb/atom): 0.8730331450441337

lamb-mossbauer factor at T=0 from g: 0.9178941523710652

Kinetic energy/atom at T=0 from g (meV): 7.691413002650823

Force constant from g (N/m): 267.46748042712693

----------beta-value coefficients from g----------

1000ln(beta56Fe/54Fe)=A1/T^2+A2/T^4+A3/T6 (T in K)

A1: 763203.8917352223

A2: -4.859503630508231e9

A3: 6.7944787603786164e13

----------Velocities from g----------

Input density (g/cc): 3.5 ± 0.

Input bulk modulus (GPa): 100. ± 0.

Debye velocity (m/s): 3275.2570075735002 ± 80.35515986064364

p-wave velocity (m/s): 6311.8426391323765 ± 47.79475222473612

s-wave velocity (m/s):2907.051203076016 ± 76.49811218733274

Poisson ratio: 0.36538109957026854

Comparison 1000ln(beta56Fe/54Fe) at 300 K----------

from A1-A3 S coefficients (‰): 7.9554729545209

from A1-A3 g coefficients (‰): 7.9733072481664555

from kinetic energy from S (‰): 7.955170542713466

from kinetic energy from g (‰): 7.985142221926598